

A Mechanistic Insight into the Nickel-Catalyzed Homocoupling Reaction of Terminal Alkynes

vom Fachbereich Chemie der Technischen Universität Kaiserslautern zur
Verleihung des akademischen Grades 'Doktor der Naturwissenschaften'

eingereichte Dissertation

D 386



vorgelegt von

Subrata Ghosh, M.Sc.

Betreuer

Prof. Hans-Jörg Krüger, Ph. D.

Tag der wissenschaftlichen Aussprache: 29. 01. 2018

Kaiserslautern 2018

Promotionskommission:

Vorsitzender: Prof. Dr. Stefan Kubik

Berichterstatter: Prof. Hans-Jörg Krüger, Ph. D.

Berichterstatter: Prof. Dr. Helmut Sitzmann

Datum der wissenschaftlichen Aussprache: 29. 01. 2018

Die vorliegende Arbeit entstand in der Zeit zwischen November 2010 und September 2017 in den Laboratorien des Fachbereichs Chemie an der Technische Universität Kaiserslautern.

Eidesstattliche Erklärung

Hiermit versichere ich, dass ich die vorliegende Arbeit eigenständig verfasst, keine anderen als die angegebenen Quellen und Hilfsmittel verwendet und Literaturzitate kenntlich gemacht habe. Ich erkläre außerdem, dass diese Arbeit weder in gleicher noch in ähnlicher Form bereits in einem anderen Prüfungsverfahren vorgelegen hat.

Kaiserslautern, den _____

Subrata Ghosh

To my parents

Abbreviations

A	Absorbance
Ad	Adamantly
ANAP	Acenaphthylene
Avg.	Average
Bu	Butyl
^t Bu	<i>tert</i> -Butyl
Cat.	Catalyst
CO	Carbon monoxide
COD	1,5-Cyclooctadiene
CT	Charge transfer
Cy	Cyclohexyl
δ	Chemical shift
d	Doublet
DCE	1,2-Dichloroethene
DFT	Density functional theory
DMF	Dimethylformamide
dppe	1,2-Bis(diphenylphosphino)ethane
ε	Molar extinction coefficient
Equiv.	Equivalent
EPR	Electron paramagnetic resonance
ESI MS	Electrospray ionization mass spectrometry
Et	Ethyl
EtCN	Propionitrile
Et ₃ N	Triethylamine
Et ₂ O	Diethyl ether
EXAFS	Extended X-ray absorption fine structure
Fc	Ferrocene
H	Magnetic field strength
HIV	Human immunodeficiency virus
I	Nuclear spin
IR	Infrared

K	Kelvin
λ	Wavelength
LMCT	Ligand to metal charge transfer
L-N ₄ Me ₂	<i>N,N'</i> -Dimethyl-2,11-diaza[3.3](2,6)pyridinophan
Me	Methyl
MeCN	Acetonitrile
MeOH	Methanol
MLCT	Metal to ligand charge transfer
mT	Militesla
<i>m/z</i>	Mass-to-charge ratio
MW	Molecular weight
NaH	Sodium hydride
NIR	Near infrared
NMR	Nuclear magnetic resonance
Ph	Phenyl
PMe ₃	Trimethylphosphine
PPh ₃	Triphenylphosphine
Pr	Propyl
^{<i>i</i>} Pr	<i>iso</i> -Propyl
Py	Pyridine
RT	Room temperature
s	Singlet
SCE	Saturated calomel electrode
SQUID	Superconducting quantum interference device
t	Triplet
T	Temperature
TBAP	Tetrabutylammonium perchlorate
TMEDA	<i>N,N,N',N'</i> -tetramethylethylenediamine
UV-Vis	Ultraviolet visible
$\tilde{\nu}$	Wavenumber
v	Velocity
<i>vs</i>	Versus
χ_M	Molar susceptibility

Table of Contents

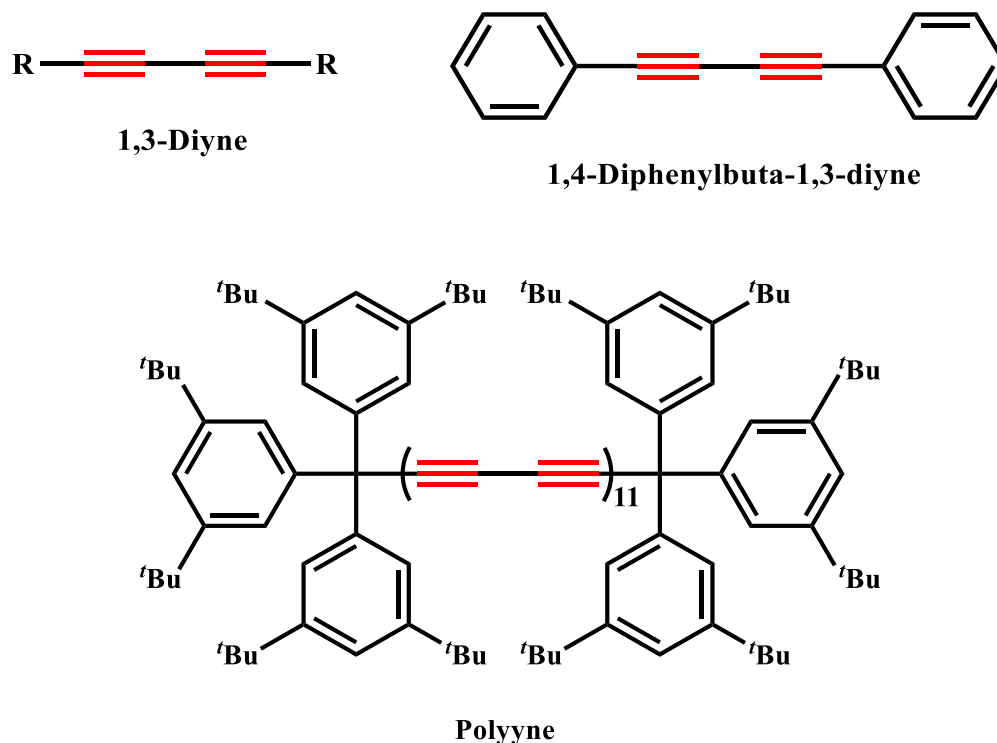
1	Introduction	1
1.1	Copper-Catalyzed Homocoupling of Terminal Alkynes	4
1.2	Palladium-Catalyzed Homocoupling of Terminal Alkynes	7
1.3	Nickel-Catalyzed Homocoupling of Terminal Alkynes.....	9
1.4	Nickel-O ₂ Chemistry	13
1.5	Motivation	19
2	Result and Discussions	21
2.1	Synthesis and Characterization of [Ni(L-N ₄ Me ₂)(MeCN) ₂](ClO ₄) ₂ (1)	21
2.2	Synthesis and Characterization of Dinuclear Nickel(I)-Diyne Complexes	27
2.2.1	Synthesis.....	28
2.2.2	X-ray Structures Analysis	28
2.2.3	Magnetochemistry	45
2.2.4	Spectroscopic Studies.....	51
2.2.5	Electrochemistry.....	63
2.2.6	Stoichiometric Reaction in Presence of Radical Inhibitor	67
2.2.7	Stoichiometric Reaction at Low Temperature	69
2.3	Synthesis and Characterization of [Ni(L-N ₄ Me ₂)(PhC ₂ Ph)](ClO ₄) · MeOH (3)	71
2.3.1	Synthesis.....	71
2.3.2	X-Ray Structure Analysis.....	72
2.3.3	Spectroscopic Studies.....	75
2.3.4	Electrochemistry.....	78
2.4	Reactivity of [{Ni(L-N ₄ Me ₂) ₂ (μ-RC ₄ R)](ClO ₄) ₂ [R = Ph] (2a) with Molecular Oxygen	80
2.4.1	Spectroscopic Studies.....	80
2.4.2	Reactivity in Presence of Lithium Perchlorate.....	90
2.5	Reactivity of [Ni(L-N ₄ Me ₂)(PhC ₂ Ph)](ClO ₄) · MeOH (3) with Molecular Oxygen .	91

2.6	Generation and Characterization of $[\text{Ni}(\text{L-N}_4\text{Me}_2)(\text{O}_2)]^+$ (5).....	99
2.7	Nickel-Mediated Catalytic Reaction	104
2.8	Spectroscopy Studies on Catalytic Reaction.....	105
2.9	Proposed Mechanism	108
3	Summary	110
4	Experimental Section	112
4.1	Physical Methods	112
4.2	Starting Materials	114
4.3	Experimental Details	115
4.3.1	Synthesis of $[\text{Ni}(\text{L-N}_4\text{Me}_2)(\text{MeCN})_2](\text{ClO}_4)_2$ (1).....	115
4.3.2	Synthesis of $[\{\text{Ni}(\text{L-N}_4\text{Me}_2)\}_2(\mu\text{-RC}_4\text{R})](\text{ClO}_4)_2$ (2a-2g).....	116
4.3.3	Stoichiometric Reaction in Presence of Radical Inhibitor TEMPO.....	122
4.3.4	Stoichiometric Reaction at Low Temperature to Room Temperature	123
4.3.5	Synthesis of $[\text{Ni}(\text{L-N}_4\text{Me}_2)(\text{PhC}_2\text{Ph})](\text{ClO}_4) \cdot \text{MeOH}$ (3).....	125
4.3.6	Reactivity of $[\{\text{Ni}(\text{L-N}_4\text{Me}_2)\}_2(\mu\text{-RC}_4\text{R})](\text{ClO}_4)_2$ [R= Ph] (2a) with Molecular Oxygen	127
4.3.7	Reactivity of $[\{\text{Ni}(\text{L-N}_4\text{Me}_2)\}_2(\mu\text{-RC}_4\text{R})](\text{ClO}_4)_2$ [R= Ph] (2a) with Molecular Oxygen in Presence of Lithium Perchlorate	127
4.3.8	Reactivity of $[\text{Ni}(\text{L-N}_4\text{Me}_2)(\text{PhC}_2\text{Ph})](\text{ClO}_4) \cdot \text{MeOH}$ (3) with Molecular Oxygen	128
4.3.9	Generation of $[\text{Ni}(\text{L-N}_4\text{Me}_2)(\text{O}_2)]^+$	129
4.3.10	Nickel-Mediated Catalytic Reaction	131
5	Literature	132
6	Acknowledgement.....	143
7	Appendix	144
7.1	$[\text{Ni}(\text{L-N}_4\text{Me}_2)(\text{MeCN})_2](\text{ClO}_4)_2$ (1)	144
7.2	$[\{\text{Ni}(\text{L-N}_4\text{Me}_2)\}_2(\mu\text{-RC}_4\text{R})](\text{ClO}_4)_2$ (2a-2g)	147

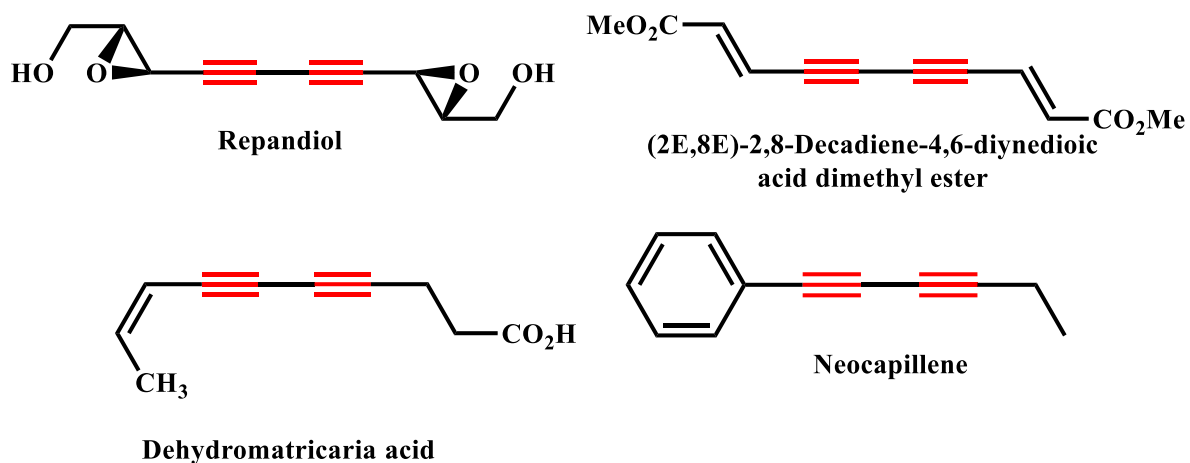
7.2.1	[{Ni(L-N ₄ Me ₂) ₂ (μ-RC ₄ R)](ClO ₄) ₂ [R = Ph] (2a).....	147
7.2.2	[{Ni(L-N ₄ Me ₂) ₂ (μ-RC ₄ R)](ClO ₄) ₂ [R = C ₆ H ₄ Me-4] (2b).....	154
7.2.3	[{Ni(L-N ₄ Me ₂) ₂ (μ-RC ₄ R)](ClO ₄) ₂ [R = C ₆ H ₄ F-4] (2c).....	161
7.2.4	[{Ni(L-N ₄ Me ₂) ₂ (μ-RC ₄ R)](ClO ₄) ₂ [R = C ₆ H ₄ OMe-4] (2d).....	168
7.2.5	[{Ni(L-N ₄ Me ₂) ₂ (μ-RC ₄ R)](ClO ₄) ₂ [R = C ₆ H ₄ NMe ₂ -4] (2e).....	175
7.2.6	[{Ni(L-N ₄ Me ₂) ₂ (μ-RC ₄ R)](ClO ₄) ₂ [R = ⁿ C ₃ H ₇] (2f).....	182
7.2.7	[{Ni(L-N ₄ Me ₂) ₂ (μ-RC ₄ R)](ClO ₄) ₂ · EtOH [R = Fc] (2g).....	188
7.3	[Ni(L-N ₄ Me ₂)(PhC ₂ Ph)](ClO ₄) · MeOH (3).....	198
7.4	Reactivity of [{Ni(L-N ₄ Me ₂) ₂ (μ-RC ₄ R)](ClO ₄) ₂ [R = Ph] (2a) with Oxygen.....	201
7.5	Reactivity of [Ni(L-N ₄ Me ₂)(PhC ₂ Ph)](ClO ₄)·MeOH (3) with Oxygen.....	203
7.6	[Ni(L-N ₄ Me ₂)(O ₂)] ⁺ (4).....	205
7.7	Nickel-Mediated Catalytic Reaction.....	206
7.8	Spectroscopy Studies on Catalytic Reaction.....	207
8	Curriculum Vitae.....	209

1 Introduction

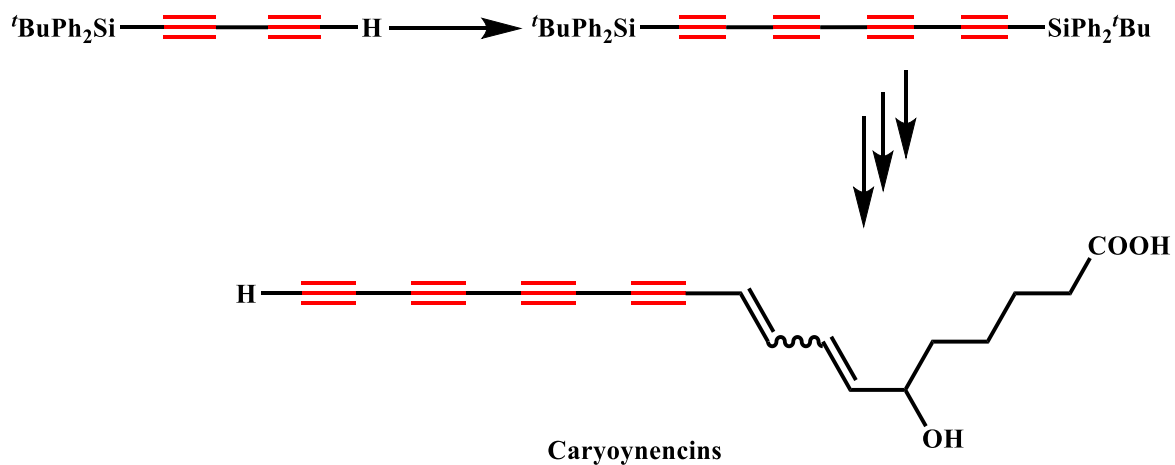
1,3-Diynes are a kind of conjugated diyne units with the rod-like molecular structure (Scheme 1.1).^[1] They are frequently found as an important structural motif in natural products, pharmaceuticals and other bioactive compounds with anti-HIV, antifungal, anti-inflammatory and antibacterial or anticancer properties (Scheme 1.2).^[2-10] They have been isolated from numerous natural sources which includes plants, fungi, bacteria, marine sponges and corals.^[8] For example, symmetrical 1,3-diyne repandiol isolated from the hedgehog mushroom (*Hydnum repandum*), displays cytotoxic activity against several types of tumor cells.^[11] Caryoynencins (Scheme 1.3), isolated from liquid culture of the plant pathogen *Pseudomonas caryophylli* are polyne antibiotics with effective antibacterial activities.^[12-13] (2E,8E)-2,8-Decadiene-4,6-diyndioic acid dimethyl ester has been isolated from the waxcap mushroom (*Hygrophorus virgineus*).^[14] 1,3-Diynes have been played an integral role in the construction of supramolecular materials, macrocyclic annulenes, and carbon rich oligomers and polymers (Scheme 1.4 and Scheme 1.5).^[15-19] They are also found as essential building blocks in synthetic transformations, liquid crystals, non-linear materials and molecular wires.^[20-22] Therefore, much consideration has been dedicated in the synthesis of 1,3-diyne derivatives.



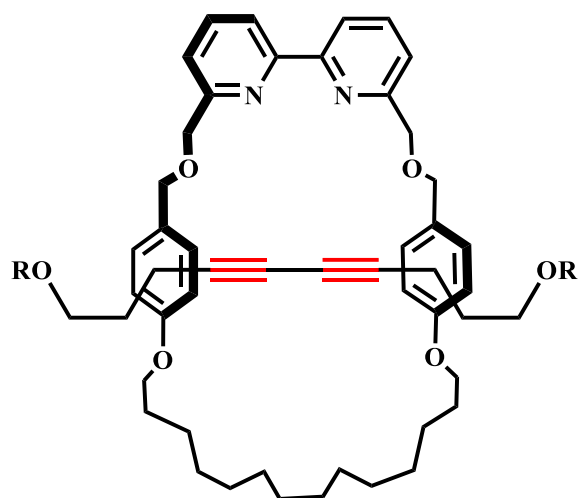
Scheme 1.1: 1,3-Diynes.

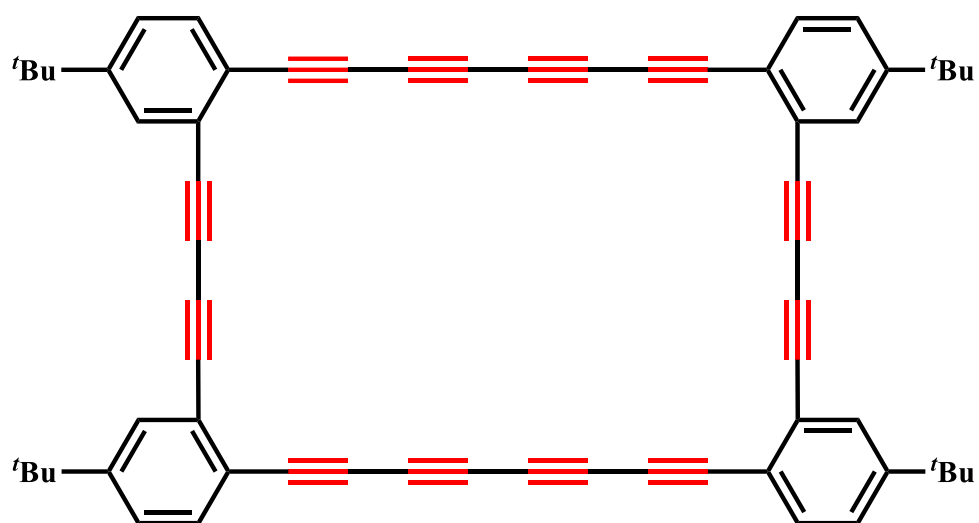
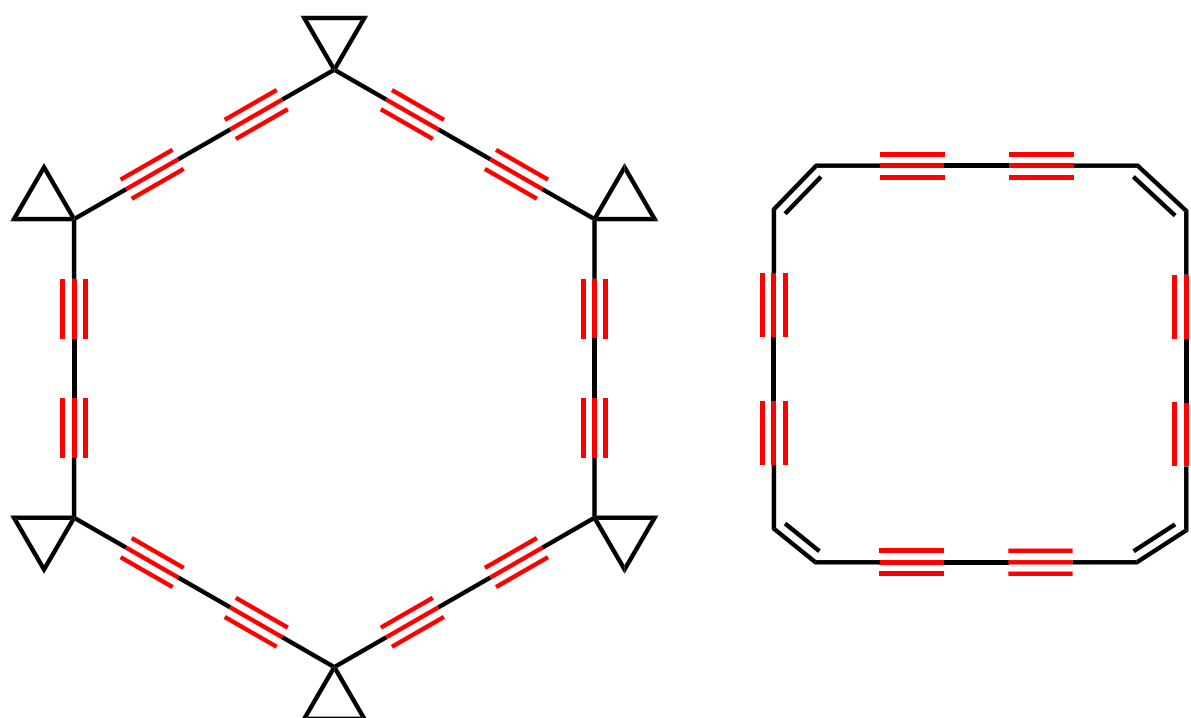


Scheme 1.2: Examples of natural 1,3-diyne.



Scheme 1.3: Synthesis of caryoynencins.

Scheme 1.4: Supramolecular material containing 1,3-diyne unit; $\text{R} = (4\text{'BuC}_6\text{H}_4)_3\text{CC}_6\text{H}_4$.

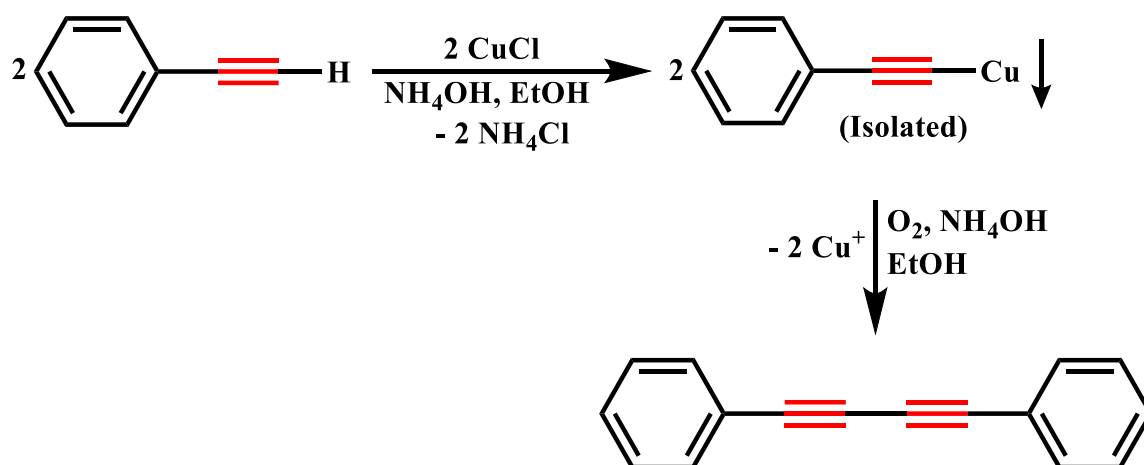


Scheme 1.5: Examples of macrocyclic 1,3-diyne.

Transition metal-mediated oxidative homocoupling reaction of terminal alkynes is an important method for the synthesis of 1,3-diynes.

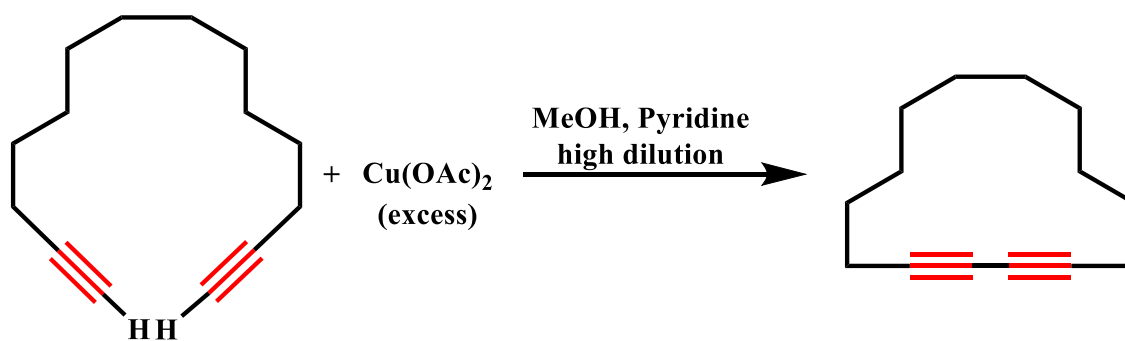
1.1 Copper-Catalyzed Homocoupling of Terminal Alkynes

Homocoupling reaction of terminal alkynes was first reported by Carl Glaser in 1869.^[23] Copper(I) phenylacetylide, prepared by the reaction of copper(I) chloride and phenylacetylene, undergoes oxidative dimerization to 1,4-diphenylbuta-1,3-diyne (diphenyldiacetylene) when exposed to air (Scheme 1.6).



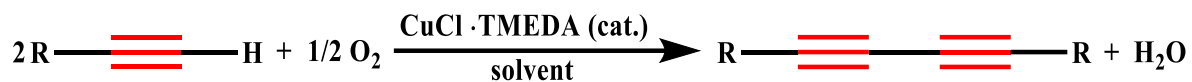
Scheme 1.6: Glaser coupling reaction.

Two important modifications in Glaser reaction were independently introduced by Eglinton and Hay.^[24-26] In 1956, Eglinton and Galbraith reported the improvement of the homocoupling reaction by using stoichiometric or excess amount of copper(II) acetate in the presence of methanolic pyridine (Scheme 1.7).



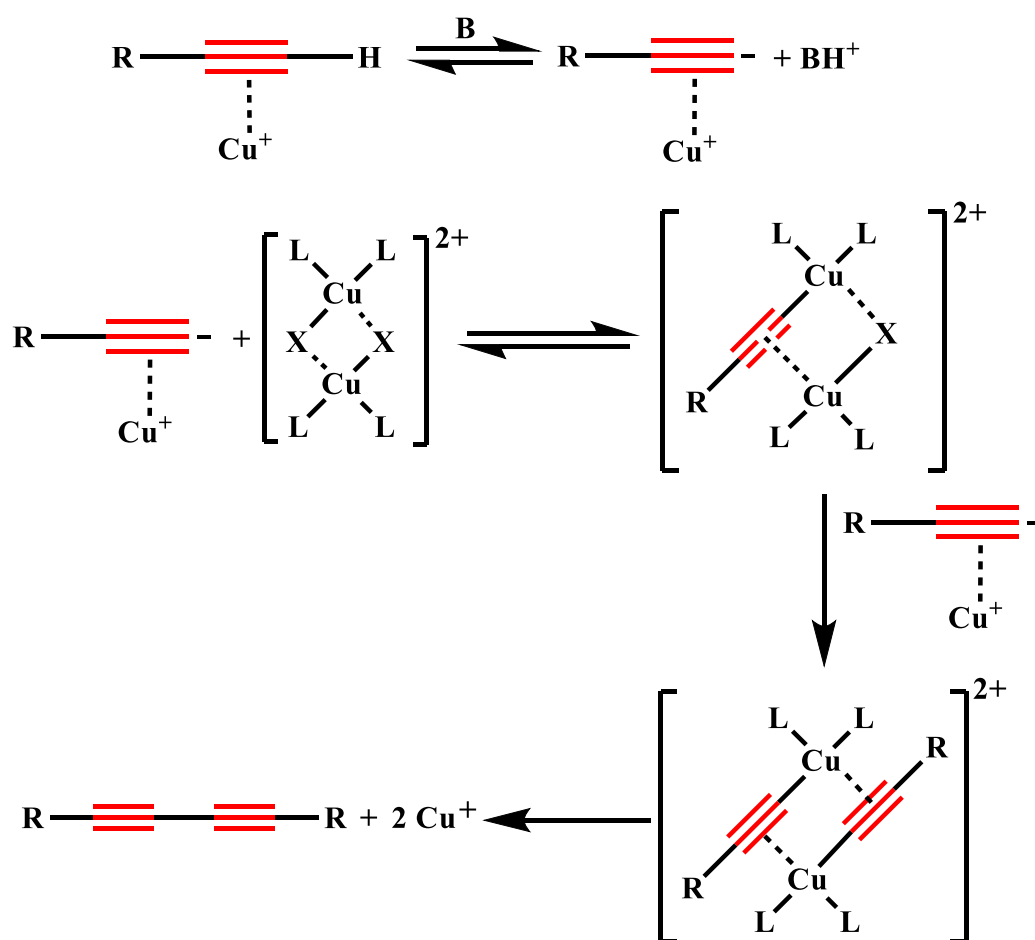
Scheme 1.7: Eglinton reaction conditions.

In 1962, Hay published oxidative homocoupling reaction with oxygen in presence of catalytic amount of copper(I) chloride and bidentate ligand TMEDA (*N,N,N',N'*-tetramethylethylenediamine) (Scheme 1.8). Since then, several modified copper-mediated Glaser-Eglinton-Hay coupling reactions have been widely used in the synthesis of 1,3-diyne derivatives.^[27-33]



Scheme 1.8: Hay coupling reaction.

The well accepted mechanism for copper-mediated homocoupling reaction was proposed by Bohlmann in 1964 (Scheme 1.9).^[34] Initially, the side-on coordination of Cu(I) ions to the alkyne triple bond activate its deprotonation in aid of base.



Scheme 1.9: General mechanism for copper-catalyzed homocoupling reaction of terminal alkynes. L = N ligand; X = Cl⁻, OAc⁻; B = base (e.g. TMEDA).

Subsequently, deprotonated terminal alkyne reacts with copper(II) species to produce dinuclear copper(II) acetylide complex, which collapses through innersphere electron transfer, generating coupling product 1,3-diyne and copper(I) species. Regeneration of copper(II) species was fulfilled by the oxidation of copper(I) species with oxidant to complete the catalytic cycle. However, isolation of these dinuclear copper(II) acetylide and a copper(I) intermediate along with detailed information regarding the crucial cycle closing oxidation step from copper(I) to copper(II) species has remained elusive to date.

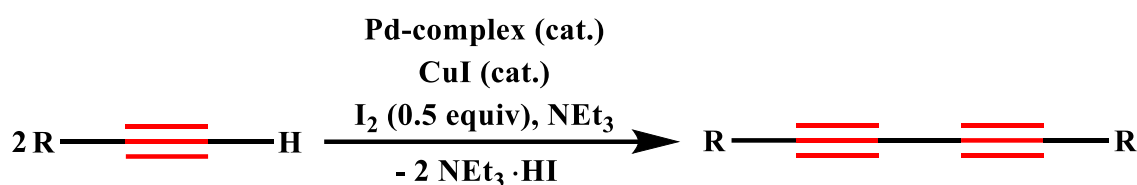
Recently, Lei and coworkers provided the evidence for the reduction of copper(II) to copper(I) species by terminal alkynes in the presence of TMEDA in a stoichiometric reaction, in which TMEDA plays dual role as both ligand and base (Scheme 1.10).^[35] The structures of the starting Cu(II) species and the obtained Cu(I) species were determined by EXAFS spectroscopy as [(TMEDA)CuCl₂] and [(TMEDA)CuCl]₂ dimer complex, respectively.



Scheme 1.10: Stoichiometric reaction conditions by Lei and coworkers.

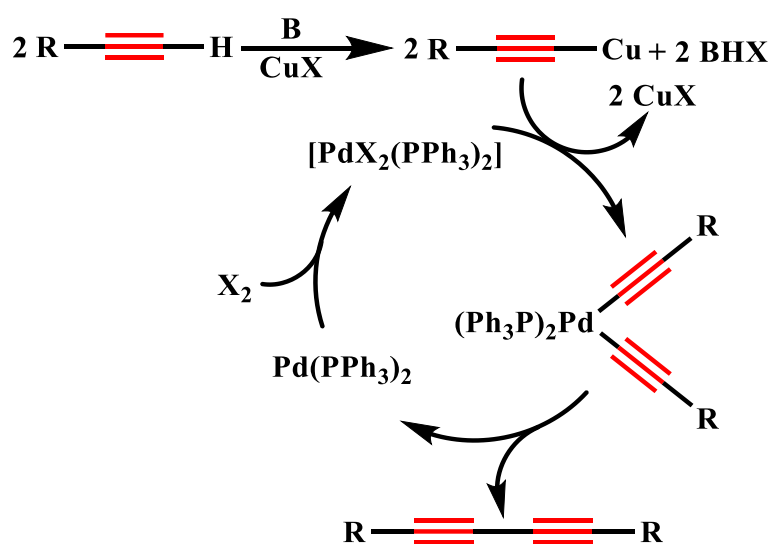
1.2 Palladium-Catalyzed Homocoupling of Terminal Alkynes

Palladium-catalyzed homocoupling of terminal alkynes have been represented as a major alternative to Glaser coupling reaction for the synthesis of 1,3-diyne derivatives. The reaction was first reported by Sonagashira and co-workers in 1975.^[36] Formation of 1,3-diyne was observed as a side product during the reaction of $[\text{Pd}(\text{PPh}_3)_2\text{Cl}_2]$ and terminal alkyne in presence of copper(I) iodide and diethylamine. In 1985, Rossi and co-workers described significant modification using $[\text{Pd}(\text{PPh}_3)_4]$ and copper(I) iodide.^[37] From then onward, several modified palladium-mediated homocoupling reaction of terminal alkynes have been widely applied in the synthesis of 1,3-diynes.^[38-44] A general procedure for palladium-mediated homocoupling reaction of terminal alkynes is shown in Scheme 1.11.



Scheme 1.11: Palladium-mediated homocoupling of terminal alkynes.

The well accepted mechanisms for palladium-catalyzed homocoupling of terminal alkynes are depicted in Scheme 1.12.

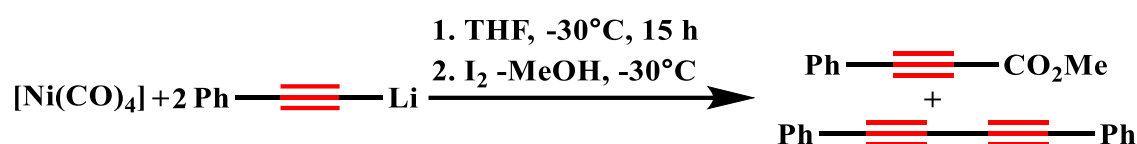


Scheme 1.12: Mechanism proposed for palladium-mediated homocoupling reaction of terminal alkynes.
 $\text{X} = \text{Cl, I}$; $\text{B} = \text{base (e.g. NEt}_3, \text{ }^i\text{Pr}_2\text{NH)}$.

The catalytic cycle involves formation of the dialkynylpalladium(II) intermediate by transmetalation of copper(I) acetylide, which is formed *in situ* by the reaction of copper(I) iodide and terminal alkyne in presence of a base. Successive reductive elimination leads to the dimerized product 1,3-diyne and a palladium(0) species, which is reoxidized to palladium(II) by oxidant. Evidence for the formation of dialkynylpalladium(II) intermediate and its isolation and structural characterization has to be determined.

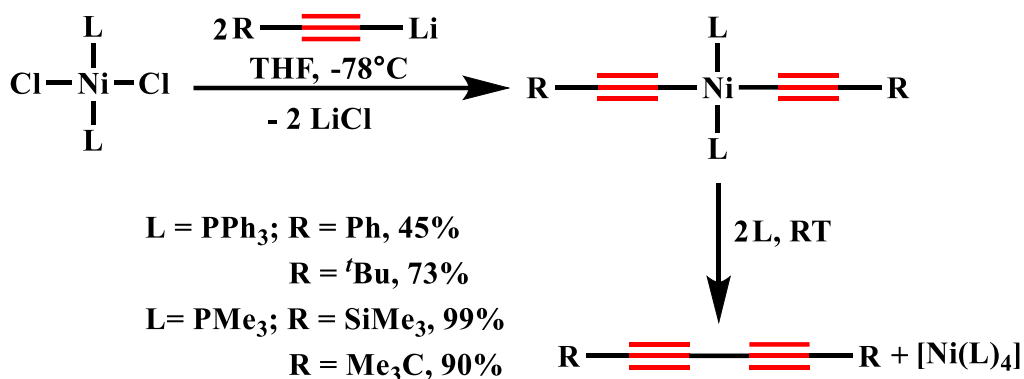
1.3 Nickel-Catalyzed Homocoupling of Terminal Alkynes

There has been less thorough investigation of the potential of nickel complexes for the synthesis of 1,3-diyne derivatives by homocoupling of terminal alkynes in comparison to copper- or palladium-mediated reactions. Nickel-mediated homocoupling reaction was first reported by Rhee and co-workers in 1969.^[45] Formation of 1,3-diyne product diphenyldiacetylene was observed in 48% yield as a side product from the reaction of $[\text{Ni}(\text{CO})_4]$ with two equivalent lithium phenylacetylide in THF at -30°C over 15 h stirring and subsequent addition of iodine-methanol solution (Scheme 1.13). A detailed description about mechanism was not reported by the authors.



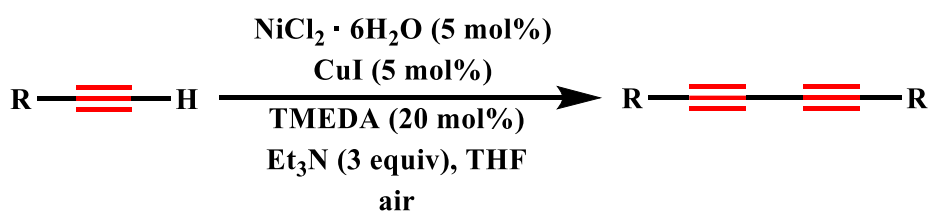
Scheme 1.13: Formation of diphenyldiacetylene from reaction of $\text{Ni}(\text{CO})_4$ with lithium phenylacetylide.

In 1989 and 1994, Klein *et al* and Smith *et al* independently found that the stoichiometric reaction of $[\text{Ni}(\text{PR}_3)_2\text{Cl}_2]$ with two equivalents of lithium acetylide gave the desired 1,3-diyne in good yield (Scheme 1.14).^[46-47] The *trans*-dialkynynickel(II) complexes ($\text{R} = \text{SiMe}_3$ and Me_3C) can be isolated at -78°C and undergo reductive elimination to corresponding 1,3-diyne and nickel(0) species upon warm to room temperature under inert atmosphere. The same *trans*-dialkynynickel(II) complex ($\text{R} = \text{Me}_3\text{C}$) produces 1,3-diyne and $[\text{Ni}(\text{PMe}_3)_4]$ upon reaction with two equivalent PMe_3 at room temperature over 15 h.^[46] Whereas, Smith *et al* described that addition of lithium acetylide to $[\text{Ni}(\text{PPh}_3)_2\text{Cl}_2]$ in THF at -78°C under inert atmosphere and subsequent stirring for 12 h under air at room temperature resulted in moderate to good yields of the homocoupled products, 1,3-diynes. The authors also suggested from the results of cross-coupling experiments that the 1,3-diynes are produced by reductive elimination from intermediate dialkynynickel(II) species.^[47] Recently homocoupling reaction of terminal alkynes for the synthesis of rotaxanes using stoichiometric amounts of nickel and copper salts have been reported.^[48]



Scheme 1.14: Nickel-mediated stoichiometric homocoupling reactions.

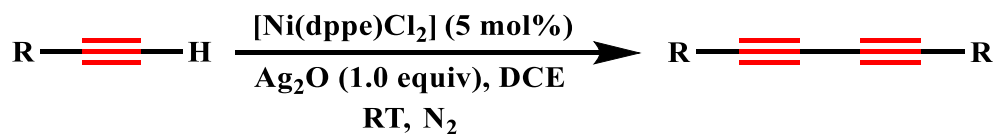
In the year 2009, for the first time, Lei and co-workers carried out oxidative homocoupling reaction of terminal alkynes using catalytic amounts of NiCl₂·6H₂O and CuI in presence of air (Scheme 1.15).^[49]



Scheme 1.15: Nickel-catalyzed homocoupling reaction by Lei and co-workers.

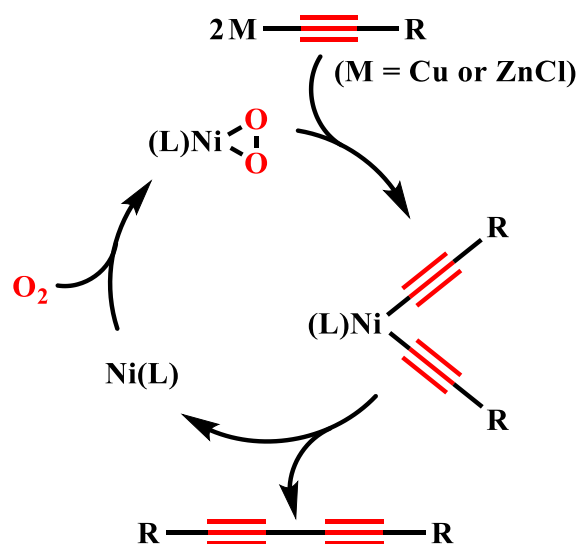
The authors found that the homocoupling of phenylacetylene using modified Hay conditions [CuI (5 mol%), TMEDA (20 mol%)] under air gave 25% 1,3-diyne product after 1 h. Unexpectedly, addition of 5 mol% of NiCl₂·6H₂O greatly enhanced the reaction, and the homocoupling was completed within 1 h in 93% yield. The authors described this enhanced reaction rate by cooperative effect where nickel complex undergoes redox reaction with oxygen and form a NiO₂ species, while copper forms copper acetylide that transmetalate to nickel complex and generates a dialkynylnickel intermediate. The final reductive elimination releases the coupling product and regenerates the nickel(0) complex. Isolation and structure determination or spectroscopic evidence for the formation of dialkynylnickel intermediate and NiO₂ species which could be nickel(II)-superoxo or nickel(III)-peroxo were not described.

Recently homocoupling reaction of aromatic terminal alkynes using catalytic amount of [Ni(dppe)Cl₂] with stoichiometric amount of Ag₂O as a base and as an oxidant was reported by Yang and co-workers (Scheme 1.16).^[50]

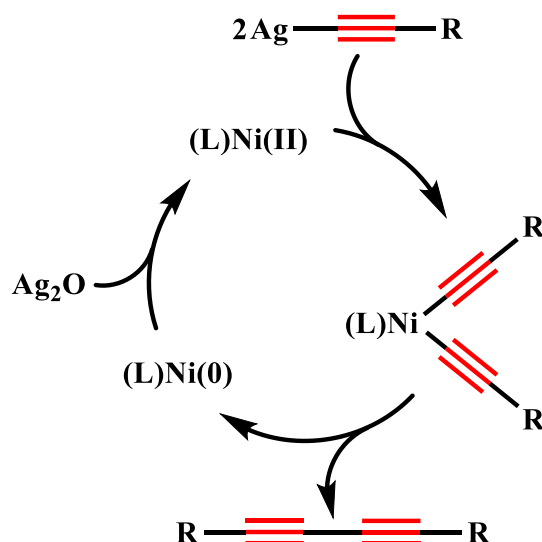


Scheme 1.16: Nickel-catalyzed homocoupling reaction by Yang and co-workers.

Although a detailed study on the reported nickel-acetylene chemistry has not been carried out, a generalized mechanism features a nickel(II)/nickel(0) catalytic cycle (Scheme 1.17 and Scheme 1.18). The general mechanism is composed of three steps: (a) transmetalation of nickel(II) with metal acetylide to form a dialkynylnickel(II) intermediate, (b) subsequent reductive elimination of dialkynylnickel(II) species to give 1,3-diyne product and a nickel(0) species, and (c) reoxidation of nickel(0) to nickel(II) by an oxidant.



Scheme 1.17: Mechanism proposed by Lei and co-workers for nickel-catalyzed homocoupling reaction of terminal alkynes ; L = TMEDA.

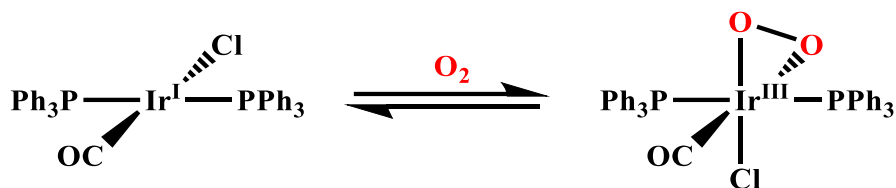


Scheme 1.18: Mechanism proposed by Yang and co-workers for nickel-catalyzed homocoupling reaction of terminal alkynes; L = dppe.

Apart from copper, palladium and nickel, other transition metals have been barely used for the homocoupling reaction of terminal alkynes. TiCl_4 , $\text{Co}_2(\text{CO})_8$, $\text{Fe}(\text{acac})_3$, $[\text{Au}(\text{PPh}_3)(\text{NTf}_2)]$ and $[\text{Ru}(\text{dppp})_2(\text{CH}_3\text{CN})\text{Cl}][\text{BPh}_4]$ have been used as catalyst for homocoupling of terminal alkynes.^[51-55] There has been no detailed mechanistic investigations through intermediates isolation and spectroscopic characterization. Most studies have focused on the examination of different substrates, catalyst precursors, and additives. Periasamy *et al* reported that the reaction of TiCl_4 with a mixture of terminal alkynes and triethylamines produces 1,3-diynes in moderate to good yield over 6 h (62% with phenylacetylene).^[55] Krafft *et al* described that homocoupling of terminal alkynes proceeds using $\text{Co}_2(\text{CO})_8$ pretreated with phenanthroline to give good yields of 1,3-diynes under mild conditions.^[54] $\text{Fe}(\text{acac})_3/\text{Cu}(\text{acac})_2$ promoted oxidative homocoupling reaction of terminal alkynes using K_2CO_3 as a base and air as an oxidant in DMF at 50°C within 8 - 12 h in good yield has been studied by Meng *et al*.^[53] Bhattacharjee and co-authors carried out the homocoupling reaction in the presence of $[\text{Ru}(\text{dppp})_2(\text{CH}_3\text{CN})\text{Cl}][\text{BPh}_4]$ and AgNO_3 in DMF at 90°C under air over 0.5 – 5 h in moderate to good yields.^[51]

1.4 Nickel-O₂ Chemistry

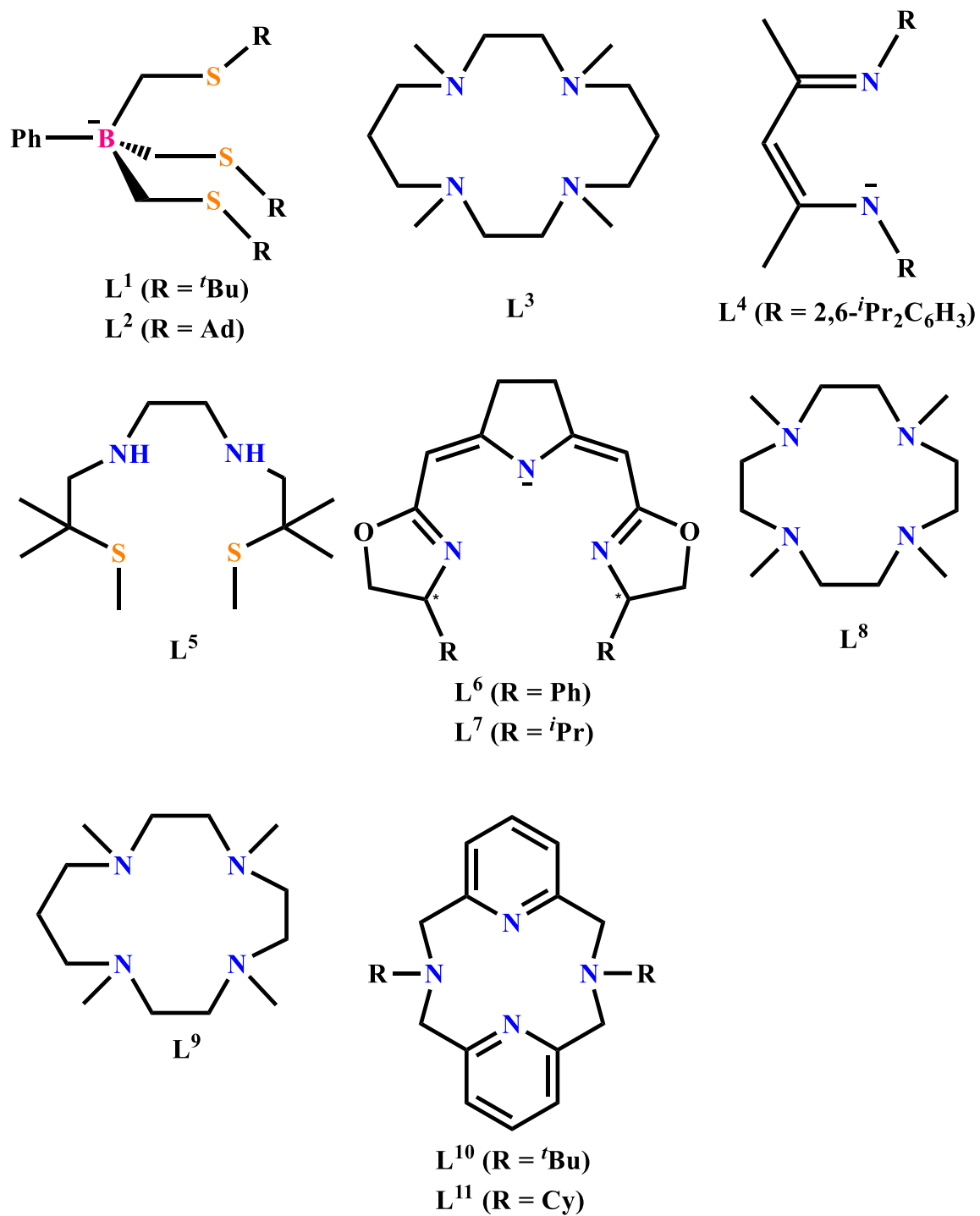
Oxygen is an excellent oxidant from both economic and environmental point of view. Oxidation of low valent transition metals by oxygen has been considered as a fundamental reaction in the transition metal-catalyzed oxidative reactions. After the first report of reversible coordination of oxygen with the iridium(I) center in [(Ph₃P)₂Ir(CO)Cl] by Vaska (Scheme 1.19), several dioxygen adducts of transition metals have been described.^[56-59]



Scheme 1.19: Reaction of Vaska compound with O₂.

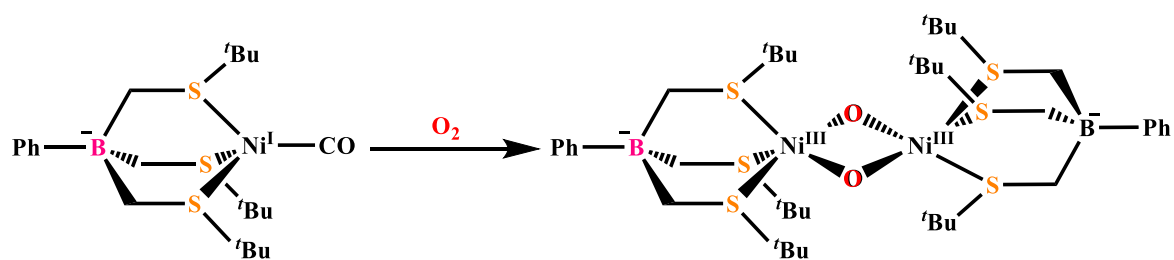
Reaction with low valent copper and palladium complexes with molecular oxygen has been extensively investigated in stoichiometric and catalytic reactions.^[60-76] In comparison to Cu/O₂ or Pd/O₂ reaction, there has been very little investigation towards Ni/O₂ chemistry.

Scheme 1.20 illustrates the ligands used in Ni/O₂-reactions. Heimbach and Otsuka separately reported the formation of NiO₂ species by the reaction of Ni(0) complex containing PPh₃ or RNC (R = ^tBu, Cy) ligand and O₂.^[77-78]



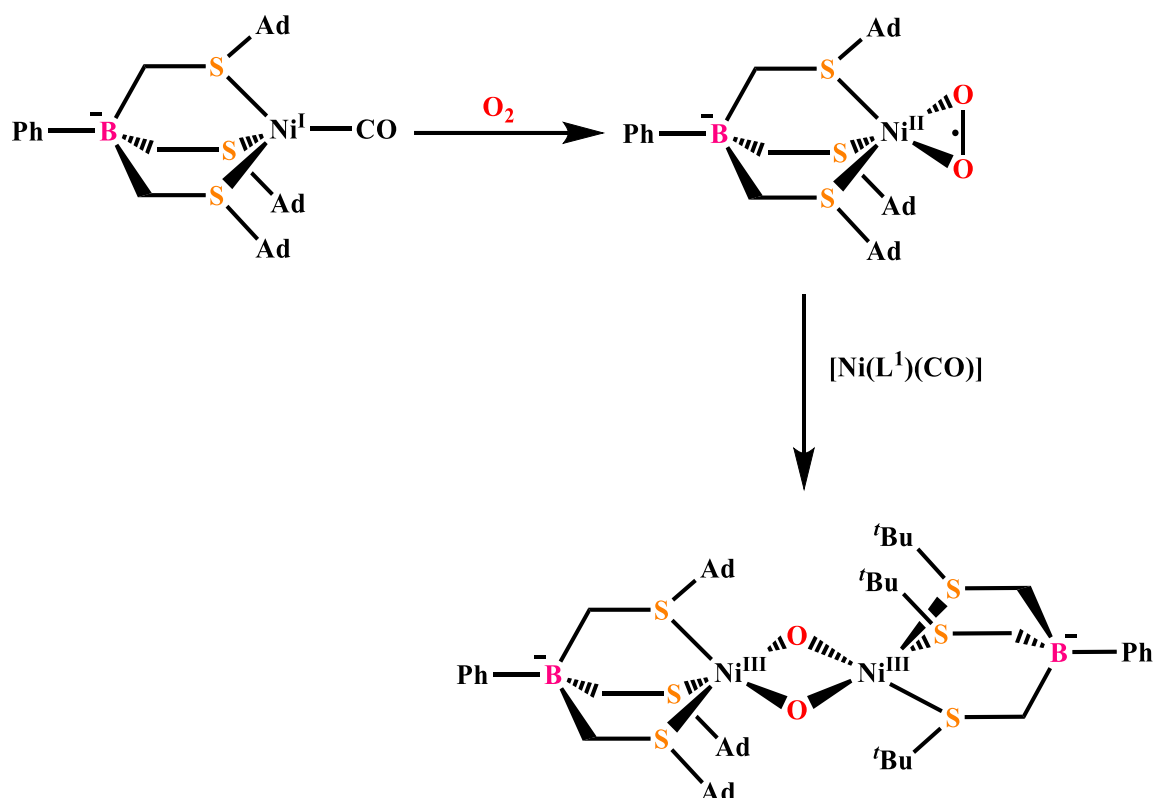
Scheme 1.20: Ligands used in previously reported Ni/O₂ chemistry.

In 2001, Riordon and co-workers studied that reaction of $[\text{Ni}^{\text{I}}(\text{L}^1)(\text{CO})]$ with oxygen generates nickel(III)-bis- μ -oxo complex (Scheme 1.21).^[79]



Scheme 1.21: Reaction of $[\text{Ni}^{\text{I}}(\text{L}^1)(\text{CO})]$ with O_2 .

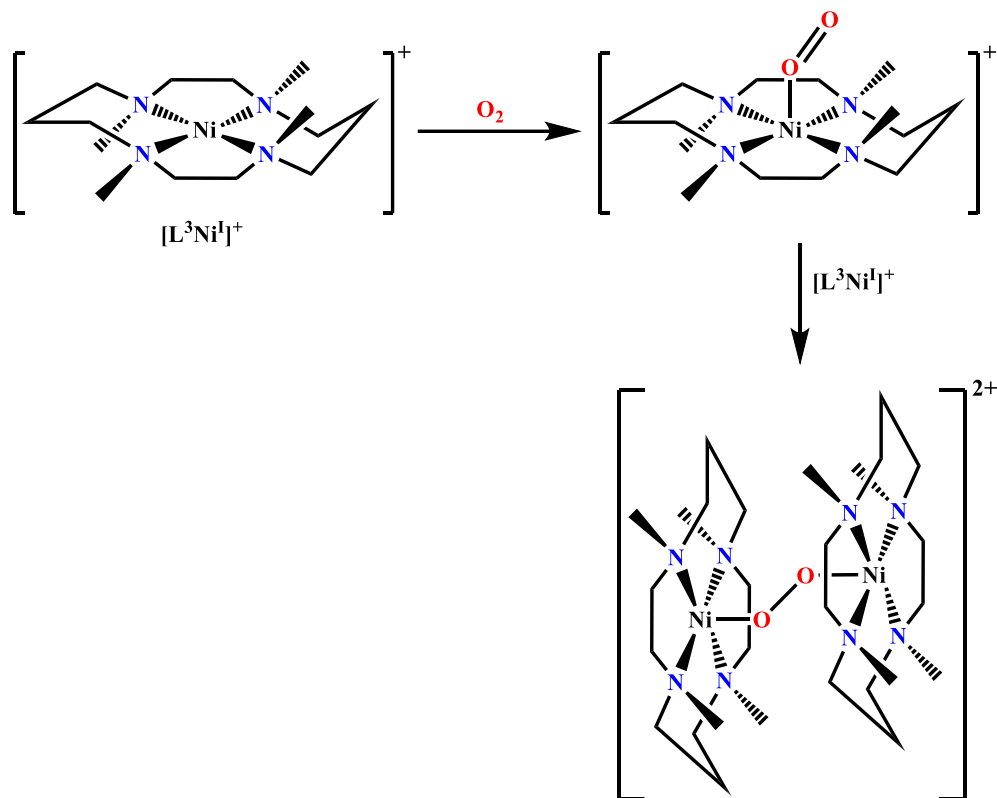
Later they isolated a side-on coordinated nickel(II)-superoxo complex by the reaction of $[\text{Ni}^{\text{I}}(\text{L}^2)(\text{CO})]$ with oxygen (Scheme 1.22).^[80]



Scheme 1.22: Formation of Ni(II)-superoxo complex and its conversion to Ni(III)-bis- μ -oxo complex.

In 2004 and 2006 respectively, Riordon and co-workers also described the identification of a dinuclear trans- μ -1,2-peroxo nickel(II) species and a mononuclear end-on nickel(II)-superoxo species, produced by the reaction of nickel(I) precursor with oxygen at different conditions (Scheme 1.23).^[81-83] Driess and co-workers synthesized and structurally characterized a planar

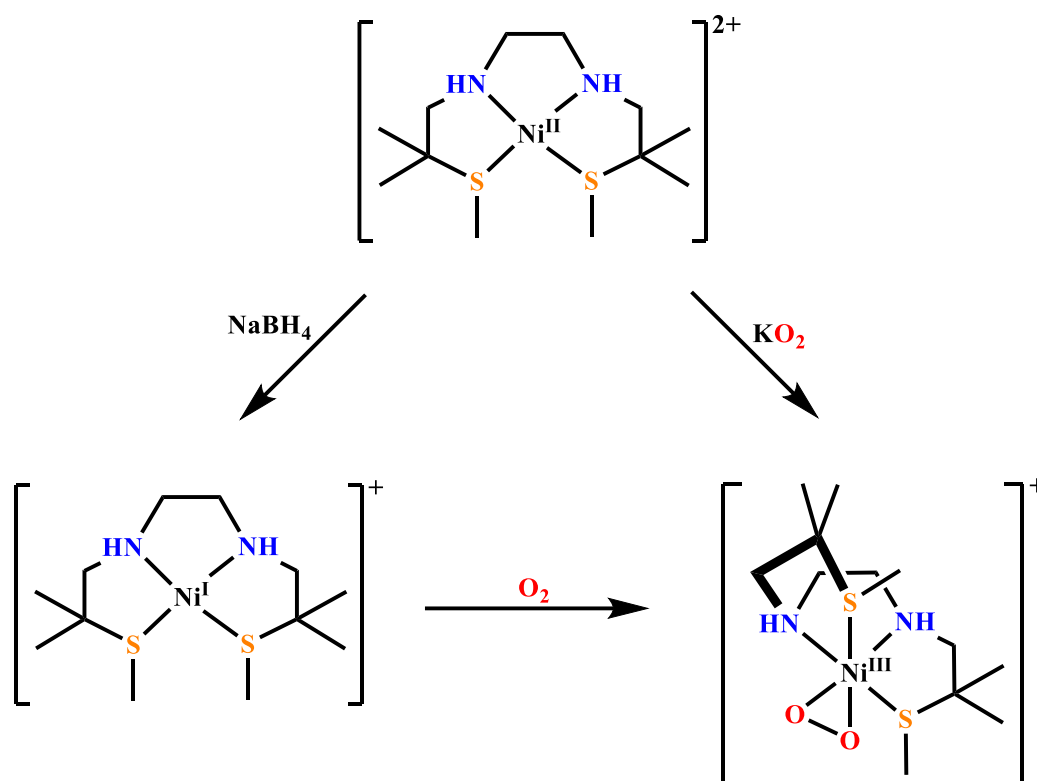
tetraordinated side-on nickel(II)-superoxo complex formed by the reaction of $[\{\text{Ni}^{\text{I}}(\text{L}^4)\}_2(\text{toluene})]$ with oxygen.^[84]



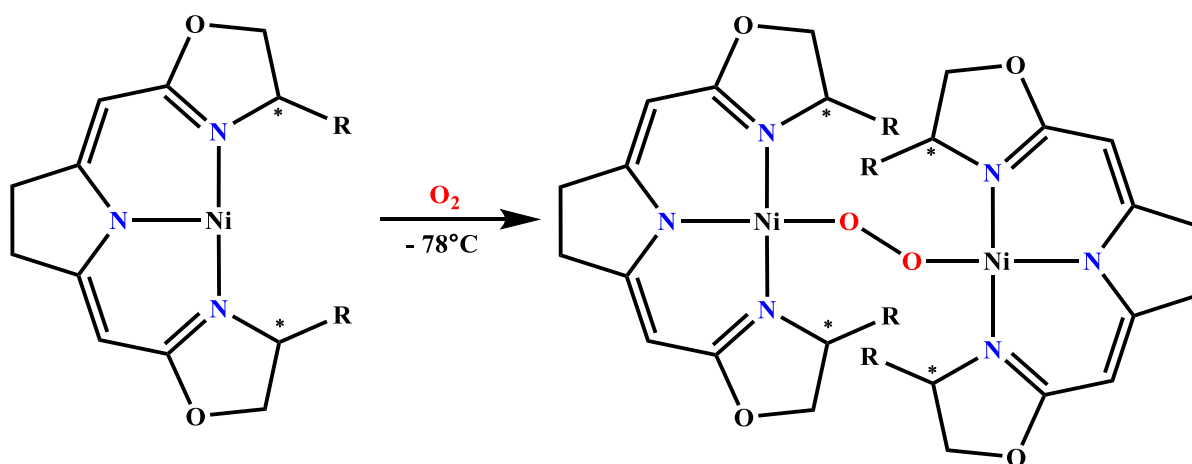
Scheme 1.23: Reaction of $[\text{Ni}^{\text{I}}(\text{L}^3)]^+$ with O_2 .

Later, Masuda and co-workers reported the formation of a mononuclear nickel(III)-peroxo complex $[\text{Ni}^{\text{III}}(\text{L}^5)(\text{O}_2)]^+$ by reacting $[\text{Ni}^{\text{II}}(\text{L}^5)](\text{ClO}_4)_2$ with KO_2 in methanol at room temperature (Scheme 1.24).^[85] It was also described that the same nickel(III)-peroxo can be prepared by the reaction of $[\text{Ni}^{\text{II}}(\text{L}^5)](\text{ClO}_4)_2$ with NaBH_4 and subsequent addition of O_2 .

Recently, Gade and co-workers found that nickel(I) complexes containing chiral pincer ligands (L^5 and L^6 ; Scheme 1.20) react with molecular oxygen at low temperature to form dinuclear trans- μ -1,2-peroxo nickel(II) complexes (Scheme 1.25).^[86]

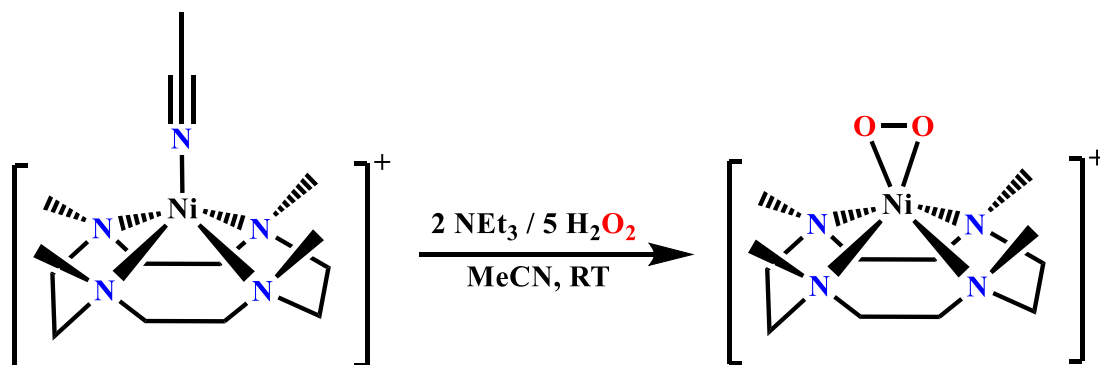


Scheme 1.24: Generation of Ni(III)-peroxo species $[\text{Ni}^{\text{III}}(\text{L}^5)(\text{O}_2)]^+$.



Scheme 1.25: Formation of dinuclear nickel(II)-peroxo complex.

Nickel(III)-peroxo and nickel(II)-superoxo complexes have also been prepared by reacting nickel(II) complex with H_2O_2 in presence of base (e.g. triethylamine, tetramethylammonium hydroxide). Nam and co-workers synthesized and structurally characterized mononuclear nickel(III)-peroxo complexes $[\text{Ni}^{\text{III}}(\text{L}^8)(\text{O}_2)](\text{ClO}_4)$ and $[\text{Ni}^{\text{III}}(\text{L}^9)(\text{O}_2)](\text{ClO}_4)$ by the reaction of $[\text{Ni}^{\text{II}}(\text{L}^8)(\text{CH}_3\text{CN})](\text{ClO}_4)_2$ and $[\text{Ni}^{\text{II}}(\text{L}^9)(\text{CH}_3\text{CN})](\text{ClO}_4)_2$ with five equivalent H_2O_2 in the presence of two equivalent triethylamine (TEA) in CH_3CN at room temperature, respectively (Scheme 1.26).^[87-88]



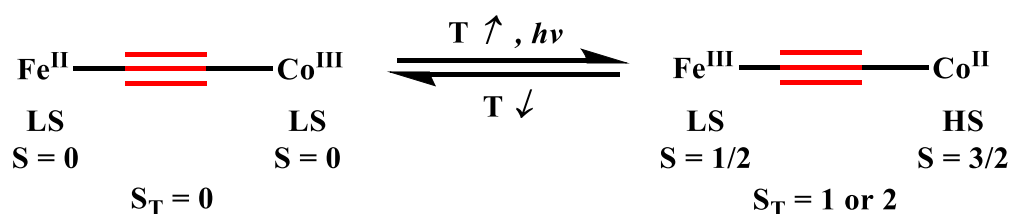
Scheme 1.26: Preparation of $[\text{Ni}^{\text{III}}(\text{L}^8)(\text{O}_2)]^+$.

They also prepared and spectroscopically characterized mononuclear end-on nickel(II)-superoxo complex $[\text{Ni}^{\text{II}}(\text{L}^9)(\text{O}_2)](\text{ClO}_4)$ by reacting $[\text{Ni}^{\text{II}}(\text{L}^9)(\text{CH}_3\text{CN})](\text{ClO}_4)_2$ with five equivalent H_2O_2 in the presence of two equivalent tetramethylammonium hydroxide (TMAH) in CH_3CN at -40°C .^[88] Recently, Cho and co-workers described the synthesis and characterization of mononuclear nickel(III)-peroxo complexes $[\text{Ni}^{\text{III}}(\text{L}^{10})(\text{O}_2)]^+$ and $[\text{Ni}^{\text{III}}(\text{L}^{11})(\text{O}_2)]^+$, produced in the similar way.^[89] Nickel- O_2 chemistry with $\text{L-N}_4\text{Me}_2$ ligand will be described herein and is also currently underway in Prof. Krüger research group.

1.5 Motivation

Cyanide bridge propagates magnetic and electronic interactions between two metal ions.^[90-93] Cyanide-bridged complexes have been extensively investigated in a wide range of shapes and arrangements such as squares, cubes and trigonal bipyramids.^[94-105] These have been established considerable attention for their physical properties, such as multi-step redox, spin crossover, single-molecule magnetism (SMM), and charge-transfer induced spin transitions (CTIST).^[94, 96, 99-105]

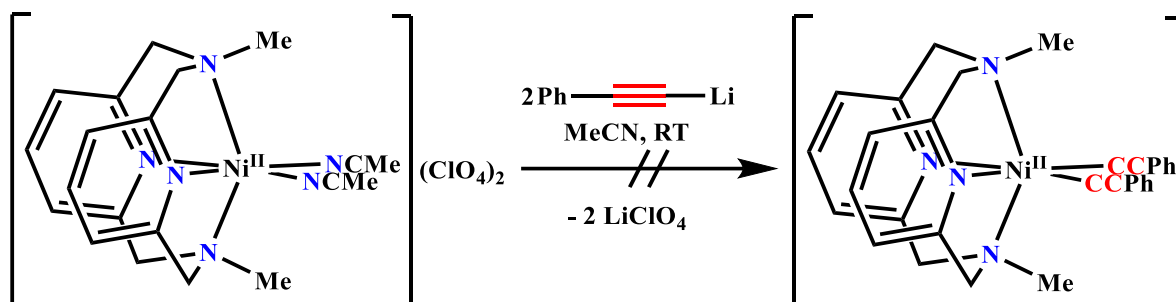
Prof Krüger and co-workers observed a problem in cyanide-bridged square complexes containing $L-N_4Me_2$ as ligand (e.g. $[\{Ni(L-N_4Me_2)(CN)\}_4](ClO_4)_4$, $[\{Cu(L-N_4Me_2)(CN)\}_4](ClO_4)_4$, $[\{Fe(L-N_4Me_2)(CN)\}_4](ClO_4)_4$ and $[\{Co(L-N_4Me_2)(CN)\}_4](ClO_4)_4$).^[106] The exact positions of carbon and nitrogen atoms in the cyanide ligand is not clearly understood by x-ray structure determination. To solve this problem and produce magnetic materials, particularly for charge-transfer induced spin transitions (CTIST) (Scheme 1.27), I propose to replace cyanide with the isoelectronic acetylide anion ligand, $[C\equiv C]^{2-}$, for which the symmetric nature and higher charge are expected to increase the strength of the magnetic interactions with increasing the overlap between ligand and metal orbitals.



Scheme 1.27: Thermally and photoinduced interconversion of $Fe^{\text{II}}(\mu\text{-CC})Co^{\text{III}}$ and $Fe^{\text{III}}(\mu\text{-CC})Co^{\text{II}}$ units.

Initially, I started with 1,4-diethynylbenzene dianion (*para*-DEB²⁻) derivative of $[C\equiv C]^{2-}$ ligand. But the reaction of $[Ni(L-N_4Me_2)(MeCN)_2](ClO_4)_2$ (**1**) and *para*-DEB²⁻ ended with insoluble, inconclusive product formation. To understand Ni-C_{alkynyl} bond formation, I performed the reaction between $[Ni(L-N_4Me_2)(MeCN)_2](ClO_4)_2$ (**1**) and lithium phenylacetylide under nitrogen at room temperature to produce a mononuclear nickel(II)-dialkynyl complex $[Ni(L-N_4Me_2)(CCPh)_2]$ (Scheme 1.28), instead I isolated a dinuclear nickel(I)-diyne complex, where nickel(II) reduces to nickel(I) and lithium phenylacetylide forms diphenyldiacetylene with C–C bond formation. With the isolation of this dinuclear complex, my motivation shifted towards nickel-mediated C–C bond formation reactions and

mechanistic investigation of such reactions through intermediates isolation and characterization.



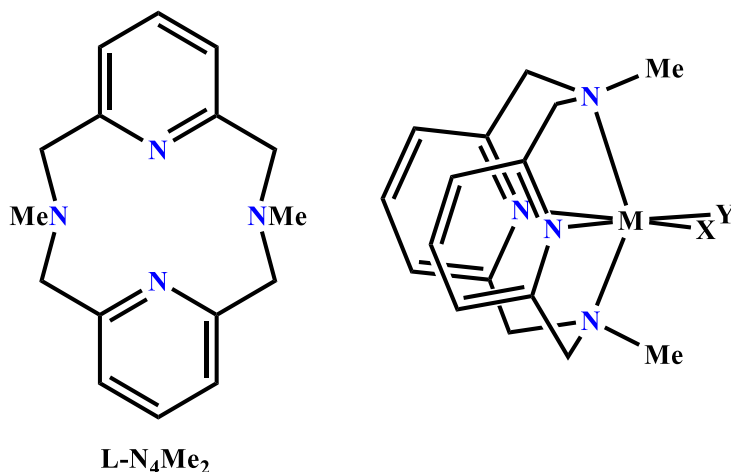
Scheme 1.28: Reaction of 1 with lithium phenylacetylide.

As already discussed in introduction, mechanistic evidence for transition metal-catalyzed homocoupling reaction of terminal alkynes has to be elucidated. A single electron redox process with a dinuclear copper(II) acetylide and a copper(I) intermediates are proposed in copper-catalyzed oxidative homocoupling reaction (Scheme 1.9). Isolation of these intermediates has remained elusive to date, spectroscopic detection of copper(I) species was recently reported. Whereas palladium-catalyzed reactions are based on a palladium(II)/palladium(0) catalytic cycle, and proceed through two electron transfer polar (non-radical) mechanism. Similarly, nickel(II)/nickel(0) catalytic cycles with two electron redox process in nickel catalyzed reaction has been proposed, although the easy availability of nickel(III) and nickel(I) oxidation states might alter the modes of reactivity. Moreover, a NiO₂ species as an intermediate is assumed in nickel-catalyzed oxidative homocoupling reaction in the presence of oxygen as an oxidant (Scheme 1.17), but no isolation and characterization or spectroscopic evidence for the formation of NiO₂ was provided. Therefore, isolation and characterization of reaction intermediates involved in catalytic reaction by experiments remain important and challenging to gain detailed mechanistic insights.

Herein, I disclose a detailed mechanistic aspect of the nickel-mediated homocoupling reaction of terminal alkynes.

2 Result and Discussions

Our studies initiated with the synthesis of a nickel(II) complex $[\text{Ni}(\text{L-N}_4\text{Me}_2)(\text{MeCN})_2](\text{ClO}_4)_2$ (**1**) containing a tetradentate *N,N'*-dimethyl-2,11-diaza[3.3](2,6)pyridinophane ($\text{L-N}_4\text{Me}_2$) as ligand. The ligand coordinates to a transition metal ion in a distorted octahedral geometry leaving two *cis*-coordination sites vacant for other monodentate or bidentate chelating ligand(s) (Scheme 2.1).^[107-108]



Scheme 2.1: Schematic presentation of $\text{L-N}_4\text{Me}_2$ and its coordination mode.

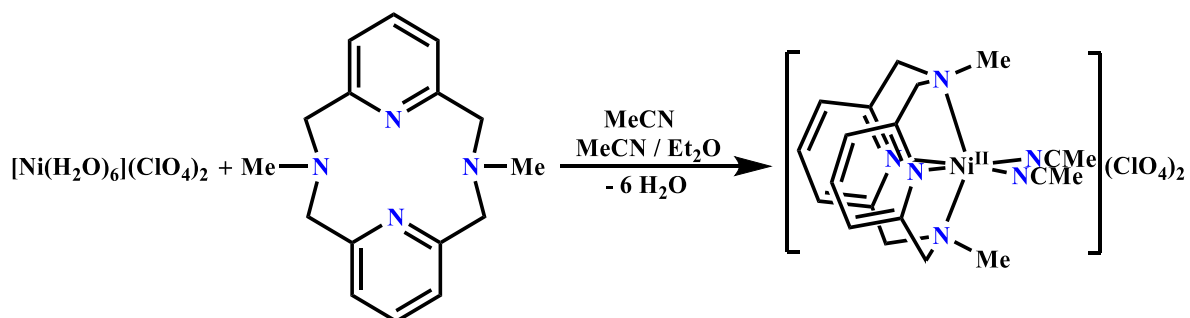
2.1 Synthesis and Characterization of $[\text{Ni}(\text{L-N}_4\text{Me}_2)(\text{MeCN})_2](\text{ClO}_4)_2$ (**1**)

The complex $[\text{Ni}(\text{L-N}_4\text{Me}_2)(\text{MeCN})_2](\text{ClO}_4)_2$ (**1**) was synthesized according to the modified literature procedure.^[106, 108] X-ray structure determination, spectroscopic characterization (IR and UV-Vis-NIR) with electrochemistry of **1** were previously performed by Prof. Krüger and co-workers.^[106] Figure 2.1 shows a perspective view of the complex cation in **1**. I remeasure these spectroscopies and electrochemistry, and use collective information for this study purpose. In addition, I characterize the complex **1** by electrospray ionization mass spectrometry (ESI-MS).

Synthesis

The reaction between $\text{Ni}(\text{ClO}_4)_2 \cdot 6\text{H}_2\text{O}$ and equivalent amounts of $\text{L-N}_4\text{Me}_2$ in acetonitrile under air produced a violet solution. After slow diffusion of diethyl ether into the solution, analytically pure product $[\text{Ni}(\text{L-N}_4\text{Me}_2)(\text{MeCN})_2](\text{ClO}_4)_2$ (**1**) was obtained as violet crystals (yield 84%) (Scheme 2.2). The purity of the complex was confirmed by elemental analysis, which showed

excellent agreement between the calculated and experimental C, H, and N values (*see experimental section*).



Scheme 2.2: Synthesis of $[\text{Ni}(\text{L-N}_4\text{Me}_2)(\text{MeCN})_2](\text{ClO}_4)_2$ (**1**).

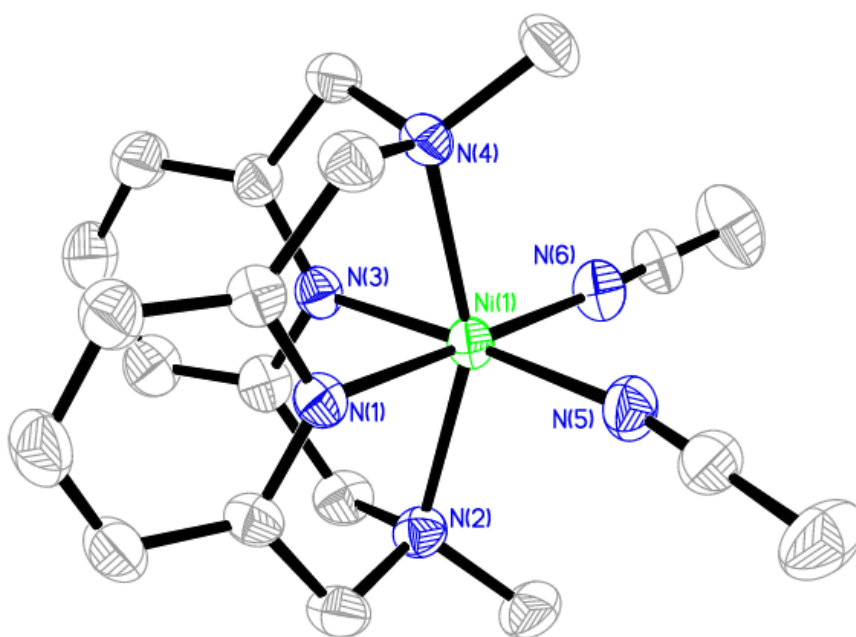


Figure 2.1: Perspective view of the complex cation in **1**.

IR Spectroscopy

Infrared (IR) absorption spectrum of $[\text{Ni}(\text{L-N}_4\text{Me}_2)(\text{MeCN})_2](\text{ClO}_4)_2$ (**1**) was measured on KBr pellet at room temperature. The spectrum displays typical absorption of coordinated diazapyridinophane ligand, L-N₄Me₂ (*appendix* Figure 7.1). The spectrum of **1** also exhibits characteristic stretching frequency of C–N triple bond ($\nu_{\text{C}\equiv\text{N}}$) of coordinated acetonitrile molecules at 2285 and 2313 cm^{-1} . The complex is dicationic in nature, having ClO_4^- as the counter anion. The stretching vibrations of ClO_4^- are found at 1093 and 623 cm^{-1} .

ESI Mass Spectrometry

The ESI-MS spectrum of the complex $[\text{Ni}(\text{L-N}_4\text{Me}_2)(\text{MeCN})_2](\text{ClO}_4)_2$ (**1**) in acetonitrile at room temperature is displayed in Figure 2.2. The spectrum shows a prominent ion peak at a mass-to-charge ratio (m/z) of 424.9 with a relatively lower abundance peak at a m/z of 162.9, whose mass and isotope distribution pattern correspond to $[\text{Ni}(\text{L-N}_4\text{Me}_2)(\text{ClO}_4)]^+$ (calculated m/z 425.0) and $[\text{Ni}(\text{L-N}_4\text{Me}_2)]^{2+}$ (calculated m/z 163.0) respectively (Figure 2.3 and Figure 2.4).

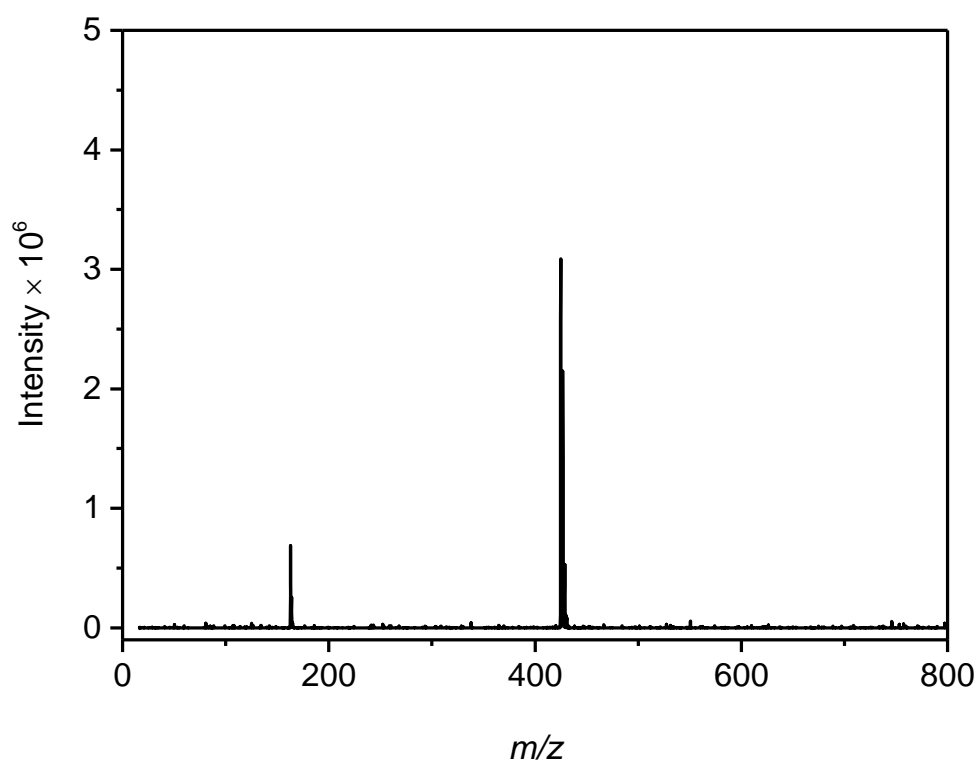


Figure 2.2: ESI-MS spectrum of **1** in MeCN.

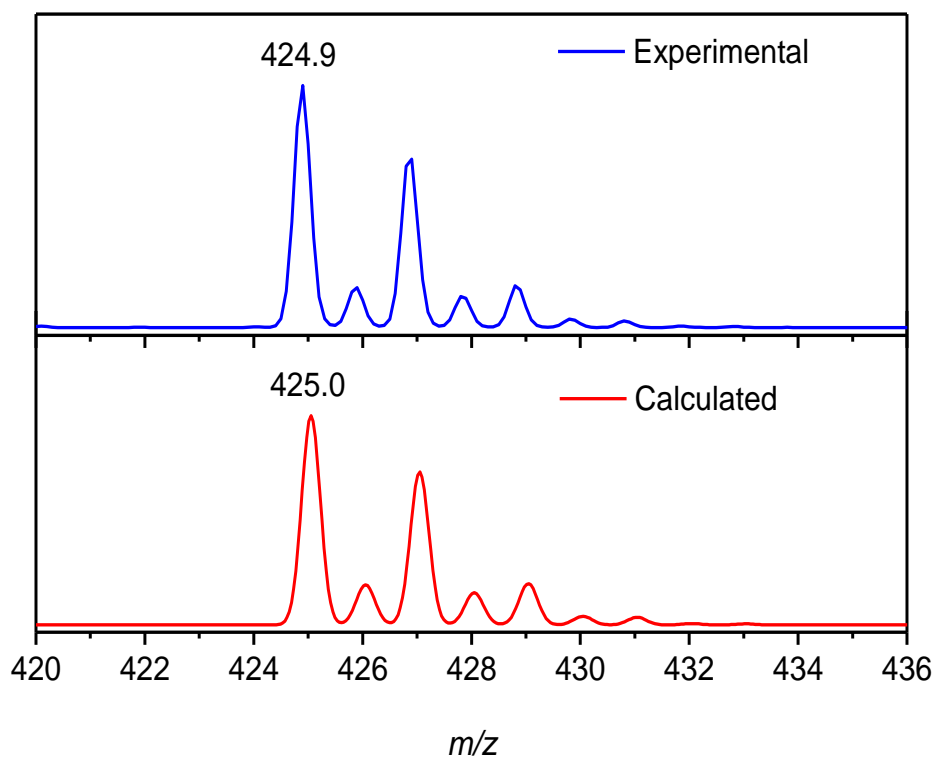


Figure 2.3: The experimental and calculated isotope distribution for $[\text{Ni}(\text{L-N}_4\text{Me}_2)(\text{ClO}_4)]^+$.

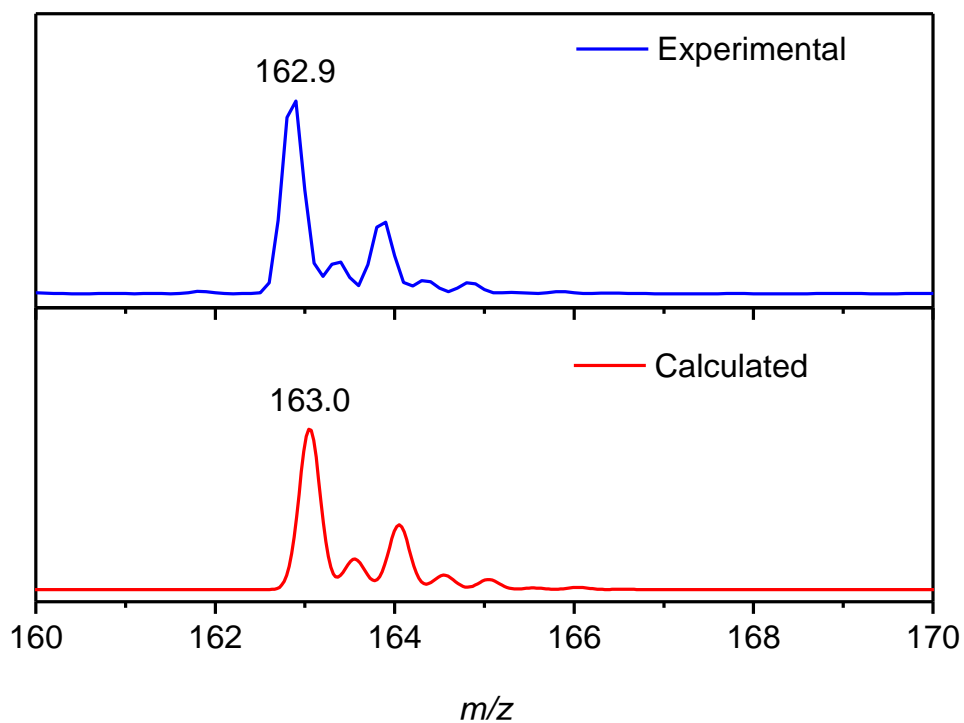


Figure 2.4: The experimental and calculated isotope distribution for $[\text{Ni}(\text{L-N}_4\text{Me}_2)]^{2+}$.

UV-Vis-NIR Spectroscopy

The complex $[\text{Ni}(\text{L-N}_4\text{Me}_2)(\text{MeCN})_2](\text{ClO}_4)_2$ (**1**) was also characterized by electronic absorption spectroscopy in acetonitrile at room temperature. *Appendix* Figure 7.2 shows the electronic absorption spectrum of **1**. The complex exhibits characteristic d-d transitions for distorted octahedral Ni(II) system at 516 (${}^3\text{A}_{2g} \rightarrow {}^3\text{T}_{1g}$), 816 (${}^3\text{A}_{2g} \rightarrow {}^1\text{E}_g$) and 920 (${}^3\text{A}_{2g} \rightarrow {}^3\text{T}_{2g}$) nm. The complex also shows charge transfer bands at 339 and 261 nm.

Electrochemistry

Electrochemical property of the complex $[\text{Ni}(\text{L-N}_4\text{Me}_2)(\text{MeCN})_2](\text{ClO}_4)_2$ (**1**) was investigated by cyclic voltammetry in acetonitrile solution. The cyclic voltammograms of the complex are displayed in Figure 2.5 and Figure 2.6. The compound exhibits a quasireversible oxidation for nickel(II) center at 1.85 V vs SCE ($E_{\text{pa}} = 1.91$ V and $E_{\text{pc}} = 1.79$ V). Apart from the oxidation, the cyclic voltammogram of **1** also reveals two quasireversible reduction processes at -1.135 V vs. SCE ($E_{\text{pc}} = -1.25$ V and $E_{\text{pa}} = -1.02$ V) and -1.69 V vs. SCE ($E_{\text{pc}} = -1.75$ V and $E_{\text{pa}} = -1.63$ V), which corresponds to reduction of nickel(II) center and ligand L-N₄M₂, respectively. These studies indicate that the L-N₄Me₂ ligand may be suitable to stabilize nickel(I) complex.

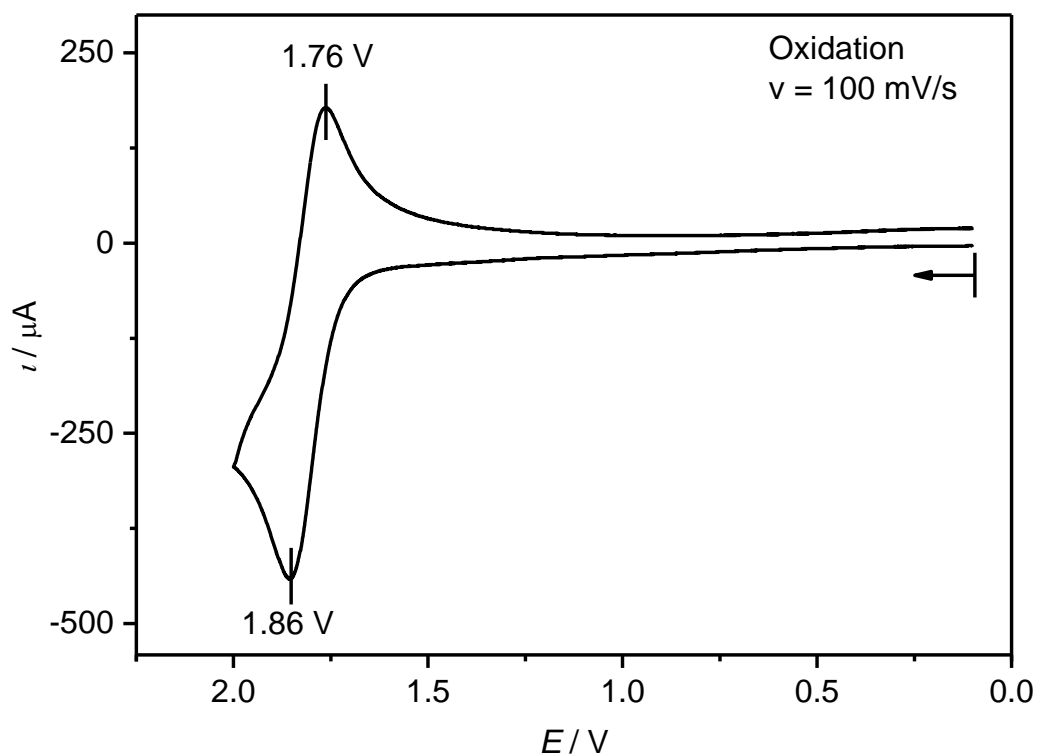


Figure 2.5: Cyclic voltammogram for the oxidation of 1 in 0.2 M TBAP/MeCN sweeping with a scan rate of 100 mV s^{-1} . All potentials are given vs. SCE.

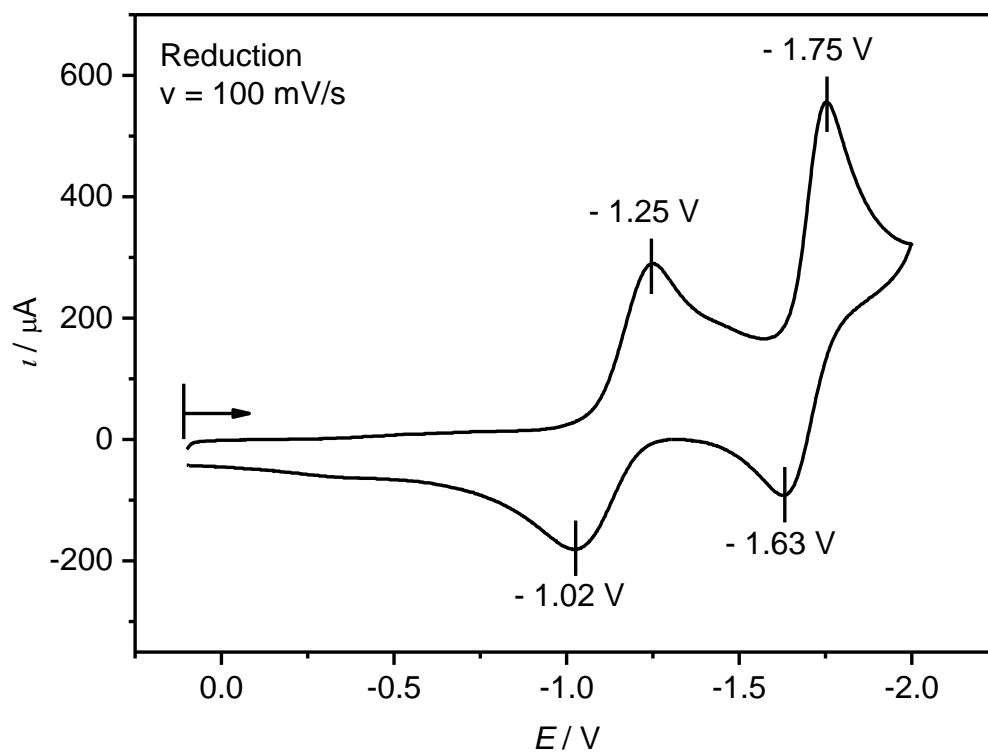
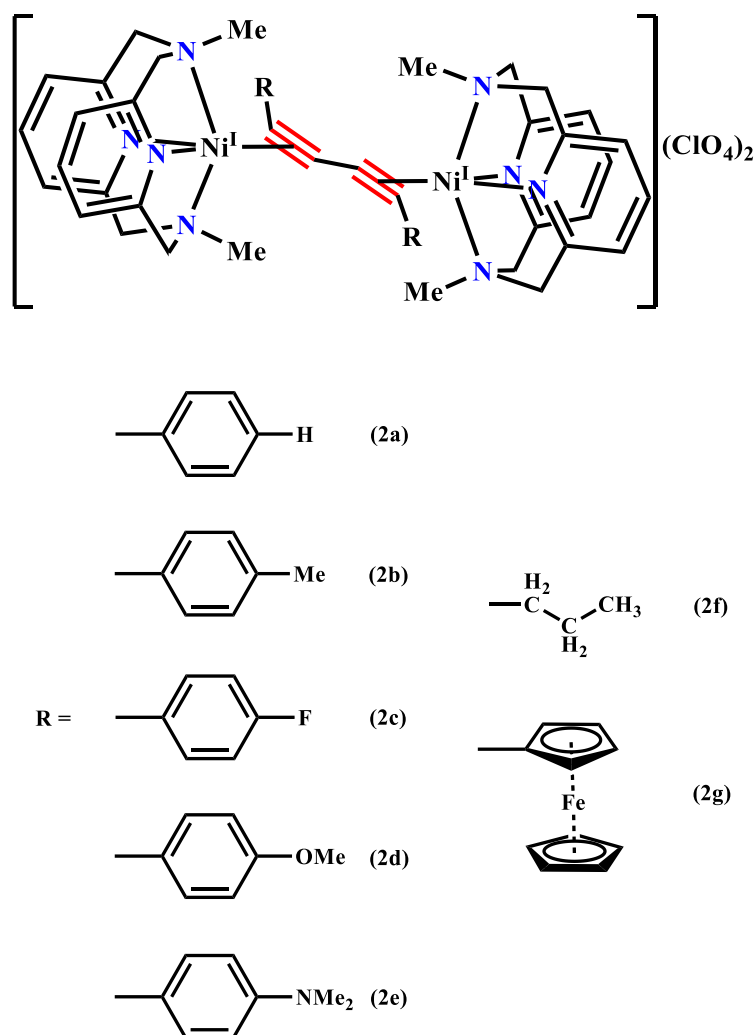


Figure 2.6: Cyclic voltammogram for the reduction of 1 in 0.2 M TBAP/MeCN sweeping with a scan rate of 100 mV s^{-1} . All potentials are given vs. SCE.

2.2 Synthesis and Characterization of Dinuclear Nickel(I)-Diyne Complexes

The reaction of $[\text{Ni}(\text{L-N}_4\text{Me}_2)(\text{MeCN})_2](\text{ClO}_4)_2$ (**1**) with two equivalent lithium acetylide (phenyl, *p*-substituted phenyl, propyl and ferrocenyl derivatives) under a pure nitrogen atmosphere at room temperature led us to isolate dinuclear nickel(I)-diyne species (**2a-2g**) with the reduction of nickel(II) to nickel(I) and formation of C-C bond (Scheme 2.3).



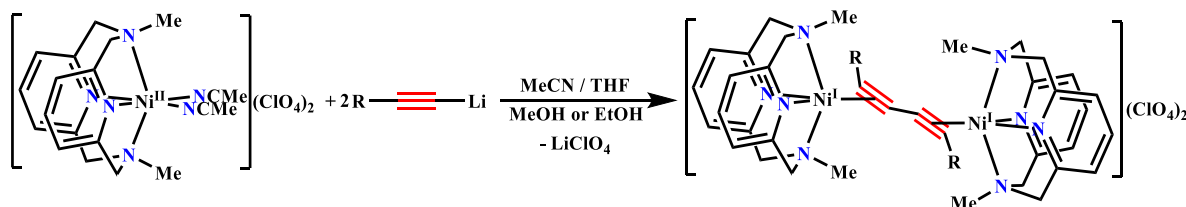
Scheme 2.3: Dinuclear nickel(I)-diyne complexes (**2a-2g**).

A search of the literature revealed that there is a quite number of well characterized nickel-alkyne complexes. Mononuclear systems with nickel(0), however, are relatively common.^[109-114] Nevertheless, even a few alkyne compounds of mononuclear nickel(II) and nickel(I) have been isolated and structurally characterized.^[115-117] In contrast, structural data on dinuclear nickel(0)-diyne complexes are extremely limited and dinuclear nickel(I)-diyne complexes are not available.^[118-119]

2.2.1 Synthesis

Lithium acetylides (RCCLi) were prepared *in situ* by the reaction between corresponding terminal alkyne (RCCH) and 2.5 M ⁿBuLi in tetrahydrofuran at -78°C.

The reaction of [Ni(L-N₄Me₂)(MeCN)₂](ClO₄)₂ (**1**) in acetonitrile with two equivalent lithium acetylide (RCCLi) in tetrahydrofuran at room temperature afforded a dark brown solution. After removing the volatiles, the resulting dark residue obtained was dissolved in a minimum volume of methanol (for **2a-2b**) or ethanol (for **2c-2g**). The solution was refluxed shortly, cooled to room temperature, and allowed to stand for 2-3 days to afford analytically pure, crystalline products [{"Ni(L-N₄Me₂)₂(μ-RC₄R)](ClO₄)₂ (**2a-2f**) and [{"Ni(L-N₄Me₂)₂(μ-RC₄R)](ClO₄)₂ · EtOH [R = Fc] (**2g**) in yields of 55 – 65% (Scheme 2.4).



Scheme 2.4: Preparation of **2a-2g**.

The purity of these dark brown compounds was confirmed by elemental analyses, which showed excellent agreement between the calculated and experimental C, H, and N values (*see experimental section*).

2.2.2 X-ray Structures Analysis

Single crystals suitable for X-ray structure analysis were obtained from hot methanolic (**2a-2b**) or ethanolic (**2c-2g**) solution of the complexes. The perspective view of the complex cation in the complexes are shown in the Figure 2.7 to Figure 2.13. Selected bond lengths and angles are given in Table 2.1 to Table 2.5. X-ray structure measurements were performed at 150 (**2a-2g**, except **2b**), 193 (**2a** and **2b**) and 293 K (**2a**). The complexes (**2a-2e**) crystallize in triclinic space group $P\bar{1}$, while other two complexes (**2f** and **2g**) crystallize in triclinic space group $P21/n$ and monoclinic space group $C2/c$, respectively.

In all the complexes (**2a-2g**), two nickel centers are coordinated with tetraazamacrocyclic diazapyridinophane ligand, L-N₄Me₂ and bridged by a 1,3-diyne unit. In the complex, each nickel center is coordinated to the four nitrogen donor atoms of the ligand L-N₄Me₂ and alkyne group of 1,3-diyne ligand in side-on fashion and is best described with a distorted trigonal bipyramidal coordination environment. The tetradentate ligand is folded along the N_{amine}-N_{amine} axis due to small macrocycle ring size. The amine nitrogen atoms of the tetradentate ligand occupy axial position while pyridine nitrogen atoms occupy equatorial position and the remaining equatorial position occupy by alkyne group of diyne ligand in trigonal bipyramidal coordination environment. The complexes (except **2e** and **2g**) have a crystallographically imposed inversion center located at the middle of C_{sp}-C_{sp} single bond of diyne ligand. The C≡C-C≡C backbone of diyne unit in the complexes adopts a distorted *trans* conformation. Similar conformation has been noticed in the dinuclear rhodium(I)-diyne complex $[\{\text{Rh}(\text{PMe}_3)_3(\text{Cl})\}_2(\mu\text{-RC}_4\text{R})]$ (R = C₆H₄CF₃-4).^[120]

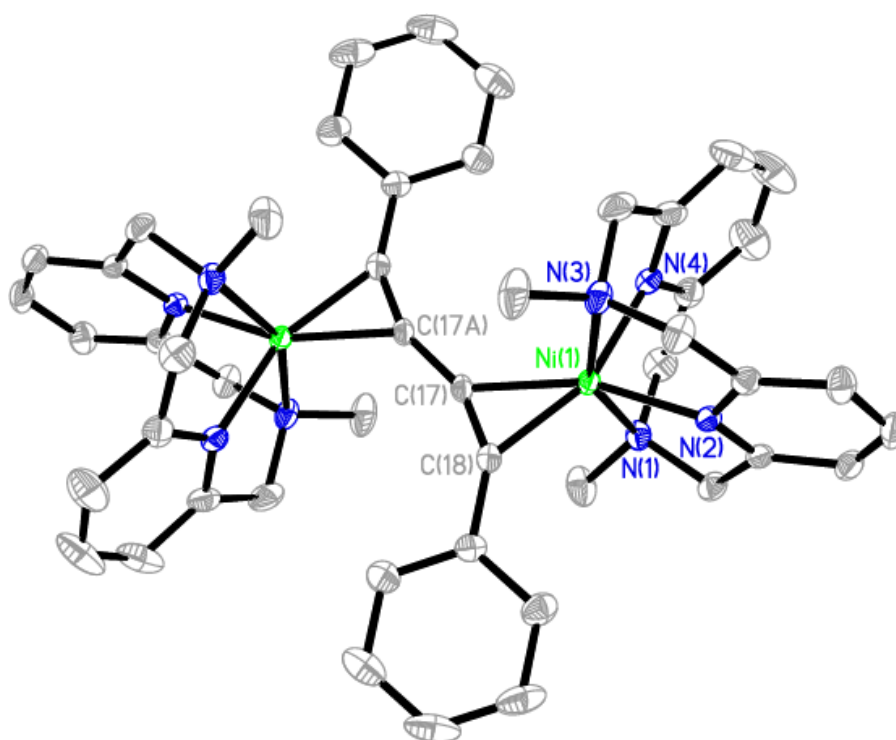


Figure 2.7: Perspective view of the complex cation in **2a**.

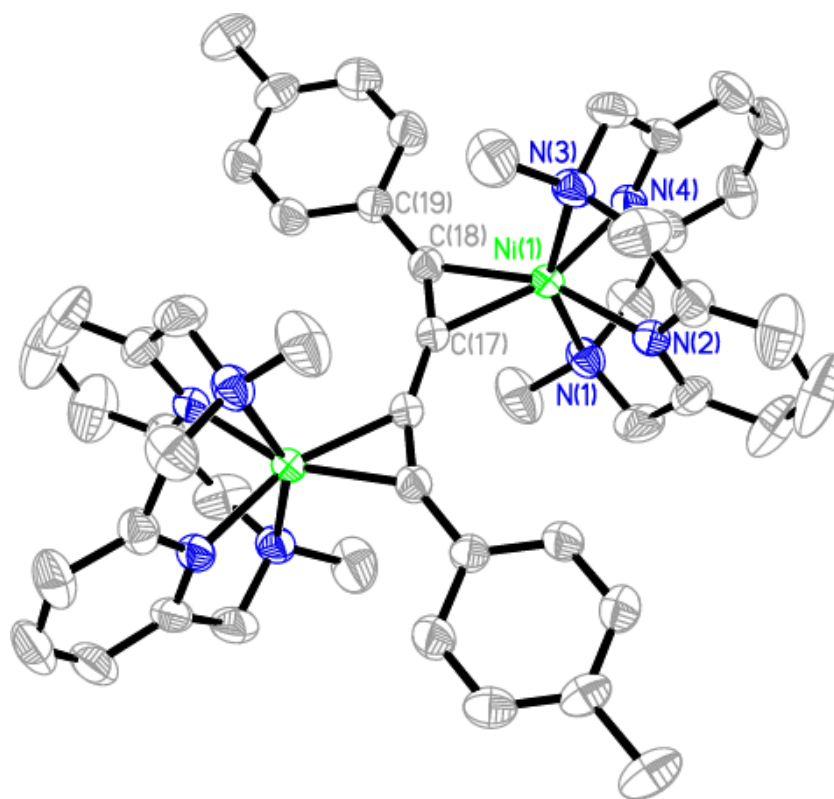


Figure 2.8: Perspective view of the complex cation in 2b.

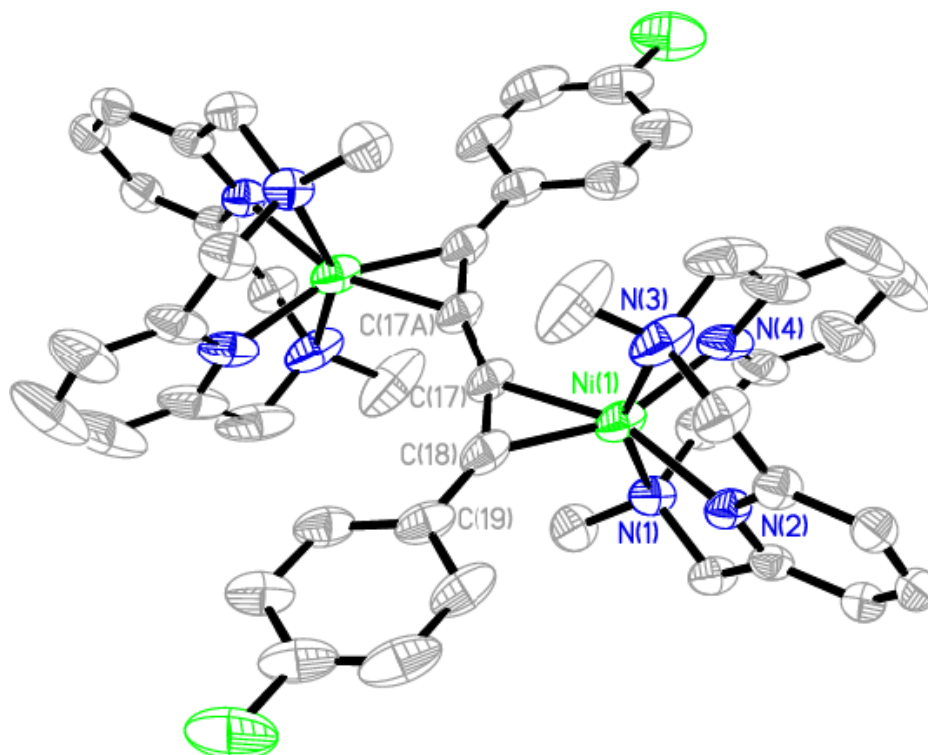


Figure 2.9: Perspective view of the complex cation in 2c.

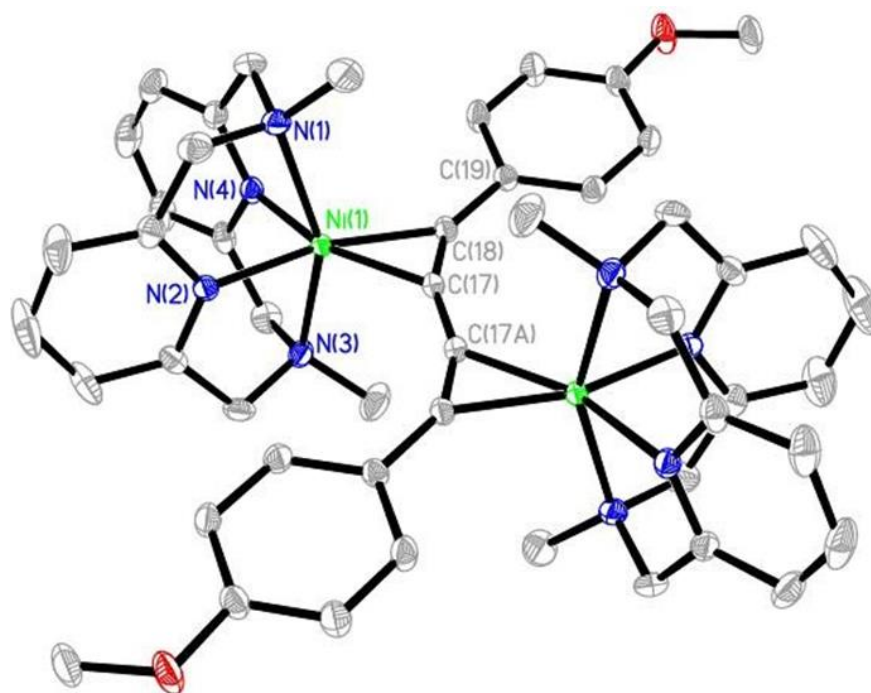


Figure 2.10: Perspective view of the complex cation in 2d.

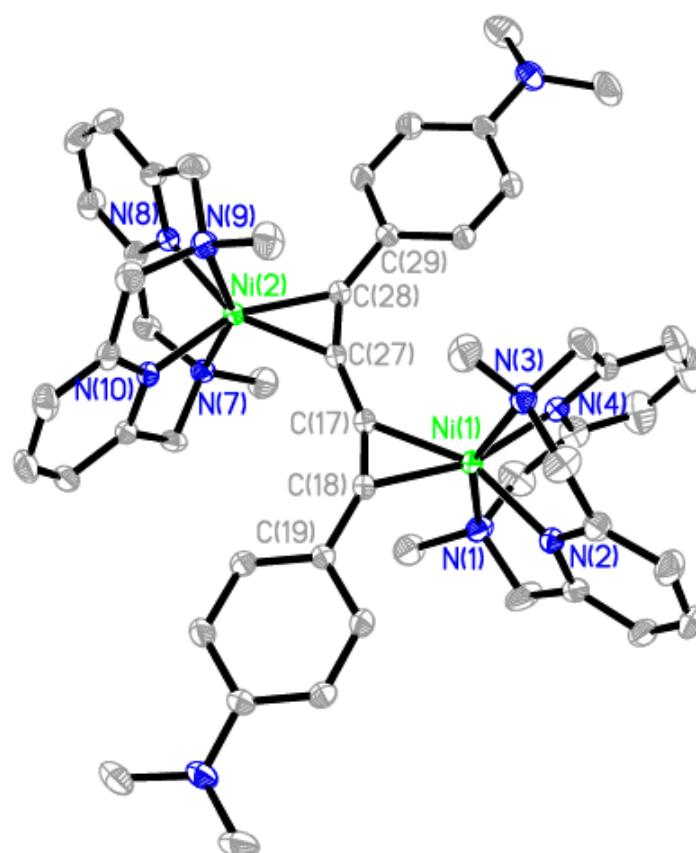


Figure 2.11: Perspective view of the complex cation in 2e.

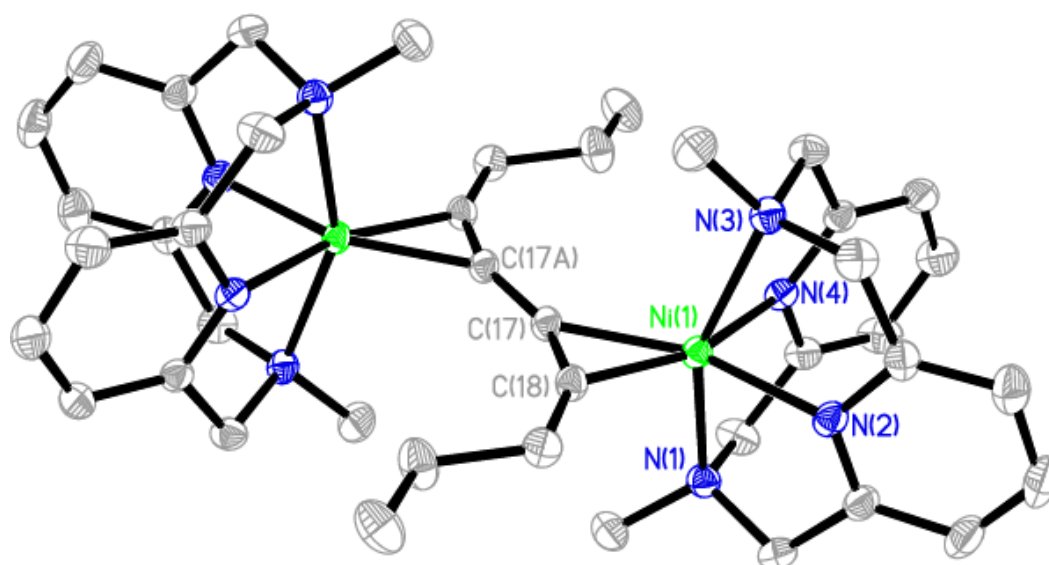


Figure 2.12: Perspective view of the complex cation in 2f.

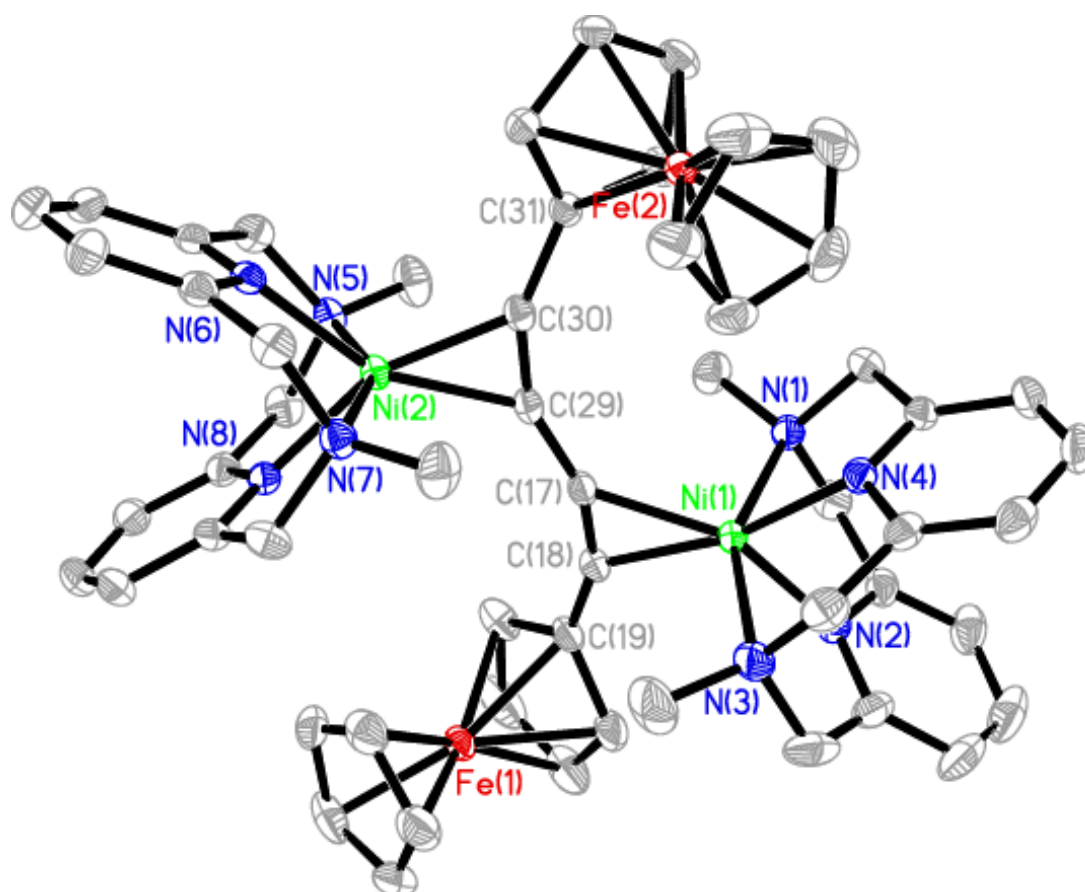


Figure 2.13: Perspective view of the complex cation in 2g.

Table 2.1: Selected bond lengths [Å] and angles [°] in $[\{\text{Ni}(\text{L}-\text{N}_4\text{Me}_2)\}_2(\mu\text{-RC}_4\text{R})](\text{ClO}_4)_2$ [R = Ph] (2a) at 150, 193 and 293 K.

	T = 150 K	T = 193 K	T = 293 K
Ni(1)-N(1)	2.2282(15)	2.2179(16)	2.2353(16)
Ni(1)-N(2)	2.0016(15)	1.9944(14)	2.0029(14)
Ni(1)-N(3)	2.2346(15)	2.2230(14)	2.2391(16)
Ni(1)-N(4)	1.9957(16)	1.9901(14)	1.9917(17)
Ni(1)-C(17)	1.9940(17)	1.9887(15)	1.9915(16)
Ni(1)-C(18)	1.9586(18)	1.9461(15)	1.9582(18)
C(17)-C(18)	1.270(3)	1.264(2)	1.268(2)
C(18)-C(19)	1.448(3)	1.443(3)	1.440(3)
C(17)-C(17A)	1.394(4)	1.384(3)	1.398(3)
N(1)-Ni(1)-N(2)	80.27(6)	80.37(6)	80.10(6)
N(1)-Ni(1)-N(3)	153.58(6)	153.49(5)	153.11(6)
N(1)-Ni(1)-N(4)	80.17(6)	80.08(6)	80.03(7)
N(1)-Ni(1)-C(17)	105.30(6)	105.13(6)	105.10(6)
N(1)-Ni(1)-C(18)	101.20(6)	101.14(6)	101.34(7)
N(2)-Ni(1)-N(3)	80.343(6)	80.31(5)	80.27(6)
N(2)-Ni(1)-N(4)	84.81(6)	84.82(6)	84.84(6)
N(2)-Ni(1)-C(17)	156.34(7)	156.36(6)	156.12(7)
N(2)-Ni(1)-C(18)	119.22(7)	119.26(7)	118.97(7)
N(3)-Ni(1)-N(4)	80.27(6)	80.26(6)	80.07(7)
N(3)-Ni(1)-C(17)	99.60(6)	99.84(6)	100.29(6)
N(3)-Ni(1)-C(18)	103.91(6)	104.08(6)	104.18(7)
N(4)-Ni(1)-C(17)	118.66(7)	118.64(6)	118.91(7)
N(4)-Ni(1)-C(18)	155.91(7)	155.86(7)	156.14(7)
C(17)-Ni(1)-C(18)	37.48(8)	37.46(7)	37.43(7)
C(17)-C(18)-C(19)	148.16(18)	148.04(16)	148.61(18)
C(18)-C(17)-C(17A)	157.3(2)	157.78(19)	157.4(2)

Table 2.2: Selected bond lengths [Å] and angles [°] in $[\{\text{Ni}(\text{L}-\text{N}_4\text{Me}_2)_2(\mu\text{-RC}_4\text{R})\}(\text{ClO}_4)_2]$ [**R** = **C₆H₄Me-4**] (**2b**) at 293 K, $[\{\text{Ni}(\text{L}-\text{N}_4\text{Me}_2)_2(\mu\text{-RC}_4\text{R})\}(\text{ClO}_4)_2]$ [**R** = **C₆H₄F-4**] (**2c**) and $[\{\text{Ni}(\text{L}-\text{N}_4\text{Me}_2)_2(\mu\text{-RC}_4\text{R})\}(\text{ClO}_4)_2]$ [**R** = **C₆H₄OMe-4**] (**2d**) at 150 K.

	2b	2c	2d
Ni(1)-N(1)	2.2295(13)	2.222(2)	2.2444(11)
Ni(1)-N(2)	1.9804(12)	2.008(2)	2.0023(11)
Ni(1)-N(3)	2.2324(13)	2.232(2)	2.2176(11)
Ni(1)-N(4)	1.9998(12)	1.988(3)	1.9898(11)
Ni(1)-C(17)	1.9956(14)	1.994(3)	2.0026(13)
Ni(1)-C(18)	1.9485(15)	1.952(3)	1.9464(13)
C(17)-C(18)	1.2710(19)	1.265(4)	1.2676(17)
C(18)-C(19)	1.446(2)	1.454(4)	1.4447(17)
C(17)-C(17A)	1.388(3)	1.405(5)	1.392(2)
N(1)-Ni(1)-N(2)	80.61(5)	80.49(8)	80.01(4)
N(1)-Ni(1)-N(3)	153.55(5)	153.61(10)	153.30(4)
N(1)-Ni(1)-N(4)	80.30(5)	80.62(10)	79.90(4)
N(1)-Ni(1)-C(17)	100.25(5)	98.67(10)	106.05(5)
N(1)-Ni(1)-C(18)	103.99(6)	103.26(10)	101.29(5)
N(2)-Ni(1)-N(3)	80.31(5)	80.03(9)	80.49(4)
N(2)-Ni(1)-N(4)	85.72(5)	84.35(9)	85.04(4)
N(2)-Ni(1)-C(17)	116.99(5)	158.10(11)	118.65(5)
N(2)-Ni(1)-C(18)	154.37(6)	121.20(10)	155.76(5)
N(3)-Ni(1)-N(4)	80.16(5)	79.91(11)	80.41(4)
N(3)-Ni(1)-C(17)	104.68(5)	106.01(10)	99.24(5)
N(3)-Ni(1)-C(18)	101.14(6)	102.00(12)	103.99(5)
N(4)-Ni(1)-C(17)	157.18(5)	117.26(11)	156.08(5)
N(4)-Ni(1)-C(18)	119.86(5)	154.42(10)	119.13(5)
C(17)-Ni(1)-C(18)	37.57(6)	37.37(12)	37.41(5)
C(17)-C(18)-C(19)	149.56(15)	147.7(3)	147.72(13)
C(18)-C(17)-C(17A)	158.01(18)	158.7(4)	157.07(16)

Table 2.3: Selected bond lengths [Å] and angles [°] in $[\{\text{Ni}(\text{L}-\text{N}_4\text{Me}_2)\}_2(\mu\text{-RC}_4\text{R})](\text{ClO}_4)_2$ [R = C₆H₄NMe₂-4] (2e) at 150 K.

Ni(1)-N(1)	2.2350(14)	Ni(2)-N(7)	2.2200(14)
Ni(1)-N(2)	1.9933(13)	Ni(2)-N(8)	1.9618(13)
Ni(1)-N(3)	2.2311(14)	Ni(2)-N(9)	2.2134(14)
Ni(1)-N(4)	1.9959(14)	Ni(2)-N(10)	1.9581(13)
Ni(1)-C(17)	2.0049(15)	Ni(2)-C(27)	1.9856(16)
Ni(1)-C(18)	1.9479(16)	Ni(2)-C(28)	1.9373(16)
C(17)-C(18)	1.266(2)	C(27)-C(28)	1.271(2)
C(18)-C(19)	1.442(2)	C(28)-C(29)	1.440(2)
C(17)-C(27)	1.396(2)	C(17)-C(27)	1.396(2)
N(1)-Ni(1)-N(2)	80.16(5)	N(7)-Ni(2)-N(8)	80.62(5)
N(1)-Ni(1)-N(3)	153.45(5)	N(7)-Ni(2)-N(9)	151.50(5)
N(1)-Ni(1)-N(4)	80.47(6)	N(7)-Ni(2)-N(10)	79.31(5)
N(1)-Ni(1)-C(17)	102.00(6)	N(7)-Ni(2)-C(27)	104.21(6)
N(1)-Ni(1)-C(18)	98.47(6)	N(7)-Ni(2)-C(28)	106.35(6)
N(2)-Ni(1)-N(3)	80.51(5)	N(8)-Ni(2)-N(9)	79.49(5)
N(2)-Ni(1)-N(4)	85.22(5)	N(8)-Ni(2)-N(10)	91.98(5)
N(2)-Ni(1)-C(17)	153.92(6)	N(8)-Ni(2)-C(27)	153.03(6)
N(2)-Ni(1)-C(18)	116.64(6)	N(8)-Ni(2)-C(28)	115.24(6)
N(3)-Ni(1)-N(4)	79.94(5)	N(9)-Ni(2)-N(10)	81.19(5)
N(3)-Ni(1)-C(17)	103.37(6)	N(9)-Ni(2)-C(27)	102.78(6)
N(3)-Ni(1)-C(18)	106.41(6)	N(9)-Ni(2)-C(28)	100.52(6)
N(4)-Ni(1)-C(17)	120.85(6)	N(10)-Ni(2)-C(27)	114.97(6)
N(4)-Ni(1)-C(18)	157.77(6)	N(10)-Ni(2)-C(28)	152.67(6)
C(17)-Ni(1)-C(18)	37.32(7)	C(27)-Ni(2)-C(28)	37.80(6)
C(17)-C(18)-C(19)	150.22(16)	C(27)-C(28)-C(29)	146.27(16)
C(18)-C(17)-C(27)	158.09(16)	C(28)-C(27)-C(17)	155.24(16)

Table 2.4: Selected bond lengths [\AA] and angles [$^\circ$] in $[\{\text{Ni}(\text{L}-\text{N}_4\text{Me}_2)\}_2(\mu\text{-RC}_4\text{R})](\text{ClO}_4)_2$ [$\text{R} = {}^n\text{C}_3\text{H}_7$] (**2f**) at 150 K.

	2f
Ni(1)-N(1)	2.2427(14)
Ni(1)-N(2)	1.9929(14)
Ni(1)-N(3)	2.2290(15)
Ni(1)-N(4)	2.0135(13)
Ni(1)-C(17)	2.0016(15)
Ni(1)-C(18)	1.9572(15)
C(17)-C(18)	1.254(2)
C(18)-C(19)	1.485(2)
C(17)-C(17A)	1.398(3)
N(1)-Ni(1)-N(2)	80.15(6)
N(1)-Ni(1)-N(3)	153.37(5)
N(1)-Ni(1)-N(4)	79.85(5)
N(1)-Ni(1)-C(17)	103.43(6)
N(1)-Ni(1)-C(18)	103.12(6)
N(2)-Ni(1)-N(3)	80.81(6)
N(2)-Ni(1)-N(4)	84.56(5)
N(2)-Ni(1)-C(17)	152.85(6)
N(2)-Ni(1)-C(18)	115.93(6)
N(3)-Ni(1)-N(4)	79.96(5)
N(3)-Ni(1)-C(17)	102.02(6)
N(3)-Ni(1)-C(18)	101.88(6)
N(4)-Ni(1)-C(17)	122.59(6)
N(4)-Ni(1)-C(18)	159.51(6)
C(17)-Ni(1)-C(18)	36.92(6)
C(17)-C(18)-C(19)	150.07(16)
C(18)-C(17)-C(17A)	157.7(2)

Table 2.5: Selected bond lengths [Å] and angles [°] in $[\{\text{Ni}(\text{L}-\text{N}_4\text{Me}_2)\}_2(\mu\text{-RC}_4\text{R})](\text{ClO}_4)_2 \cdot \text{EtOH}$ [R = Fc] (2g) at 150 K.

Ni(1)-N(1)	2.2458(15)	Ni(2)-N(5)	2.2208(15)
Ni(1)-N(2)	1.9969(15)	Ni(2)-N(6)	2.0145(14)
Ni(1)-N(3)	2.2174(16)	Ni(2)-N(7)	2.2395(15)
Ni(1)-N(4)	2.0107(14)	Ni(2)-N(8)	1.9996(14)
Ni(1)-C(17)	2.0323(16)	Ni(2)-C(29)	2.0109(16)
Ni(1)-C(18)	1.9488(17)	Ni(2)-C(30)	1.9558(16)
C(17)-C(18)	1.264(2)	C(29)-C(30)	1.269(2)
C(18)-C(19)	1.438(2)	C(30)-C(31)	1.443(2)
C(17)-C(29)	1.398(2)	C(17)-C(29)	1.398(2)
N(1)-Ni(1)-N(2)	80.04(6)	N(5)-Ni(2)-N(6)	80.31(6)
N(1)-Ni(1)-N(3)	153.58(6)	N(5)-Ni(2)-N(7)	153.18(5)
N(1)-Ni(1)-N(4)	79.94(6)	N(5)-Ni(2)-N(8)	80.04(6)
N(1)-Ni(1)-C(17)	99.98(6)	N(5)-Ni(2)-C(29)	100.92(6)
N(1)-Ni(1)-C(18)	101.24(6)	N(5)-Ni(2)-C(30)	102.16(6)
N(2)-Ni(1)-N(3)	80.40(6)	N(6)-Ni(2)-N(7)	79.72(6)
N(2)-Ni(1)-N(4)	84.36(6)	N(6)-Ni(2)-N(8)	84.17(5)
N(2)-Ni(1)-C(17)	148.18(6)	N(6)-Ni(2)-C(29)	155.50(6)
N(2)-Ni(1)-C(18)	111.42(7)	N(6)-Ni(2)-C(30)	118.29(6)
N(3)-Ni(1)-N(4)	80.62(6)	N(7)-Ni(2)-N(8)	80.28(6)
N(3)-Ni(1)-C(17)	106.00(6)	N(7)-Ni(2)-C(29)	104.69(6)
N(3)-Ni(1)-C(18)	102.34(7)	N(7)-Ni(2)-C(30)	103.00(6)
N(4)-Ni(1)-C(17)	127.24(6)	N(8)-Ni(2)-C(29)	120.26(6)
N(4)-Ni(1)-C(18)	164.19(7)	N(8)-Ni(2)-C(30)	157.53(6)
C(17)-Ni(1)-C(18)	36.96(7)	C(29)-Ni(2)-C(30)	37.28(7)
C(17)-C(18)-C(19)	156.45(18)	C(29)-C(30)-C(31)	150.15(17)
C(18)-C(17)-C(29)	157.32(17)	C(30)-C(29)-C(17)	155.11(17)

X-ray structure measurements were performed on suitable single crystal of $[\{\text{Ni}(\text{L-N}_4\text{Me}_2)\}_2(\mu\text{-RC}_4\text{R})](\text{ClO}_4)_2$ [$\text{R} = \text{Ph}$] (**2a**) at 150, 193 and 293 K. Figure 2.7 shows the perspective view of the complex cation in the complex **2a**. Selected bond lengths and angles are listed in Table 2.1. In the complex **2a**, $\text{L-N}_4\text{Me}_2$ coordinated nickel centers are bridged by the diyne ligand $\text{C}_{16}\text{H}_{10}$ ($\text{Ph-C}\equiv\text{C-C}\equiv\text{C-Ph}$).

At 150 K, in the complex $\text{N}_{\text{amine-Ni-N}_{\text{amine}}}$ and $\text{N}_{\text{py-Ni-N}_{\text{py}}}$ angles are $153.58(6)^\circ$ and $84.81(6)^\circ$, which are deviated from ideal value of 180° and 120° respectively in trigonal bipyramidal geometry. The $\text{C}_{\text{alkyne-Ni-C}_{\text{alkyne}}}$ angle is $37.48(8)^\circ$, in equatorial plane. In addition, in the complex, the $\text{N}_{\text{py}(2)\text{-Ni-C}_{\text{centroid}(\text{C}=\text{C})}}$ and $\text{N}_{\text{py}(4)\text{-Ni-C}_{\text{centroid}(\text{C}=\text{C})}}$ angles are 138.02° and 137.16° , respectively. The sum of the angles of the equatorial ligands is 360° , and the axial-to-equatorial bond angles are $\sim 90^\circ$ for both $\text{N}_{\text{amine-Ni-N}_{\text{py}}}$ ($80.17^\circ - 80.43^\circ$) and $\text{N}_{\text{amine-Ni-C}}$ (104.02° and 102.40°), supporting the description of a distorted trigonal bipyramidal coordination environment.

In a five coordinated system, information about the coordination environment around the metal center as a square-pyramid or a trigonal bipyramid can be obtained by determining the structural index τ , which represents the relative amount of trigonality [square pyramid, $\tau = 0$; trigonal bipyramid, $\tau = 1$; $\tau = (\beta - \alpha)/60$; where α and β being the two largest angles around the central atom].^[121] In addition, according to this model, out of the equatorial ligands (A, D, E), A is chosen such that the M-A bond length is longer than M-D/E and A should not be any one of the four donor atoms forming the two largest angles (Figure 2.14).

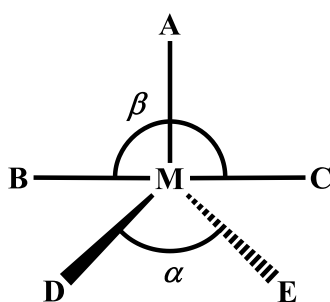


Figure 2.14: Five-coordinated compound

The obtained value of 0.26 for the structural index τ for **2a** reveals that the coordination environment around each nickel center is best described as distorted square-pyramid, which contrasts with the above described structural features. This could be explained by the large

deviation of $N_{\text{amine}}\text{-Ni-}N_{\text{amine}}$ angle ($153.58(6)^\circ$) from 180° and presence of two largest angles $N_{\text{py}}(2)\text{-Ni-}C_{\text{centroid}(\text{C}\equiv\text{C})}$ and $N_{\text{py}}(4)\text{-Ni-}C_{\text{centroid}(\text{C}\equiv\text{C})}$ angles (138.02° and 137.16°) instead of one. Thus, characterization of coordination environment around nickel centers in the nickel(I)-diyne complexes by this model is insignificant.

In the complex, the axial $\text{Ni-}N_{\text{amine}}$ bonds with an average length of $2.231 \pm 0.003 \text{ \AA}$ are longer than the equatorial $\text{Ni-}N_{\text{py}}$ bonds which average to $1.999 \pm 0.002 \text{ \AA}$. However, these $\text{Ni-}N_{\text{amine}}$ and $\text{Ni-}N_{\text{py}}$ bond lengths are very similar to those in other octahedral nickel(II) complexes containing $\text{L-N}_4\text{Me}_2$ as ligand (Table 2.6).^[106, 108] The average $\text{Ni-}C_{\text{alkyne}}$ bond length is about $1.967 \pm 0.021 \text{ \AA}$. Notably, the inner $\text{Ni-}C_{17}$ bond ($1.9940(17) \text{ \AA}$) is slightly longer than the outer $\text{Ni-}C_{18}$ ($1.9586(18) \text{ \AA}$) and such differences could be caused by the steric crowding. In addition, the average $\text{Ni-}C_{\text{alkyne}}$ bond length of $1.967 \pm 0.021 \text{ \AA}$ is on the higher end of the reported $\text{Ni-}C_{\text{alkyne}}$ bonds ($1.856 - 1.960 \text{ \AA}$) in nickel π -alkyne complexes.^[115, 118]

Table 2.6: Average $\text{Ni-}N_{\text{amine}}$ and $\text{Ni-}N_{\text{py}}$ bond lengths [\AA] in **2a, **1** and $[\text{Ni}(\text{L-N}_4\text{Me}_2)\text{Cl}(\text{H}_2\text{O})]\text{Cl}$.**

	2a	1 ^[106]	$[\text{Ni}(\text{L-N}_4\text{Me}_2)\text{Cl}(\text{H}_2\text{O})]\text{Cl}$ ^[108]
$\text{Ni-}N_{\text{amine}}$	2.231	2.172	2.199
$\text{Ni-}N_{\text{py}}$	1.999	2.009	2.021

In the complex **2a**, the relevant C-C triple bond ($C_{17}\text{-}C_{18}$) and C-C single bond ($C_{17}\text{-}C_{17A}$) lengths in coordinated diphenyldiacetylene ligand ($\text{Ph-}C_{18}\equiv C_{17}\text{-}C_{17A}\equiv C_{18A}\text{-Ph}$) are $1.270(3) \text{ \AA}$ and $1.394(4) \text{ \AA}$ respectively, which are slightly longer than that of the free diyne ($1.205(2)$ and $1.363(2) \text{ \AA}$).^[122] In addition, C-C triple bond length is less close to the value of a typical double bond (1.331 \AA), and comparable to those found in nickel π -alkyne complexes.^[111, 115-119] The $C_{\text{Ph}}\text{-}C_{18}$ bond length of $1.448(3) \text{ \AA}$ is slightly longer than that (1.435 \AA) of the free diyne.^[122] Moreover, the $C_{17A}\text{-}C_{17}\text{-}C_{18}$ and $C_{17}\text{-}C_{18}\text{-}C_{19}$ angles are $157.3(2)^\circ$ and $148.16(18)^\circ$ respectively, which are more bent compared to those in free diyne ($179.6(2)^\circ$ and $178.57(11)^\circ$).^[122] These angles are comparable to those found in nickel π -alkyne complexes.^[111, 115-119] Elongation of C-C bonds and bending of C-C-C angles indicate σ -donation from alkyne group of diyne ligand to the nickel center and π -back donation from the nickel center to alkyne group of diyne ligand. In the complex, the distance between two nickel centers is 5.036 \AA . The complex **2a** shows very similar structural properties at 193 and 293 K.

The bonding in transition metal-alkyne complex can be described by Dewar-Chatt-Duncanson model.^[123-127] Within this model, there are three resonance structures for the bonding interaction, π -complex (**A**) and metallacyclopropene (**B** and **C**) (Figure 2.15). Although in **A** and **B** the alkyne acts as a two-electron donor ligand, the difference between the resonance structures **A** and **B** appear from the extent of π -back-bonding, which occurs between the metal atom and the alkyne ligand. The resonance structure **B** can also be described as a M^{2+} species being coordinated by a $[\eta^2\text{-alkenediyl}]^{2-}$ ligand. In addition, for electron-poor metal centers, the alkyne can act as an additional π -donor ligand, providing electron density to the metal atom via the orthogonal π -system and therefore acting as a four-electron donor ligand (Figure 2.15, **C**).

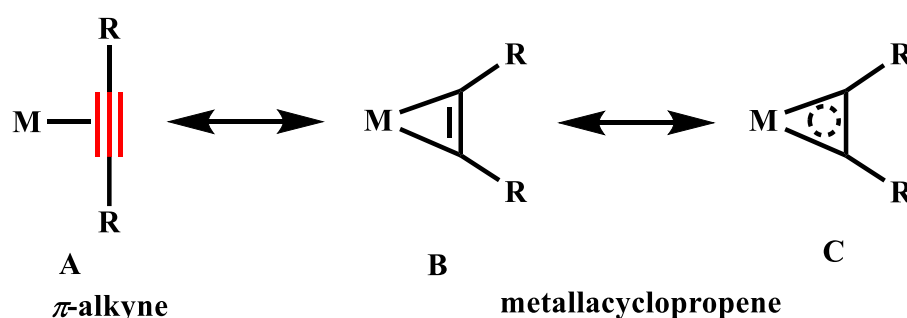


Figure 2.15: Resonance structures of transition metal-alkyne complex.

Based on the molecular structure of dicationic complex **2a**, two resonance structures for each nickel center of **2a** could be outlined: (i) nickel(I) π -alkyne complex with d^9 electronic configuration and (ii) nickel metallacyclopropene complex (Ni(III) with a $[\eta^2\text{-alkenediyl}]^{2-}$ ligand) with d^7 electronic configuration. But, aforesaid structural parameters of **2a** clearly suggest the formation of a nickel(I) π -alkyne complex instead of a nickel metallacyclopropene complex (Ni(III) with a $[\eta^2\text{-alkenediyl}]^{2-}$ ligand).

In addition, for nickel(I) complexes with the ligand $L\text{-N}_4\text{Me}_2$ in an octahedral coordination environment, an elongation of the Ni-N bonds either in the axial or the equatorial positions is expected (Figure 2.16). But I did not observe any kind of bond elongation in **2a** (Table 2.6), which also supports the formulation of a trigonal bipyramidal $L\text{-N}_4\text{Me}_2$ coordinated nickel(I)-diyne complex with $(d_{xz}, d_{yz})^4 (d_{xy}, d_{x^2-y^2})^4 (d_{z^2})^1$ electronic configuration (assuming an idealized D_{3h} ligand field description with the z -axis oriented along $N_{\text{amine}}\text{-N}_{\text{amine}}$ axis), instead of octahedral nickel(I)-diyne complex with N_4C_2 coordination environment (alkyne group as bidentate ligand with small bite angle).

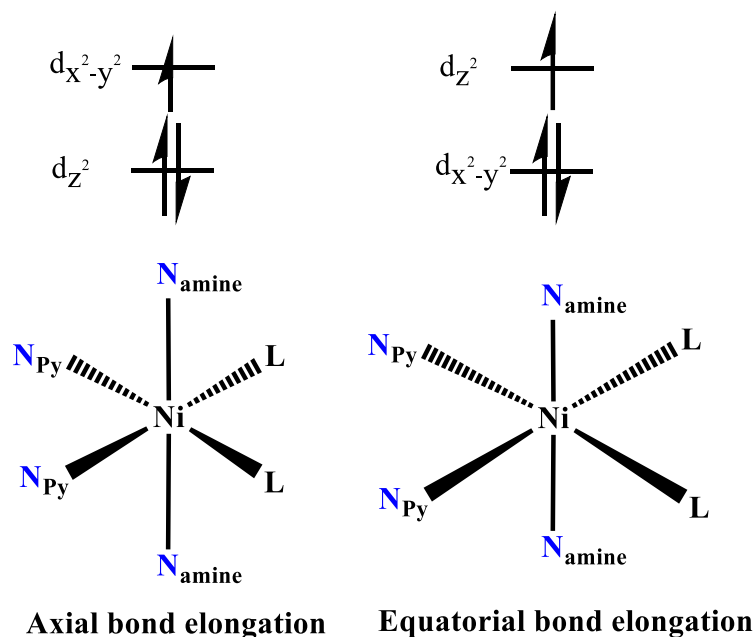


Figure 2.16: Bonds elongation in L-N₄Me₂ coordinated nickel(I) complexes in octahedral coordination environment; L = other mono or bidentate ligand(s).

To the best of my knowledge, **2a** represents the first structurally characterized dinuclear nickel(I)-diyne complex.

All the other complexes **2b-2g** also exhibits very similar structural properties. A comparison of selected bond lengths and angles in these complexes with **2a** are given in Table 2.7 and Table 2.8. The structural differences, particularly in Ni-N, Ni-C, and C≡C bond lengths and C_R-C≡C angle are not large enough to consider as significant. The C≡C bond length in **2a**, **2f** and **2g**, in contrast, show significant deviations, with the **2a** complex showing the largest elongation (1.270(3) Å), closely followed by the **2g** (1.267 (avg.) Å) and then **2f** (1.254(2) Å) (Table 2.7).

In addition, in the complex **2g**, L-N₄Me₂ coordinated nickel centers are connected by diyne ligand FcC₄Fc. Each ferrocenyl group with co-planar and eclipsed cyclopentadienyl rings represents a linear sandwich structure with a characteristic [η⁵-Fe-η⁵] coordination mode. The iron atom is coordinated to the free and substituted cyclopentadienyl rings with ring centroid-iron lengths of 1.651/1.643 (Fe1) and 1.645/1.642 (Fe2) Å, and with ring centroid-iron-ring centroid angle of 177.8° (Fe1) and 179.3° (Fe2). The average Fe-C_{Cp} and Fe-C_{Cp'} bond lengths are 2.041/2.040 (Fe1) and 2.037/2.041 (Fe2) Å. The average carbon carbon bond lengths in iron coordinated free and substituted cyclopentadienyl rings are 1.409/1.423 (Fe1) and 1.412/1.426 (Fe2) Å. These bond lengths and angles indicate that there is an iron(II) oxidation state in each ferrocenyl group.^[128-129]

DFT calculation of **2b** also shows it is a complex with two nickel(I) centers. The spin density is well localized on the nickel atoms and the d_{z^2} orbital is singly occupied (Figure 2.17).

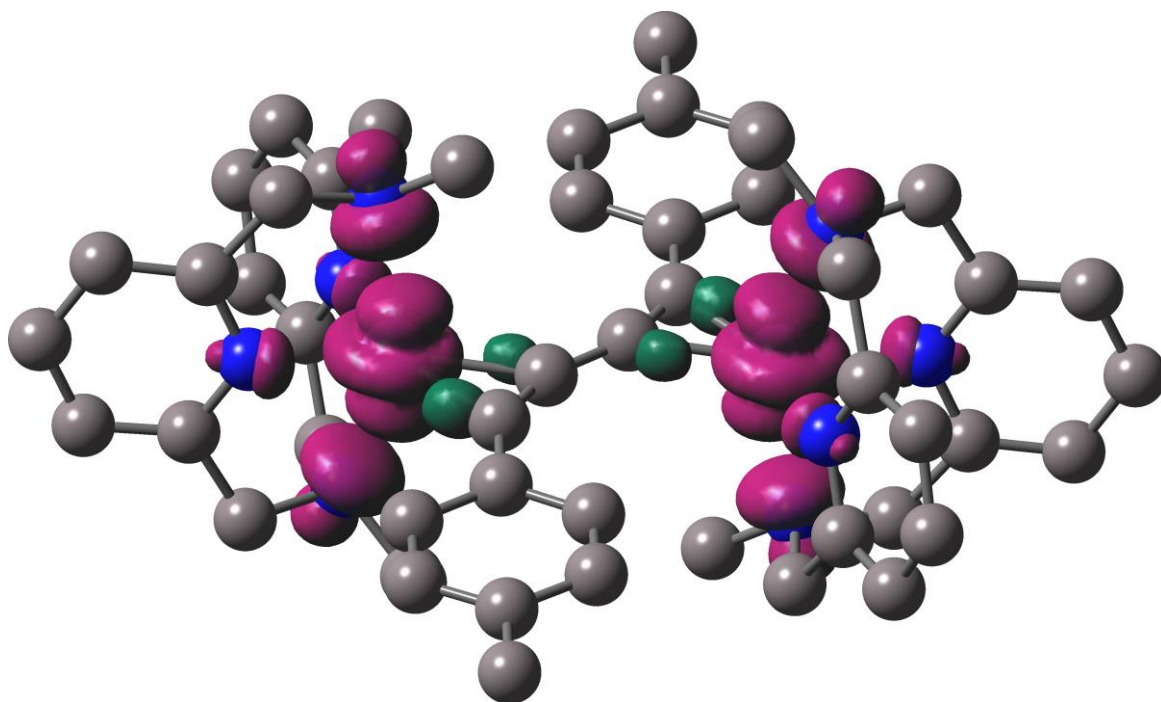


Figure 2.17: Spin density plot of **2b**. Hydrogen atoms are removed for clarity.

Table 2.7: Selected bond lengths [Å] in $[\{\text{Ni}(\text{L}-\text{N}_4\text{Me}_2)\}_2(\mu\text{-RC}_4\text{R})](\text{ClO}_4)_2$ (2a–2g).

	2a	2b	2c	2d	2e	2f	2g
Ni–N _{amine} (avg.)	2.232 ± 0.004	2.231 ± 0.001	2.226 ± 0.006	2.231 ± 0.013	2.233 ± 0.002 2.217 ± 0.003	2.236 ± 0.007	2.232 ± 0.014 2.230 ± 0.009
Ni–N _{py} (avg.)	1.999 ± 0.003	1.990 ± 0.010	1.9928 ± 0.010	1.996 ± 0.006	1.995 ± 0.001 1.960 ± 0.002	2.003 ± 0.010	2.004 ± 0.007 2.007 ± 0.007
Ni–C _{alkyne}	1.9940(17) 1.9586(18)	1.9956(14) 1.9485(15)	1.994(3) 1.952(3)	2.0026(13) 1.9464(13)	2.0049(15) 1.9479(16) 1.9856(16) 1.9373(16)	2.0016(15) 1.9572(15)	2.0323(16) 1.9488(17) 2.0109(16) 1.9558(16)
Ni–C _{C≡C} ^a	1.870	1.867	1.869	1.870	1.879 1.856	1.878	1.888 1.879
C≡C	1.270(3)	1.2710(19)	1.265(4)	1.2676(17)	1.266(2) 1.271(2)	1.254(2)	1.264(2) 1.269(2)
C _{sp} –C _{sp}	1.394(4)	1.388(3)	1.405(5)	1.392(2)	1.396(2)	1.398(3)	1.398(2)
C _R –C	1.448(3)	1.446(2)	1.454(4)	1.4447(17)	1.442(2) 1.440(2)	1.485(2)	1.438(2) 1.443(2)
Ni···Ni ^b	5.042	5.038	5.033	5.072	5.064	5.056	5.110
C _{C≡C} ···C _{C≡C}	2.613	2.611	2.624	2.607	2.609	2.602	2.604

^acentroid, ^bDistance between two centers

Table 2.8: Selected angles [°] in $[\{\text{Ni}(\text{L-N}_4\text{Me}_2)\}_2(\mu\text{-RC}_4\text{R})](\text{ClO}_4)_2$ (2a–2g).

	2a	2b	2c	2d	2e	2f	2g
$\text{N}_{\text{amine}}\text{-Ni-N}_{\text{amine}}$	153.58(6)	153.55(5)	153.61(5)	153.30(5)	153.45(5) 151.50(5)	153.37(5)	153.58(6) 153.18(5)
$\text{N}_{\text{py}}\text{-Ni-N}_{\text{py}}$	84.81(6)	85.72(5)	84.35(9)	85.04(5)	85.22(5) 91.98(5)	84.56(5)	84.36(6) 84.17(5)
$\text{C}_{\text{alkyne}}\text{-Ni-C}_{\text{alkyne}}$	37.48(8)	37.57(6)	37.37(12)	37.41(5)	37.32(7) 37.80(6)	36.92(6)	36.96(7) 37.28(7)
$\text{C}_{\text{R}}\text{-C}\equiv\text{C}$	148.16(18)	149.56(15)	147.7(4)	147.72(13)	150.22(16) 146.27(16)	150.07(16) ^o	156.45(18) 150.15(17)
$\text{C}\equiv\text{C-C}$	157.3(2)	158.01(18)	158.7(3)	157.07(16)	158.09(16) 155.24(16)	157.7(2)	157.32(17) 155.11(17)
$\text{N}_{\text{amine}}\text{-Ni-C}_{\text{C}\equiv\text{C}}^{\text{a}}$	103.98 104.18	103.98 103.67	101.55 104.82	102.23 104.47	100.83/102.34 105.71/106.16	102.61 104.01	101.18/102.18 104.99/104.64
δ^{b}	81.95	83.49	81.94	81.11	81.89 85.49	89.76	89.13 89.43

^acentroid, ^bdihedral angle between $\text{N}_{\text{amine}}\text{-Ni-N}_{\text{amine}}$ and $\text{C}_{\text{R}}\text{-C}\equiv\text{C-C}$ plane

2.2.3 Magnetochemistry

X-ray structure determination and DFT calculation confirmed that the dinuclear nickel(I)-diyne complexes have two spin carriers. To know, how these spins interact with each other and the impact of substituents to 1,3-butadiyne on magnetic interaction, magnetic susceptibility measurements were carried out on the nickel(I)-diyne complexes **2a-2g** at a magnetic field of 0.5 T in the temperature range 2–295 K. The temperature dependence of the magnetic susceptibility for the complexes (**2a-2g**) are shown in Figure 2.18 to Figure 2.24.

The $\chi_M T$ values at 295 K are $0.83 \text{ cm}^3 \text{ K mol}^{-1}$ – $0.89 \text{ cm}^3 \text{ K mol}^{-1}$, which are slightly higher than the expected spin-only value of $0.75 \text{ cm}^3 \text{ K mol}^{-1}$ of two nickel(I) ($S = 1/2$) centers in the absence of any exchange coupling with a Lande' g -factor of 2.00. In all the complexes, the $\chi_M T$ values decrease gradually with lowering temperature and reach zero at 2 K, indicating antiferromagnetic coupling between two nickel(I) centers.

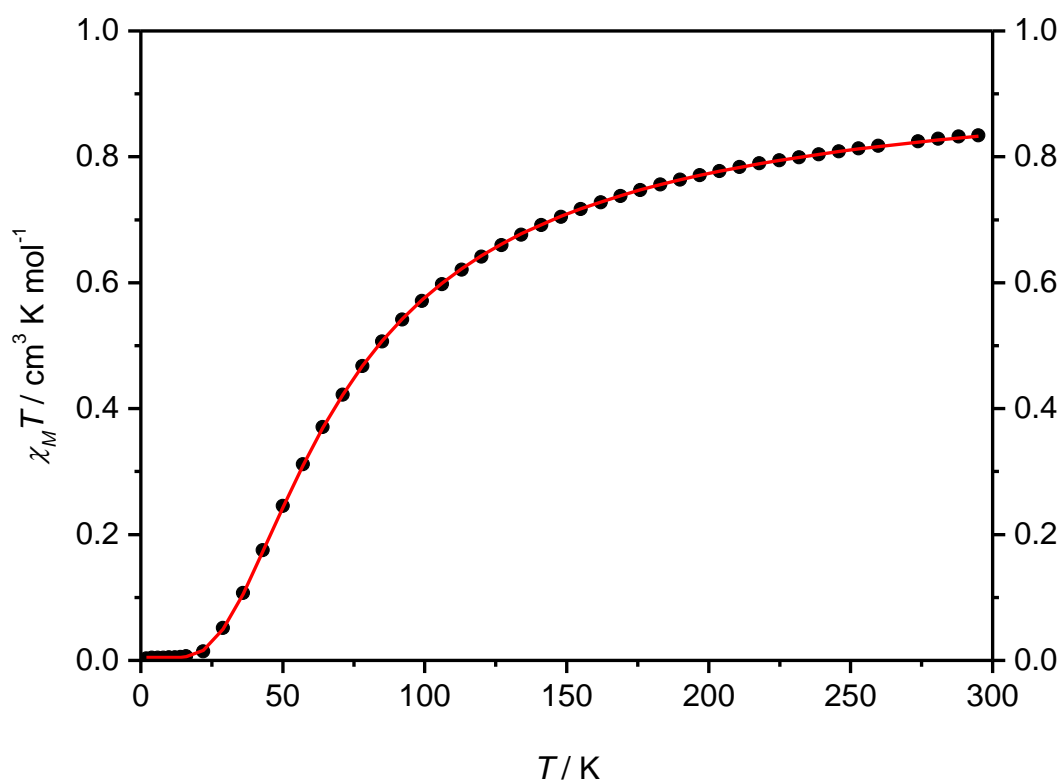


Figure 2.18: Variation of the product $\chi_M T$ with temperature for solid **2a** at an applied magnetic field of 0.5 T. The solid line represents the best fit of the data.

The magnetic susceptibility data were fitted using Heisenberg–Dirac–van-Vleck (HDvV) spin Hamiltonian for isotropic exchange coupling and Zeeman splitting (equation 1).

$$\hat{H} = -2J\hat{S}_1\hat{S}_2 + g\mu_B(\hat{S}_1 + \hat{S}_2)B \quad (1)$$

Table 2.9 includes the selected parameters that obtained from simulation of the SQUID data. Additional parameters are listed in *appendix* Table 7.10. The least squares fit of the experimental data lead to $g_1 = g_2 = 2.252$ to 2.341 and $J = -33.83$ to -46.23 for the complexes **2a–2g**, which indicate that two nickel(I) centers are antiferromagnetically coupled.

Table 2.9: Parameters obtained from simulation of the SQUID data.

Complex	Spin	g	J [cm^{-1}]
2a [R = Ph]	$S_1 = 1/2, S_2 = 1/2$	2.252, 2.252	- 44.27
2b [R = C ₆ H ₄ Me-4]	$S_1 = 1/2, S_2 = 1/2$	2.254, 2.254	- 39.27
2c [R = C ₆ H ₄ F-4]	$S_1 = 1/2, S_2 = 1/2$	2.341, 2.341	- 46.23
2d [R = C ₆ H ₄ OMe-4]	$S_1 = 1/2, S_2 = 1/2$	2.252, 2.252	- 42.56
2e [R = C ₆ H ₄ NMe ₂ -4]	$S_1 = 1/2, S_2 = 1/2$	2.285, 2.285	- 41.53
2f [R = ⁿ Pr]	$S_1 = 1/2, S_2 = 1/2$	2.272, 2.272	- 33.83
2g [R = Fc]	$S_1 = 1/2, S_2 = 1/2$	2.296, 2.296	- 37.55

It is known that the magnitude and nature of magnetic interaction of ligand-bridged dinuclear complexes depends on several structural parameters such as metal-metal distance, metal-ligand-metal bridge angle, metal-ligand bond distance and coordination environment around metal centers and electronic nature of bridging ligand.^[130-133] These parameters effect the overlap between the magnetic metal atomic orbitals and the bridging ligand orbitals. The magnetic orbitals of dinuclear nickel(I)-diyne complexes are d_z^2 , which are antiferromagnetically coupled through diyne ligand. A weak antiferromagnetic interaction in the diyne-bridged dinuclear nickel(I) complexes in distorted trigonal bipyramidal coordination environment is expected. Since the magnetic orbital and the bridging diyne ligand are bonded in the orthogonal plane, the overlap of the magnetic d_z^2 orbitals are weaker and less effective. However, a strong antiferromagnetic coupling is observed for the dinuclear complexes, which suggests a strong interaction between the magnetic orbital and the bridging diyne ligand. The effect of substituents to diyne ligand on the structural parameters are not very different (Table 2.7 and Table 2.8) and therefore electronic nature could provide a basis for the explanation of the

different magnetic behaviors for the dinuclear nickel(I)-diyne complexes. The strength of the antiferromagnetic interaction in nickel(I)-diyne complexes (**2a-2e**) decreases with increasing electron richness of diyne ligand, which could be explained by the destabilization of HOMO.^[130, 132] In addition, antiferromagnetic coupling constant value is greatest for **2a**, followed by **2g** and **2f** (Table 2.9).

In addition, the polycrystalline powder and frozen solution of the dinuclear nickel(I)-diyne complexes are EPR silent at room temperature and 77 K, which also confirm the strong antiferromagnetic coupling.

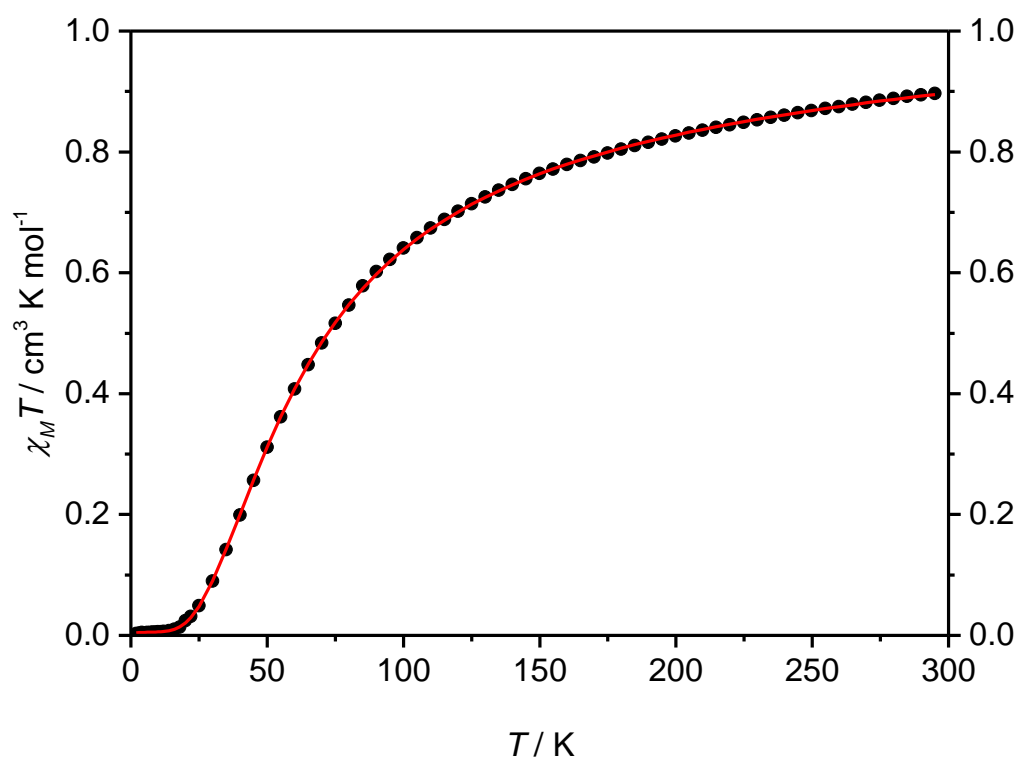


Figure 2.19: Variation of the product $\chi_M T$ with temperature for solid 2b at an applied magnetic field of 0.5 T. The solid line represents the best fit of the data.

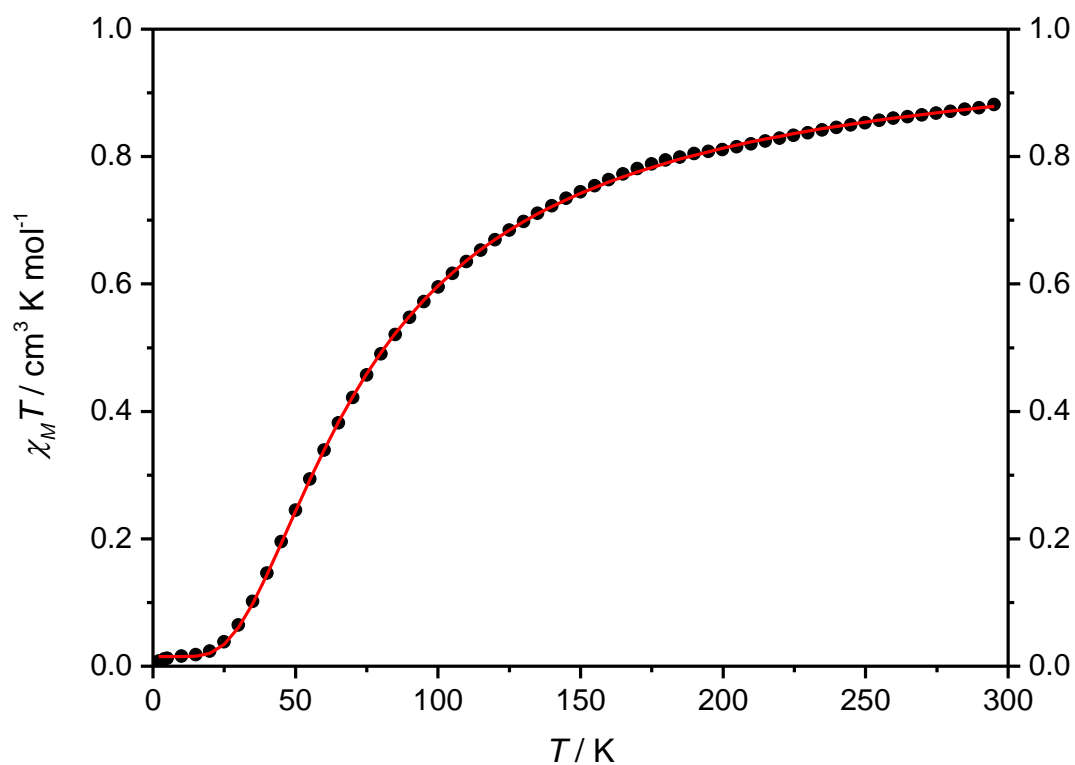


Figure 2.20: Variation of the product $\chi_M T$ with temperature for solid 2c at an applied magnetic field of 0.5 T. The solid line represents the best fit of the data.

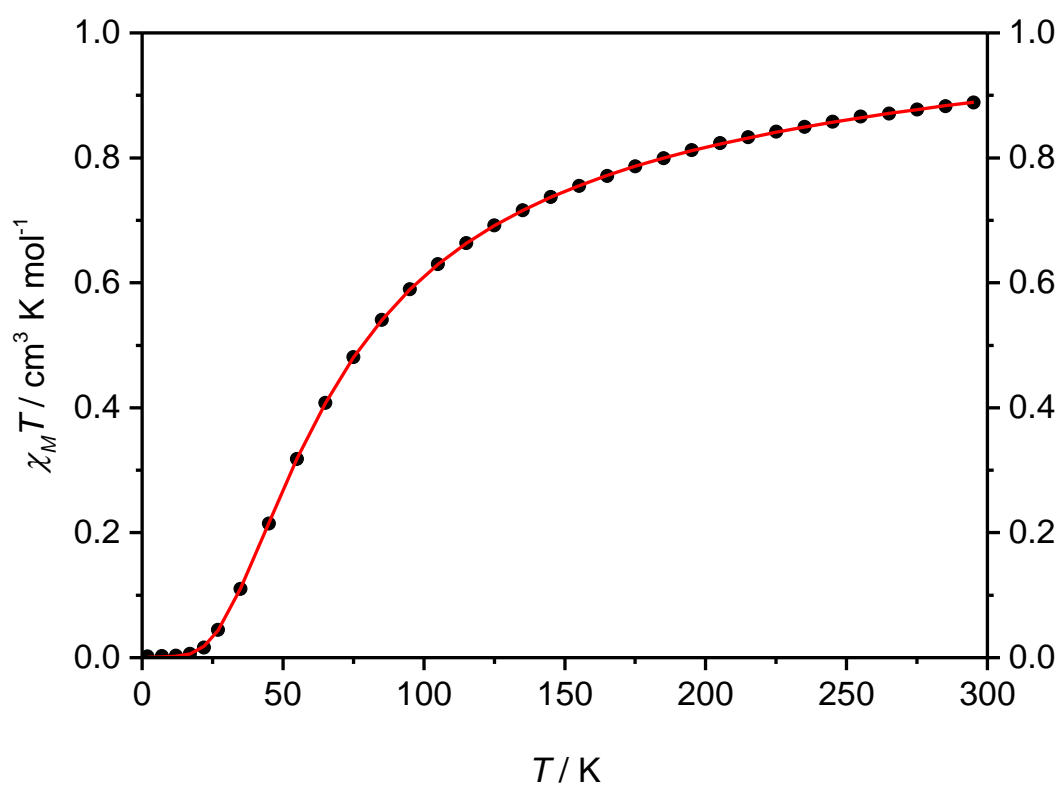


Figure 2.21: Variation of the product $\chi_M T$ with temperature for solid 2d at an applied magnetic field of 0.5 T. The solid line represents the best fit of the data.

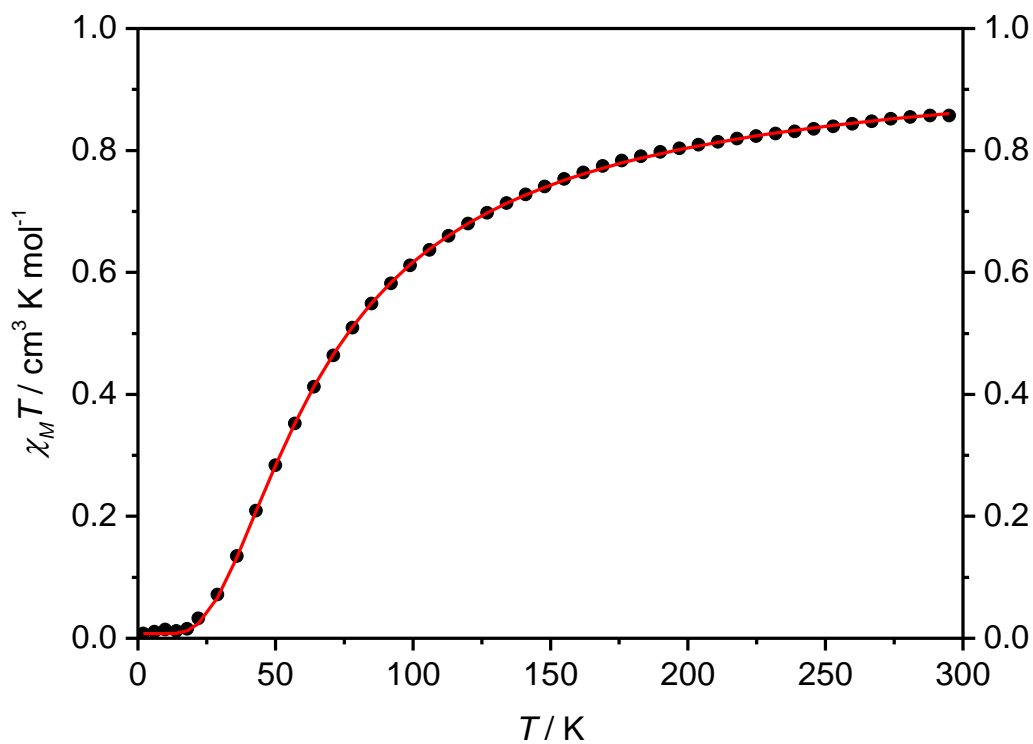


Figure 2.22: Variation of the product $\chi_M T$ with temperature for solid 2e at an applied magnetic field of 0.5 T. The solid line represents the best fit of the data.

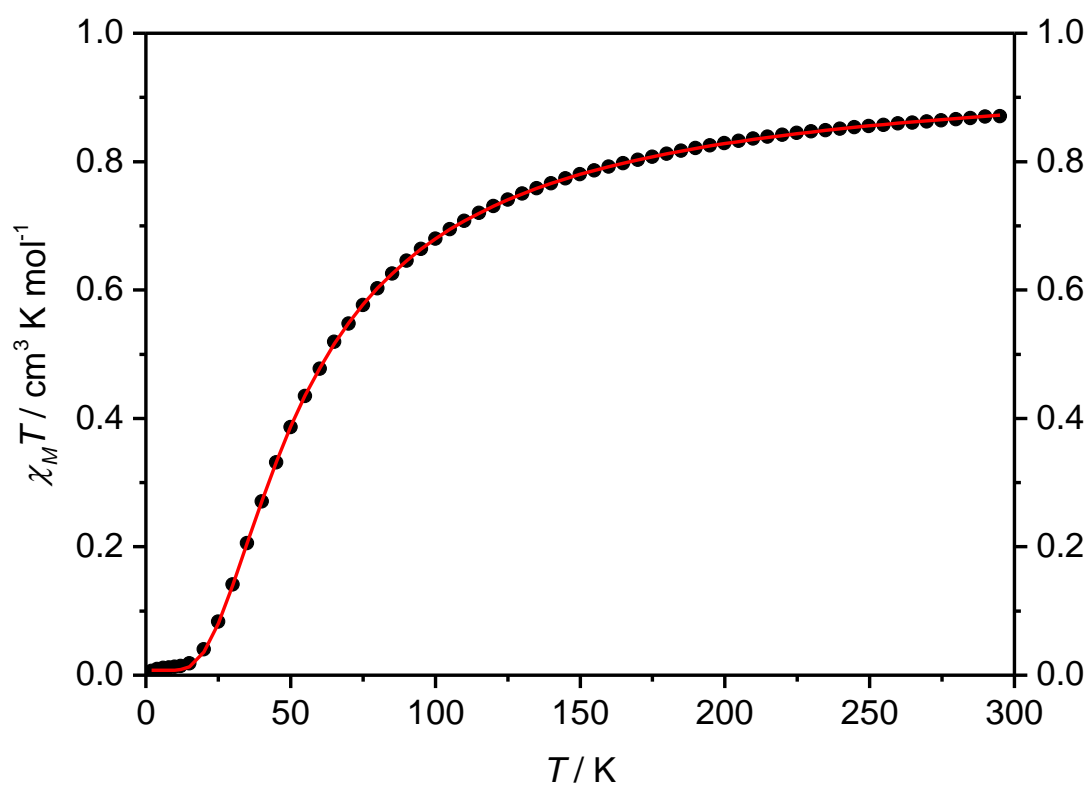


Figure 2.23: Variation of the product $\chi_M T$ with temperature for solid 2f at an applied magnetic field of 0.5 T. The solid line represents the best fit of the data.

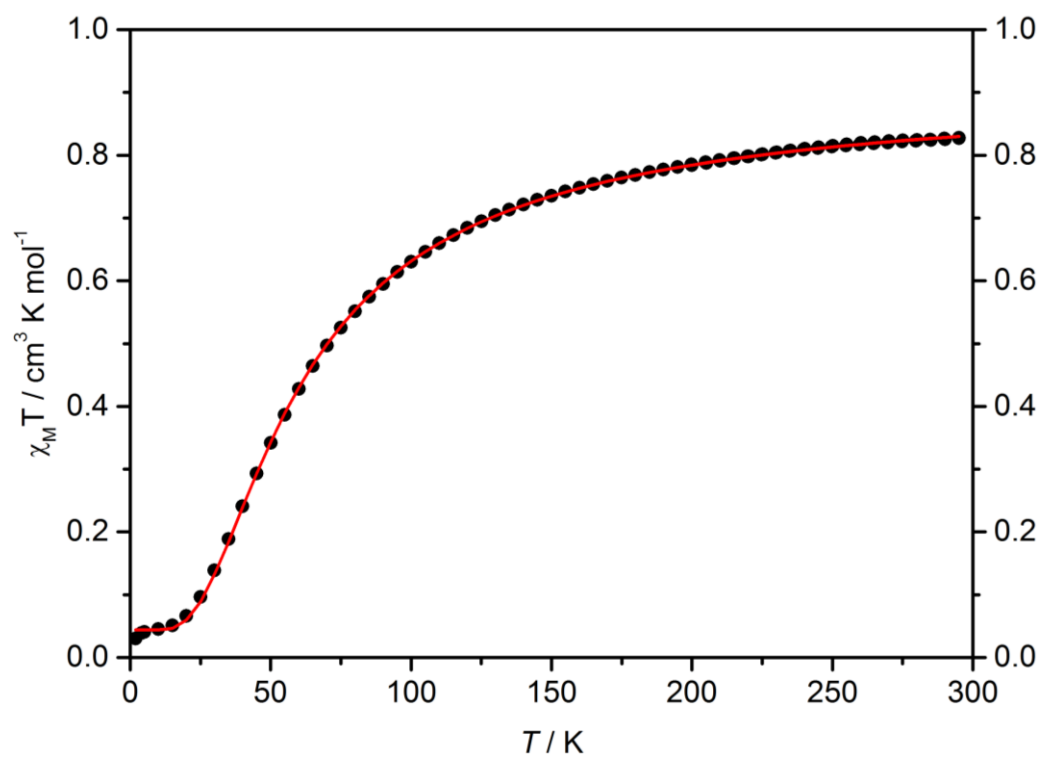


Figure 2.24: Variation of the product $\chi_M T$ with temperature for solid 2g at an applied magnetic field of 0.5 T. The solid line represents the best fit of the data.

2.2.4 Spectroscopic Studies

The complexes $[\{\text{Ni}(\text{L-N}_4\text{Me}_2)\}_2(\mu\text{-RC}_4\text{R})](\text{ClO}_4)_2$ (**2a-2g**) are well characterized by IR spectroscopy, ESI-MS and UV-Vis-NIR spectroscopy.

IR Spectroscopy

The C \equiv C vibrational frequencies have often been used to determine relative C \equiv C bond strengths and the nature of metal alkyne bonding, as the strength of the C \equiv C bond in an alkyne complex depends on the metal alkyne interactions. Therefore, IR spectroscopy measurements of the nickel(I)-diyne complexes were performed as KBr pellet at room temperature. IR spectrum of the complex **2a** is depicted in Figure 2.25. IR spectra of the other nickel(I)-diyne complexes (**2b-2g**) are displayed in *appendix* section. A comparison of the IR data of nickel-diyne complexes (**2a-2g**) is summarized in Table 2.10. IR spectra of the complexes display typical absorption of coordinated diazapyridinophane ligand, L-N $_4$ Me $_2$ at around 1605, 1475, 1445 and 1378 cm $^{-1}$. The complexes are dicationic in nature, having two ClO $_4^-$ as the counter anions. The stretching vibrations of ClO $_4^-$ are found at 1092 – 1096 cm $^{-1}$ and 621 – 623 cm $^{-1}$.

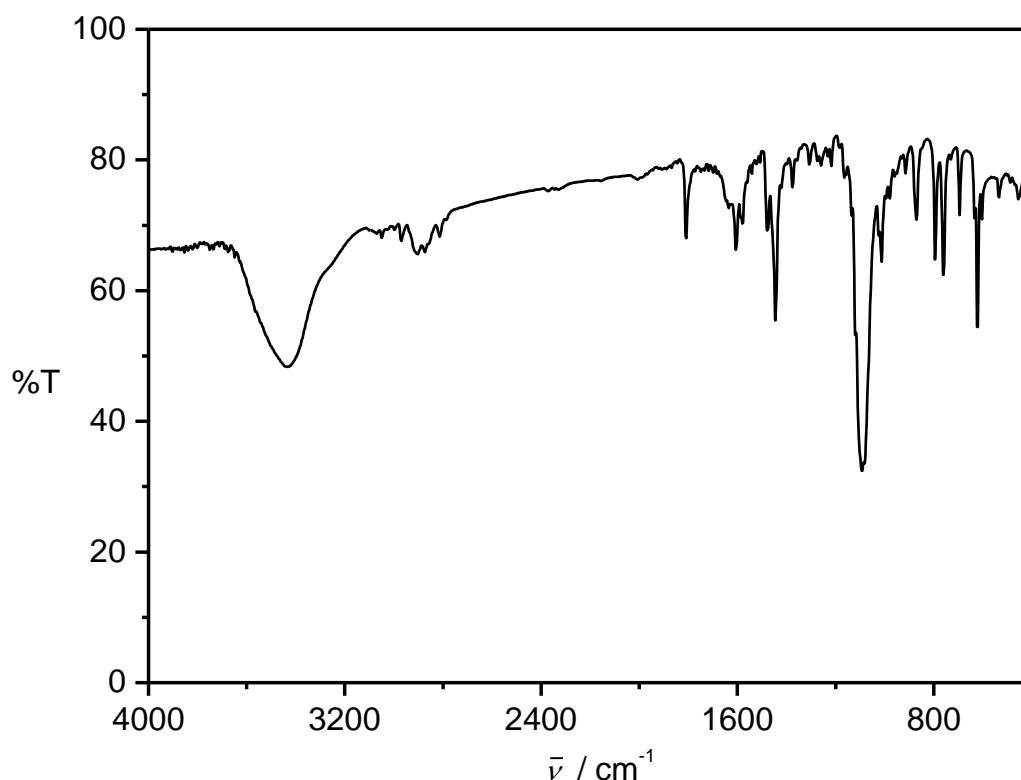


Figure 2.25: IR spectrum (KBr pellet) of **2a**.

Table 2.10: Comparison of IR data (in cm⁻¹) for $[\{\text{Ni}(\text{L}-\text{N}_4\text{Me}_2)\}_2(\mu\text{-RC}_4\text{R})](\text{ClO}_4)_2$ (2a–2g).

2a	2b	2c	2d	2e	2f	2g
						3088
2970	2964	2966	2959	2963	2965	
2904	2906	2908	2909	2895	2921	2916
	2875	2878	2877		2872	
2814	2813	2815	2813	2813	2817	2814
					1855	
1809	1813	1808	1810	1806		1820
1607	1604	1606		1601	1605	1604
1579	1579	1592	1579		1582	1579
		1493	1499	1513		
1479	1473	1475	1474	1474	1473	1472
1444	1444	1445	1444	1444	1447	1444
1375	1377	1378	1376	1361	1378	1375
			1285	1285		1303
			1250	1250		
		1222	1218			1213
1165		1151	1161	1161	1162	1162
1134	1132	1119			1120	
1093	1093	1095	1095	1092	1099	1096
			1025			
1012	1012	1012	1014	1013	1014	1012
				945		
870	872	871	871	871	870	870
		843	837		821	828
794	791	794	793	794	792	792
760			758	758	757	
694						
634						
621	623	623	623	623	623	623

IR spectra of the complexes exhibit bands around 1809-1852 cm^{-1} which are assigned to asymmetric stretching frequency of coordinated $\text{C}\equiv\text{C}$ of diyne ligand. Table 2.11 shows a comparison of $\text{C}\equiv\text{C}$ stretching frequency ($\nu_{\text{C}\equiv\text{C}}$) between the coordinated diyne in complexes and the free diyne. The relatively lower $\nu_{\text{C}\equiv\text{C}}$ stretching compared to free diyne confirms the extent of π -interaction in complexes.

Table 2.11: Comparison of selected IR data of $[\{\text{Ni}(\text{L}-\text{N}_4\text{Me}_2)\}_2(\mu\text{-RC}_4\text{R})](\text{ClO}_4)_2$ (2a**–**2g**) with free diyne.**

Complex	$\nu_{\text{C}\equiv\text{C}}$ in cm^{-1} ($\text{C}\equiv\text{C}$ in \AA)	$\nu_{\text{C}\equiv\text{C}}$ in cm^{-1} (Free RC_4R) ^[134-137]
2a [R = Ph]	1809 (1.270(3))	2147
2b [R = $\text{C}_6\text{H}_4\text{Me-4}$]	1813 (1.271(2))	2142
2c [R = $\text{C}_6\text{H}_4\text{F-4}$]	1808 (1.265(4))	2143
2d [R = $\text{C}_6\text{H}_4\text{OMe-4}$]	1810 (1.267(2))	2138
2e [R = $\text{C}_6\text{H}_4\text{NMe}_2\text{-4}$]	1806 (1.268)	2140
2f [R = ${}^n\text{Pr}$]	1852 (1.254(2))	-
2g [R = Fc]	1820 (1.267)	2140

The impact of the para substituents to the aryl group of the diyne ligand ($4\text{-XC}_6\text{H}_4\text{-C}\equiv\text{C-C}\equiv\text{C-C}_6\text{H}_4\text{X-4}$) on the profile of $\text{C}\equiv\text{C}$ stretching frequency is insensitive (Figure 2.26). In contrast, for Ph, Fc and ${}^n\text{Pr}$ group as substituents to 1,3-dibutadiyne ($\text{R-C}\equiv\text{C-C}\equiv\text{C-R}$), $\text{C}\equiv\text{C}$ stretching frequency of diyne shifted to higher energy in order of **2f** > **2g** > **2a** [$\bar{\nu}_{\text{C}\equiv\text{C}} = 1809 \text{ cm}^{-1}$ for **2a** (R = Ph), 1820 cm^{-1} for **2f** (R = Fc) and 1852 cm^{-1} for **2g** (R = ${}^n\text{Pr}$)] (Figure 2.27). This trend is also consistent with the $\text{C}\equiv\text{C}$ bond length of coordinated diyne in the nickel(I)-diyne complexes (Table 2.7). Overall, X-ray and IR data suggest that the combined effect of the alkyne \rightarrow nickel σ -bond and nickel \rightarrow alkyne π -bond is greatest for **2a**, followed by **2g** and **2f**.

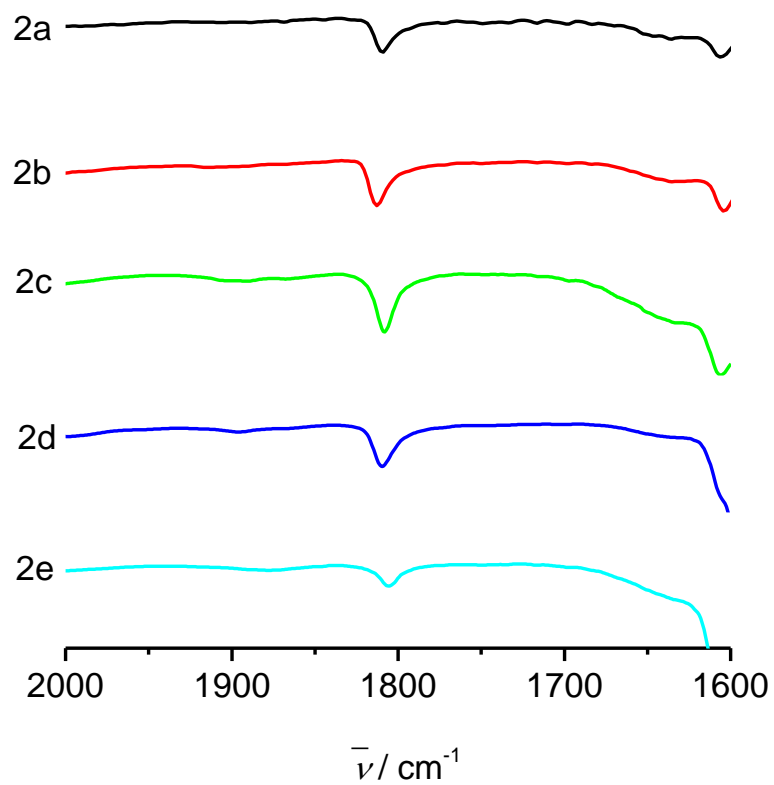


Figure 2.26: Selected IR spectra of 2a-2e.

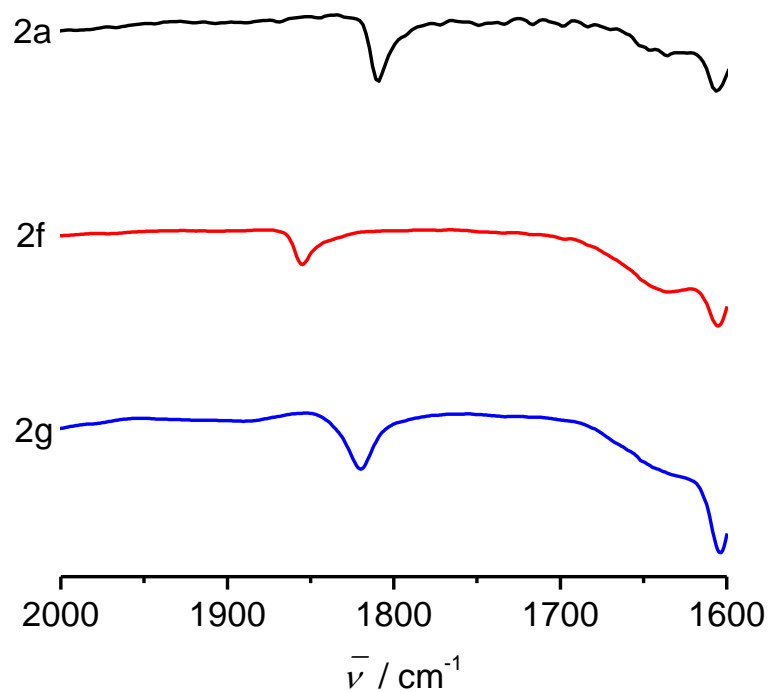


Figure 2.27: Selected IR spectra of 2a, 2f and 2g.

ESI mass spectrometry

The ESI-MS studies of the dinuclear nickel(I)-diyne complexes $[\{\text{Ni}(\text{L-N}_4\text{Me}_2)\}_2(\mu\text{-RC}_4\text{R})](\text{ClO}_4)_2$ (**2a-2g**) are conducted in acetonitrile at room temperature under nitrogen atmosphere. ESI-MS spectrum of the complex **2a** is depicted in Figure 2.28. ESI-MS spectra of the other nickel(I)-diyne complexes (**2b-2g**) are displayed in *appendix* section. ESI-MS data is summarized in Table 2.12.

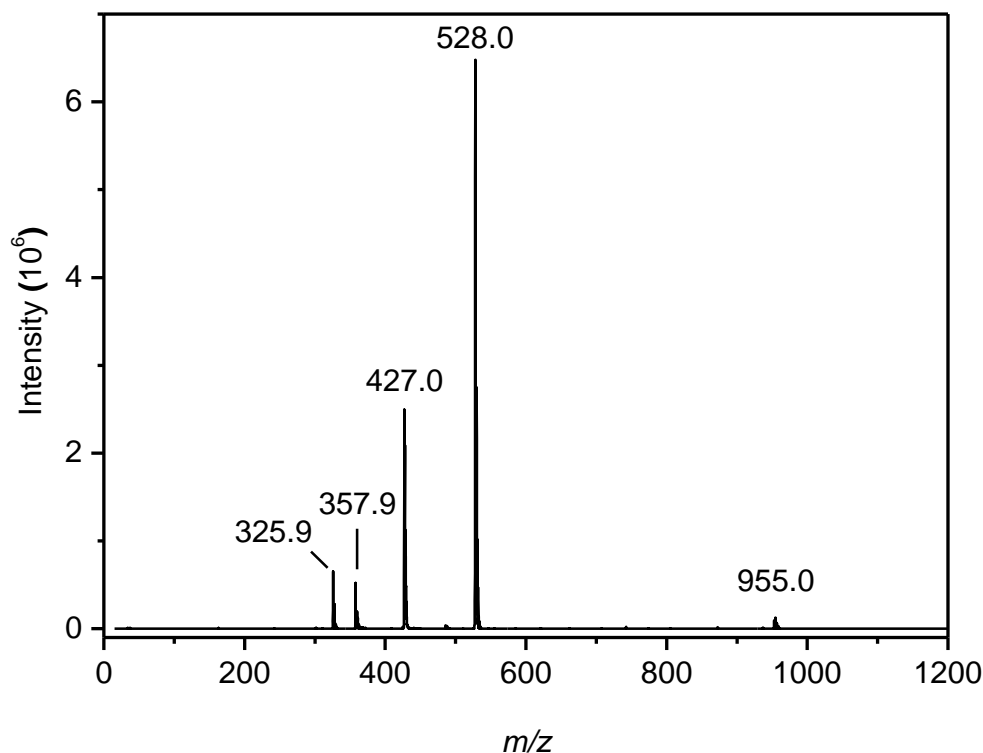


Figure 2.28: ESI-MS spectrum of **2a** in MeCN.

The spectrum of $[\{\text{Ni}(\text{L-N}_4\text{Me}_2)\}_2(\text{RC}_4\text{R})](\text{ClO}_4)_2$ [$\text{R} = \text{Ph}$] (**2a**) reveals four prominent ion peaks at m/z of 955.2, 528.0, 427.1 and 325.9, whose mass and isotope distribution pattern correspond to $[\{\text{Ni}(\text{L-N}_4\text{Me}_2)\}_2(\mu\text{-PhC}_4\text{Ph})(\text{ClO}_4)]^+$ (calculated m/z 955.0), $[\text{Ni}(\text{L-N}_4\text{Me}_2)(\text{PhC}_4\text{Ph})]^+$ (calculated m/z 528.2), $[\{\text{Ni}(\text{L-N}_4\text{Me}_2)\}_2(\mu\text{-PhC}_4\text{Ph})]^{2+}$ (calculated m/z 427.0) and $[\text{Ni}(\text{L-N}_4\text{Me}_2)]^+$ (calculated m/z 326.1) respectively (Figure 2.29 to Figure 2.32).

ESI-MS spectra of the other nickel(I)-diyne complexes (**2b-2g**, except **2f**) show similar ion distribution. The spectra of these complexes resulted in ion peaks corresponding to $[\{\text{Ni}(\text{L-N}_4\text{Me}_2)\}_2(\mu\text{-RC}_4\text{R})(\text{ClO}_4)]^+$, $[\text{Ni}(\text{L-N}_4\text{Me}_2)(\text{RC}_4\text{R})]^+$, $[\{\text{Ni}(\text{L-N}_4\text{Me}_2)\}_2(\mu\text{-RC}_4\text{R})]^{2+}$ and $[\text{Ni}(\text{L-N}_4\text{Me}_2)]^+$. The ESI-MS spectrum of **2f** displays ion peaks corresponding to $[\text{Ni}(\text{L-N}_4\text{Me}_2)(\text{RC}_4\text{R})]^+$ and $[\text{Ni}(\text{L-N}_4\text{Me}_2)]^+$.

Table 2.12: ESI MS data (in m/z) for $[\{\text{Ni}(\text{L-N}_4\text{Me}_2)\}_2(\mu\text{-RC}_4\text{R})(\text{ClO}_4)_2$ (2a-2g).

	2a	2b	2c	2d	2e	2f	2g
	Calc. Found	Calc. Found	Calc. Found	Calc. Found	Calc. Found	Calc. Found	Calc. Found
$[\{\text{Ni}(\text{L-N}_4\text{Me}_2)\}_2(\mu\text{-RC}_4\text{R})(\text{ClO}_4)]^+$	955.2 955.0	983.3 983.0	991.1 990.9	1013.3 1013.0	1041.3 1041.1	-	1171.1 1171.0
$[\{\text{Ni}(\text{L-N}_4\text{Me}_2)\}_2(\mu\text{-RC}_4\text{R})]^{2+}$	427.0 427.2	441.2 441.1	445.1 445.0	457.2 457.1	470.2 470.1	-	535.1 534.9
$[\text{Ni}(\text{L-N}_4\text{Me}_2)(\text{RC}_4\text{R})]^+$	528.2 528.0	556.2 556.1	544.2 544.0	588.2 588.1	614.3 614.2	460.1 460.0	744.1 743.9
$[\text{Ni}(\text{L-N}_4\text{Me}_2)]^+$	326.1 325.9	326.1 325.9	326.1 325.9	326.1 325.9	326.1 325.9	326.1 325.9	326.1 325.9
$[\text{Ni}(\text{L-N}_4\text{Me}_2)(\text{O}_2)]^+$	358.1 357.9	358.1 357.9	358.1 357.9	358.1 357.9	358.1 357.9	358.1 357.9	358.1 357.9

The complex $[\{\text{Ni}(\text{L-N}_4\text{Me}_2)\}_2(\text{RC}_4\text{R})(\text{ClO}_4)_2$ [$\text{R} = \text{Ph}$] (**2a**) dissociates into a mononuclear nickel(I)-diyne complex $[\text{Ni}^{\text{I}}(\text{L-N}_4\text{Me}_2)(\text{PhC}_4\text{Ph})]^+$ with strong signal intensity and a mononuclear bisphenoidal nickel(I) complex $[\text{Ni}^{\text{I}}(\text{L-N}_4\text{Me}_2)]^+$ with moderate signal intensity in gas phase. Formation of this mononuclear $[\text{Ni}^{\text{I}}(\text{L-N}_4\text{Me}_2)(\text{PhC}_4\text{Ph})]^+$ complex provides important insights into the generation and isolation of L-N₄Me₂ coordinated mononuclear nickel(I)-alkyne complex in condense phase. The mononuclear complex $[\text{Ni}^{\text{I}}(\text{L-N}_4\text{Me}_2)]^+$ is both electron-rich and has an open coordination site, so that it is able to react with substrate molecules. Activation of CO₂ molecule by $[\text{Ni}^{\text{I}}(\text{L-N}_4\text{Me}_2)]^+$ complex in gas phase was investigated in collaboration with Prof. Mark A. Johnson's group at Yale University. The reaction of $[\text{Ni}^{\text{I}}(\text{L-N}_4\text{Me}_2)]^+$ with CO₂ molecule forms mononuclear complex $[\text{Ni}^{\text{II}}(\text{L-N}_4\text{Me}_2)(\text{CO}_2^{\cdot-})]^+$, where nickel(I) oxidized to nickel(II) and CO₂ reduced to CO₂^{•-}.^[138]

In addition, for all complexes, I also found a prominent ion peak at a m/z of 357.9, whose mass and isotope distribution pattern correspond to $[\text{Ni}(\text{L-N}_4\text{Me}_2)(\text{O}_2)]^+$ (calculated m/z 358.1) (*appendix* Figure 7.6). The $[\text{Ni}(\text{L-N}_4\text{Me}_2)(\text{O}_2)]^+$ species could be formed by the reaction of $[\text{Ni}^{\text{I}}(\text{L-N}_4\text{Me}_2)]^+$ and O₂ (present in small amounts in the instrument chamber).

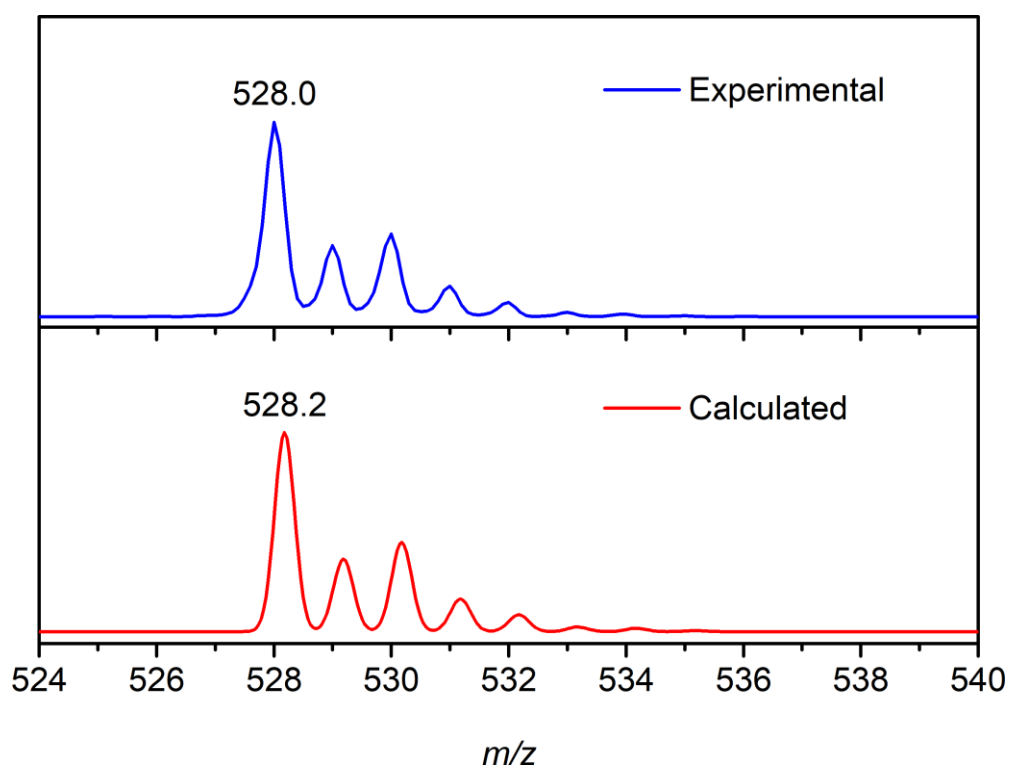


Figure 2.29: The experimental and calculated isotope distribution for $[\text{Ni}(\text{L-N}_4\text{Me}_2)(\text{PhC}_4\text{Ph})]^+$.

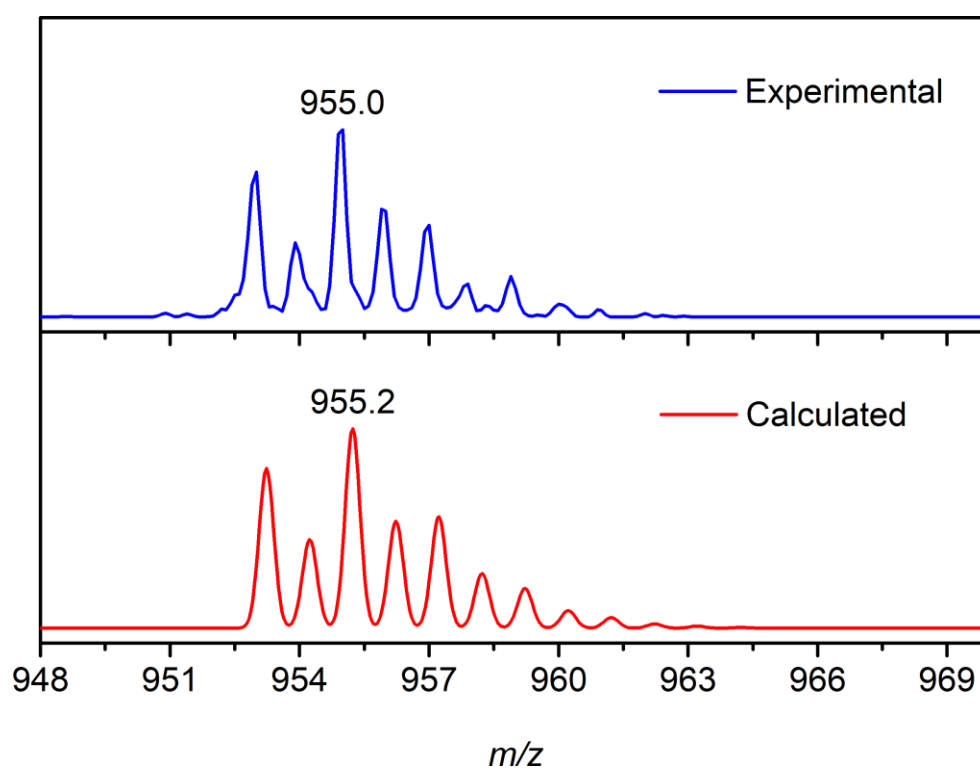


Figure 2.30: The experimental and calculated isotope distribution for $[\{\text{Ni}(\text{L-N}_4\text{Me}_2)\}_2(\mu\text{-PhC}_4\text{Ph})(\text{ClO}_4)]^+$.

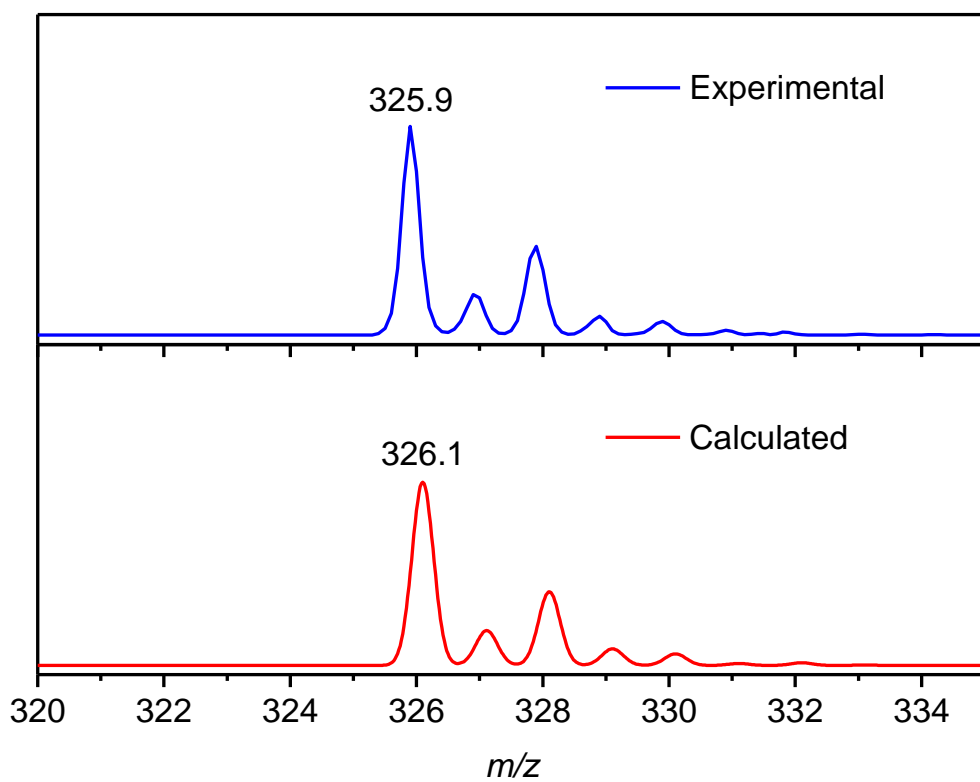


Figure 2.31: The experimental and calculated isotope distribution for $[\text{Ni}(\text{L-N}_4\text{Me}_2)]^+$.

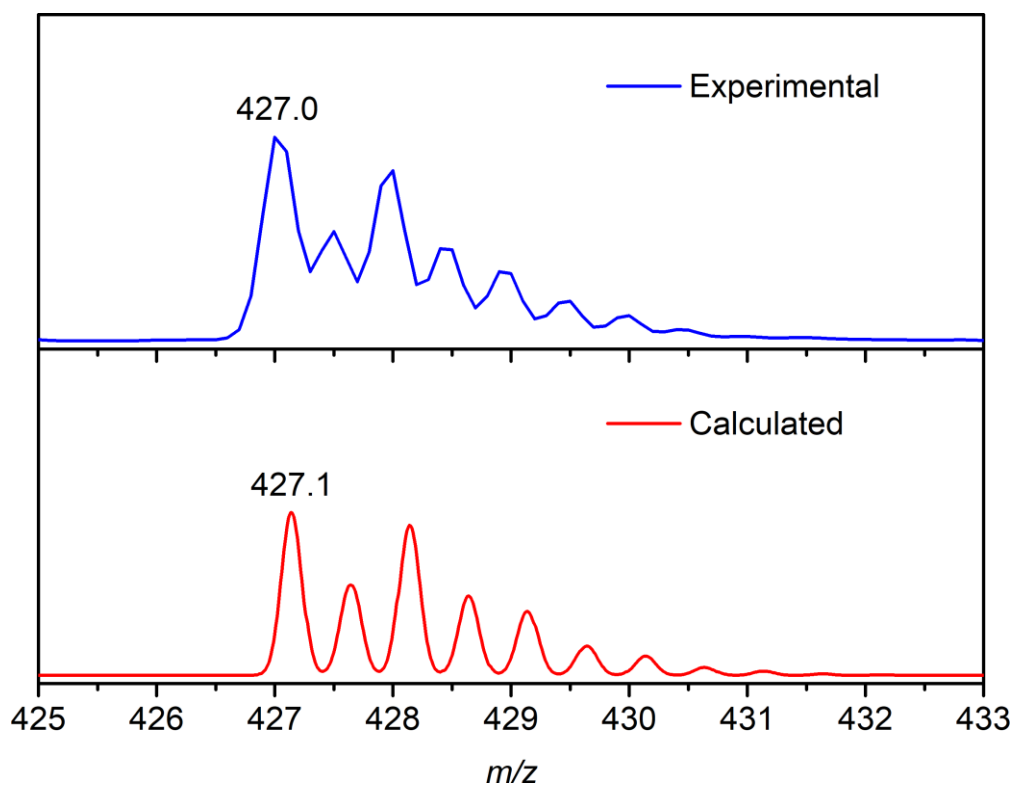


Figure 2.32: The experimental and calculated isotope distribution for $[\{\text{Ni}(\text{L-N}_4\text{Me}_2)\}_2(\mu\text{-PhC}_4\text{Ph})]^{2+}$.

UV-Vis-NIR Spectroscopy

Electronic absorption spectra of nickel(I)-diyne complexes $[\{\text{Ni}(\text{L}-\text{N}_4\text{Me}_2)\}_2(\mu\text{-RC}_4\text{R})](\text{ClO}_4)_2$ (**2a-2g**) were recorded in acetonitrile under pure nitrogen atmosphere at room temperature. UV-Vis-NIR spectrum of the complex **2a** is depicted in Figure 2.33. Deconvoluted UV-Vis-NIR spectrum of **2a** is shown in *appendix* Figure 7.8. UV-Vis-NIR spectra of the other nickel(I)-diyne complexes (**2b-2g**) are displayed in *appendix* section. A comparison of electronic absorption data of nickel-diyne complexes (**2a-2g**) is given in Table 2.13.

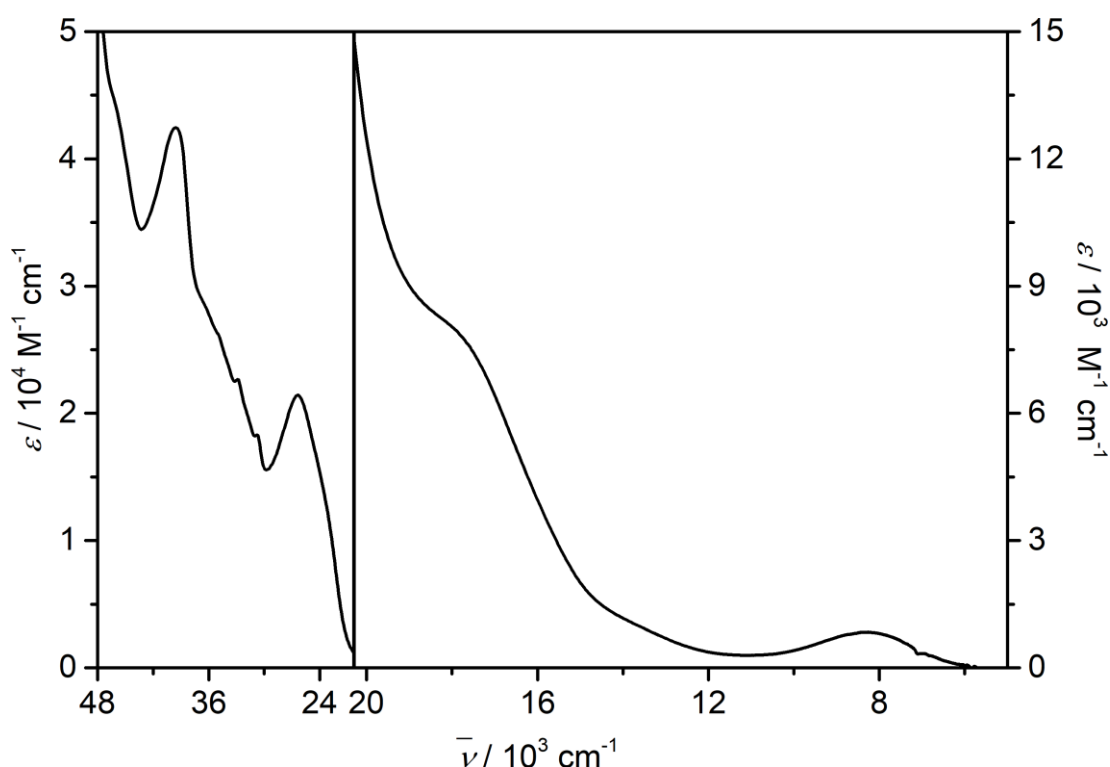


Figure 2.33: UV-Vis-NIR spectrum of **2a** in MeCN.

The complexes **2a-2g** exhibit broad band at around $7806 - 8306 \text{ cm}^{-1}$ ($\epsilon = 73 - 91 \text{ M}^{-1} \text{ cm}^{-1}$) and a shoulder at around $12594 - 13369 \text{ cm}^{-1}$ ($\epsilon = 85 - 146 \text{ M}^{-1} \text{ cm}^{-1}$) in visible-NIR region, which are attributed to d-d transitions ($d_{xy}, d_{x^2-y^2} \rightarrow d_{z^2}$ and $d_{xz}, d_{yz} \rightarrow d_{z^2}$ respectively). The complexes also show a shoulder at around $16000 - 18182 \text{ cm}^{-1}$ ($\epsilon = 491 - 823 \text{ M}^{-1} \text{ cm}^{-1}$) and an intense band at $24875 - 26738 \text{ cm}^{-1}$ ($\epsilon = 7200 - 35180 \text{ M}^{-1} \text{ cm}^{-1}$), which are assigned CT transitions. In addition, the spectra reveal band or shoulder assigned to L-N₄Me₂ ligand based ILCT transition at around $39215 - 39840 \text{ cm}^{-1}$ ($\epsilon = 24818 - 42460 \text{ M}^{-1} \text{ cm}^{-1}$).^[108] The complexes display bands and/or shoulders corresponding to diyne ligand based ILCT transitions at around $30211 - 36100 \text{ cm}^{-1}$ ($\epsilon = 7411 - 38288 \text{ M}^{-1} \text{ cm}^{-1}$).^[139-140]

Table 2.13: UV-Vis-NIR data (in cm^{-1}) for $[\{\text{Ni}(\text{L}-\text{N}_4\text{Me}_2)\}_2(\mu\text{-RC}_4\text{R})](\text{ClO}_4)_2$ (**2a-2g**).

Complex	$\bar{\nu}_{\text{max}} / \text{cm}^{-1}$ ($\epsilon / \text{M}^{-1} \text{cm}^{-1}$)
2a [R = Ph]	39525 (42460), 35087 (sh, 26230), 32895 (22660), 30769 (18310), 26385 (21434), 18018 (sh, 808), 13210 (sh, 146) and 8299 (91)
2b [R = C ₆ H ₄ Me-4]	39525 (42285), 34130 (sh, 27724), 32362 (sh, 23415), 30211 (sh, 18511), 26385 (20907), 17921 (sh, 769), 13369 (sh, 99) and 8264 (87)
2c [R = C ₆ H ₄ F-4]	39682 (37313), 35714 (sh, 25349), 32362 (sh, 20629), 26525 (21572), 18182 (sh, 784), 13333 (sh, 85) and 8319 (87)
2d [R = C ₆ H ₄ OMe-4]	39290 (39290), 36101 (sh, 33373), 32787 (sh, 27015), 26178 (26956), 17761 (sh, 754), 13158 (sh, 95) and 8157 (89)
2e [R = C ₆ H ₄ NMe ₂ -4]	42373 (sh, 42416), 39682 (sh, 37569), 30864 (38288), 24875 (35180), 17391 (sh, 823), 12970 (sh, 117) and 7968 (81)
2f [R = ⁿ Pr]	39840 (24818), 32051 (sh, 7411), 25839 (7200), 17212 (sh, 506), 12594 (sh, 98) and 7806 (73)
2g [R = Fc]	39215 (sh, 33894), 35587 (sh, 22482), 26738 (19175), 16000 (sh, 551), 12987 (sh, 103) and 7968 (74)

The absorption maxima in the range of 26500 – 25000 cm^{-1} of the complexes **2a-2e** bearing electronically different diyne display modest bathochromic shifts going from **2c** to **2a** and **2b**, whereas a significant shift to lower energy was observed in the case of **2d** to **2e** (*appendix* Figure 7.84). The extent of the observed red shift is consistent with the increasing electron donating nature of the diyne in the order F < H < Me < OMe < NMe₂. Furthermore, absorption maxima in the range of 26500 – 25000 cm^{-1} is greatest for **2g**, followed by **2a** and **2f** (*appendix* Figure 7.85).

A closer inspection of the absorptions corresponding to the d-d (d_{xy} , $d_{x^2-y^2} \rightarrow d_z^2$) transition in the spectra reveal that the impact of the *para* substituents to the aryl group of the diyne ligand (4-XC₆H₄-C≡C-C≡C-C₆H₄X-4) on the profile of the absorption band in NIR region is not dramatic (Figure 2.34). The peak maximum marginally red-shifts to energy as the electron-donating ability of the diyne increases [$\bar{\nu}_{\text{max}} = 8306 \text{ cm}^{-1}$ for **2c** (X = F), 8299 cm^{-1} for **2a** (X = H), 8264 cm^{-1} for **2b** (X = Me), 8156 cm^{-1} for **2d** (X = OMe) and 7968 cm^{-1} for **2e** (X =

NMe₂)]. However, impact of Ph, Fc and ⁿPr substituents to 1,4-dibutadiyne (R–C≡C–C≡C–R) on the profile of the absorption band in NIR region is intense (Figure 2.35). The peak maximum red-shifts to energy on the substitution of Ph, Fc and ⁿPr group respectively to RC₄R [$\bar{\nu}_{\max}$ = 8299 cm⁻¹ for **2a** (R = Ph), 7968 cm⁻¹ for **2g** (R = Fc) and 7806 cm⁻¹ for **2f** (R = ⁿPr)]. These results indicate that the ligand field strength exerted by the diyne ligand onto the nickel center is enhanced in the order of PhC₄Ph > FcC₄Fc > ⁿPrC₄ⁿPr.

Table 2.14: UV-Vis-NIR data (in nm) for [{Ni(L-N₄Me₂)₂(μ-RC₄R)](ClO₄)₂ (**2a-2g**).

Complex	λ_{\max} / nm (ϵ / M ⁻¹ cm ⁻¹)
2a [R = Ph]	253 (42460), 286 (sh, 26230), 304 (22660), 325 (18310), 379 (21434), 554 (sh, 808), 690 (sh, 146) and 1205 (91)
2b [R = C ₆ H ₄ Me-4]	253 (42285), 291(sh, 27724), 309 (sh, 23415), 330 (sh, 18511), 379 (20907), 558 (sh, 769), 747 (sh, 99) and 1210 (86)
2c [R = C ₆ H ₄ F-4]	252 (37313), 273 (sh, 25349), 306 (sh, 20629), 377 (21572), 550 (sh, 784), 750 (sh, 85) and 1202 (87)
2d [R = C ₆ H ₄ OMe-4]	252 (39290), 282 (sh, 33373), 313 (sh, 27015), 382 (26956), 563 (sh, 754), 760 (sh, 95) and 1226 (89)
2e [R = C ₆ H ₄ NMe ₂ -4]	237 (sh, 42416), 254 (sh, 37569), 324 (38288), 402 (35180), 575 (sh, 823), 771 (sh, 117) and 1255 (81)
2f [R = ⁿ Pr]	251 (24818), 316 (sh, 7411), 386 (7200), 558 (sh, 506), 794 (sh, 98) and 1281 (73)
2g [R = Fc]	254 (sh, 33894), 282 (sh, 22482), 374 (19174), 610 (sh, 551), 770 (sh, 103) and 1255 (74)

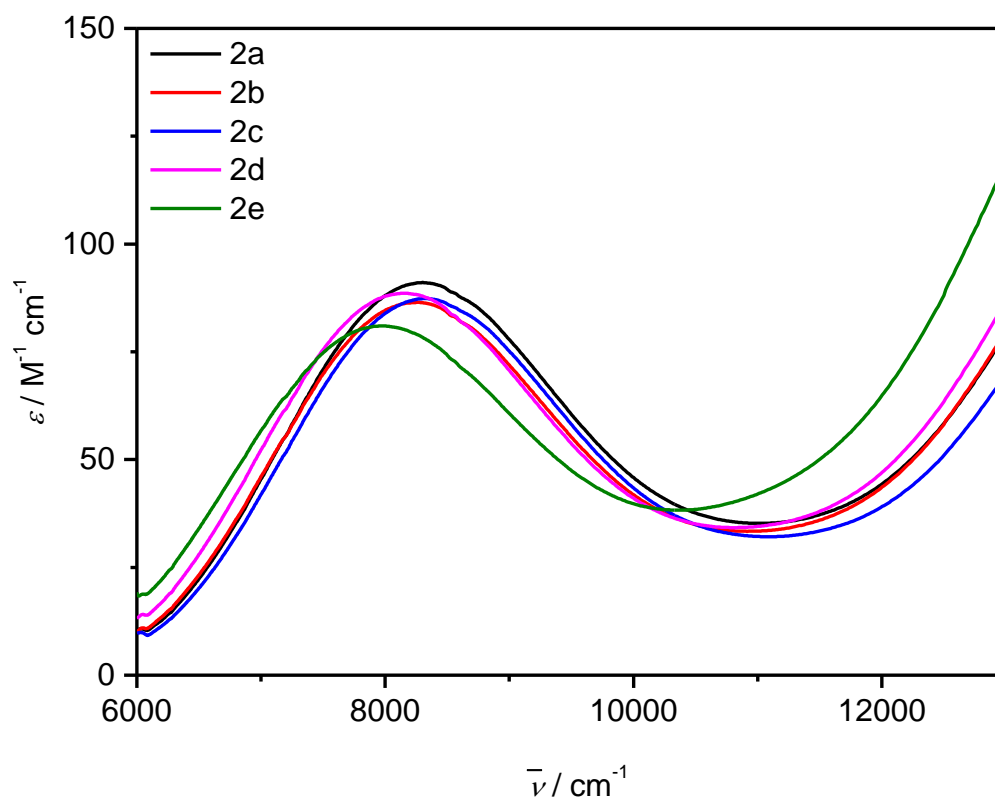


Figure 2.34: UV-Vis-NIR spectra of 2a-2e (region 6000 – 13000 cm^{-1}) in MeCN.

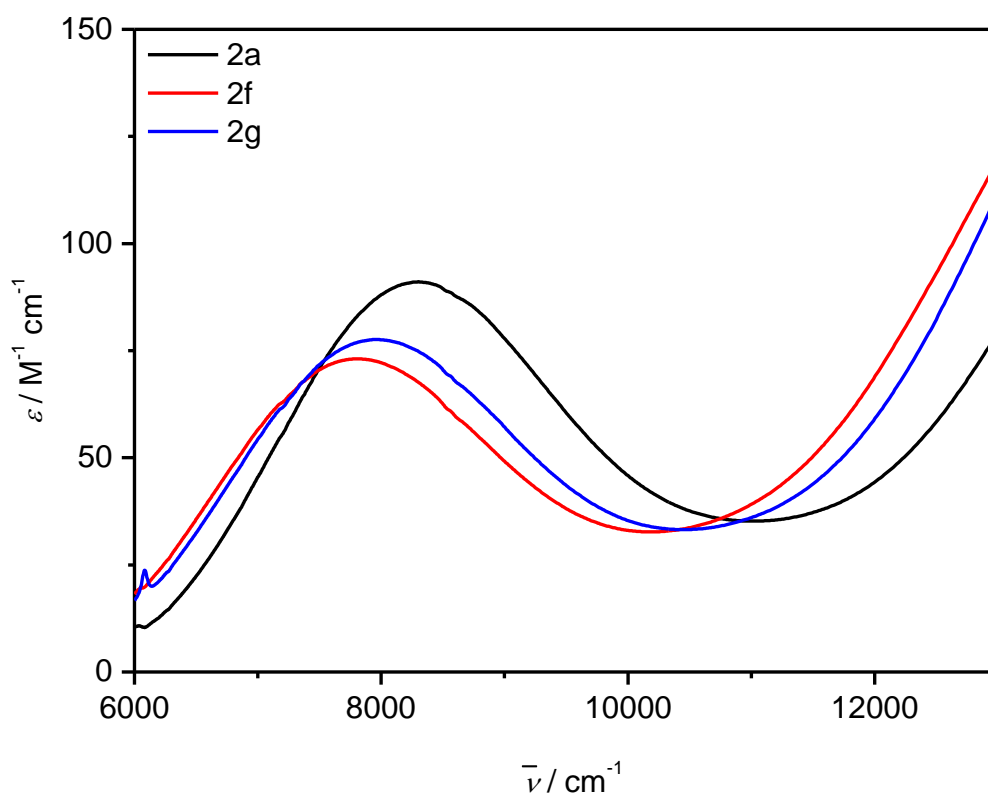


Figure 2.35: UV-Vis-NIR spectra of 2a, 2f and 2g (region 6000 – 13000 cm^{-1}) in MeCN.

2.2.5 Electrochemistry

The electrochemical behaviors of the dinuclear nickel(I)-diyne complexes $[\{\text{Ni}(\text{L-N}_4\text{Me}_2)\}_2(\mu\text{-RC}_4\text{R})](\text{ClO}_4)_2$ (**2a-2g**) are studied by cyclic voltammetry and coulometry in acetonitrile solution. Cyclic voltammogram for the oxidation of the complex **2a** is depicted in Figure 2.36. Cyclic voltammograms of the other nickel(I)-diyne complexes (**2b-2g**) are displayed in appendix section. The electrochemical data of the complexes (**2a-2g**) is summarized in Table 2.15.

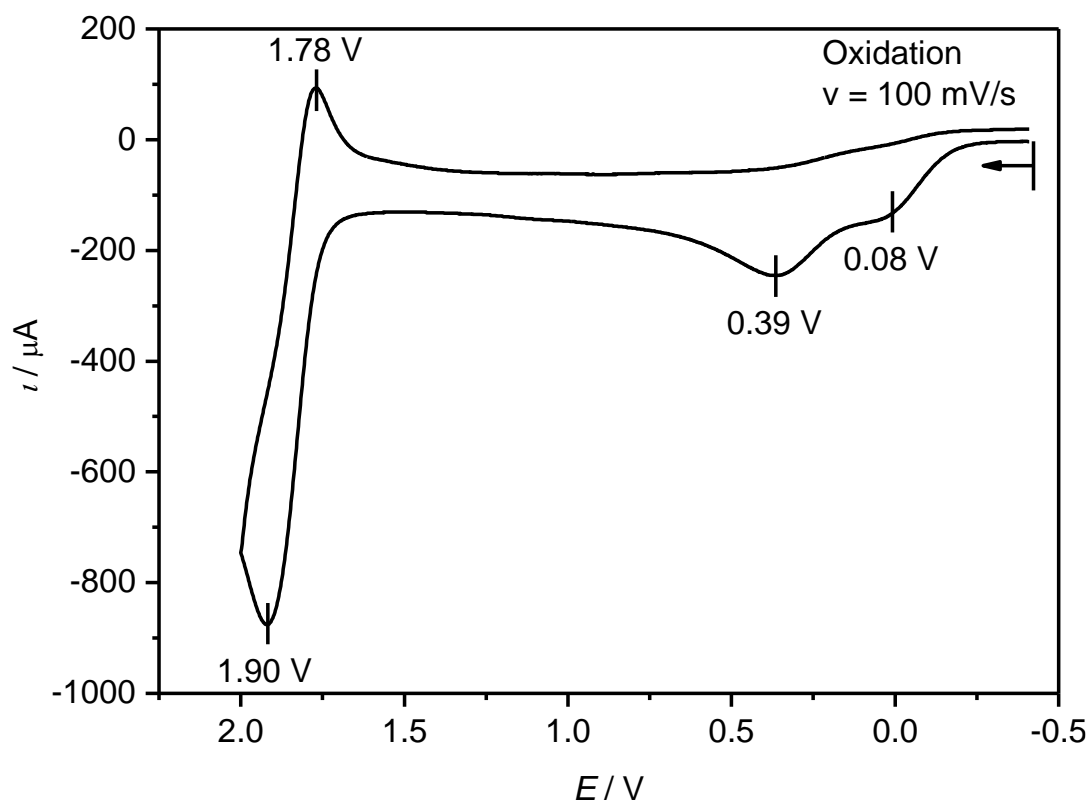


Figure 2.36: Cyclic voltammogram for the oxidation of **2a** in 0.2 M TBAP/MeCN sweeping with a scan rate of 100 mV s^{-1} . All potentials are given vs. SCE.

The cyclic voltammogram of the complex $[\{\text{Ni}(\text{L-N}_4\text{Me}_2)\}_2(\mu\text{-RC}_4\text{R})](\text{ClO}_4)_2$ [$\text{R} = \text{Ph}$] (**2a**) exhibits two irreversible oxidation at $+0.08 \text{ V}$ and $+0.39 \text{ V}$ vs SCE for the two nickel(I) centers followed by another quasireversible oxidations at $+1.84 \text{ V}$ vs SCE (Figure 2.36). The oxidation potential $+1.84 \text{ V}$ vs SCE is similar with that of $[\text{Ni}(\text{L-N}_4\text{Me}_2)(\text{MeCN})_2](\text{ClO}_4)_2$ (**1**) (Figure 2.5), which indicates that after successive oxidation of two nickel(I) centers, PhC_4Ph falls apart and produces $[\text{Ni}(\text{L-N}_4\text{Me}_2)(\text{MeCN})_2](\text{ClO}_4)_2$ (**1**). In addition, the cyclic voltammogram for the reduction of **2a** display two irreversible reductions at -1.54 V and -1.82 V vs SCE (appendix Figure 7.9).

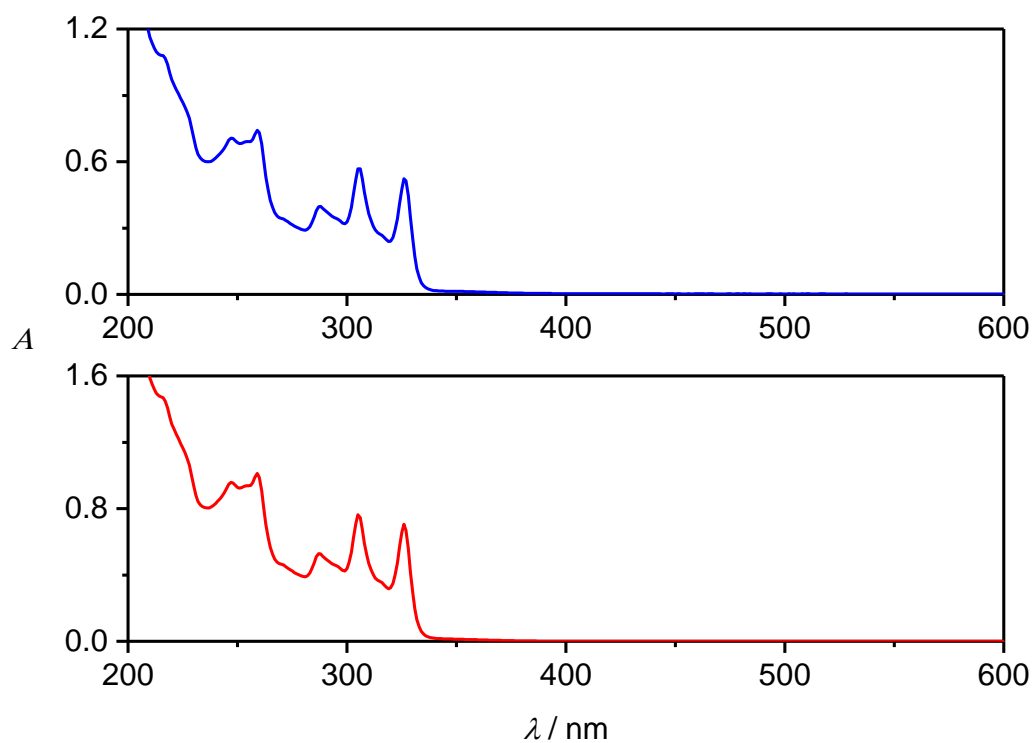


Figure 2.37: UV-Vis spectra of electrochemically generated solution of 2a with 25 times dilution in 0.2 M TBAP/MeCN (top) and a 2:1 mixture of 1 (0.0048 mM) with PhC₄Ph (0.0024 mM) in 0.2 M TBAP/MeCN (bottom). [Path length = 0.1 cm].

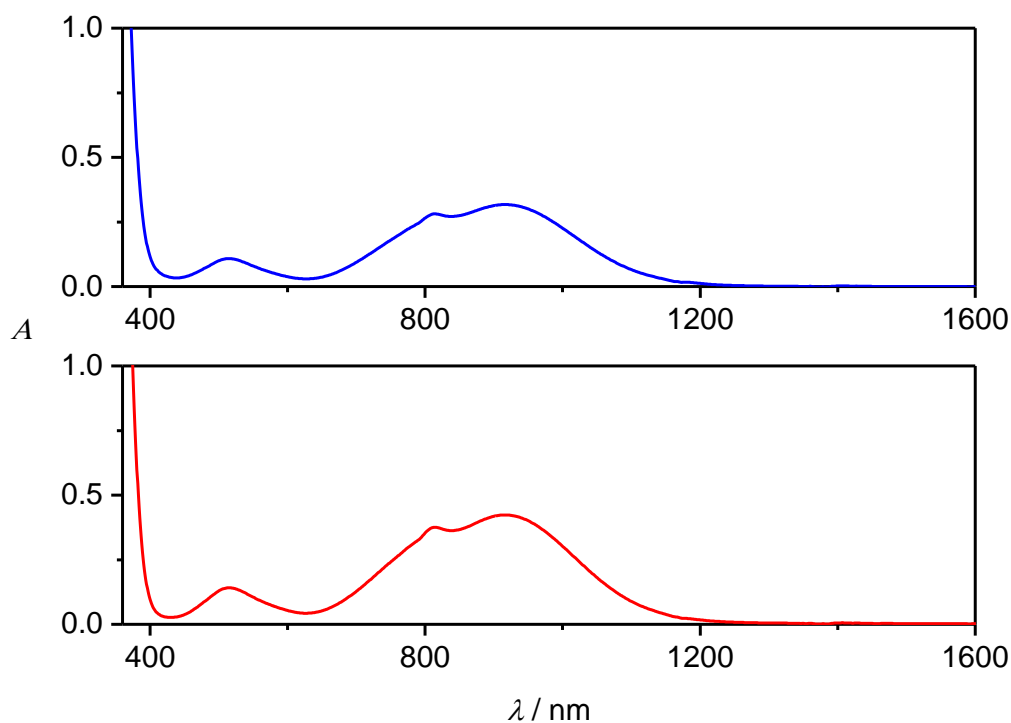
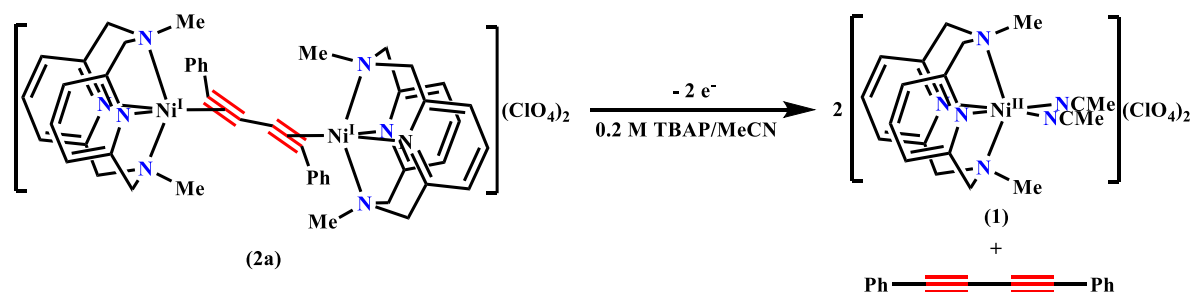


Figure 2.38: UV-Vis-NIR spectra of electrochemically generated solution of 2a in 0.2 M TBAP/MeCN (top) and a 2:1 mixture of 1 (0.12 mM) with PhC₄Ph (0.06 mM) in 0.2 M TBAP/MeCN (bottom). [Path length = 1 cm].

Coulometric experiments show two electrons per molecule are transferred during oxidation of **2a** at +0.8 V vs SCE and subsequent electronic absorption measurement of generated violet solution confirms the formation of $[\text{Ni}(\text{L}-\text{N}_4\text{Me}_2)(\text{MeCN})_2](\text{ClO}_4)_2$ (**1**) and free diphenyldiacetylene (Scheme 2.5) (Figure 2.37 and Figure 2.38).



Scheme 2.5: Electrochemical oxidation of **2a**.

Similar to the complex **2a**, the cyclic voltammograms of the complexes **2b-2g** show two irreversible oxidations for the two nickel(I) centers at -290 mV to +188 mV and +2 mV to +515 mV vs SCE, followed by another quasireversible oxidation for the follow-up product $[\text{Ni}(\text{L}-\text{N}_4\text{Me}_2)(\text{MeCN})_2](\text{ClO}_4)_2$ (**1**). The oxidation potential of nickel center varied depending on the nature of the diyne ligand. In the complexes **2a-2e**, oxidation potential decreases with increasing electron richness of diyne ligand (Table 2.15 and Figure 2.39). Furthermore, the oxidation potential of nickel center is greatest for **2a**, followed by **2g** and **2f** (Table 2.15 and appendix Figure 7.86).

Table 2.15: Electrochemical Properties for the Complexes $[\{\text{Ni}(\text{L}-\text{N}_4\text{Me}_2)\}_2(\mu\text{-RC}_4\text{R})](\text{ClO}_4)_2$ (**2a-2g**)

Complex	$E_{\text{pa}1}$ (V)	$E_{\text{pa}2}$ (V)	$E_{\text{pa}3}$ (V)	$E_{\text{pa}4}$ (V)
2a [R = Ph]	0.08	0.39	-	-
2b [R = C ₆ H ₄ Me-4]	0.035	0.36	-	-
2c [R = C ₆ H ₄ F-4]	0.19	0.52	-	-
2d [R = C ₆ H ₄ OMe-4]	0.02	0.35	1.49	-
2e [R = C ₆ H ₄ NMe ₂ -4]	-0.07	0.11	.83	.95
2f [R = ⁿ Pr]	-0.29	0.02	-	-
2g [R = Fc]	-0.14	0.02	0.58 ^a	0.70 ^a

^aReversible wave ($E_{1/2}$)

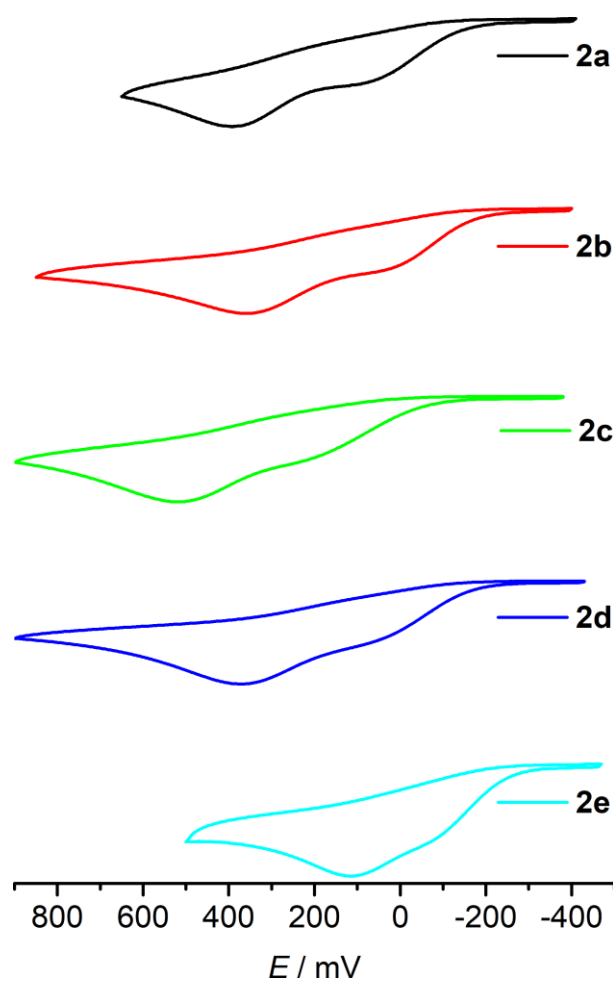


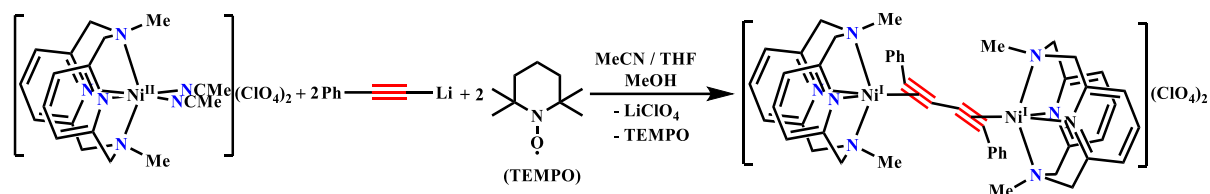
Figure 2.39: Cyclic voltammograms for the oxidation of **2a-2e** in 0.2 M TBAP/MeCN sweeping with different scan rates. All potentials are given vs. SCE.

In addition, the cyclic voltammogram of the complex **2d** shows an additional irreversible oxidation at 1.49 V vs SCE (*appendix* Figure 7.47), and complex **2e** displays two additional irreversible oxidations at 816 mV and 948 mV vs SCE (*appendix* Figure 7.60). These additional irreversible oxidation of **2d** and **2e** could be explained by oxidation of L-N₄Me₂ coordinated nickel(II) complexes containing RC₄R ligand, coordinated through OMe and NMe₂ groups for **2d** and **2e** respectively. Furthermore, the cyclic voltammogram of the complex **2g** also exhibits two additional oxidations at 586 mV and 704 mV vs SCE for follow-up product FcC₄Fc (*appendix* Figure 7.80).^[141]

Moreover, the cyclic voltammograms for the reduction of the nickel(I)-diyne complexes [$\{\text{Ni}(\text{L-N}_4\text{Me}_2)\}_2(\mu\text{-RC}_4\text{R})\}(\text{ClO}_4)_2$ (**2a-2g**) display two irreversible reductions (*see appendix section*).

2.2.6 Stoichiometric Reaction in Presence of Radical Inhibitor

To accumulate further insight into the formation of dinuclear nickel(I)-diyne complex, radical scavenger such as TEMPO ((2,2,6,6-tetramethylpiperidin-1-yl)oxidanyl),^[142-145] was employed in the stoichiometric reaction (Scheme 2.6).

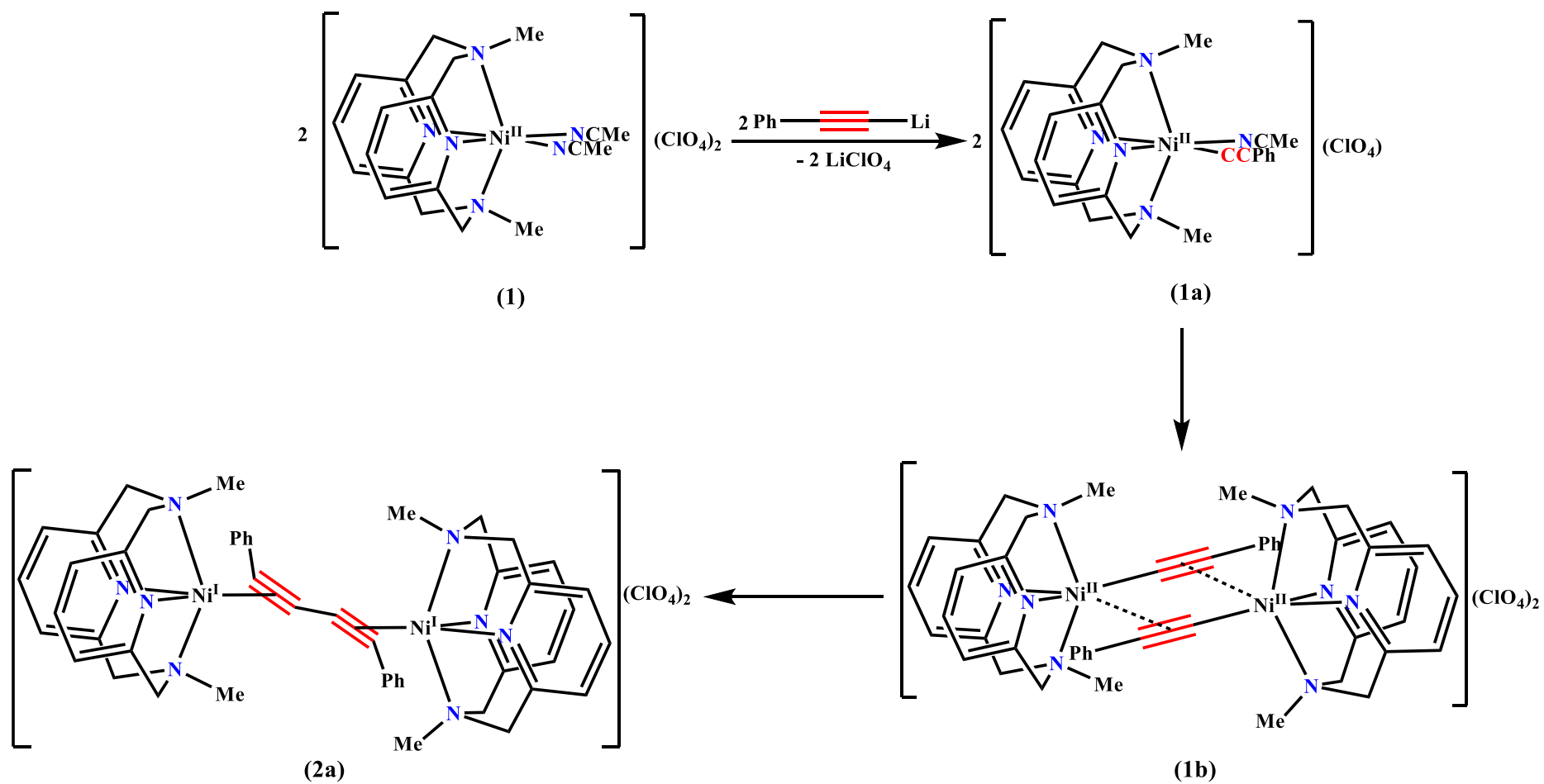


Scheme 2.6: Radical trapping experiment.

The reaction of $[\text{Ni}(\text{L}-\text{N}_4\text{Me}_2)(\text{MeCN})_2](\text{ClO}_4)_2$ (**1**) and two equivalents radical inhibitor TEMPO in acetonitrile with two equivalents lithium phenylacetylide in tetrahydrofuran at room temperature under a pure nitrogen atmosphere afforded a dark brown solution. After removing the volatiles, the resulting dark residue obtained was dissolved in a minimum volume of methanol. The solution was refluxed shortly, cooled to room temperature, and allowed to stand for 2-3 days to afford analytically pure crystalline product $[\{\text{Ni}(\text{L}-\text{N}_4\text{Me}_2)\}_2(\mu\text{-RC}_4\text{R})](\text{ClO}_4)_2$ [$\text{R} = \text{Ph}$] (**2a**) (yield 67%).

The stoichiometric reaction between **1** and lithium phenylacetylide in presence of radical trap TEMPO does not alter the yield of **2a**. This result suggests that the reactions occurring during the reduction of nickel(II) to nickel(I) and C–C bond formation of diphenyldiacetylene do not follow a free radical mechanism.

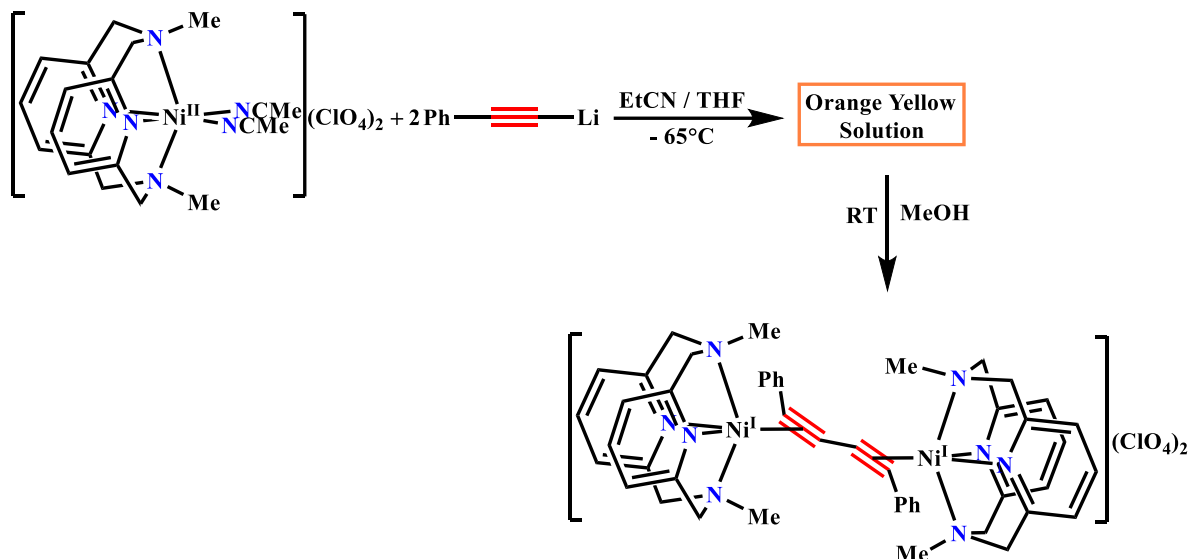
A concerted pathway might be involved in the formation of **2a** as depicted in Scheme 2.7. Lithium phenylacetylide reacted with $[\text{Ni}(\text{L}-\text{N}_4\text{Me}_2)(\text{MeCN})_2](\text{ClO}_4)_2$ (**1**) to produce a mononuclear nickel(II) phenylacetylide complex (**1a**), which converts to a dinuclear nickel(II) phenylacetylide species (**1b**). The dinuclear nickel(II) phenylacetylide species (**1b**) complex collapses through innersphere electron transfer to generate dinuclear nickel(I) complex $[\{\text{Ni}(\text{L}-\text{N}_4\text{Me}_2)\}_2(\mu\text{-RC}_4\text{R})](\text{ClO}_4)_2$ [$\text{R} = \text{Ph}$] (**2a**). A similar concerted mechanism has been proposed for copper-mediated homocoupling reaction of terminal alkynes (Scheme 1.9).^[34-35]



Scheme 2.7: Proposed concerted mechanism for the formation of 2a.

2.2.7 Stoichiometric Reaction at Low Temperature

To gain deeper insights into the aforesaid concerted mechanism (Scheme 2.7), a stoichiometric reaction was performed at low temperature ($-65\text{ }^{\circ}\text{C}$) in propionitrile (Scheme 2.8).



Scheme 2.8: Stoichiometric reaction at low temperature to room temperature.

Addition of two equivalent lithium phenylacetylide in tetrahydrofuran to a cooled ($-65\text{ }^{\circ}\text{C}$), violet solution of $[\text{Ni}(\text{L-N}_4\text{Me}_2)(\text{MeCN})_2](\text{ClO}_4)_2$ (**1**) in propionitrile afforded an orange-yellow solution. After stirring for 8 h, the reaction mixture was allowed to warm to room temperature and stirred further for 2 h. In the course of stirring at room temperature, the color of the solution changes from orange-yellow to dark brown. After removing the volatiles, the resulting dark residue obtained was dissolved in a minimum volume of methanol. The solution was refluxed shortly, cooled to room temperature, and allowed to stand for 2-3 days to afford analytically pure crystalline product $[\{2\text{Ni}(\text{L-N}_4\text{Me}_2)(\mu\text{-RC}_4\text{R})\}](\text{ClO}_4)_2$ [$\text{R} = \text{Ph}$] (**2a**) (yield 68%).

The above described stoichiometric reaction was also monitored via UV-Vis-NIR spectroscopy at $-60\text{ }^{\circ}\text{C}$ in propionitrile (Figure 2.40). A solution of lithium phenylacetylide (100 μL , 1.6 M) in tetrahydrofuran was added to a precooled solution of $[\text{Ni}(\text{L-N}_4\text{Me}_2)(\text{MeCN})_2](\text{ClO}_4)_2$ (**1**) (4 mL, 20 mM) in propionitrile at $-60\text{ }^{\circ}\text{C}$. UV-Vis-NIR measurements were performed at different time intervals (*appendix* Figure 7.13). The orange-yellow intermediate was detected, which displayed absorption bands at 774, 821 and 1270 nm. The intermediate converted to **2a** upon warming the solution to $20\text{ }^{\circ}\text{C}$. The orange-yellow species could not be isolated after several

attempts. Presumably, the species corresponds to a mononuclear nickel(II) phenylacetylide (**1a**) and/or a dinuclear nickel(II) phenylacetylide complex (**1b**) (Scheme 2.7).

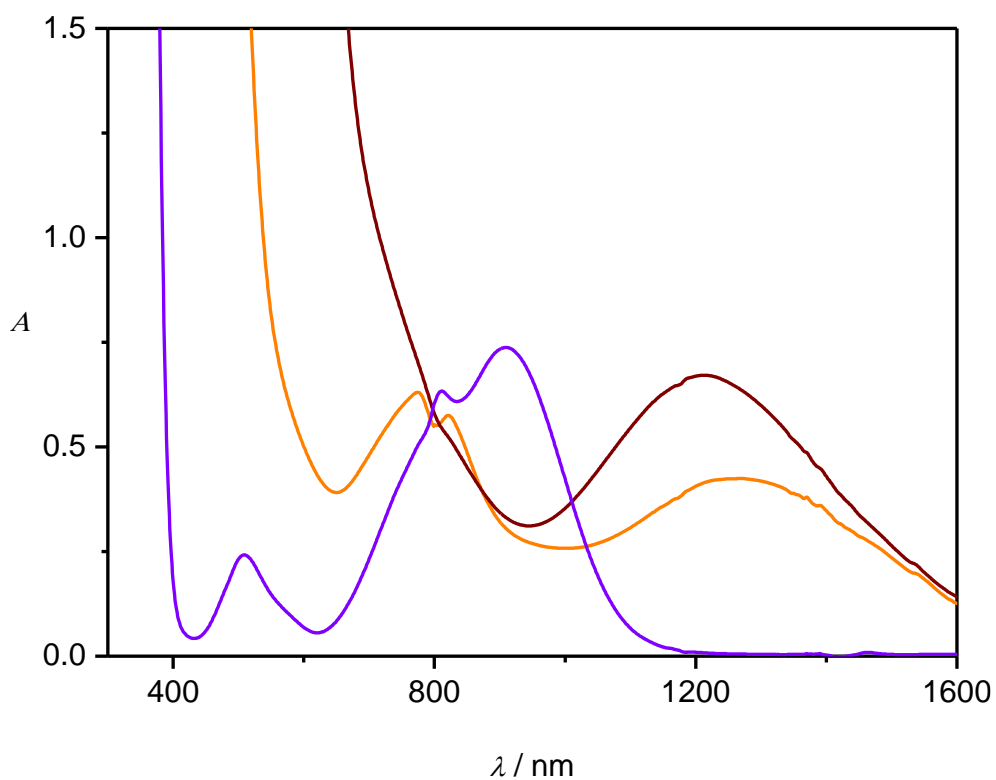


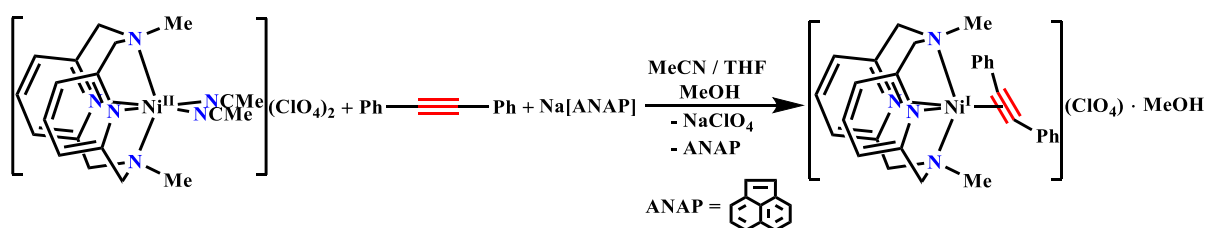
Figure 2.40: UV-Vis-NIR spectrum of **1** (violet), the reaction product **2a** (brown), and intermediate **1b** (orange yellow) in EtCN.

2.3 Synthesis and Characterization of $[\text{Ni}(\text{L-N}_4\text{Me}_2)(\text{PhC}_2\text{Ph})](\text{ClO}_4) \cdot \text{MeOH}$ (**3**)

Cyclic voltammogram of the complex $[\text{Ni}(\text{L-N}_4\text{Me}_2)(\text{MeCN})_2](\text{ClO}_4)_2$ (**1**) has provided the insights into the formation of nickel(I) containing L-N₄Me₂ ligand. Further, ESI-MS investigations of dinuclear nickel(I)-diyne complexes also have given the evidences for the formulation of L-N₄Me₂ coordinated mononuclear nickel(I)-alkyne complexes ($[\text{Ni}(\text{L-N}_4\text{Me}_2)(\text{RC}_4\text{R})]^+$). On the basis of these results, I have tried to prepare a L-N₄Me₂ coordinated mononuclear nickel(I) complex containing diphenylacetylene (PhC₂Ph) ligand $[\text{Ni}(\text{L-N}_4\text{Me}_2)(\text{PhC}_2\text{Ph})](\text{ClO}_4) \cdot \text{MeOH}$ (**3**) to investigate the structural and electronic properties.

2.3.1 Synthesis

The reaction of $[\text{Ni}(\text{L-N}_4\text{Me}_2)(\text{MeCN})_2](\text{ClO}_4)_2$ (**1**) and diphenylacetylene (PhC₂Ph) in acetonitrile with reducing agent sodium acenaphthylene (prepared *in situ* by the reaction of sodium and acenaphthylene) in THF under a pure nitrogen atmosphere afforded dark brown complex $[\text{Ni}(\text{L-N}_4\text{Me}_2)(\text{PhC}_2\text{Ph})](\text{ClO}_4) \cdot \text{MeOH}$ (**3**), which was crystalized from hot methanolic solution as analytically pure compound (yield 46%).



Scheme 2.9: Preparation of $[\text{Ni}(\text{L-N}_4\text{Me}_2)(\text{PhC}_2\text{Ph})](\text{ClO}_4) \cdot \text{MeOH}$ (3**).**

The purity of the dark brown compound was confirmed by elemental analysis, which showed excellent agreement between the calculated and experimental C, H, and N values (*see experimental section*).

2.3.2 X-Ray Structure Analysis

The X-ray diffraction analysis was performed on suitable single crystal of $[\text{Ni}(\text{L-N}_4\text{Me}_2)(\text{PhC}_2\text{Ph})](\text{ClO}_4)\cdot\text{MeOH}$ (**3**) at 150 K. Figure 2.41 shows a perspective view of the complex cation in **3**. Selected bond lengths and angles are given in Table 2.16, in comparison with dinuclear nickel(I)-diyne complex $[\{\text{Ni}(\text{L-N}_4\text{Me}_2)\}_2(\mu\text{-RC}_4\text{R})](\text{ClO}_4)_2$ [$\text{R} = \text{Ph}$] (**2a**). The monocationic complex (**3**) crystallizes in triclinic space group $\text{P}\bar{1}$ with one perchlorate ion as counter anion.

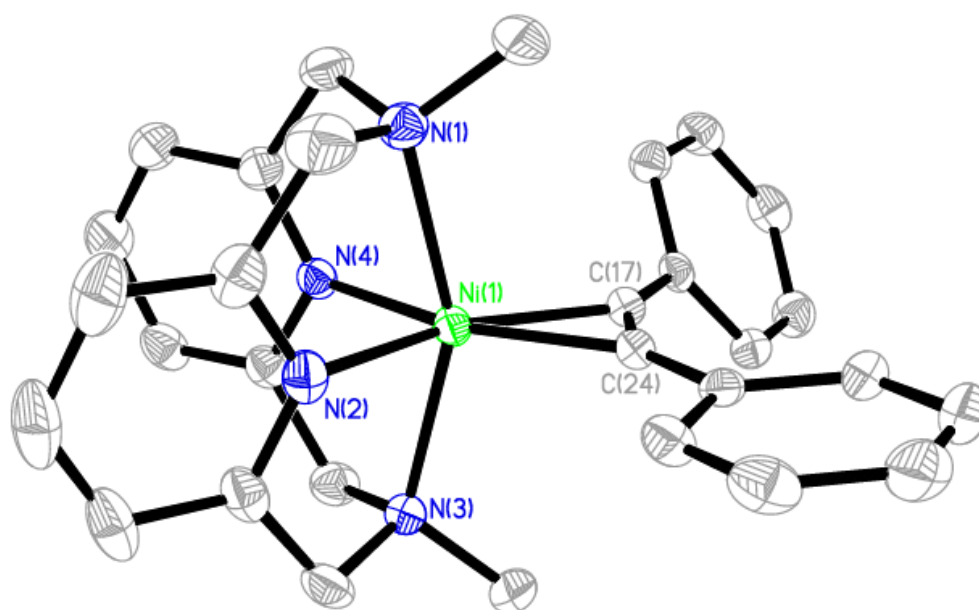


Figure 2.41: Perspective view of the complex cation in **3**.

In the complex, nickel center is coordinated to the four nitrogen donor atoms of the tetraazamacrocyclic diazapyridinophane ligand, $\text{L-N}_4\text{Me}_2$ and alkyne group of diphenylacetylene ligand in side-on fashion. As in the previously described nickel(I)-diyne complexes of $\text{L-N}_4\text{Me}_2$, the twelve-membered tetraazamacrocycle in the nickel containing complex is folded along the $\text{N}_{\text{amine}}\text{-N}_{\text{amine}}$ axis due to the small macrocycle ring size. The amine nitrogen atoms of the tetradentate ligand occupy axial position, while pyridine nitrogen atoms occupy equatorial position and the remaining equatorial position was occupied by alkyne group of diphenylacetylene ligand in trigonal bipyramidal coordination environment.

Table 2.16: Selected bond lengths [Å] and angles [°] in [Ni(L-N₄Me₂)(PhC₂Ph)](ClO₄)·MeOH (**3**) and {[Ni(L-N₄Me₂)₂(μ-RC₄R)](ClO₄)₂ [R = Ph] (**2a**) at 150 K.

3	T = 150 K	2a	T = 150 K
Ni(1)-N(1)	2.2212(13)	Ni(1)-N(1)	2.2282(15)
Ni(1)-N(2)	1.9914(13)	Ni(1)-N(2)	2.0016(15)
Ni(1)-N(3)	2.2245(13)	Ni(1)-N(3)	2.2346(15)
Ni(1)-N(4)	1.9917(17)	Ni(1)-N(4)	1.9957(16)
Ni(1)-C(17)	1.9652(15)	Ni(1)-C(17)	1.9940(17)
Ni(1)-C(24)	1.9603(15)	Ni(1)-C(18)	1.9586(18)
C(17)-C(24)	1.258(2)	C(17)-C(18)	1.270(3)
C(17)-C(18)	1.452(2)	C(18)-C(19)	1.448(3)
N(1)-Ni(1)-N(2)	80.83(5)	N(1)-Ni(1)-N(2)	80.27(6)
N(1)-Ni(1)-N(3)	154.21(5)	N(1)-Ni(1)-N(3)	153.58(6)
N(1)-Ni(1)-N(4)	80.02(5)	N(1)-Ni(1)-N(4)	80.17(6)
N(1)-Ni(1)-C(17)	103.36(6)	N(1)-Ni(1)-C(17)	105.30(6)
N(1)-Ni(1)-C(24)	102.68(5)	N(1)-Ni(1)-C(18)	101.20(6)
N(2)-Ni(1)-N(3)	80.55(5)	N(2)-Ni(1)-N(3)	80.343(6)
N(2)-Ni(1)-N(4)	85.60(5)	N(2)-Ni(1)-N(4)	84.81(6)
N(2)-Ni(1)-C(17)	156.52(6)	N(2)-Ni(1)-C(17)	156.34(7)
N(2)-Ni(1)-C(24)	119.17(6)	N(2)-Ni(1)-C(18)	119.22(7)
N(3)-Ni(1)-N(4)	80.91(5)	N(3)-Ni(1)-N(4)	80.27(6)
N(3)-Ni(1)-C(17)	100.84(5)	N(3)-Ni(1)-C(17)	99.60(6)
N(3)-Ni(1)-C(24)	101.92(5)	N(3)-Ni(1)-C(18)	103.91(6)
N(4)-Ni(1)-C(17)	117.84(6)	N(4)-Ni(1)-C(17)	118.66(7)
N(4)-Ni(1)-C(24)	155.22(6)	N(4)-Ni(1)-C(18)	155.91(7)
C(17)-Ni(1)-C(24)	37.39(6)	C(17)-Ni(1)-C(18)	37.48(8)
C(24)-C(17)-C(18)	148.75(15)	C(17)-C(18)-C(19)	148.16(18)
C(17)-C(24)-C(25)	152.79(15)	C(18)-C(17)-C(17A)	157.3(2)

In the complex **3**, the average Ni–N_{amine} and Ni–N_{py} bond lengths are 2.223 ± 0.002 Å and 1.991 ± 0.001 Å respectively, whereas the average bond length for Ni–C_{alkyne} bond is 1.962 ± 0.002 Å. These bond lengths are very similar to those found in dinuclear nickel(I)-diyne complexes (2.220 ± 0.003 Å, 1.992 ± 0.002 Å and 1.967 ± 0.021 Å in $[\{\text{Ni}(\text{L}-\text{N}_4\text{Me}_2)\}_2(\mu\text{-RC}_4\text{R})](\text{ClO}_4)_2$ [R = Ph] (**2a**)). As in the previously described nickel(I)-diyne complexes, these Ni–N_{amine} and Ni–N_{py} bond lengths are very similar to those in other octahedral nickel(II) complexes containing L–N₄Me₂ as ligand.^[106, 108]

The structural aspects, particularly the angles and their deviation from ideal values for trigonal bipyramidal coordination environment, closely resemble those found in the dinuclear nickel(I)-diyne complexes. In the complex **3**, N_{amine}–Ni–N_{amine} and N_{py}–Ni–N_{py} angles are $154.21(5)^\circ$ and $85.60(5)^\circ$, which are deviated from 180° and 120° respectively, in an ideal trigonal bipyramidal coordination environment. The C_{alkyne}–Ni–C_{alkyne} angle is $37.39(6)^\circ$ in equatorial plane. The angles N_{amine}–Ni–N_{amine}, N_{py}–Ni–N_{py} and C_{alkyne}–Ni–C_{alkyne} are very similar to those found in dinuclear nickel(I)-diyne complexes ($153.58(6)^\circ$, $84.81(6)^\circ$ and $37.48(8)^\circ$ respectively in $[\{\text{Ni}(\text{L}-\text{N}_4\text{Me}_2)\}_2(\mu\text{-RC}_4\text{R})](\text{ClO}_4)_2$ [R = Ph] (**2a**)). The sum of the angles of the equatorial ligands is 360° , and the axial-to-equatorial angles are $\sim 90^\circ$ for both N_{amine}–Ni–N_{py} ($80.02^\circ - 80.91^\circ$) and N_{amine}–Ni–C_{alkyne} ($100.84^\circ - 103.36^\circ$), supporting the description of a distorted trigonal bipyramidal coordination environment.

The C–C triple bond and C–C_{Ph} single bond lengths in coordinated diphenylacetylene ligand (Ph–C≡C–Ph) are $1.258(2)$ Å and $1.452(2)$ Å respectively, which are elongated compared to free diphenylacetylene ($1.198(4)$ Å and $1.437(4)$ Å).^[146] The C₁₈–C₁₇–C₂₄ and C₂₅–C₂₄–C₁₇ angles are $152.79(15)^\circ$ and $148.75(15)^\circ$ respectively, which are more bent compared to that in free diphenylacetylene ($178.4(2)^\circ$).^[146] Elongation of C–C bonds and bending of C–C–C angles indicate σ -donation from alkyne group of diphenylacetylene to the nickel center and π -back donation from the nickel center to alkyne group of diphenylacetylene.

The structural aspects of complex **3** in comparison with the dinuclear nickel(I)-diyne complex **2a**, particularly Ni–N, C≡C bond lengths and C_{Ph}–C≡C angle confirm the formulation of a trigonal bipyramidal L–N₄Me₂ coordinated nickel(I)-diphenylacetylene complex with (d_{xz} , d_{yz})⁴(d_{xy} , $d_{x^2-y^2}$)⁴(d_{z^2})¹ electronic configuration (assuming an idealized D_{3h} ligand field description with the Z-axis oriented along N_{amine}–N_{amine} axis), instead of a nickel metallacyclopentene complex (Ni(III) with a [η^2 -alkenediyl]²⁻ ligand).

2.3.3 Spectroscopic Studies

IR Spectroscopy

IR spectrum of $[\text{Ni}(\text{L-N}_4\text{Me}_2)(\text{PhC}_2\text{Ph})](\text{ClO}_4)\cdot\text{MeOH}$ (**3**) was measured as KBr pellet at room temperature. The spectrum is depicted in Figure 2.42. The spectrum displays typical absorption of coordinated diazapyridinophane ligand, L-N₄Me₂ at around 1606, 1474, 1442 and 1376 cm⁻¹. The spectrum of **3** also exhibits a characteristic stretching frequency of coordinated triple bond of diphenylacetylene ($\nu_{\text{C}\equiv\text{C}}$) at 1885 cm⁻¹. The relatively lower $\nu_{\text{C}\equiv\text{C}}$ stretching frequency compared to free diphenylacetylene ($\nu_{\text{C}\equiv\text{C}} = 2220$ cm⁻¹, Raman active) confirms the extent of π -interaction in the complex.^[147] The complex is monocationic in nature, having ClO₄⁻ as the counter anion. The stretching vibrations of ClO₄⁻ are found at 1095 and 623 cm⁻¹.

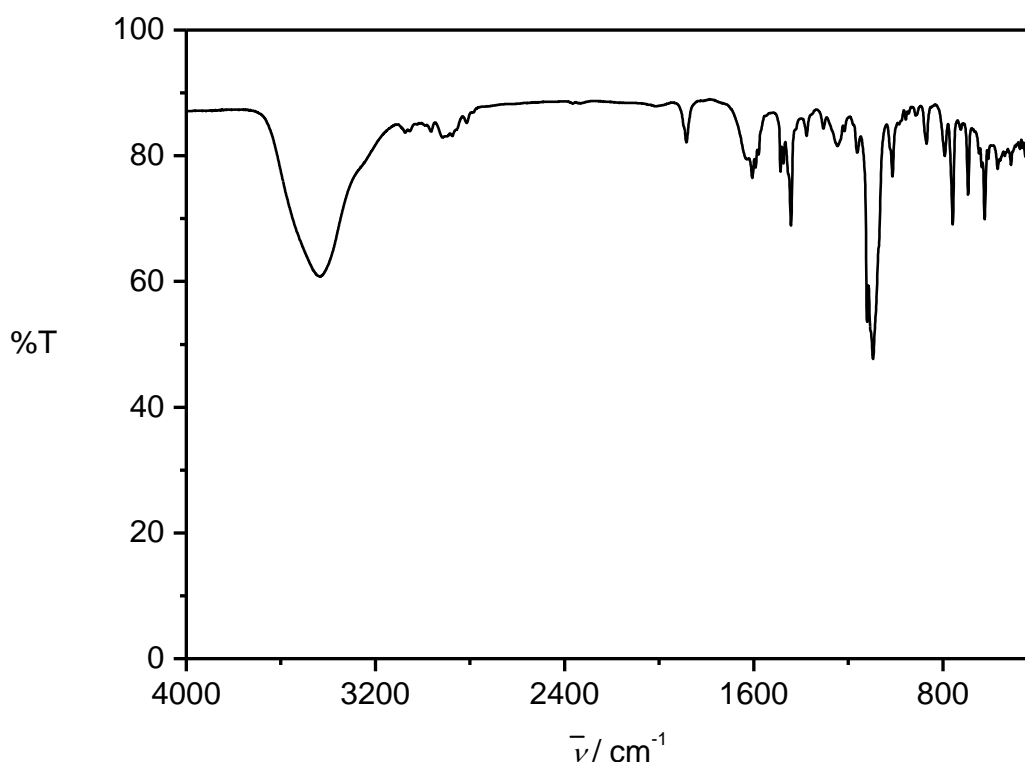


Figure 2.42: IR spectrum of **3** in KBr Pellet.

ESI mass spectrometry

The ESI-MS spectrum of $[\text{Ni}(\text{L-N}_4\text{Me}_2)(\text{PhC}_2\text{Ph})](\text{ClO}_4)\cdot\text{MeOH}$ (**3**) in acetonitrile at room temperature shows a prominent ion peak at a m/z of 504.0 (Figure 2.43), whose mass and isotope distribution pattern correspond to $[\text{Ni}(\text{L-N}_4\text{Me}_2)(\text{PhC}_2\text{Ph})]^+$ (calculated m/z 504.1) (Figure 2.44).

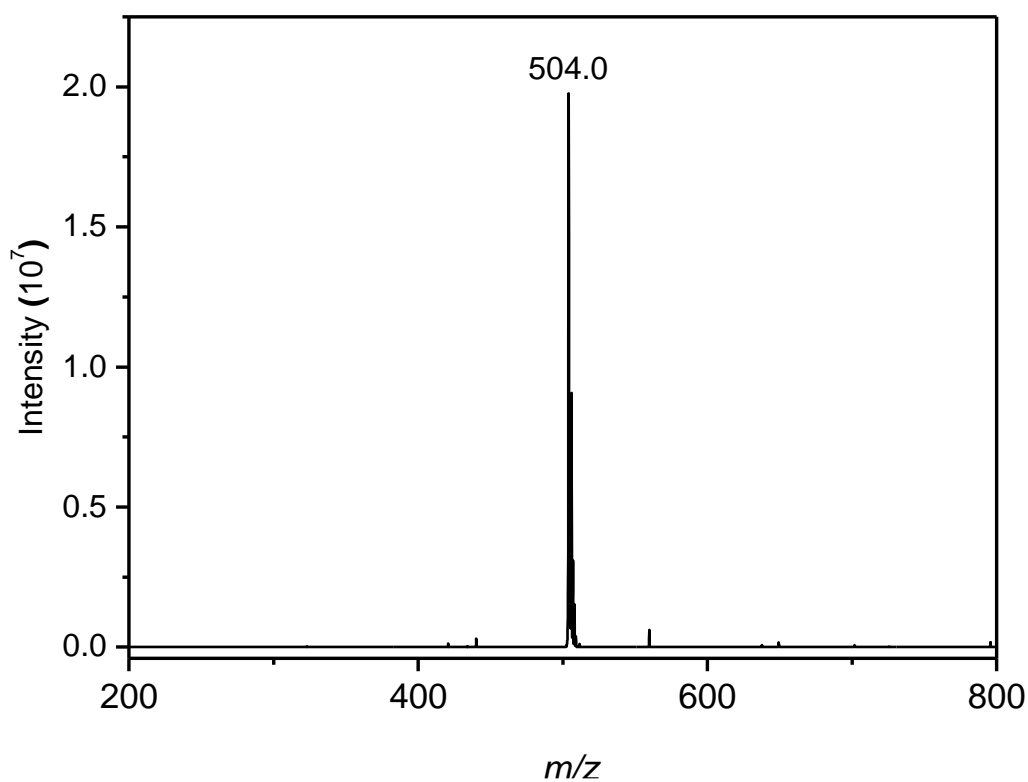


Figure 2.43: ESI-MS spectrum of **3** in MeCN.

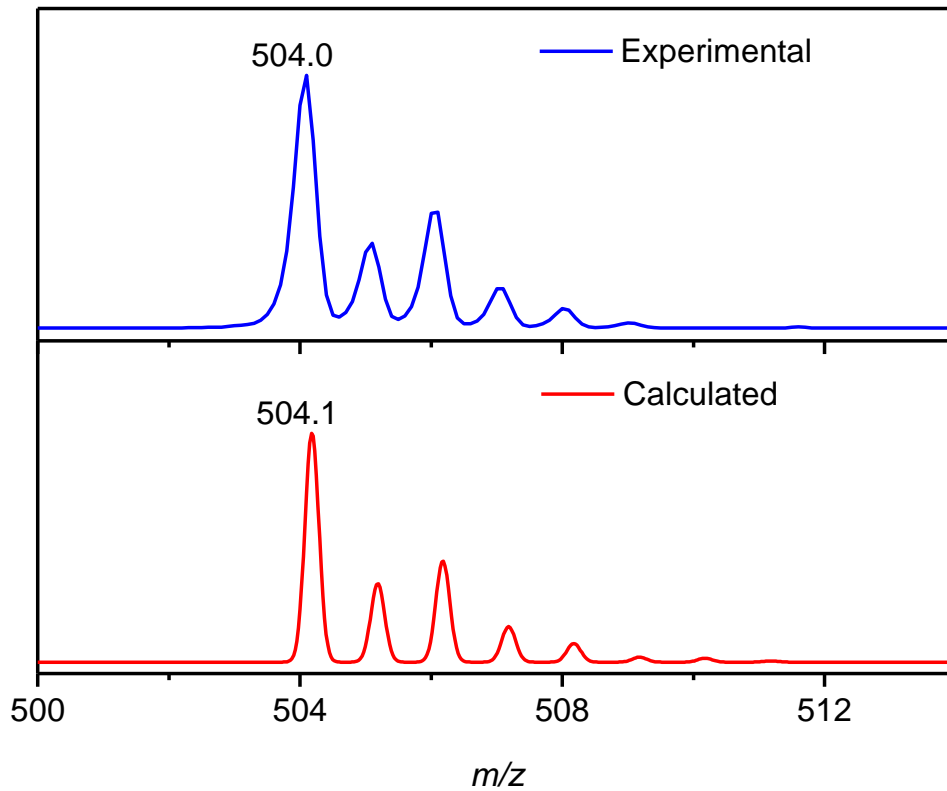


Figure 2.44: The experimental and calculated isotope distribution for $[\text{Ni}(\text{L}-\text{N}_4\text{Me}_2)(\text{PhC}_2\text{Ph})]^+$.

UV-Vis-NIR Spectroscopy

The complex $[\text{Ni}(\text{L-N}_4\text{Me}_2)(\text{PhC}_2\text{Ph})](\text{ClO}_4)\cdot\text{MeOH}$ (**3**) was characterized by UV-Vis-NIR spectroscopy in acetonitrile at room temperature under nitrogen atmosphere. Figure 2.45 shows the UV-Vis-NIR spectrum of $[\text{Ni}(\text{L-N}_4\text{Me}_2)(\text{PhC}_2\text{Ph})](\text{ClO}_4)\cdot\text{MeOH}$ (**3**).

The UV-Vis spectrum exhibits absorption bands at 675 ($\varepsilon = 34 \text{ M}^{-1} \text{ cm}^{-1}$) and 1220 ($\varepsilon = 44 \text{ M}^{-1} \text{ cm}^{-1}$) in visible-NIR region, which are assigned to d-d transitions $d_{xz}, d_{yz} \rightarrow d_z^2$ and $d_{xy}, d_{x^2-y^2} \rightarrow d_z^2$, respectively. A comparison of the lowest energy absorption band suggests that the diphenylacetylene ligand is weaker field than diphenyldiacetylene ligand (*appendix* Figure 7.87).

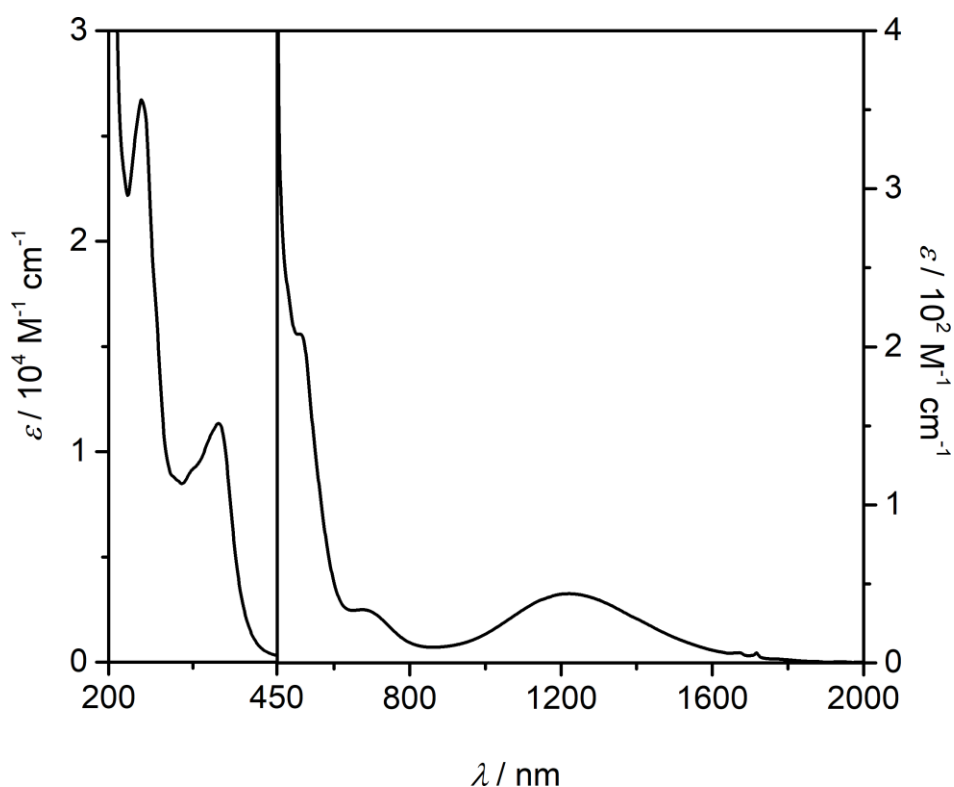


Figure 2.45: UV-Vis-NIR spectrum of **3** in MeCN.

The absorption spectrum also shows a shoulder at around 514 nm ($\varepsilon = 208 \text{ M}^{-1} \text{ cm}^{-1}$) and an intense band at 364 nm ($\varepsilon = 11338 \text{ M}^{-1} \text{ cm}^{-1}$), which are assigned to CT transitions. In addition, the band at 249 nm ($\varepsilon = 26720 \text{ M}^{-1} \text{ cm}^{-1}$) is assigned as L-N₄Me₂ ligand based ILCT transition.^[108] The shoulder at around 324 nm ($\varepsilon = 9120 \text{ M}^{-1} \text{ cm}^{-1}$) is assigned as diphenylacetylene ligand based ILCT transition (*appendix* Figure 7.94).

EPR Spectroscopy

The EPR measurement was performed on a frozen solution of $[\text{Ni}(\text{L-N}_4\text{Me}_2)(\text{PhC}_2\text{Ph})](\text{ClO}_4)\cdot\text{MeOH}$ (**3**) in acetonitrile containing 0.2 M TBAP at 77 K. The EPR spectrum is depicted in Figure 2.46. The EPR spectrum reveals a rhombic signal with g values of 2.300, 2.213 and 2.008, suggesting an $S = \frac{1}{2}$ ground state for the complex. The high anisotropy of the rhombic signal and the quintet splitting of the high field g_{zz} component with a hyperfine coupling constant of 36.70 MHz due to the interaction between the electron spin and the nuclear spin ($I=1$) of two axial amine nitrogen atoms are consistent with the formation of a $\text{L-N}_4\text{Me}_2$ coordinated nickel(I) species with a $(d_z^2)^1$ ground state.

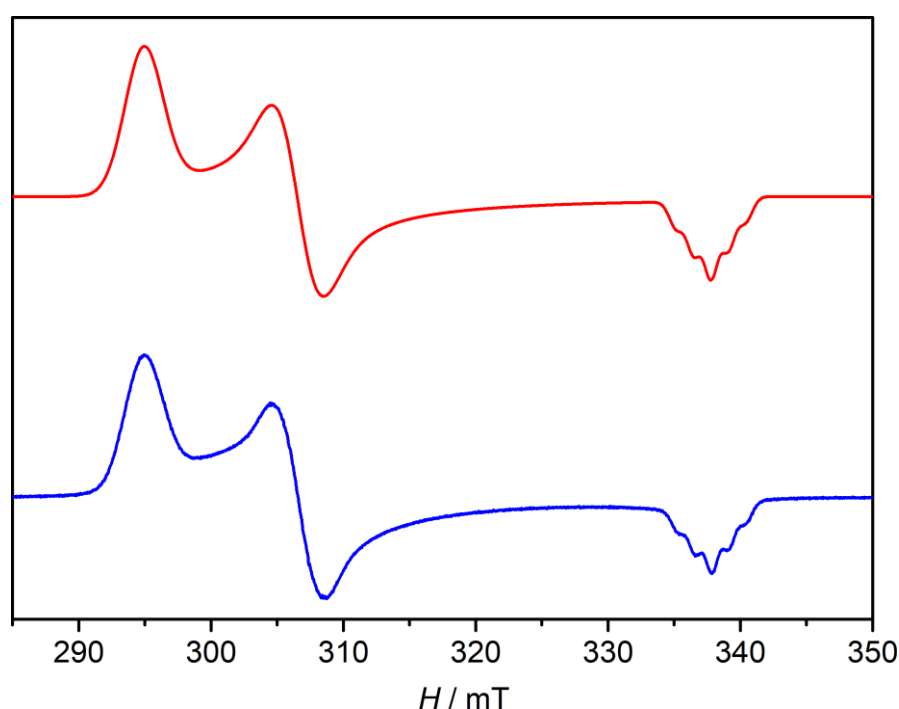


Figure 2.46: EPR spectrum of **6** in 0.2 M solution of TBAP in MeCN at 77 K, experimental (blue) and simulation (red).

2.3.4 Electrochemistry

The electrochemical properties of the complex $[\text{Ni}(\text{L-N}_4\text{Me}_2)(\text{PhC}_2\text{Ph})](\text{ClO}_4)\cdot\text{MeOH}$ (**3**) was investigated by cyclic voltammetry in acetonitrile solution. The cyclic voltammogram for the oxidation of the complex **3** is displayed in Figure 2.47. The cyclic voltammogram exhibits an irreversible oxidation at + 152 mV vs SCE for the nickel(I) centers followed by another quasireversible oxidation at + 1.84 V vs SCE. The oxidation potential +1.84 V vs SCE is similar with the oxidation potential of $[\text{Ni}(\text{L-N}_4\text{Me}_2)(\text{MeCN})_2](\text{ClO}_4)_2$ (**1**) (Figure 2.5), which indicates

that after oxidation of nickel(I) center, PhC₂Ph falls apart and produces [Ni(L-N₄Me₂)(MeCN)₂](ClO₄)₂ (**1**). In addition, the cyclic voltammogram for the reduction of the complex **3** shows an irreversible reduction at -1.72 V vs SCE (*appendix* Figure 7.88).

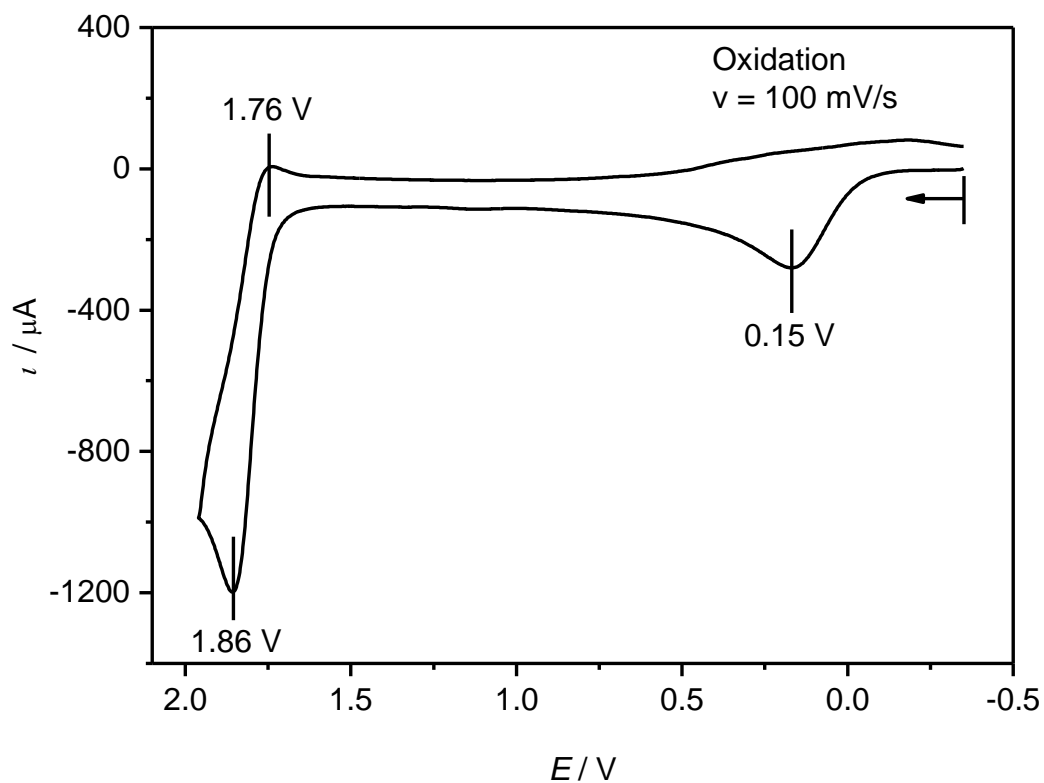


Figure 2.47: Cyclic voltammogram for the oxidation of **3** in 0.2 M TBAP/MeCN sweeping with a scan rate of 100 mV s^{-1} . All potentials are given vs. SCE.

2.4 Reactivity of $[\{\text{Ni}(\text{L-N}_4\text{Me}_2)\}_2(\mu\text{-RC}_4\text{R})](\text{ClO}_4)_2$ [R = Ph] (**2a**) with Molecular Oxygen

2.4.1 Spectroscopic Studies

The reactivity of $[\{\text{Ni}(\text{L-N}_4\text{Me}_2)\}_2(\mu\text{-RC}_4\text{R})](\text{ClO}_4)_2$ [R = Ph] (**2a**) with molecular oxygen in acetonitrile at room temperature was studied by *in situ* UV-Vis-NIR, NMR and EPR spectroscopies and ESI-MS.

UV-Vis-NIR Spectroscopy

Upon reaction with molecular oxygen, the complex $[\{\text{Ni}(\text{L-N}_4\text{Me}_2)\}_2(\mu\text{-RC}_4\text{R})](\text{ClO}_4)_2$ [R = Ph] (**2a**) shows a spectral change in absorption spectrum as shown in Figure 2.48 and Figure 2.49. The spectral change at the higher energy region (Figure 2.48) was observed as a decrease in absorption of CT band of **2a** at 380 nm with appearance of two prominent bands at 305 and 326 nm, which are the characteristic bands for free diphenyldiacetylene (*appendix* Figure 7.90).

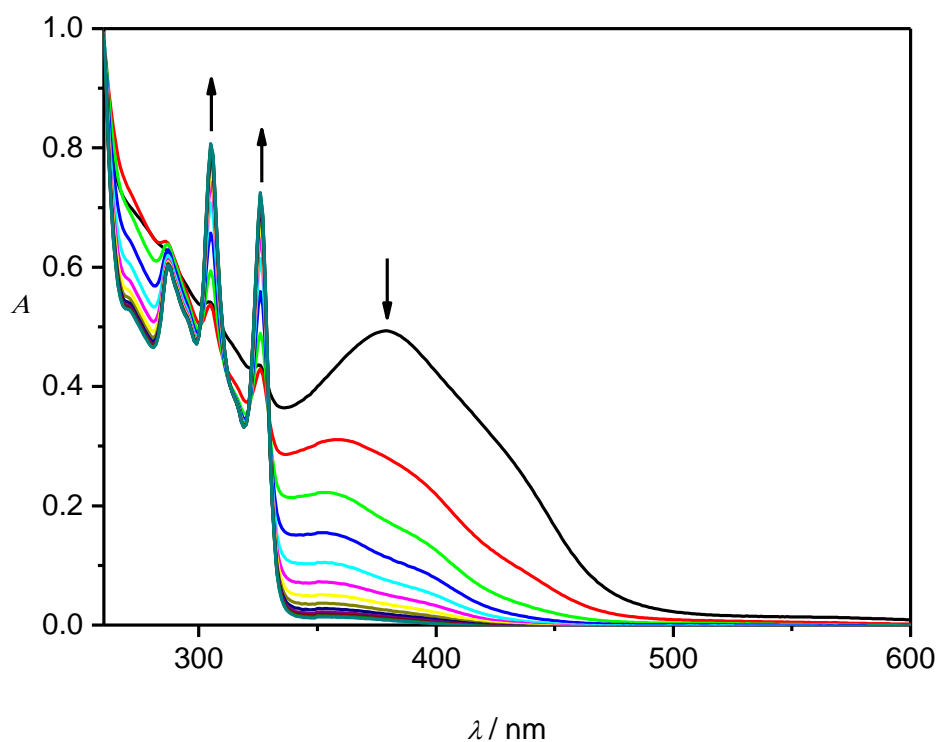


Figure 2.48: UV-Vis spectral change during the reaction of **2a** (0.023 mM) and O₂ in MeCN at room temperature in 30 min intervals. The arrows indicate how the intensities of absorption bands change over time.

Whereas the spectral change at the visible NIR region (Figure 2.49) was observed as a decrease in the d-d band of **2a** at 1205 nm with appearance of three bands at 592, 822 and 996 nm (*appendix* Figure 7.91), which are the characteristic d-d bands for Ni(II) distorted octahedral complexes with L-N₄Me₂ as ligand.^[108]

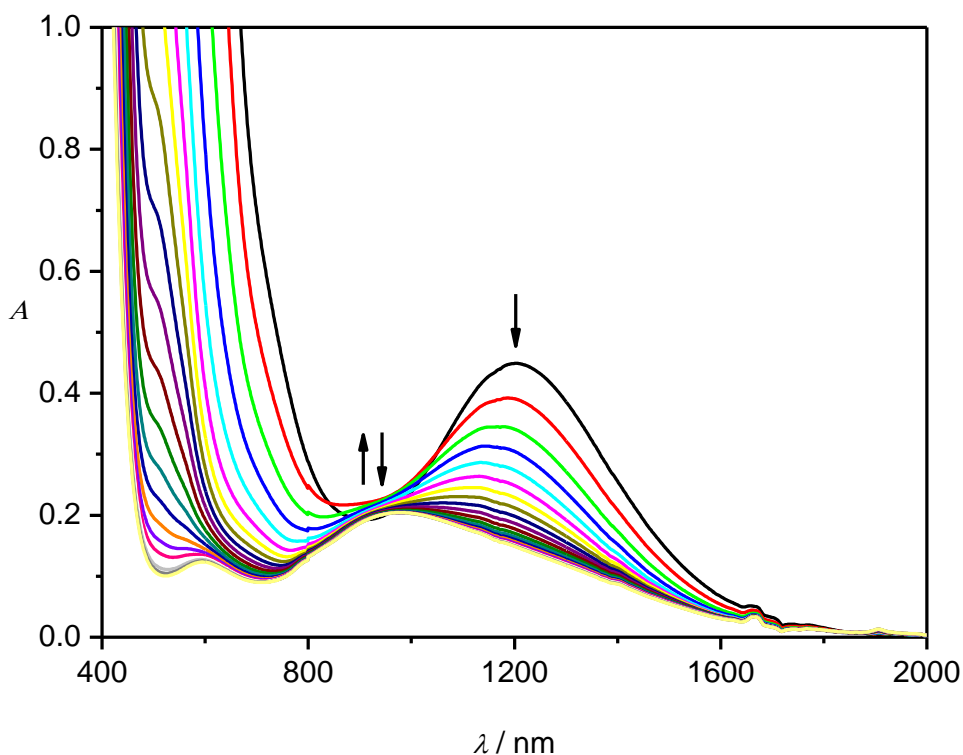


Figure 2.49: UV-Vis-NIR spectral change during the reaction of **2a** (5.33 mM) and O₂ in MeCN at room temperature in 15 min intervals. The arrows indicate how the intensities of absorption bands change over time.

NMR Spectroscopy

The reaction of **2a** and molecular oxygen was carried out in CD₃CN for a period of 24 h and subsequent ¹H and ¹³C NMR measurements of generated solution confirm the formation of free diphenyldiacetylene (Figure 2.50 and Figure 2.51). Broadening of ¹H signals also indicate the presence of paramagnetic nickel species.

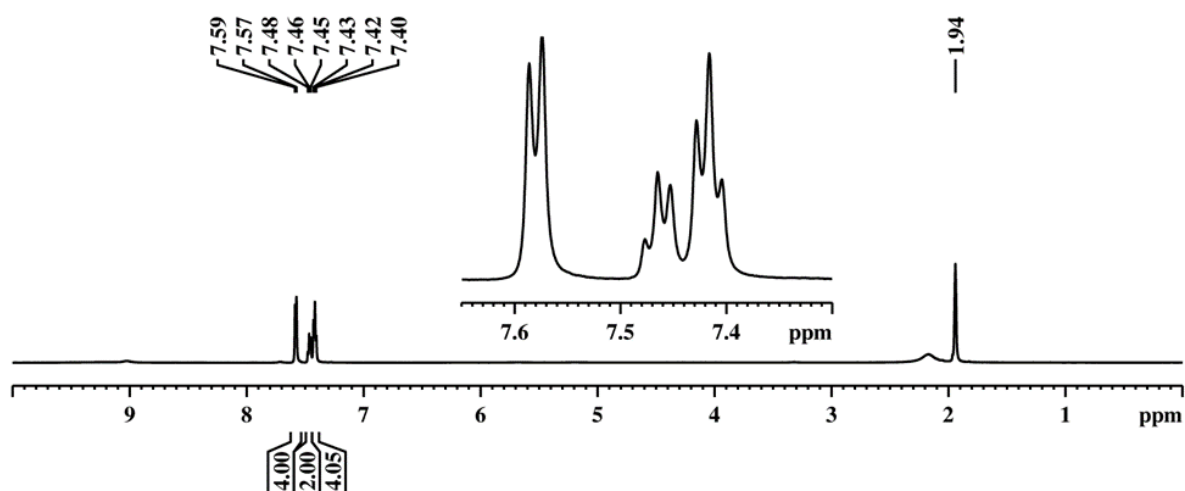


Figure 2.50: ¹H NMR (600 MHz) spectrum of the reaction mixture of 2a and O₂ in CD₃CN at room temperature (after 24 h stirring); δ (ppm) = 7.57-7.59 (d, 4 H, $J = 12$ Hz), 7.40-7.48 (m, 6 H). Inset shows the magnified region.

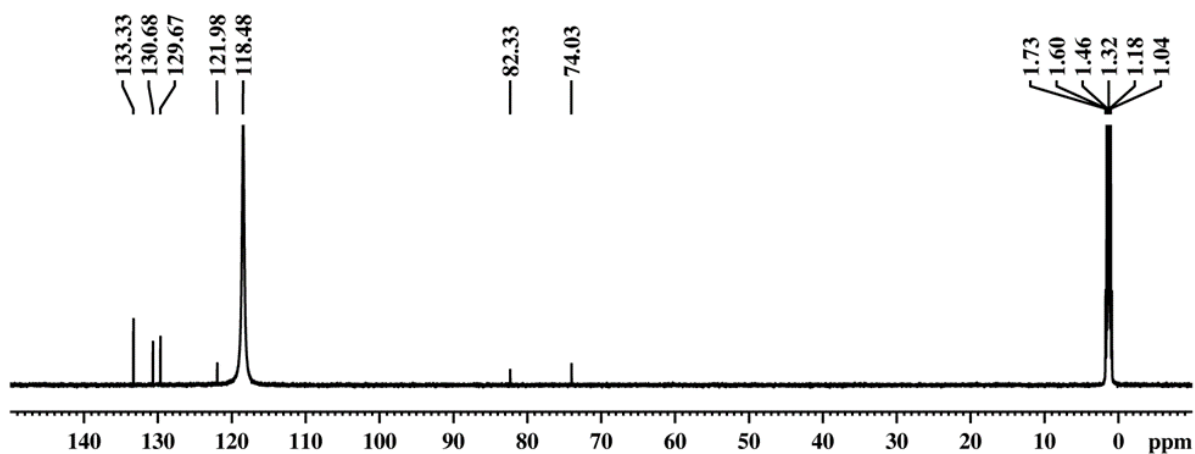


Figure 2.51: ¹³C NMR (150.1 MHz) spectrum of the reaction mixture of 2a and O₂ in CD₃CN at room temperature (after 24 h stirring); δ (ppm) = 74.03, 82.34, 121.98, 129.67, 130.69 and 133.33.

ESI mass spectrometry

In ESI-MS spectra (Figure 2.52), I observed a prominent ion peak at m/z of 528.0, whose mass and isotope distribution pattern correspond to $[\text{Ni}(\text{L}-\text{N}_4\text{Me}_2)(\text{PhC}_4\text{Ph})]^+$ (**4a**) (calculated m/z 528.1) (Figure 2.53). This mononuclear nickel(I)-diyne species **4a** exhibited an interesting rise-and-decay profile during the course of reaction. The peak intensity radically increased to the maximum and then decreased gradually with the time of the reaction.

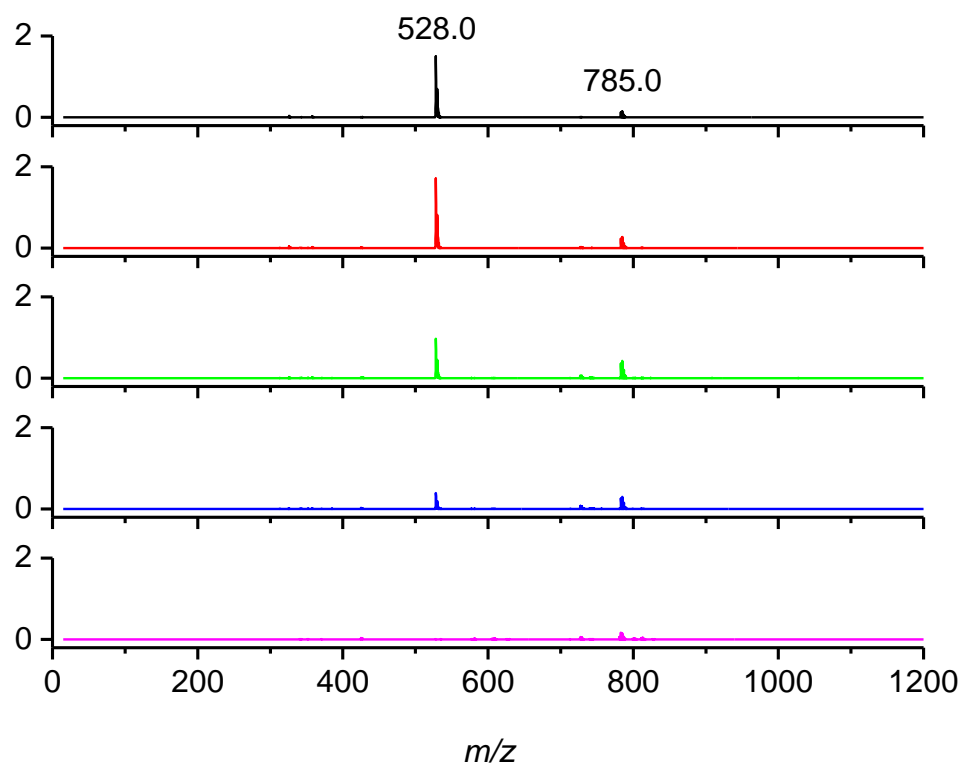


Figure 2.52: Time-course of ESI-MS spectra of the reaction mixture of **2a** and O_2 in MeCN (top to bottom: 15, 30, 75, 105 and 210 min). Y axis: Relative Intensity (10^7).

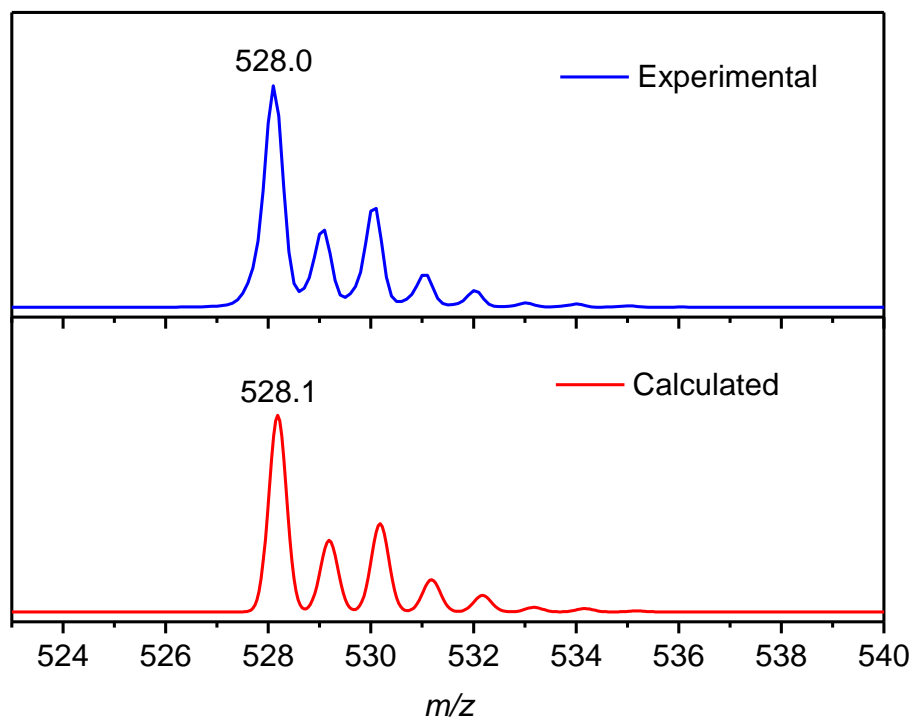


Figure 2.53: The experimental and calculated isotope distribution for $[\text{Ni}(\text{L-N}_4\text{Me}_2)(\text{PhC}_4\text{Ph})]^+$ (**4a**).

I was also able to detect ion peaks at m/z of 357.9 and 785.0, whose mass and isotope distribution patterns correspond to $[\text{Ni}(\text{L-N}_4\text{Me}_2)(\text{O}_2)]^+$ (**5**) (calculated m/z 358.1) and $[\{\text{Ni}(\text{L-N}_4\text{Me}_2)\}_2(\text{O}_2)(\text{ClO}_4)]^+$ (**6**) (calculated m/z 785.1) respectively (Figure 2.54 and Figure 2.57). Both species also exhibited rise-and-decay profiles during the course of reaction.

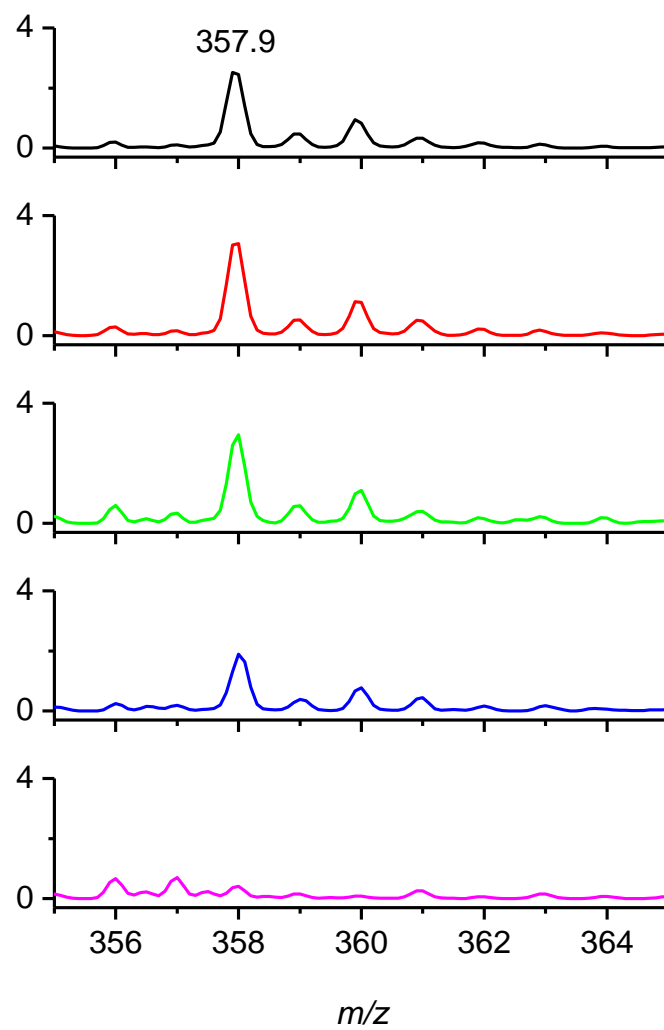


Figure 2.54: Time-course of ESI-MS spectra of the reaction mixture of 2a and O₂ in MeCN (top to bottom: 15, 30, 75, 105 and 210 min). Y axis: Relative Intensity (10^5).

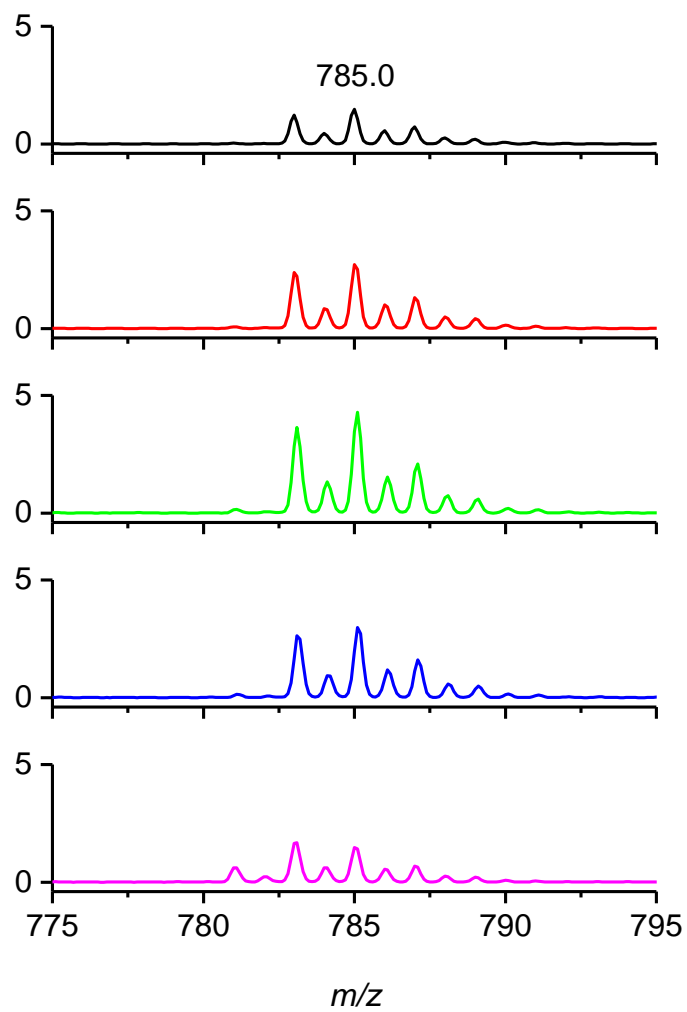


Figure 2.55: Time-course of ESI-MS spectra of the reaction mixture of 2a and O₂ in MeCN (top to bottom: 15, 30, 75, 105 and 210 min). Y axis: Relative Intensity (10^6).

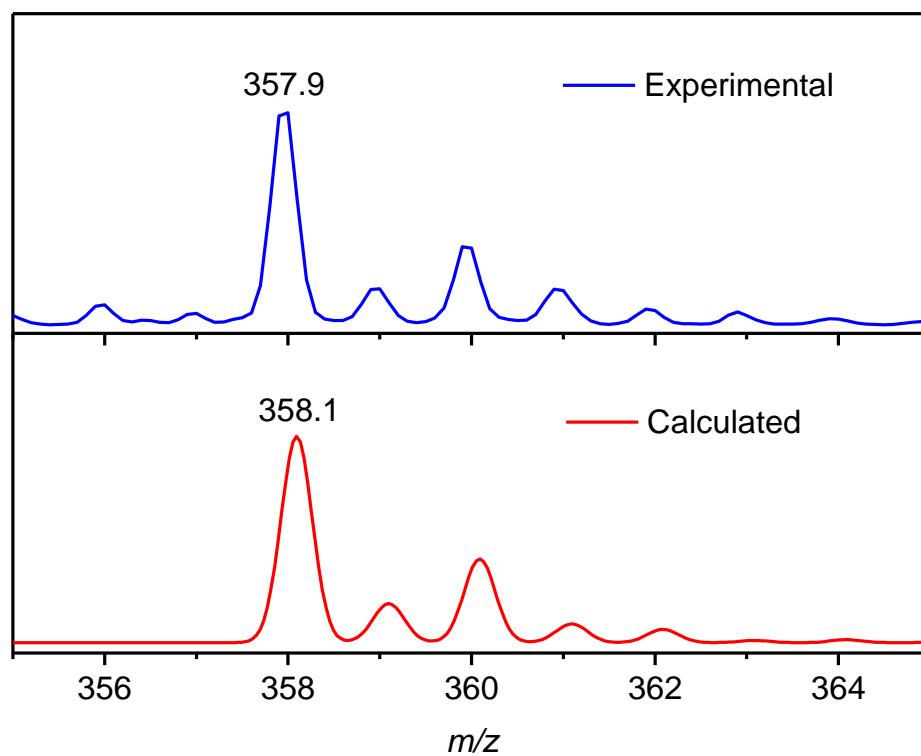


Figure 2.56: The experimental and calculated isotope distribution for $[\text{Ni}(\text{L-N}_4\text{Me}_2)(\text{O}_2)]^+$ (5).

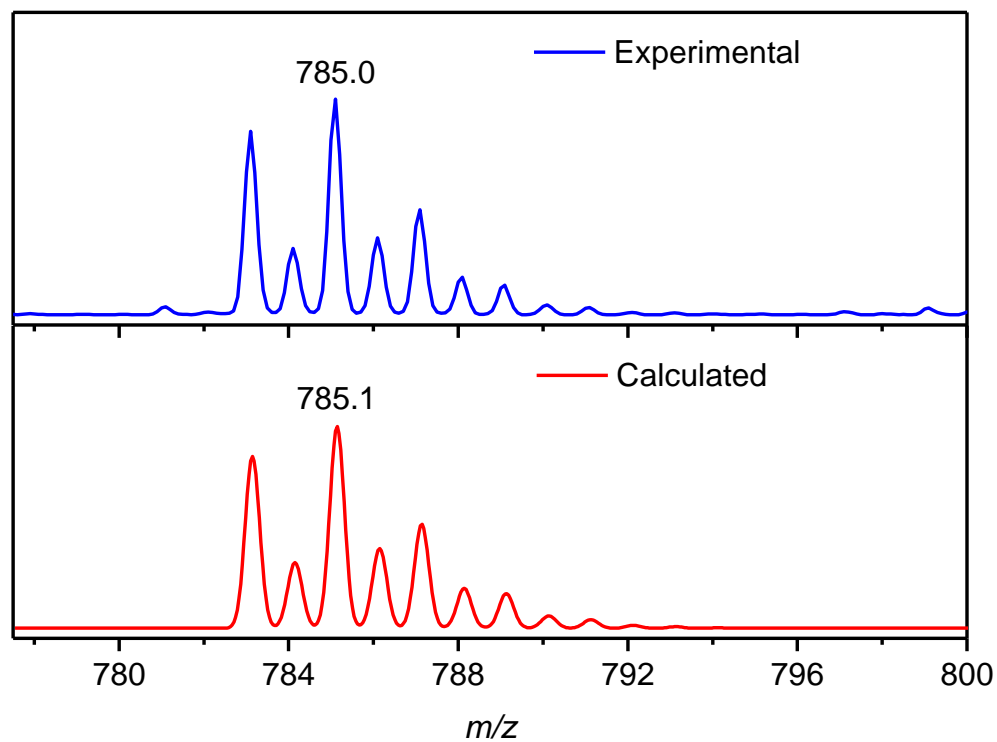


Figure 2.57: The experimental and calculated isotope distribution for $[\{\text{Ni}(\text{L-N}_4\text{Me}_2)\}_2(\text{O}_2)(\text{ClO}_4)]^+$ (6).

EPR Spectroscopy

EPR experiments were performed on the reaction mixture of **2a** (4 mM) with oxygen in acetonitrile containing 0.2 M TBAP. Aliquots from the reaction mixture then taken every few minutes over the course of 180 min and frozen in EPR tubes. EPR spectra are depicted in Figure 2.58.

From the EPR spectra, it was found that upon reaction of **2a** with oxygen two EPR active nickel species are formed in different concentration (12:3.5 ratios at 15 min). The intensities of both species continued to increase over the first 15 min and then decreased. After 180 min, the reaction mixture was EPR silent. At 15 min (Figure 2.59), the species with higher concentration exhibits a rhombic signal with g values of 2.282, 2.208 and 2.013, which is indicative of $S = \frac{1}{2}$ ground state for the species. The anisotropy of the rhombic signal and the quintet splitting of the high field g_z component with a hyperfine coupling constant of 36.70 MHz due to the interaction between the electron spin and the nuclear spin ($I = 1$) of two axial amine nitrogen atoms are consistent with the formulation as $L-N_4Me_2$ coordinated to a nickel species of $(d_z^2)^1$ electronic configuration.

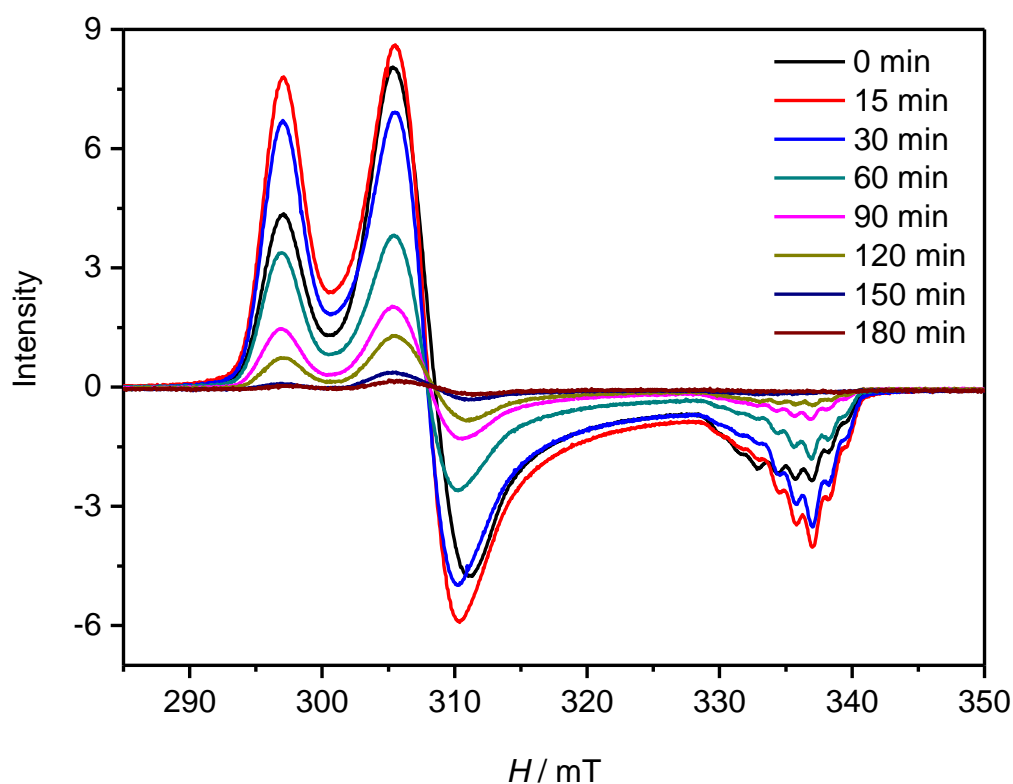


Figure 2.58: X-Band EPR spectra of frozen solution of the reaction mixture of **2a** (4 mM) and O_2 containing 0.2 M TBAP in acetonitrile at 77 K.

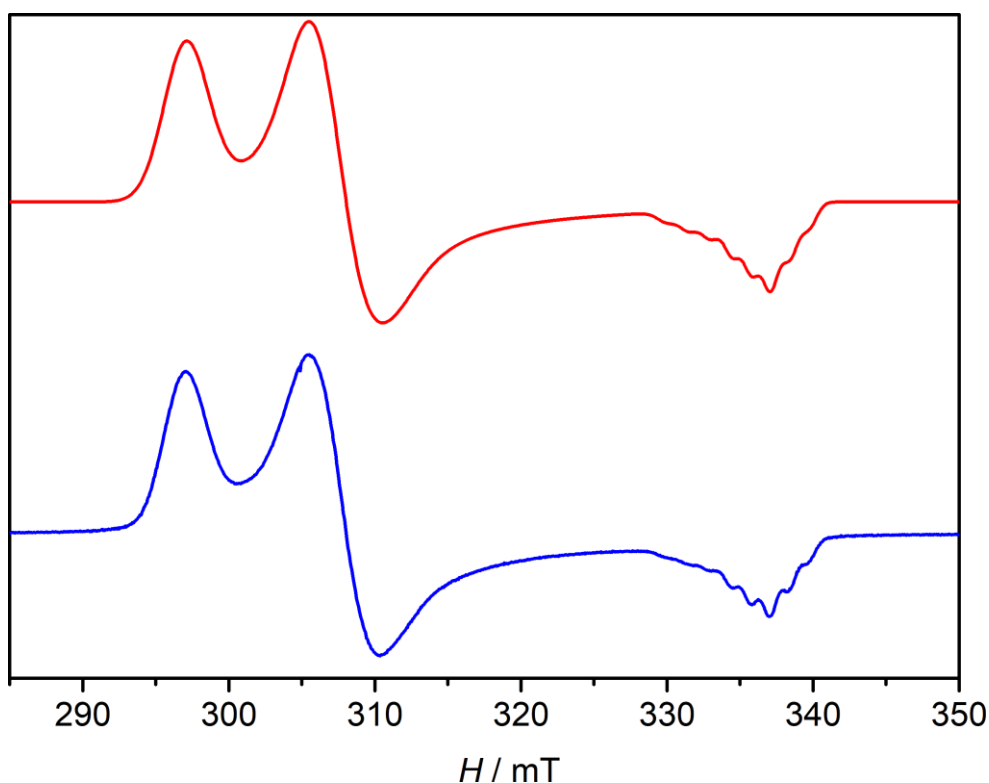
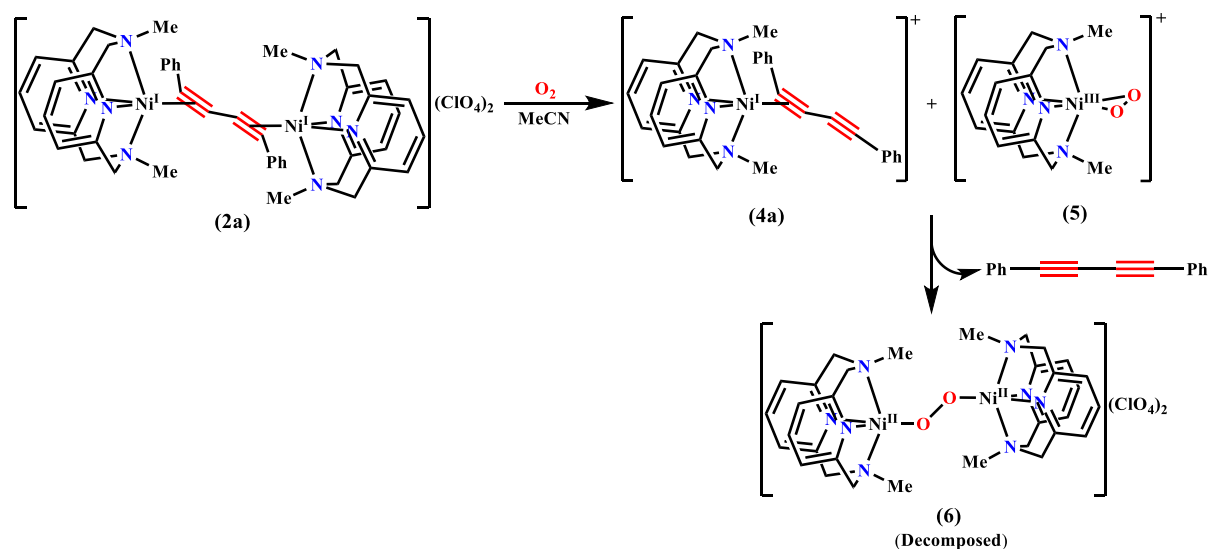


Figure 2.59: X-Band EPR spectra of frozen solution of the reaction mixture of **2a** (4 mM) and O_2 containing 0.2 M TBAP in acetonitrile at 77 K, at 15 min; experimental (blue) and simulation (red).

These spectroscopic parameters ($g_x = 2.282$, $g_y = 2.208$, $g_z = 2.013$ and $A_z = 36.70$ MHz) are very similar to those ($g_x = 2.300$, $g_y = 2.213$, $g_z = 2.008$ and $A_z = 36.70$ MHz) obtained for the mononuclear nickel(I)-alkyne complex $[Ni(L-N_4Me_2)(PhC_2Ph)](ClO_4) \cdot MeOH$ (**3**).

The other species reveals a pseudoaxial signal ($g_x = 2.220$, $g_y = 2.193$, $g_z = 2.038$) with hyperfine coupling to two axial amine nitrogen atoms ($A_z = 42.60$ MHz), which is also consistent with the formation of a L- N_4Me_2 coordinated nickel(III) species with a $(d_z^2)^1$ ground state.^[89, 108, 148-149] These spectroscopic parameters are similar to those ($g_x = 2.224$, $g_y = 2.191$, $g_z = 2.038$ and $A_z = 42.60$ MHz) obtained for the mononuclear nickel(III)-peroxo complex $[Ni^{III}(L-N_4Me_2)(O_2)]^+$ (**5**). (*see* section 2.6).

The results from these investigations suggest that the reaction of $[{Ni}(L-N_4Me_2)]_2(\mu-R_2C_4R)(ClO_4)_2$ [$R = Ph$] (**2a**) with molecular oxygen produced a mononuclear nickel(I)-diyne complex $[Ni^I(L-N_4Me_2)(PhC_4Ph)]^+$ (**4a**) and a mononuclear nickel(III)-peroxo species $[Ni^{III}(L-N_4Me_2)(O_2)]^+$ (**5**), which are converted to free diphenyldiacetylene and an unstable dinuclear nickel(II) species $[{Ni}^{II}(L-N_4Me_2)]_2(O_2)(ClO_4)^+$ (**6**) (Scheme 2.10).



Scheme 2.10: Reaction of **2a** with O_2 in MeCN.

2.4.2 Reactivity in Presence of Lithium Perchlorate

The reactivity of $[\{\text{Ni}(\text{L-N}_4\text{Me}_2)\}_2(\mu\text{-RC}_4\text{R})](\text{ClO}_4)_2$ [$\text{R} = \text{Ph}$] (**2a**) with molecular oxygen in presence of lithium ion in acetonitrile was performed. When the complex **2a** was treated with molecular oxygen in the presence of excess lithium perchlorate in acetonitrile at room temperature, a white solid was precipitated, which was collected and dried under vacuum. A solution of the solid in H_2SO_4 (0.2 M) decolorizes the violet solution of KMnO_4 (*see* experimental details), which was monitored by UV-Vis spectroscopy (*appendix* Figure 7.92). These results could suggest the formation of lithium peroxide as white precipitate during the course of the reaction between **2a** and O_2 in presence of lithium perchlorate. Raman spectrum of the isolated solid confirms the formation of lithium peroxide ($\bar{\nu}_{\text{O-O}} = 780 \text{ cm}^{-1}$) (*appendix* Figure 7.93).^[150-154]

2.5 Reactivity of $[\text{Ni}(\text{L-N}_4\text{Me}_2)(\text{PhC}_2\text{Ph})](\text{ClO}_4) \cdot \text{MeOH}$ (**3**) with Molecular Oxygen

The reactivity of $[\text{Ni}(\text{L-N}_4\text{Me}_2)(\text{PhC}_2\text{Ph})](\text{ClO}_4) \cdot \text{MeOH}$ (**3**) with molecular oxygen was also investigated by *in situ* spectroscopies (UV-Vis-NIR and EPR) and ESI-MS.

UV-Vis-NIR Spectroscopy

Upon reaction with molecular oxygen, the complex **3** shows a spectral change in absorption spectrum as shown in Figure 2.60 and Figure 2.61.

The spectral change at the higher energy region was observed as a decrease in absorption of charge transfer bands of the complex **3** at 249 and 364 nm with appearance of two new bands at 278 and 296 nm, which are the characteristic bands for free diphenylacetylene (*appendix* Figure 7.94).

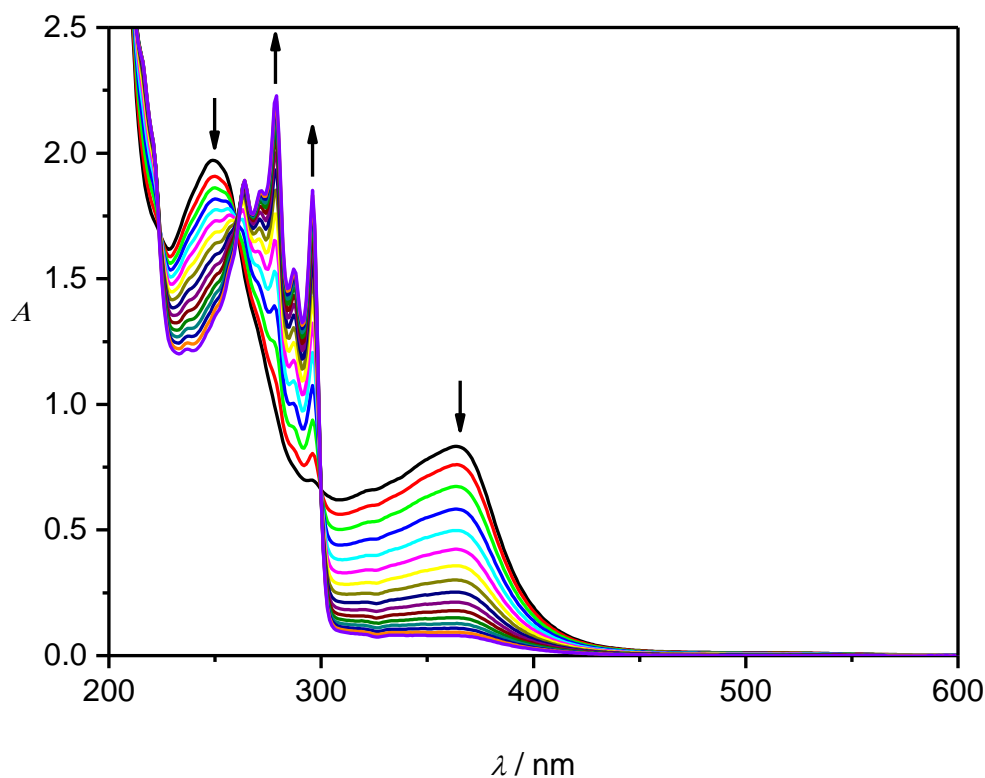


Figure 2.60: UV-Vis spectral change during the reaction of **3** (0.726 mM) and O_2 in MeCN at room temperature in 30 min intervals. The arrows indicate how the intensities of absorption bands change over time.

Whereas the spectral change at the visible NIR region was observed as a decrease in absorption of two bands and a shoulder of the complex **3** at 675, 1220 and 514 nm respectively with appearance of three new bands at 592, 822 and 996 nm (*appendix* Figure 7.95). Later bands are very similar with these of the Ni(II) distorted octahedral complexes with L-N₄Me₂ as ligand.^[108]

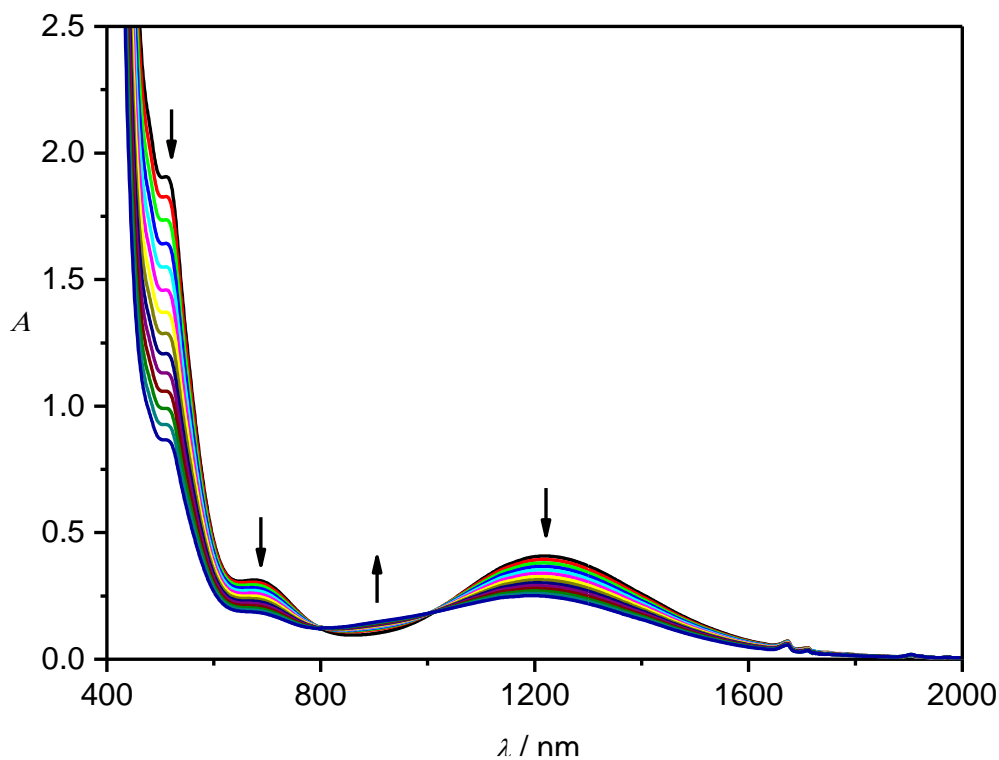


Figure 2.61: UV-Vis-NIR spectral change during the reaction of **3** (9.07 mM) and O₂ in MeCN at room temperature in 30 min intervals. The arrows indicate how the intensities of absorption bands change over time.

ESI mass spectrometry

In the course of reaction of **3** with oxygen in acetonitrile at room temperature over 420 min, the peak of the starting complex **3** ($[\text{Ni}(\text{L-N}_4\text{Me}_2)(\text{PhC}_2\text{Ph})]^+$, $m/z = 504.0$) decreased gradually with the time of reaction (Figure 2.62).

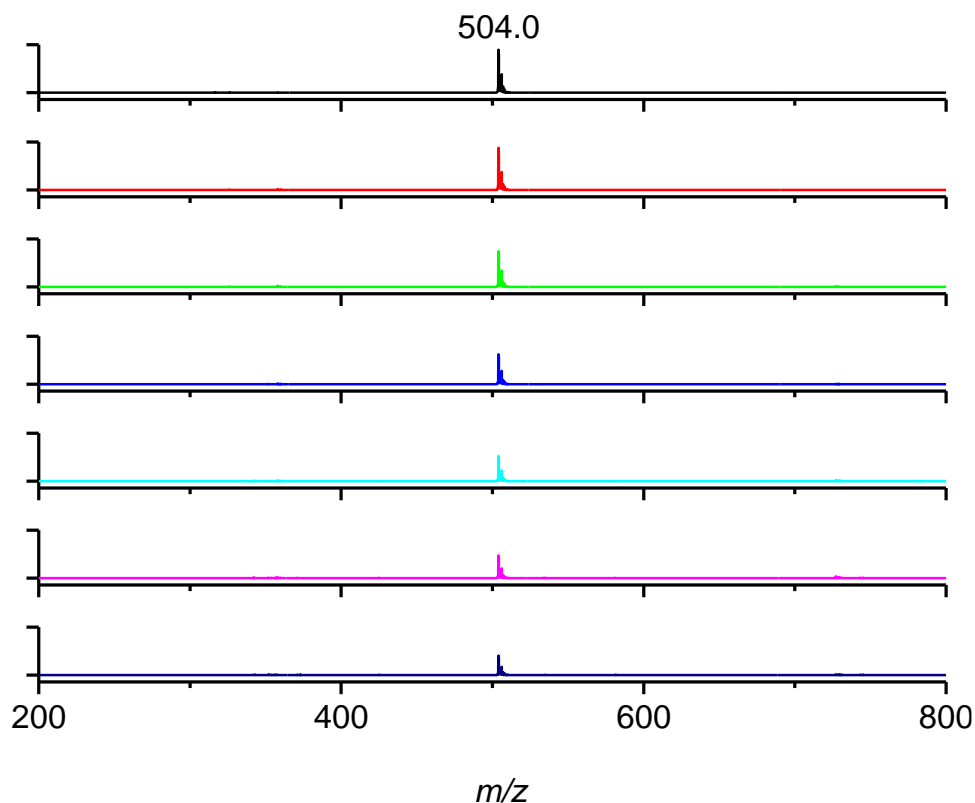


Figure 2.62.: Time-course of ESI-MS spectra of the reaction mixture of **3** and O_2 in MeCN (top to bottom: 15, 60, 120, 180, 240, 300 and 420 min). Y axis: Relative Intensity (0-7)(10^7).

I am also able to detect signals due to $[\text{Ni}(\text{L-N}_4\text{Me}_2)(\text{O}_2)]^+$ (**5**) ($m/z = 357.9$) and $[\{\text{Ni}(\text{L-N}_4\text{Me}_2)\}_2(\text{O}_2)(\text{ClO}_4)]^+$ (**6**) ($m/z = 785.0$) but with much smaller intensities as shown in Figure 2.63 and Figure 2.64. The isotope patterns agree with those obtained by computer simulations (Figure 2.65 and Figure 2.66). Both species exhibited rise-and-decay profile during the course of reaction.

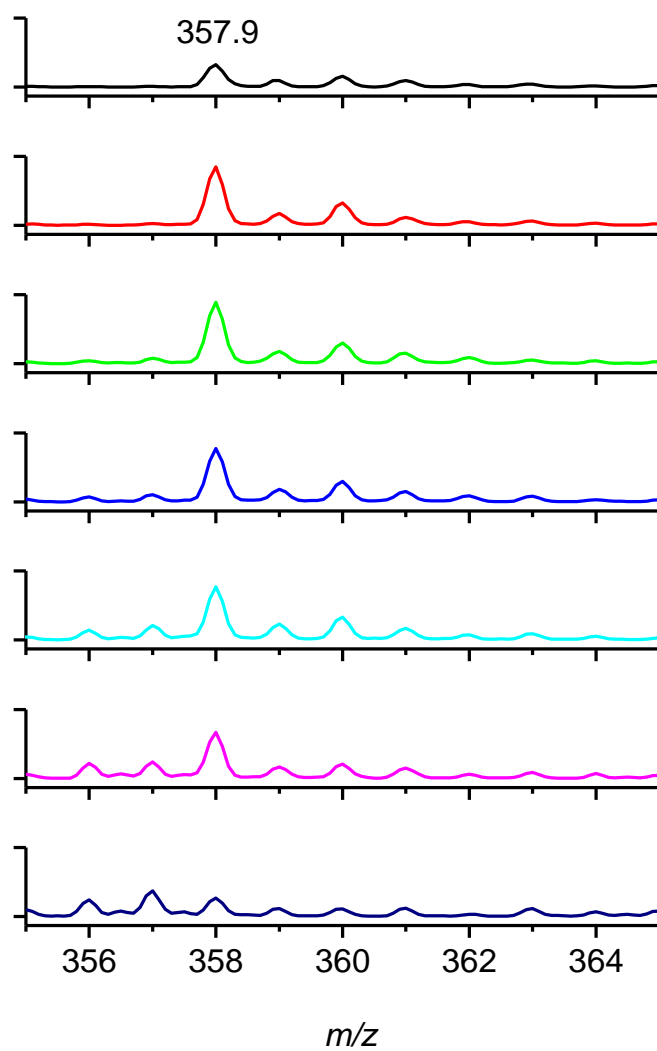


Figure 2.63: Time-course of ESI-MS spectra of the reaction mixture of 3 and O₂ in MeCN, (top to bottom: 15, 60, 120, 180, 240, 300 and 420 min). Region: *m/z* = 355-365 and Y axis: Relative Intensity (0-15) (10⁵).

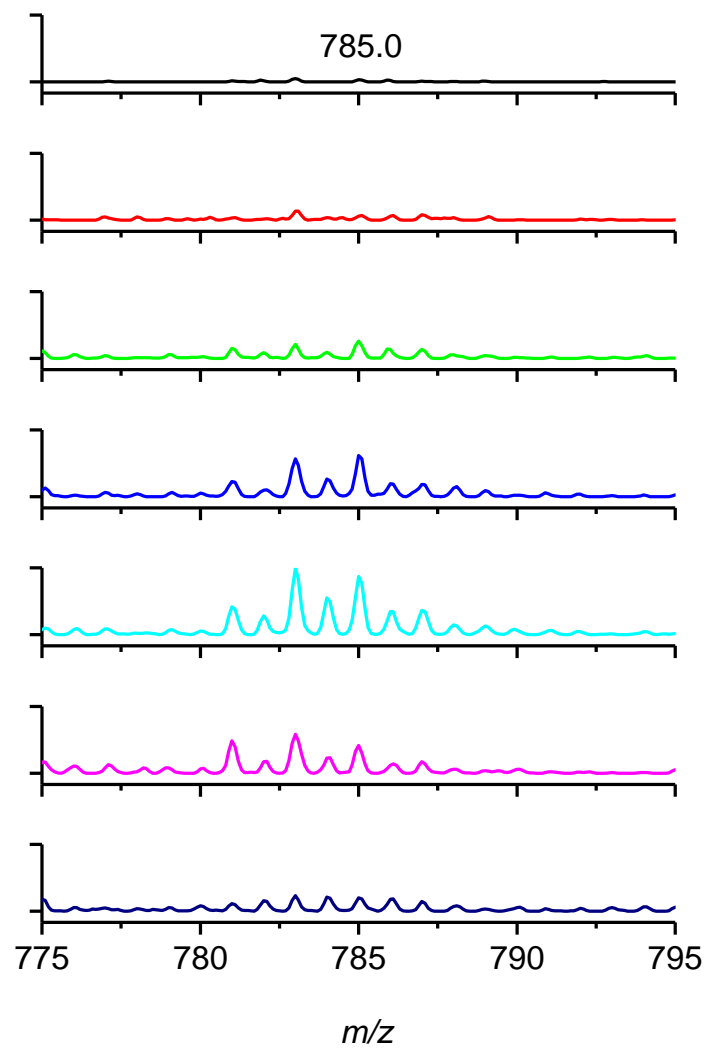


Figure 2.64: Time-course of ESI-MS spectra of the reaction mixture of **3** and O_2 in MeCN, (top to bottom: 15, 60, 120, 180, 240, 300 and 420 min). Region: $m/z = 775-795$ and Y axis: Relative Intensity $(0-3) \cdot 10^5$.

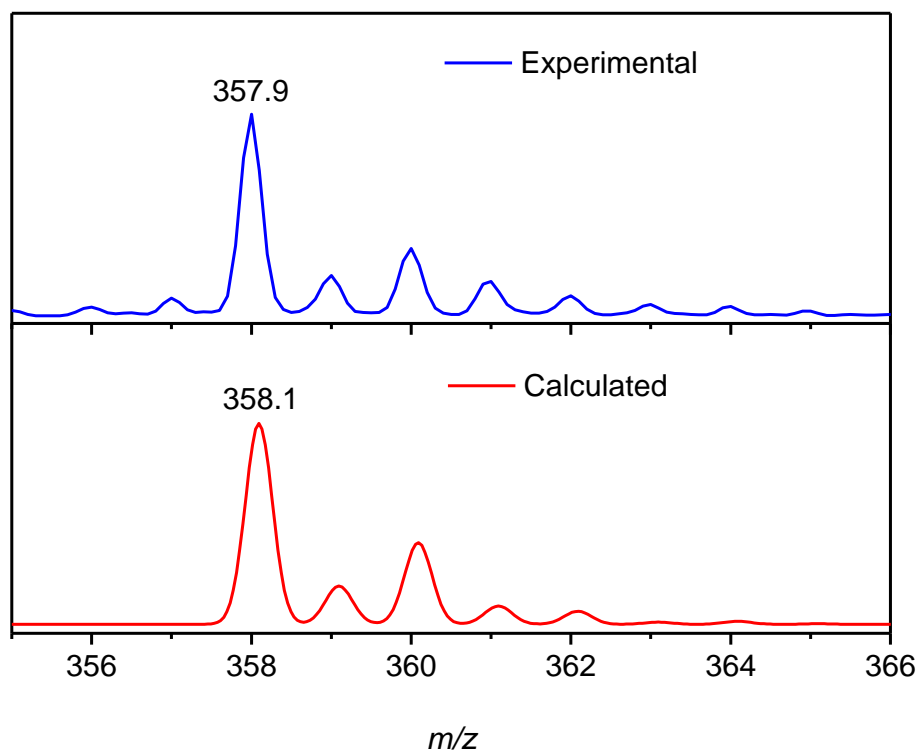


Figure 2.65: The experimental and calculated isotope distribution for $[\text{Ni}(\text{L-N}_4\text{Me}_2)(\text{O}_2)]^+$ (5).

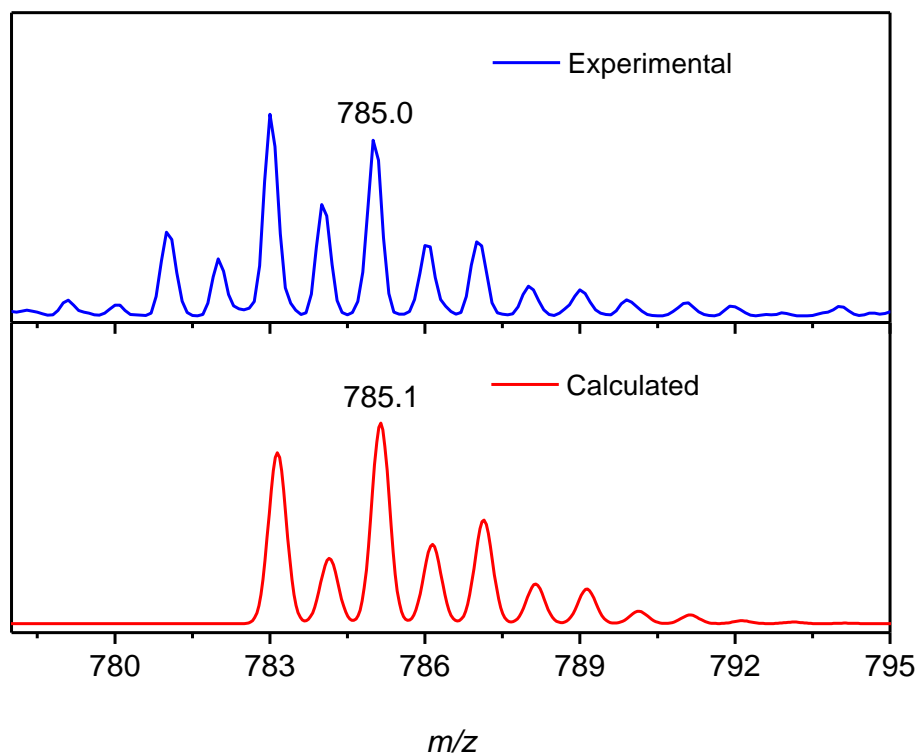


Figure 2.66: The experimental and calculated isotope distribution for $[\{\text{Ni}(\text{L-N}_4\text{Me}_2)\}(\text{O}_2)(\text{ClO}_4)]^+$ (6).

EPR Spectroscopy

EPR experiments were performed on the reaction mixture of **3** (4 mM) with oxygen in acetonitrile containing 0.2 M TBAP. Aliquots from the reaction mixture then taken every few minutes over the course of 390 min and frozen in EPR tubes. EPR spectra are depicted in Figure 2.67 and Figure 2.68.

It was found that upon reaction of **3** with oxygen, the intensity of $[\text{Ni}(\text{L-N}_4\text{Me}_2)(\text{PhC}_2\text{Ph})]^+$ species decreased gradually with the time of reaction. The EPR spectra also revealed presence of additional band nearly around $g_z = 2.038$ ($> g_z = 2.008$), whose intensity decreases to some extent with the time of reaction. The additional peak could be due to the presence of EPR active species $[\text{Ni}^{\text{III}}(\text{L-N}_4\text{Me}_2)(\text{O}_2)]^+$ (**5**).

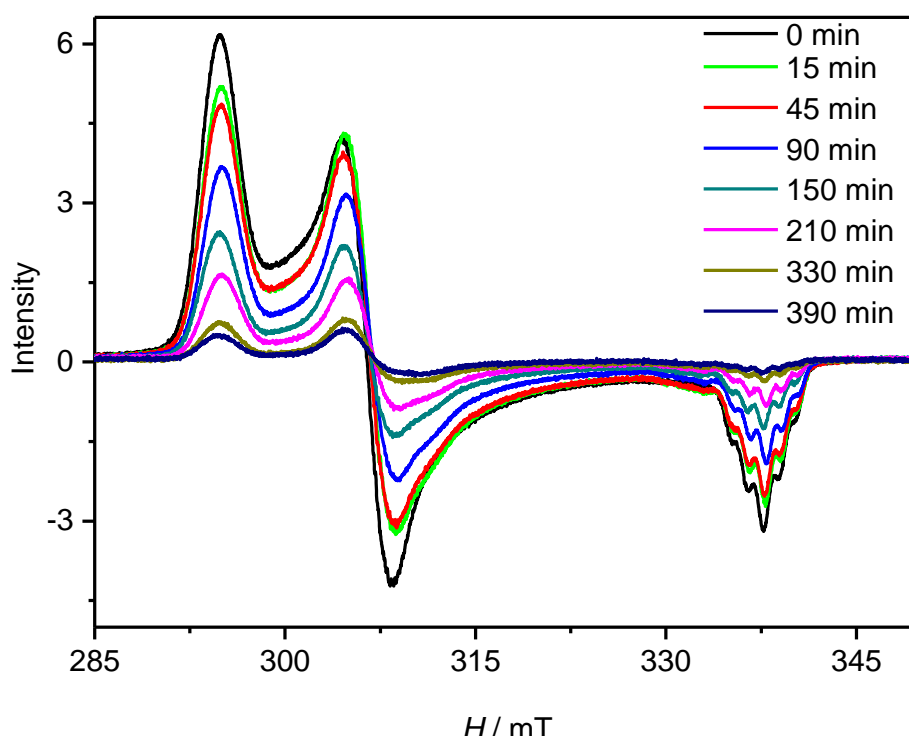


Figure 2.67: X-Band EPR spectra of frozen solution of the reaction mixture of **3** (4 mM) and O_2 containing 0.2 M TBAP in MeCN, measured at 77 K.

The results from these investigations suggest that the reaction of **3** with molecular oxygen produced diphenylacetylene and $[\text{Ni}^{\text{III}}(\text{L-N}_4\text{Me}_2)(\text{O}_2)]^+$ (**5**), which reacts with **3** to produce unstable $[\{\text{Ni}^{\text{II}}(\text{L-N}_4\text{Me}_2)\}_2(\text{O}_2)(\text{ClO}_4)]^+$ (**6**) (Scheme 2.11).

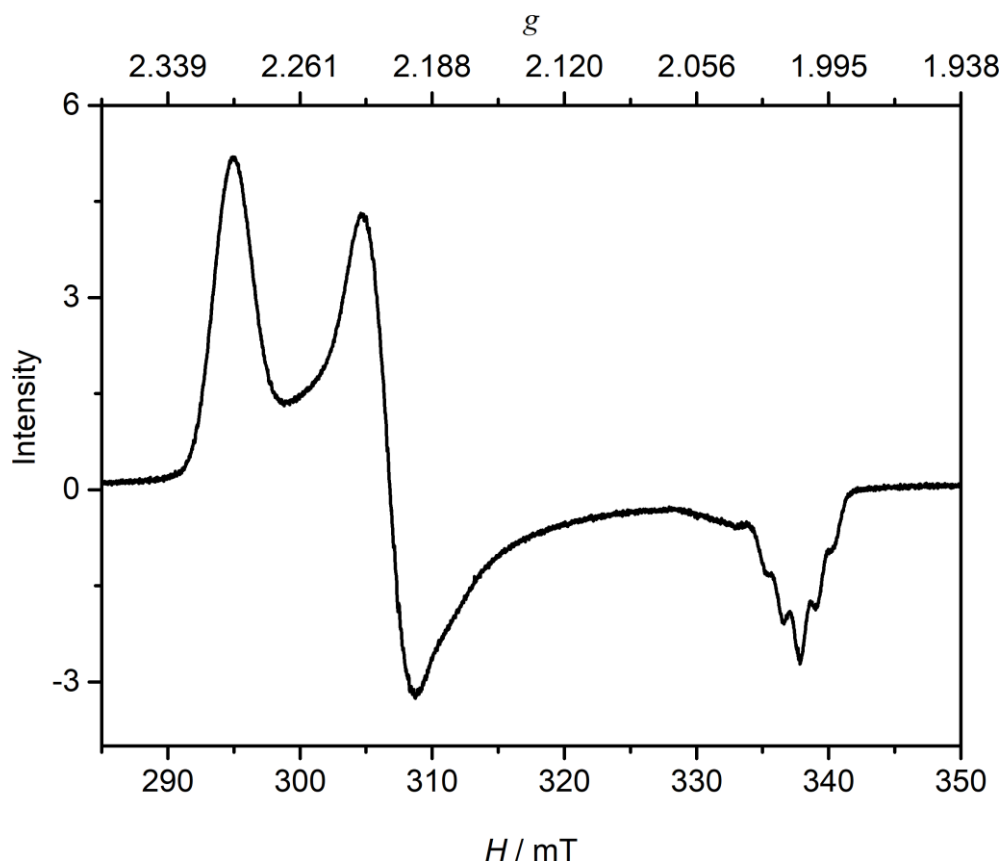
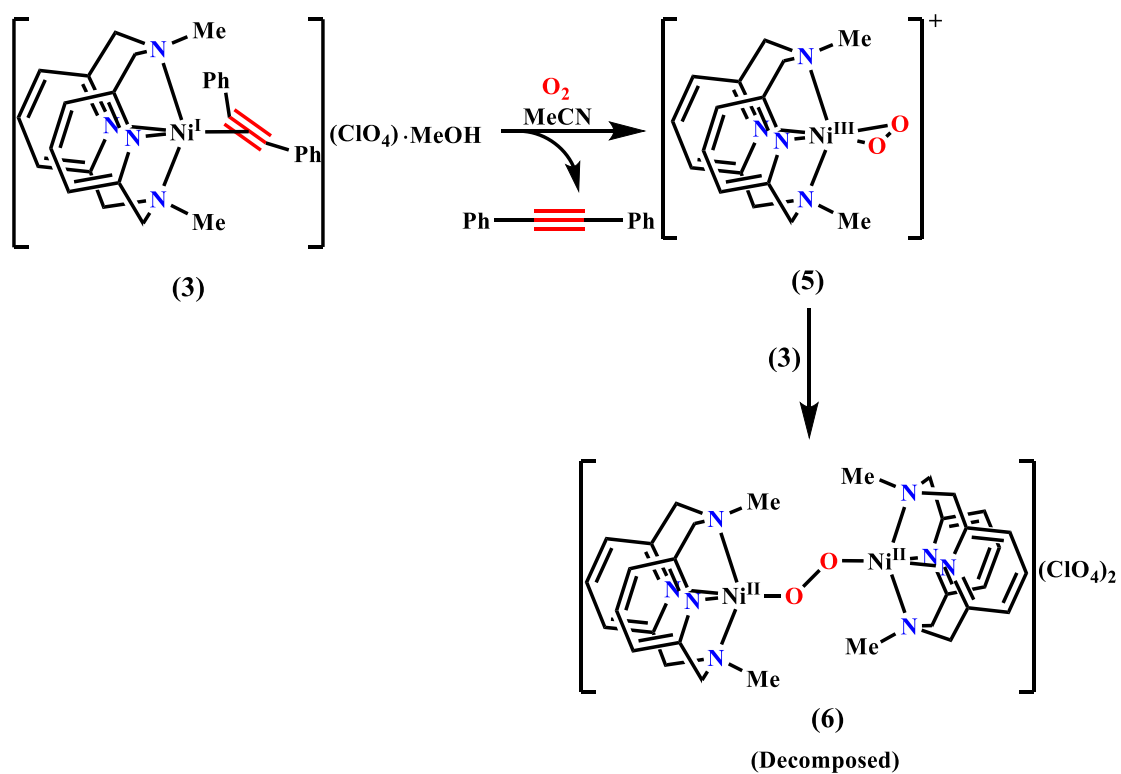


Figure 2.68: X-Band EPR spectra of frozen solution of the reaction mixture of **3** (4 mM) and O_2 containing 0.2 M TBAP in acetonitrile, measured at 77 K, at 15 min.

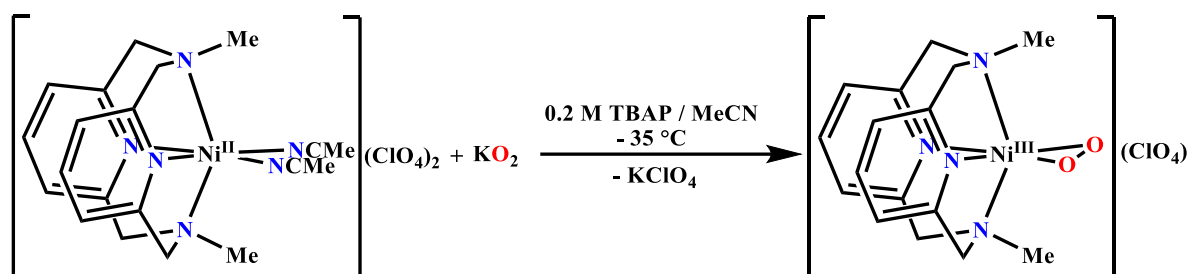


Scheme 2.11: Reaction of **3** with O_2 in MeCN.

2.6 Generation and Characterization of $[\text{Ni}(\text{L-N}_4\text{Me}_2)(\text{O}_2)]^+$ (**5**)

I have observed that upon reaction of $[\{\text{Ni}(\text{L-N}_4\text{Me}_2)\}_2(\mu\text{-RC}_4\text{R})](\text{ClO}_4)_2$ [$\text{R} = \text{Ph}$] (**2a**) with oxygen two EPR active nickel species $[\text{Ni}(\text{L-N}_4\text{Me}_2)(\text{PhC}_4\text{Ph})]^+$ (**4a**) and $[\text{Ni}(\text{L-N}_4\text{Me}_2)(\text{O}_2)]^+$ (**5**) are formed in different concentration. The species $[\text{Ni}(\text{L-N}_4\text{Me}_2)(\text{O}_2)]^+$ (**5**) shows a pseudoaxial signal with magnetic anisotropy of g value and quintet splitting of g_z component in EPR experiments. To support the formulation of $[\text{Ni}(\text{L-N}_4\text{Me}_2)(\text{O}_2)]^+$ (**5**), I performed the reaction between $[\text{Ni}(\text{L-N}_4\text{Me}_2)(\text{MeCN})_2](\text{ClO}_4)_2$ (**1**) and potassium superoxide to generate $[\text{Ni}(\text{L-N}_4\text{Me}_2)(\text{O}_2)]^+$ (**5**) species.

The reaction between $[\text{Ni}(\text{L-N}_4\text{Me}_2)(\text{MeCN})_2](\text{ClO}_4)_2$ (**1**) and 1.1 equivalent potassium superoxide affords an olive green solution in acetonitrile containing 0.2 M TBAP at -35°C .



Scheme 2.12: Generation of $[\text{Ni}(\text{L-N}_4\text{Me}_2)(\text{O}_2)]^+$ (**5**) using KO_2 .

EPR experiment was performed on the reaction mixture. Aliquot from the reaction mixture was taken in a cooled EPR tube and frozen in liquid nitrogen. The EPR spectrum of the reaction mixture is displayed in Figure 2.69. The spectrum exhibits a pseudoaxial signal with g values of 2.224, 2.191 and 2.038, which is indicative of an $S = \frac{1}{2}$ ground state for the species. The high anisotropy of the rhombic signal and the quintet splitting of the high field g_{zz} component with a hyperfine coupling constant of 42.6 MHz due to the interaction between the electron spin and the nuclear spin ($I = 1$) of two axial amine nitrogen atoms are also consistent with the formulation $[\text{Ni}^{\text{III}}(\text{L-N}_4\text{Me}_2)(\text{O}_2)]^+$ species of $(d_z^2)^1$ electronic configuration.

These spectroscopic parameters ($g_x = 2.224$, $g_y = 2.191$, $g_z = 2.038$ and $A_z = 42.6$ MHz) are similar to those ($g_x = 2.220$, $g_y = 2.193$, $g_z = 2.038$ and $A_z = 42.6$ MHz) obtained for less concentrated species $[\text{Ni}(\text{L-N}_4\text{Me}_2)(\text{O}_2)]^+$ (**5**) formed upon reaction of **2a** with molecular oxygen.

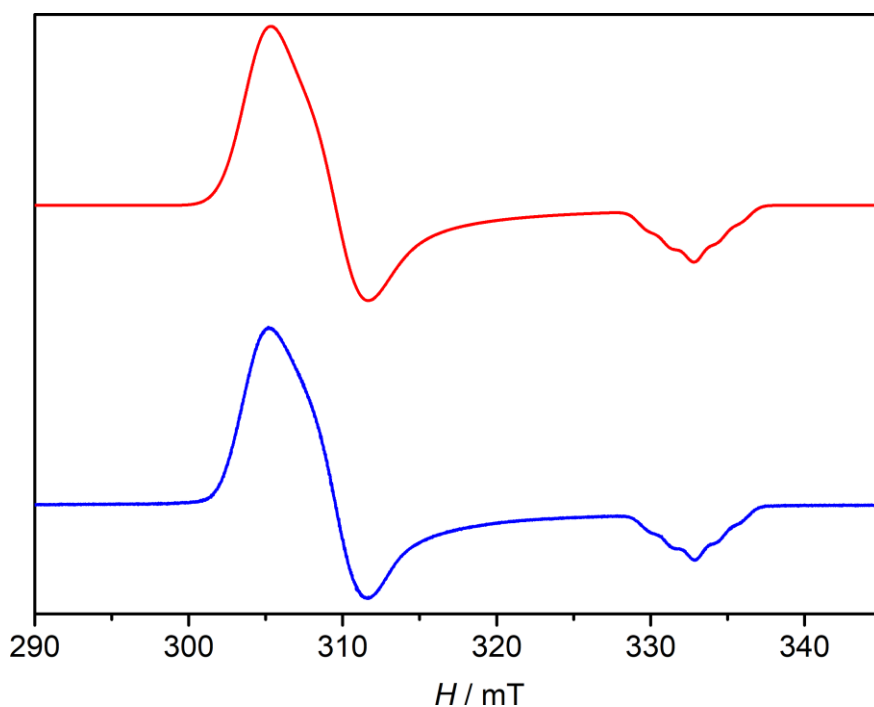


Figure 2.69: X-Band EPR spectrum of the solution from the reaction of **1** with KO_2 in MeCN containing 0.2 M TBAP at -35°C , measured at 77 K; experimental (blue) and simulation (red).

The stability of the EPR active nickel(III)-peroxide species at -35°C was also monitored by EPR measurements. Aliquots from the reaction mixture was taken at a different time interval in precooled EPR tubes and frozen in liquid nitrogen. Spectral changes are depicted in Figure 2.70 and *appendix* Figure 7.97. Spectra show the intensity of the species continued to decrease over time, which attributed to the instability of the species at -35°C in acetonitrile.

When the reaction between $[\text{Ni}(\text{L}-\text{N}_4\text{Me}_2)(\text{MeCN})_2](\text{ClO}_4)_2$ (**1**) and potassium superoxide was performed in propionitrile containing 0.1 M TBAP at -65°C , it produced same EPR active nickel(III)-peroxide species $[\text{Ni}(\text{L}-\text{N}_4\text{Me}_2)(\text{O}_2)]^+$ (**5**). The stability of the species at -65°C was also monitored by EPR measurements at different time intervals. Spectral changes are depicted in Figure 2.71 and Figure 2.72. The spectra indicate that the EPR active species is relatively stable at -65°C . In addition, spin quantification using complex **3** (5.1 mM in 0.1 M TBAP/EtCN) as standard finds that the EPR signal corresponds to around 65% of the total nickel content in the sample.

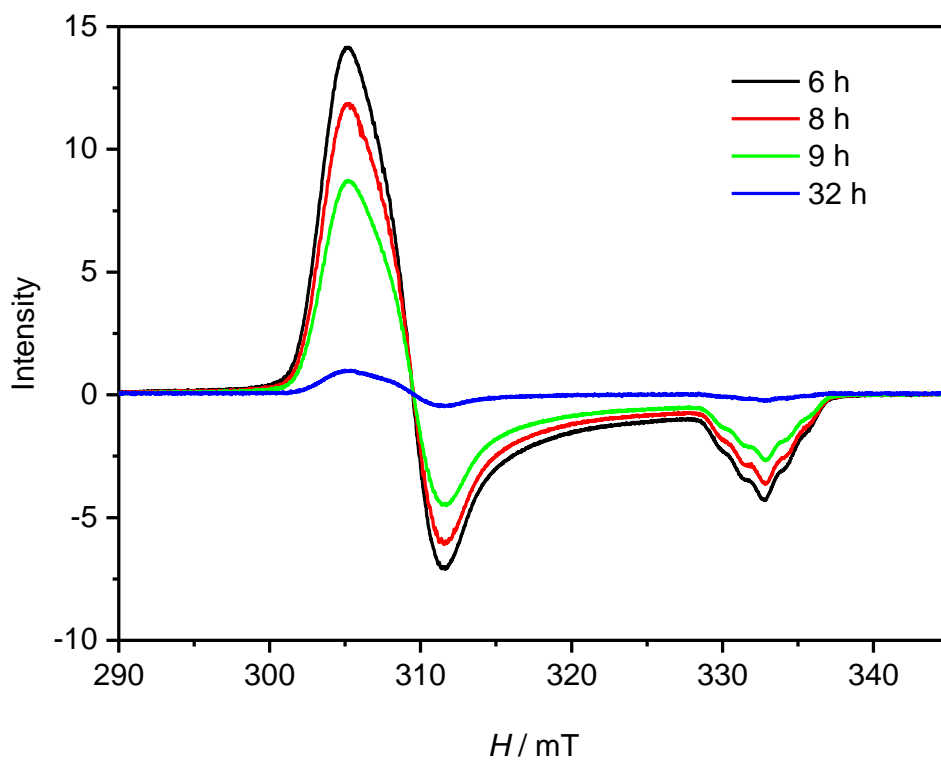


Figure 2.70: X-Band EPR spectra of the solutions from the reaction of 1 with KO_2 in 0.2 M TBAP/MeCN at -35°C at different time interval (6-32 h). All spectra are recorded at 77 K.

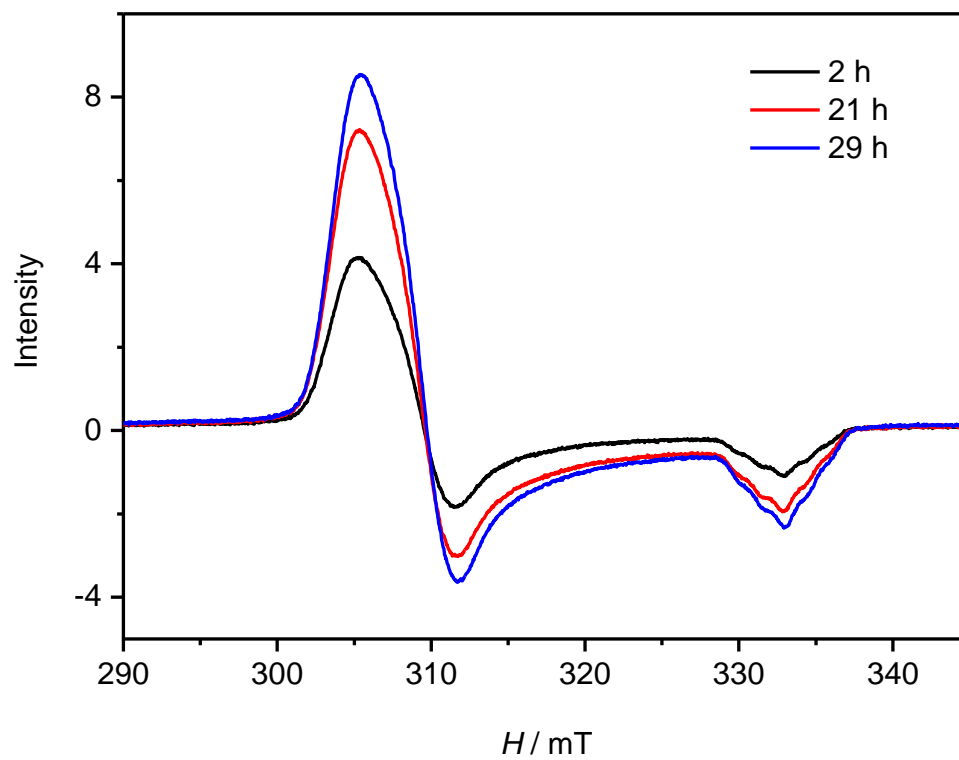


Figure 2.71: X-Band EPR spectra of the solutions from the reaction of 1 with KO_2 in 0.1 M TBAP/EtCN at -65°C at different time interval (2 - 29 h). All spectra are recorded at 77 K.

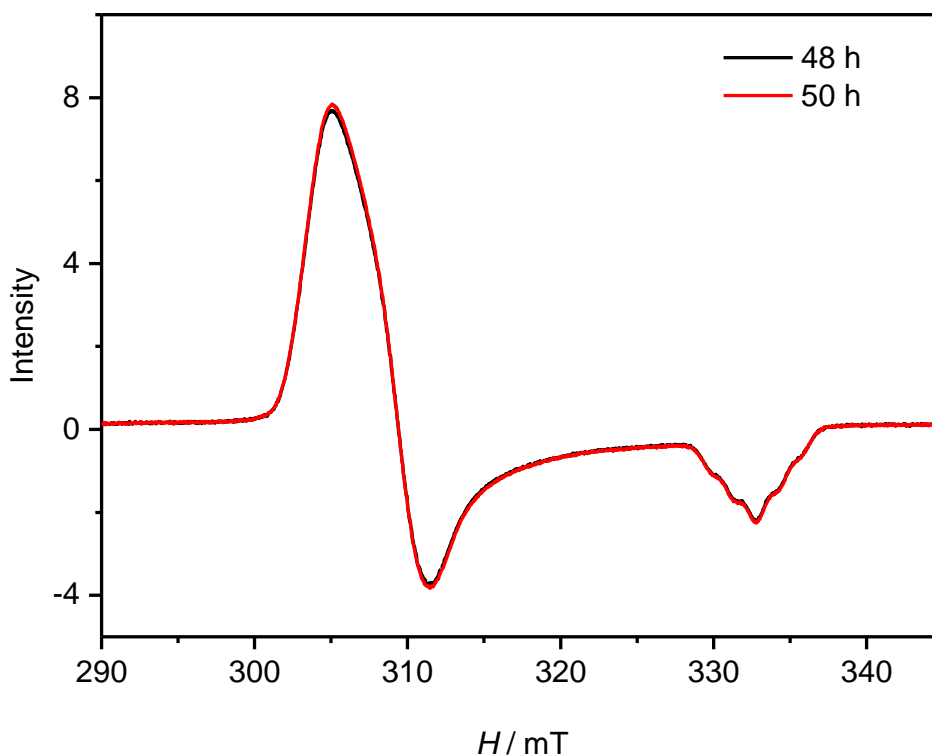
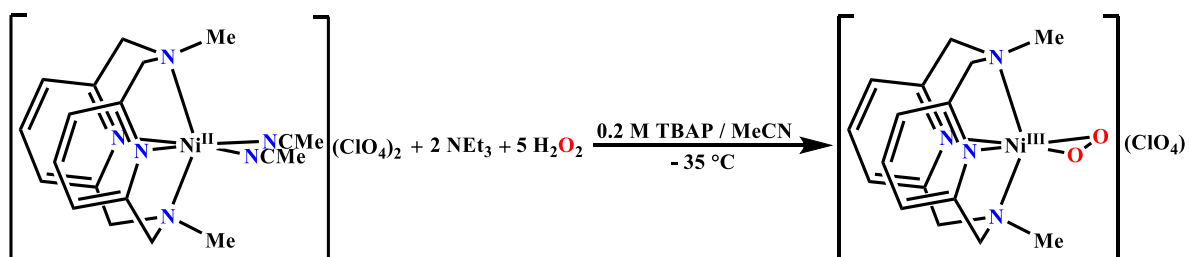


Figure 2.72: X-Band EPR spectra of the solutions from the reaction of **1** with KO_2 in 0.1 M TBAP/EtCN at -65°C at different time interval (48 - 50 h). All spectra are recorded at 77 K.

Metal(III)-peroxo complexes have been generated by reacting metal(II) complex with H_2O_2 in presence of base (e.g. triethylamine).^[87, 89, 155-158] I also generate nickel(III)-peroxo complex $[\text{Ni}(\text{L}-\text{N}_4\text{Me}_2)(\text{O}_2)]^+$ (**5**) using similar procedure.

5 equivalents of H_2O_2 was added to a solution containing $[\text{Ni}(\text{L}-\text{N}_4\text{Me}_2)(\text{MeCN})_2](\text{ClO}_4)_2$ (**1**) and two equivalents of triethylamine in 0.2 M TBAP/MeCN at -35°C (Scheme 2.13). EPR experiment was performed on the reaction mixture after 3 h stirring. Aliquot from the reaction mixture was taken in a cooled EPR tube and frozen in liquid nitrogen.



Scheme 2.13: Generation of $[\text{Ni}(\text{L}-\text{N}_4\text{Me}_2)(\text{O}_2)]^+$ (**5**) using H_2O_2 .

The EPR spectrum of the reaction mixture is depicted in Figure 2.73. The spectrum exhibits a pseudoaxial signal with the quintet splitting of the high field g_{zz} component ($g_x = 2.223$, $g_y = 2.190$, $g_z = 2.038$ and $A_z = 42.6$ MHz), suggesting formation of the same EPR active nickel(III)-peroxide species $[\text{Ni}(\text{L-N}_4\text{Me}_2)(\text{O}_2)]^+$ (**5**) upon reaction of $[\text{Ni}(\text{L-N}_4\text{Me}_2)(\text{MeCN})_2](\text{ClO}_4)_2$ (**1**) and H_2O_2 in 0.2 M TBAP/MeCN containing triethylamine at -35 °C.

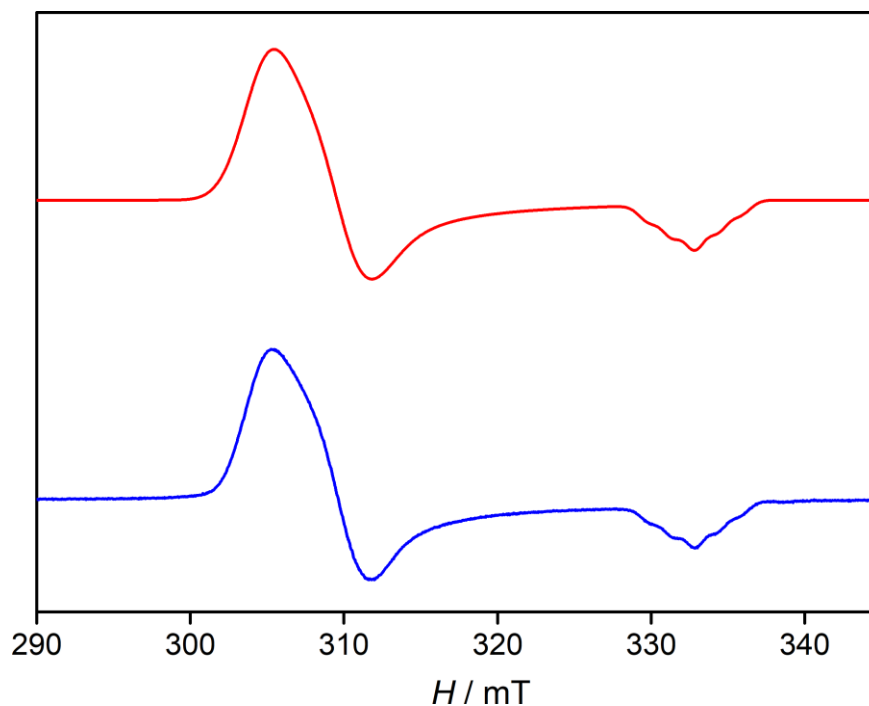
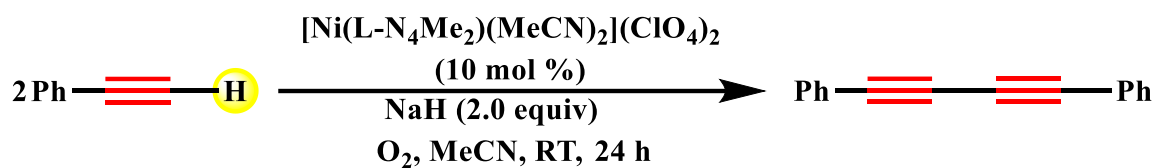


Figure 2.73: X-Band EPR spectrum of the solution mixture from the reaction of **1** with H_2O_2 in 0.2 M TBAP/MeCN containing triethylamine at -35 °C, measured at 77 K; experimental (blue) and simulation (red).

2.7 Nickel-Mediated Catalytic Reaction

The reactivity of $[\text{Ni}(\text{L-N}_4\text{Me}_2)(\text{MeCN})_2](\text{ClO}_4)_2$ (**1**) was evaluated for homocoupling reaction of phenylacetylene as a test substrate.

The reaction when conducted with catalytic quantity (10 mol%) of **1** and two equivalents of sodium hydride as base at room temperature under the oxygen atmosphere afforded 1,3-diyne (diphenyldiacetylene) in 78% yield (Scheme 2.14).

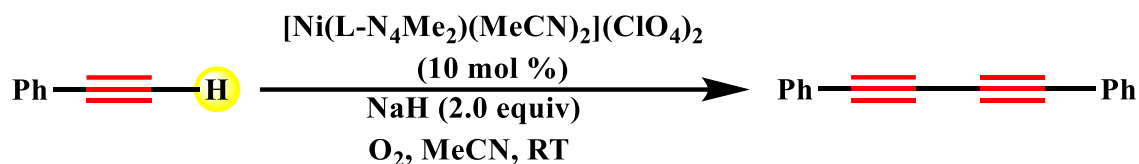


Scheme 2.14: Evaluation of **1** as catalyst.

It is important to mention that I did not observe diphenyldiacetylene formation neither in the presence of weak base like triethylamine, nor in the absence of it. These results suggest that there is no activation of terminal alkyne towards deprotonation by the coordination of C–C triple bond and nickel(II) species.

2.8 Spectroscopy Studies on Catalytic Reaction

To investigate the catalytic cycle and the intermediates involved in the aforesaid nickel-catalyzed homocoupling process, ESI-MS and EPR studies on the catalytic reaction mixture were carried out (Scheme 2.15).



Scheme 2.15: $[\text{Ni}(\text{L}-\text{N}_4\text{Me}_2)(\text{MeCN})_2](\text{ClO}_4)_2$ (**1**) catalyzed homocoupling reaction condition.

ESI mass spectrometry

To examine the catalytic reaction mixture by ESI-MS, one equivalent phenylacetylene, two equivalent NaH and $[\text{Ni}(\text{L}-\text{N}_4\text{Me}_2)(\text{MeCN})_2](\text{ClO}_4)_2$ (**1**) (10 mol%) was added in acetonitrile under oxygen atmosphere. The solution mixture was stirred for 5 min and then after microfiltration the mixture was injected to mass spectrometer for analysis.

ESI-MS spectrum is depicted in Figure 2.74. The spectrum shows signals due to ion peak at a m/z of 528.0, whose mass and isotope distribution pattern corresponds to $[\text{Ni}(\text{L}-\text{N}_4\text{Me}_2)(\text{PhC}_4\text{Ph})]^+$ (**4a**) (and Figure 2.75). ESI-MS spectrum also displays signals due to ion peaks corresponds to $[\{\text{Ni}(\text{L}-\text{N}_4\text{Me}_2)\}_2(\mu\text{-PhC}_4\text{Ph})]^{2+}$ (**2a**) ($m/z = 427.0$), $[\text{Ni}(\text{L}-\text{N}_4\text{Me}_2)(\text{O}_2)]^+$ (**5**) ($m/z = 357.9$) and $[\{\text{Ni}(\text{L}-\text{N}_4\text{Me}_2)\}_2(\text{O}_2)(\text{ClO}_4)]^+$ (**6**) ($m/z = 785.0$) with the predicted isotope patterns but with much smaller intensities as shown in *appendix* Figure 7.100 to Figure 7.103.

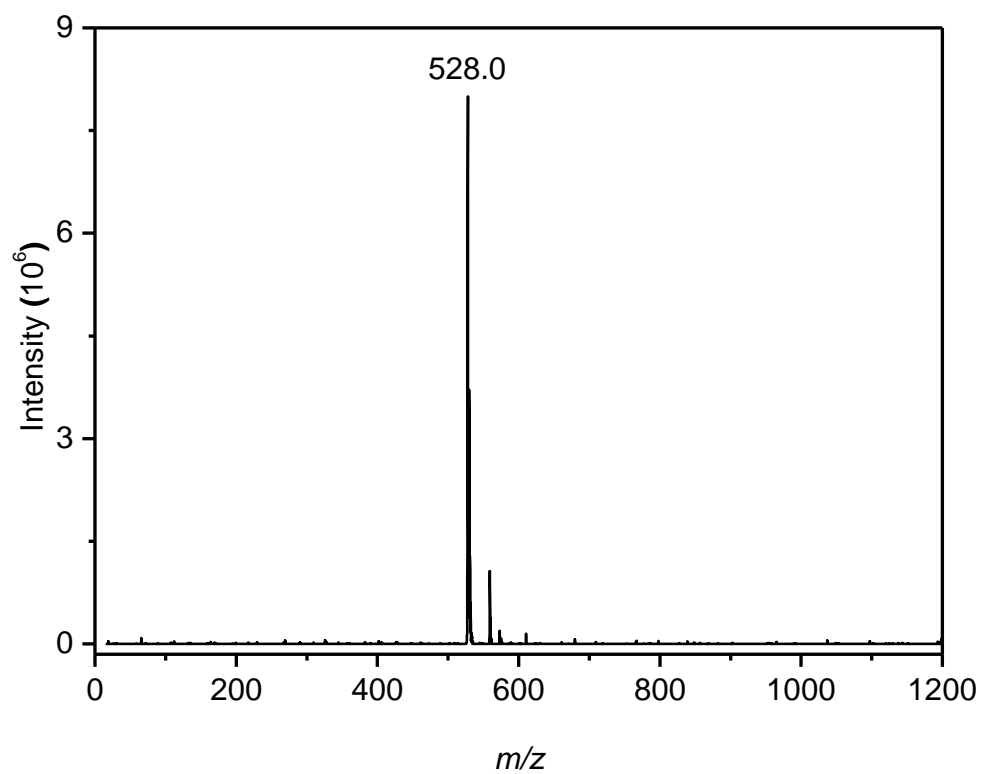


Figure 2.74: ESI-MS spectrum of catalytic reaction mixture in MeCN.

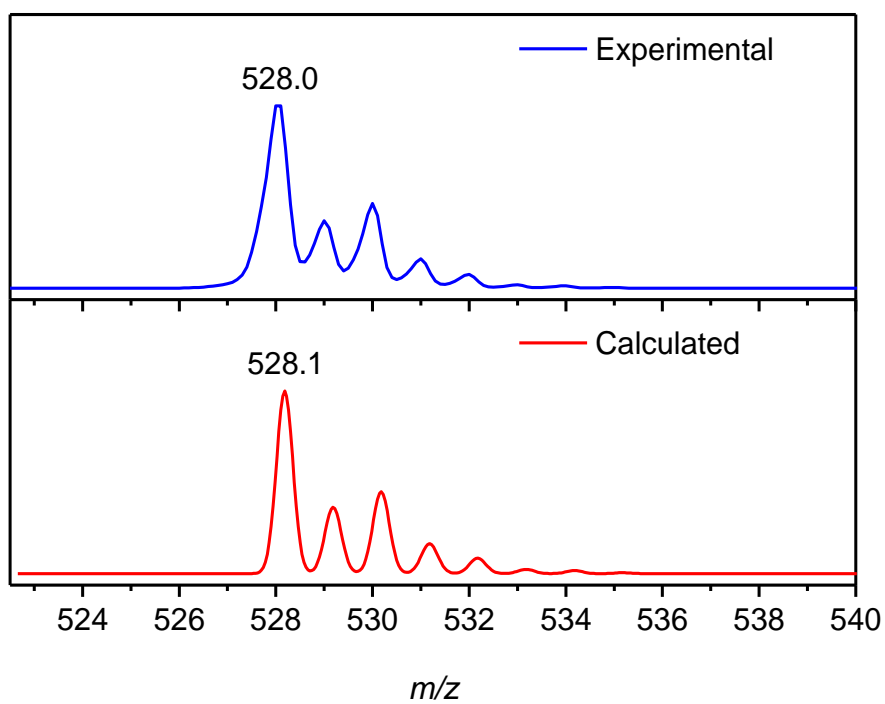


Figure 2.75: The experimental and calculated isotope distribution for [Ni(L-N₄Me₂)(PhC₄Ph)]⁺ (4a).

EPR Spectroscopy

To explore the catalytic reaction mixture by EPR spectroscopy, one equivalent phenylacetylene, two equivalent NaH and $[\text{Ni}(\text{L}-\text{N}_4\text{Me}_2)(\text{MeCN})_2](\text{ClO}_4)_2$ (**1**) (10 mol%) was added in 0.2 M TBAP acetonitrile solution under oxygen atmosphere. The solution mixture was stirred for 15 min. Aliquot from the reaction mixture was taken in a EPR tube and frozen in liquid nitrogen.

The EPR spectrum of the catalytic reaction mixture is depicted in Figure 2.76. The EPR analysis reveals a EPR signal indicating the presence of two EPR active species, $[\text{Ni}(\text{L}-\text{N}_4\text{Me}_2)(\text{PhC}_4\text{Ph})]^+$ (**4a**) and $[\text{Ni}(\text{L}-\text{N}_4\text{Me}_2)(\text{O}_2)]^+$ (**5**).

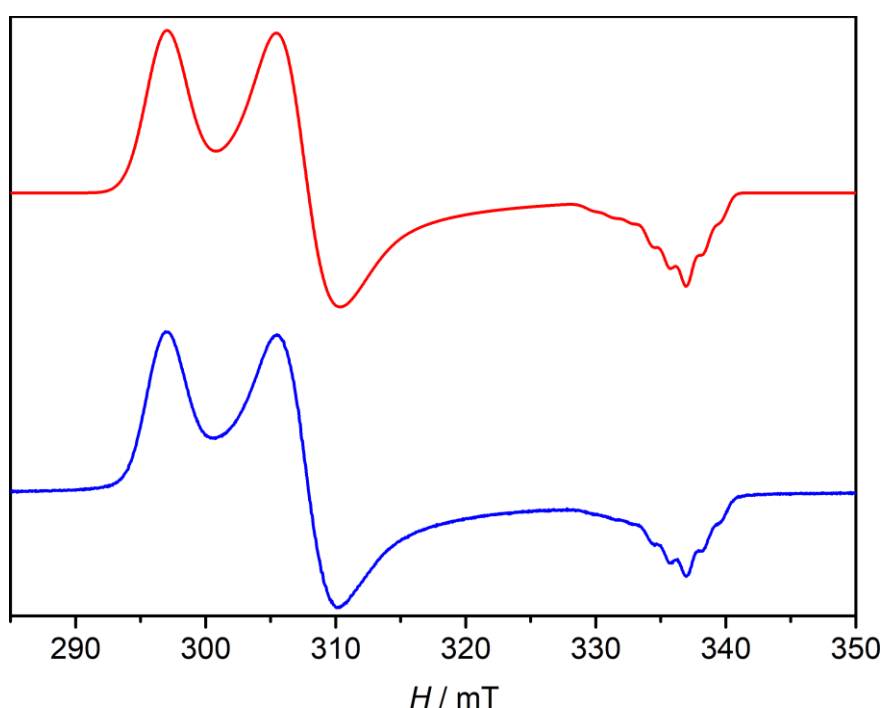
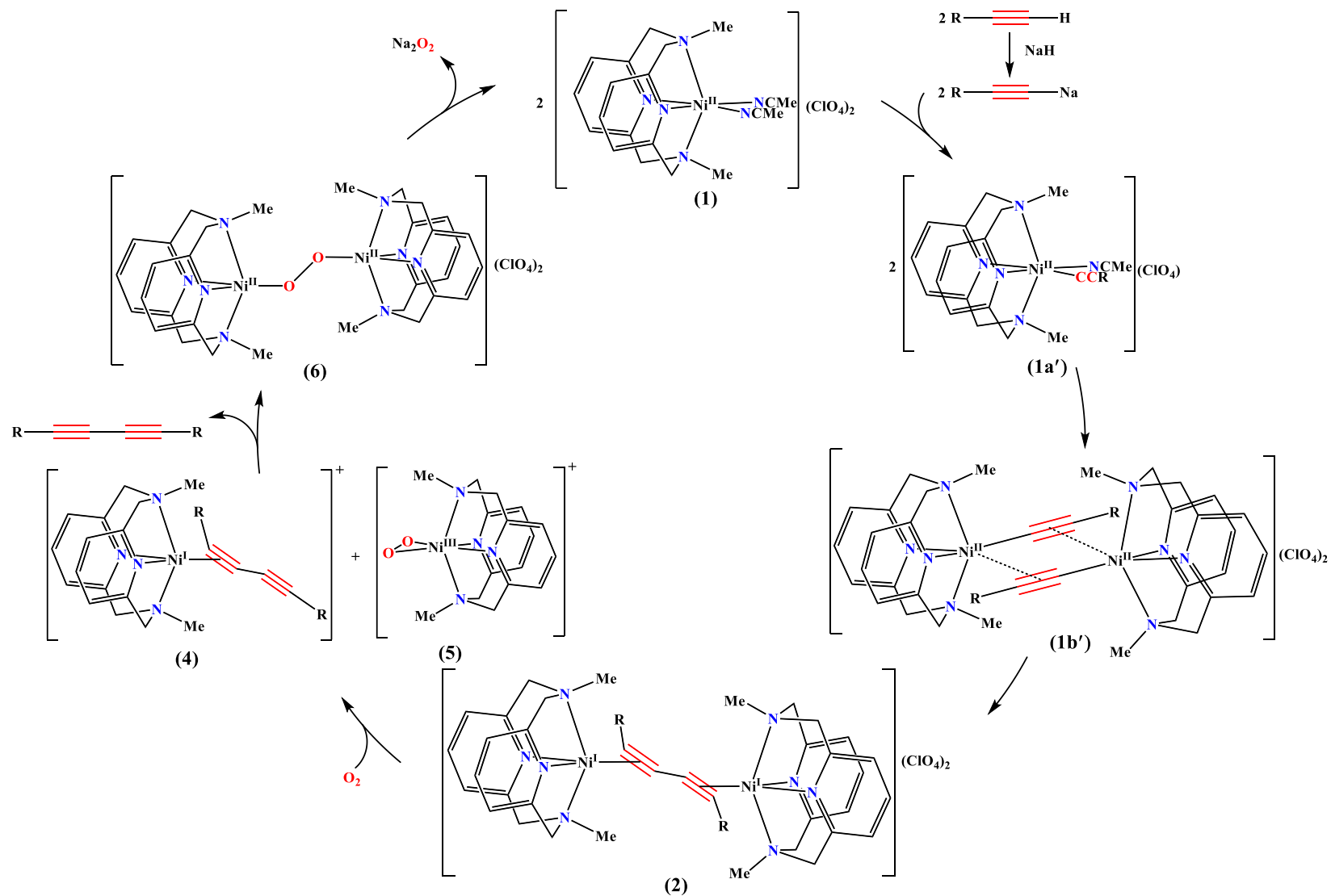


Figure 2.76: X-band EPR spectrum of the catalytic reaction mixture in 0.2 M TBAP/MeCN, measured at 77 K; experimental (blue) and simulation (red).

These results from the ESI-MS and EPR studies give evidence for the presence of $[\{\text{Ni}(\text{L}-\text{N}_4\text{Me}_2)\}_2(\mu\text{-RC}_4\text{R})](\text{ClO}_4)_2$ [R= Ph] (**2a**), $[\text{Ni}(\text{L}-\text{N}_4\text{Me}_2)(\text{PhC}_4\text{Ph})]^+$ (**4a**), $[\text{Ni}(\text{L}-\text{N}_4\text{Me}_2)(\text{O}_2)]^+$ (**5**) and $[\{\text{Ni}(\text{L}-\text{N}_4\text{Me}_2)\}_2(\text{O}_2)(\text{ClO}_4)]^+$ (**6**) complexes in the catalytic reaction mixture.

2.9 Proposed Mechanism

On the basis of experimental data obtained from both stoichiometric and catalytic reactions of nickel-mediated homocoupling reaction of terminal alkynes, the reaction mechanism is proposed as outlined in Scheme 2.16. The transmetalation reaction between complex $[\text{Ni}(\text{L-N}_4\text{Me}_2)(\text{MeCN})_2](\text{ClO}_4)_2$ (**1**) and sodium acetylide gives the mononuclear nickel(II) alkynyl complex (**1a'**). This is then converted to a dinuclear nickel(I)-diyne complex $[\{\text{Ni}(\text{L-N}_4\text{Me}_2)\}_2(\mu\text{-RC}_4\text{R})](\text{ClO}_4)_2$ (**2**) via the intermediacy of a dinuclear nickel(II) alkynyl species (**1b'**). In presence of oxygen, intermediate **2** is transformed to a mononuclear nickel(I)-diyne $[\text{Ni}(\text{L-N}_4\text{Me}_2)(\text{RC}_4\text{R})]^+$ (**4**) and nickel(III)-peroxo $[\text{Ni}(\text{L-N}_4\text{Me}_2)(\text{O}_2)]^+$ (**5**) species. Both these species (**4** and **5**) are readily converted to an unstable dinuclear nickel(II)-peroxo complex $[\{\text{Ni}(\text{L-N}_4\text{Me}_2)\}_2(\text{O}_2)(\text{ClO}_4)]^+$ (**6**) along with the concomitant release of 1,3-diyne (RC_4R). Complex **6** undergoes a solvent exchange with precipitation of sodium peroxide to give **1** which carries forward the catalytic cycle.



Scheme 2.16: Proposed mechanism for $[\text{Ni}(\text{L-NMe}_2)(\text{MeCN})_2](\text{ClO}_4)_2$ (**1**) catalyzed homocoupling reaction of terminal alkynes.

3 Summary

A detailed mechanistic aspect of the nickel-mediated homocoupling reaction of terminal alkynes is investigated through the isolation and characterization of key intermediates from both the stoichiometric and the catalytic reactions.

A series of dinuclear nickel(I)-diyne complexes bridged by a 1,3-diyne ligand is described. The complexes have been isolated from stoichiometric nickel(II)-mediated C-C bond formation reactions and thoroughly characterized by x-ray structure determination and other physical methods. The structure analyses of the complexes assign a distorted trigonal bipyramidal coordination geometry to each nickel(I) center with the ligand L-N₄Me₂ and alkyne group of 1,3-diyne ligand in side-on fashion.

The structural, magnetic, spectroscopic and theoretical investigations of these complexes confirm the formation of dinuclear nickel(I) π -diyne complex instead of nickel metallacyclopropene complex (Ni(III) with a [η^2 -alkenediyl]²⁻ ligand) with (dz²)¹ electronic ground state. The detailed magnetic investigations reveal strong antiferromagnetic coupling between the nickel centers via 1,3-diyne bridging ligand. The results of the magnetic investigations are expected to deliver valuable insights into diyne bridge-mediated exchange coupling as well as electron transfer between metal centers. The complexes not only represent as a key intermediate in nickel-mediated carbon carbon bond formation reaction of terminal alkynes, but also describe the first structurally characterized dinuclear nickel(I)-diyne complexes. In addition, the complexes constitute important addition to the family of structurally well characterized nickel(I) complexes.

The influence of substituents to the diyne ligand on structural, magnetic, electronic properties of the dinuclear nickel(I)-diyne complexes has been investigated. These studies provide important insights into the nature of interaction between nickel center and diyne ligands.

Radical trapping and low temperature UV-Vis-NIR experiments in the formation of the dinuclear nickel(I)-diyne confirm that the reactions occurring during the reduction of nickel(II) to nickel(I) and C-C bond formation of diyne follow non-radical concerted mechanism. Nevertheless, question regarding mechanistic details like formation of the mononuclear nickel(II)-alkynyl and/or dinuclear nickel(II)-alkynyl intermediates remains open.

The reactivity of dinuclear nickel(I)-diyne complex $[\{\text{Ni}(\text{L-N}_4\text{Me}_2)_2(\mu\text{-RC}_4\text{R})\}(\text{ClO}_4)_2]$ [R= Ph] (**2a**) with molecular oxygen has been investigated. The reaction yields a mononuclear nickel(I)-diyne complex $[\text{Ni}^{\text{I}}(\text{L-N}_4\text{Me}_2)(\text{PhC}_4\text{Ph})]^+$ (**4a**) and a mononuclear nickel(III)-peroxo species $[\text{Ni}^{\text{III}}(\text{L-N}_4\text{Me}_2)(\text{O}_2)]^+$ (**5**), which are converted to free diphenyldiacetylene and an unstable dinuclear nickel(II) species $[\{\text{Ni}^{\text{II}}(\text{L-N}_4\text{Me}_2)\}_2(\text{O}_2)(\text{ClO}_4)]^+$ (**6**). These species represent important key intermediates in nickel-mediated homocoupling reaction of terminal alkynes using oxygen as oxidant. The mononuclear nickel(I)-alkyne complex $[\text{Ni}(\text{L-N}_4\text{Me}_2)(\text{PhC}_2\text{Ph})](\text{ClO}_4) \cdot \text{MeOH}$ (**3**) has been isolated and well characterized, whose spectroscopic properties further confirm the formulation of $[\text{Ni}^{\text{I}}(\text{L-N}_4\text{Me}_2)(\text{PhC}_4\text{Ph})]^+$ (**4a**). Generation and spectroscopic characterization of $[\text{Ni}^{\text{III}}(\text{L-N}_4\text{Me}_2)(\text{O}_2)]^+$ (**5**) species is also described. The results from the reaction of nickel(I)-diyne complex and oxygen portend the opportunity to further explore and define nickel-O₂ chemistry, which is a subject of considerable current interest due to its practical importance in industrial and biological oxidation reactions.

Nickel-catalyzed homocoupling of phenylacetylene with catalytic amounts of $[\text{Ni}(\text{L-N}_4\text{Me}_2)(\text{MeCN})_2](\text{ClO}_4)_2$ (**1**) employing oxygen as oxidant at room temperature is investigated. Spectroscopic experiments on the catalytic reaction mixture confirms the presence of $[\{\text{Ni}(\text{L-N}_4\text{Me}_2)\}_2(\mu\text{-RC}_4\text{R})](\text{ClO}_4)_2$ [R= Ph] (**2a**), $[\text{Ni}^{\text{I}}(\text{L-N}_4\text{Me}_2)(\text{PhC}_4\text{Ph})]^+$ (**4a**), $[\text{Ni}^{\text{III}}(\text{L-N}_4\text{Me}_2)(\text{O}_2)]^+$ (**5**) and $[\{\text{Ni}^{\text{II}}(\text{L-N}_4\text{Me}_2)\}_2(\text{O}_2)(\text{ClO}_4)]^+$ (**6**) complexes as intermediates. Results of both stoichiometric and catalytic reactions suggested the mechanism involving nickel(II)/nickel(I)/nickel(III) oxidation states. These findings are expected to open a new paradigm towards nickel catalyzed organic transformations.

4 Experimental Section

4.1 Physical Methods

The elemental analyses (C, H and N) were carried out from the department of Organic Chemistry at the Technische Universität Kaiserslautern with elemental analyzer Vario MICRO cube from Elementar Analysensysteme GmbH.

The IR spectra were recorded on a FT / IR-4100 spectrometer from Jasco. The substances were measured as KBr pellet. Only the most intense bands are given.

The NMR spectra were recorded on the devices Avance DPX 400 and Avance DPX 600 from Bruker. The chemical shift is indicated by the δ scale in ppm. The signals of the residual protons (^1H) or carbons (^{13}C) atom in the deuterated solvents were used as the internal standard.^[159] The spectra were evaluated using the program TopSpin 3.1 from Bruker.

Electronic absorption spectra were recorded on a Varian Cary 5000 UV-Vis-NIR spectrometer. For low temperature measurements, Unisoku UnispeKs cryostat was used.

Electrochemical experiments were performed in 0.2 M solution of TBAP in acetonitrile using a potentiostat/galvanostat 273 A of Princeton Applied Research and a platinum foil as working electrode, a platinum net as counter electrode and a saturated calomel electrode as the reference electrode. The ferrocene/ferrocenium redox couple served as the internal reference (+0.42 V vs. SCE).

EPR measurements were carried out with a Bruker Elexsys 580 X-Band spectrometer equipped with a Bruker ER 4122 SHQE resonator in combination with an Oxford Instruments ESR 900 continuous flow cryostat controlled by an Oxford Instruments ITC 503 temperature control device. The simulation of the ESR spectra were carried out with help of Prof. H.-J. Krüger, Ph.D. from the department of Inorganic Chemistry at Technische Universität Kaiserslautern using the program EasySpin version 5.1.8.^[160]

The ESI-MS were carried out from the department of Physical Chemistry at Technische Universität Kaiserslautern. It was performed using a Paul-type quadrupole ion trap instrument (Bruker Esquire 3000plus) and data analysis was performed using Bruker Data Analysis 3.4 software.

The X-ray structure analyses were carried out by Dr. H. Kelm from the department of Inorganic Chemistry at Technische Universität Kaiserslautern with the devices Stoe IPDS and Oxford Diffraction Gemini S Ultra. The program SIR97 was used to solve the recorded data.^[161] Structural refinements were made using SHELXL-97.^[162]

DFT calculations were carried out by Prof. Dr. C. Van Wüllen from the department of Physical and Theoretical Chemistry at Technische Universität Kaiserslautern.

Raman measurement was carried out by Dr. M. Schmitz, group member of Prof. H.-J. Krüger, Ph.D. from the department of Inorganic Chemistry at Technische Universität Kaiserslautern using LabRam HR 800 UV Horiba Jobin-Yvon equipped with microscope BX41 Olympus (laser excitation wavelength: 784 nm).

Susceptibility measurement was carried out with a Quantum-Design MPMS-5S SQUID by Dr. S. Demeshko, group member of Prof. Dr. F. Meyer of the Institute of Inorganic Chemistry at the Georg-August-University Göttingen. SQUID magnetometer equipped with a 5 T magnet in the range from 298 to 2.0 K. The powdered sample was contained in a gel bucket and fixed in a nonmagnetic sample holder. The raw data file for the measured magnetic moment was corrected for the diamagnetic contribution of the sample holder and the gel bucket. The molar susceptibility was corrected by using Pascal's constants and the increment method. Experimental data for complexes were modelled by using a fitting procedure to the appropriate Heisenberg–Dirac–van-Vleck (HDvV) spin Hamiltonian for isotropic exchange coupling and Zeeman splitting [Equation (1)].^[163]

$$\hat{H} = -2J\hat{S}_1\hat{S}_2 + g\mu_B(\hat{S}_1 + \hat{S}_2)B \quad (1)$$

A temperature-independent paramagnetism (*TIP*) and a Curie-behaved paramagnetic impurity (*PI*) with spin $S = 1/2$ were included according to $\chi_{\text{calc}} = (1 - PI)\chi + PI\chi_{\text{mono}} + \chi_{\text{TIP}}$.

Simulation of the experimental magnetic data with full-matrix diagonalisation of exchange coupling and Zeeman splitting was performed with the julX program. TIP and PI values are listed in *appendix* Table 7.10

4.2 Starting Materials

ABCR: *p*-Fluorophenylacetylene, Nickel(II) perchlorate hexahydrate

Acros Organics: ⁿButyllithium (2.5M in hexane), Calcium hydride, Diphenylacetylene, Ferrocenylacetylene, 1-Pentyne, Phenylacetylene, Potassium bromide, Potassium superoxide, Propionitrile, Sodium, TEMPO ((2,2,6,6-tetramethylpiperidin-1-yl)oxidanyl), *p*-Tolylacetylene

Deutero: Chloroform-d

euriso-top: Chloroform-d, Methanol-d₄

Fisher Chemicals: Acetonitrile, Methanol, Tetrahydrofuran

Fluka Chemika: Lithium perchlorate

Maybridge: *p*-Methoxyphenylacetylene

Sigma-Aldrich: *p*-Dimethylaminophenylacetylene, Propionitrile

Laboratory Stock without manufacturer specification (Obtained from the chemical store of the department of chemistry of Technische Universität Kaiserslautern):

Acetone, Diethyl ether, Ethanol, Methanol (tech.), Pentane, Petroleum ether (40-60)

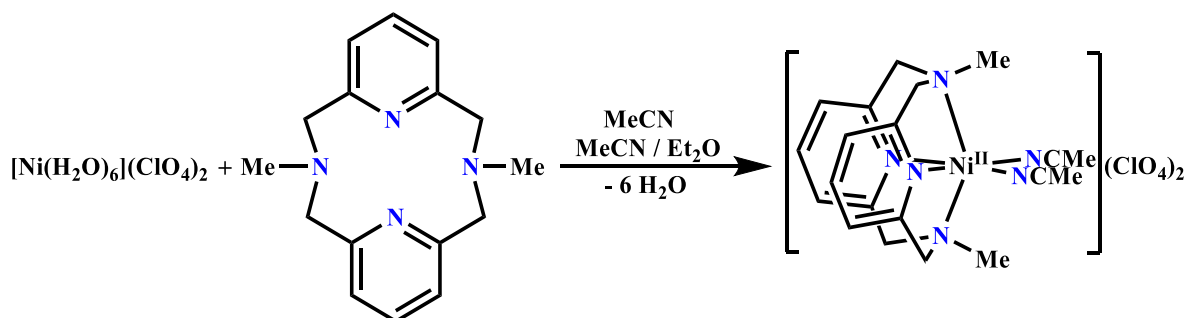
Laboratory Stock without manufacturer specification: Ferrocene, Tetrabutylammonium perchlorate (TBAP)

In addition, the following starting compound was prepared according to the stated literature procedures:

N,N'-Dimethyl-2,11-diaza[3.3](2,6)pyridinophan (L-N₄Me₂) (modified)^[164]

4.3 Experimental Details

4.3.1 Synthesis of $[\text{Ni}(\text{L-N}_4\text{Me}_2)(\text{MeCN})_2](\text{ClO}_4)_2$ (**1**)



The complex $[\text{Ni}(\text{L-N}_4\text{Me}_2)(\text{MeCN})_2](\text{ClO}_4)_2$ (**1**) was synthesized according to the modified literature procedure.^[108] Under air, a solution of L-N₄Me₂ (270 mg, 1 mmol) in acetonitrile (20 mL) was slowly added to a solution of Ni(ClO₄)₂·6H₂O (365 mg, 1 mmol) in acetonitrile (20 mL). The violet reaction mixture was then heated for a short time to reflux temperature and then allowed to cool to room temperature. The volume of the solution was reduced to approximately 15 mL. After slow diffusion of diethyl ether into the solution, analytically pure product $[\text{Ni}(\text{L-N}_4\text{Me}_2)(\text{MeCN})_2](\text{ClO}_4)_2$ (**1**) was obtained as violet crystals.

Yield: 511 mg (0.84 mmol, 84%); MW (C₂₀H₂₆N₆Cl₂NiO₈) = 608.06 g·mol⁻¹.

Characterization

Elemental analysis: Calculated: C = 39.51 % H = 4.31 % N = 13.82 %

Found: C = 39.44 % H = 4.34 % N = 13.78 %

IR (KBr Pellet): $\tilde{\nu}$ = 3086, 3004, 2976, 2936, 2824, 2313, 2285, 2012, 1608, 1585, 1478, 1454, 1380, 1304, 1268, 1220, 1167, 1093, 1032, 1003, 870, 797, 761, 694 and 623 cm⁻¹.

ESI-MS (Acetonitrile solution):

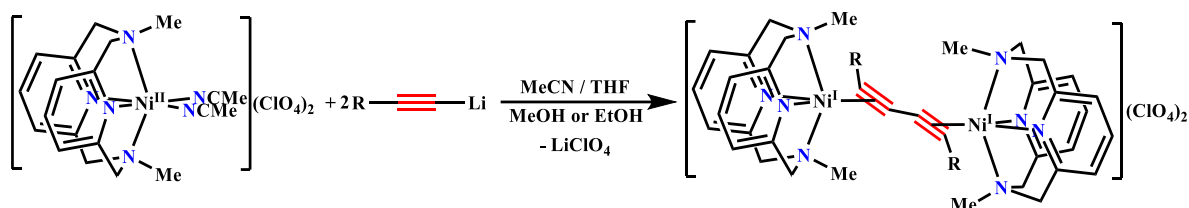
m/z = Calculated for $[\text{Ni}(\text{L-N}_4\text{Me}_2)(\text{ClO}_4)]^+$: 425.0; Found: 424.9.

Calculated for $[\text{Ni}(\text{L-N}_4\text{Me}_2)]^{2+}$: 163.0; Found: 162.9.

UV-Vis-NIR (Acetonitrile solution, Room temperature):

λ_{max} (ϵ_{M}) = 261 (7274), 339 (315), 516 (9.1), 816 (sh, 24.0) and 920 (28.2) nm (M⁻¹cm⁻¹).

4.3.2 Synthesis of $[\{Ni(L-N_4Me_2)\}_2(\mu-R_2C_2R)](ClO_4)_2$ (**2a-2g**)



Under pure nitrogen atmosphere, a solution of terminal alkyne (0.5 mmol) in absolute THF (10 mL) was cooled to $-78\text{ }^{\circ}\text{C}$. A solution of $n\text{BuLi}$ (200 μL , 2.5 M) in hexane was carefully added dropwise to the cooled solution of terminal alkyne. The resulting mixture was stirred for 0.5 h and then allowed to warm to room temperature. The mixture was stirred for an additional 1 h to give a pale yellow (for **2a-2f**) or orange (for **2g**) solution. The *in situ* generated lithium acetylide was then transferred to another flask containing $[Ni(L-N_4Me_2)(MeCN)_2](ClO_4)_2$ (**1**) (152.0 mg, 0.25 mmol) dissolved in dry acetonitrile (30 mL) via cannula. The color of the mixture changed from violet to dark brown. The solution was stirred for 2 h. After removing the volatiles, a dark residue obtained was dissolved in a minimum volume of methanol (**2a-2b**) or ethanol (for **2c-2g**). The solution was refluxed shortly, cooled to room temperature, and allowed to stand for 2-3 days to afford analytically pure, crystalline product $[\{Ni(L-N_4Me_2)\}_2(\mu-R_2C_2R)](ClO_4)_2$. The yield can be enhanced by a further reduction of the volume of the mother liquid and additional storage of it.

$[\{Ni(L-N_4Me_2)\}_2(\mu-R_2C_2R)](ClO_4)_2$ [**R = Ph**] (**2a**):

From phenylacetylene (55 μL , 0.5 mmol) a total yield of 87 mg (0.082 mmol, 66%) of crystalline dark brown product was obtained.

Yield: 87 mg (0.082 mmol, 66%); MW ($C_{48}H_{50}N_8Cl_2Ni_2O_8$) = $1055.28\text{ g}\cdot\text{mol}^{-1}$.

Characterization

Elemental analysis: Calculated: C = 54.63 % H = 4.78 % N = 10.62 %

Found: C = 54.49 % H = 4.48 % N = 10.64 %

IR (KBr Pellet):

$\tilde{\nu} = 2970, 2904, 2814, 1809, 1606, 1579, 1479, 1444, 1375, 1165, 1134, 1093, 1012, 870, 794, 760, 694, 634$ and 621 cm^{-1} .

ESI-MS (Acetonitrile solution):

m/z = Calculated for $[\{\text{Ni}(\text{L-N}_4\text{Me}_2)\}_2(\mu\text{-PhC}_4\text{Ph})(\text{ClO}_4)]^+$: 955.2; Found: 955.0.

Calculated for $[\text{Ni}(\text{L-N}_4\text{Me}_2)(\text{PhC}_4\text{Ph})]^+$: 528.1; Found: 528.2.

UV-Vis-NIR (Acetonitrile solution, Room temperature):

λ_{max} (ϵ_{M}) = 253 (42460), 286 (sh, 26230), 304 (22660), 325 (18310), 379 (21434), 554 (sh, 808), 690 (sh, 146) and 1205 (91) nm ($\text{M}^{-1} \text{cm}^{-1}$)

$[\{\text{Ni}(\text{L-N}_4\text{Me}_2)\}_2(\mu\text{-RC}_4\text{R})(\text{ClO}_4)_2$ [$\text{R} = \text{C}_6\text{H}_4\text{Me-4}$] (2b**):**

From *p*-tolylacetylene (64 μL , 0.5 mmol) a total yield of 85 mg (0.078 mmol, 62%) of crystalline dark brown product was achieved.

Yield: 85 mg (0.078 mmol, 62%); MW ($\text{C}_{50}\text{H}_{54}\text{N}_8\text{Cl}_2\text{Ni}_2\text{O}_8$) = 1083.30 $\text{g}\cdot\text{mol}^{-1}$.

Characterization

Elemental analysis: Calculated: C = 55.44 % H = 5.02 % N = 10.34 %

Found: C = 55.17 % H = 5.16 % N = 10.25 %

IR (KBr Pellet):

$\tilde{\nu}$ = 2964, 2906, 2875, 2813, 1813, 1604, 1579, 1473, 1444, 1377, 1132, 1093, 1012, 872, 821, 791 and 623 cm^{-1} .

ESI-MS (Acetonitrile solution):

m/z = Calculated for $[\{\text{Ni}(\text{L-N}_4\text{Me}_2)\}_2(\mu\text{-RC}_4\text{R})(\text{ClO}_4)]^+$: 983.3; Found: 983.0.

Calculated for $[\text{Ni}(\text{L-N}_4\text{Me}_2)(\text{RC}_4\text{R})]^+$: 556.2; Found: 556.1.

Calculated for $[\{\text{Ni}(\text{L-N}_4\text{Me}_2)\}_2(\mu\text{-RC}_4\text{R})]^{2+}$: 441.2; Found: 441.1.

Calculated for $[\text{Ni}(\text{L-N}_4\text{Me}_2)]^+$: 326.1; Found: 325.9.

UV-Vis-NIR (Acetonitrile solution, Room temperature):

$\lambda_{\max} (\epsilon_M) = 253 (42285), 291(\text{sh}, 27724), 309 (\text{sh}, 23415), 330 (\text{sh}, 18511), 379 (20907), 558 (\text{sh}, 769), 747 (\text{sh}, 99) \text{ and } 1210 (87) \text{ nm } (\text{M}^{-1} \text{ cm}^{-1}).$

[[Ni(L-N₄Me₂)]₂(μ -RC₄R)](ClO₄)₂ [R = C₆H₄Me-4] (2c):

From *p*-fluorophenylacetylene (58 μ L, 0.5 mmol) a total yield of 88 mg (0.081 mmol, 65 %) of crystalline dark brown product was obtained.

Yield: 88 mg (0.081 mmol, 65 %); MW (C₄₈H₄₈N₈Cl₂Ni₂O₈F₂) = 1091.23 g.mol⁻¹.

Elemental analysis: Calculated: C = 52.83 % H = 4.43 % N = 10.27 %

Found: C = 52.82 % H = 4.64 % N = 10.28 %

Characterization

IR (KBr Pellet):

$\tilde{\nu} = 2966, 2908, 2878, 2815, 1808, 1606, 1592, 1493, 1475, 1445, 1378, 1222, 1151, 1119, 1095, 1012, 871, 843, 794 \text{ and } 623 \text{ cm}^{-1}$

ESI-MS (Acetonitrile solution):

$m/z =$ Calculated for [[Ni(L-N₄Me₂)]₂(μ -RC₄R)](ClO₄)⁺: 991.2; Found: 990.9.

Calculated for [Ni(L-N₄Me₂)(RC₄R)]⁺: 564.2; Found: 564.0.

Calculated for [[Ni(L-N₄Me₂)]₂(μ -RC₄R)]²⁺: 445.1; Found: 445.0.

Calculated for [Ni(L-N₄Me₂)]⁺: 326.1; Found: 325.9.

UV-Vis-NIR (Acetonitrile solution, Room temperature):

$\lambda_{\max} (\epsilon_M) = 252 (37313), 273 (\text{sh}, 25349), 306 (\text{sh}, 20629), 377 (21572), 550 (\text{sh}, 784), 750 (\text{sh}, 85) \text{ and } 1202 (87) \text{ nm } (\text{M}^{-1} \text{ cm}^{-1})$

[[Ni(L-N₄Me₂)]₂(μ -RC₄R)](ClO₄)₂ [R = C₆H₄OMe-4] (2d):

From *p*-methoxyphenylacetylene (65 μ L, 0.5 mmol) a total yield of 78 mg (0.070 mmol, 56 %) of crystalline dark brown product was isolated.

Yield: 78 mg (0.070 mmol, 56%); MW ($C_{50}H_{54}N_8Cl_2Ni_2O_{10}$) = 1115.33 g.mol⁻¹.

Characterization

Elemental analysis: Calculated: C = 53.85 % H = 4.88 % N = 10.05 %

Found: C = 54.11 % H = 4.96 % N = 10.14 %

IR (KBr Pellet):

$\tilde{\nu}$ = 2959, 2909, 2877, 2813, 1810, 1597, 1579, 1499, 1474, 1444, 1376, 1285, 1250, 1218, 1161, 1095, 1025, 1014, 871, 837, 793, 758, 623 and 580 cm⁻¹

ESI-MS (Acetonitrile solution):

m/z = Calculated for $[{\{Ni(L-N_4Me_2)\}_2(\mu-R_4R)}(ClO_4)]^+$: 1013.3; Found: 1013.0.

Calculated for $[Ni(L-N_4Me_2)(R_4R)]^+$: 588.2; Found: 588.1.

Calculated for $[{\{Ni(L-N_4Me_2)\}_2(\mu-R_4R)}]^{2+}$: 457.2; Found: 457.1.

Calculated for $[Ni(L-N_4Me_2)]^+$: 326.1; Found: 325.9.

UV-Vis-NIR (Acetonitrile solution, Room temperature):

λ_{max} (ϵ_M) = 252 (39290), 282 (sh, 33373), 313 (sh, 27015), 382 (26956), 563 (sh, 754), 760 (sh, 95) and 1226 (89) nm (M⁻¹ cm⁻¹).

$[{\{Ni(L-N_4Me_2)\}_2(\mu-R_4R)}](ClO_4)_2$ [R = C₆H₄NMe₂-4] (2e):

From *p*-dimethylaminophenylacetylene (72.6 mg, 0.5 mmol) a total yield of 82 mg (0.072 mmol, 57 %) of crystalline dark brown product was obtained.

Yield: 82 mg (0.072 mmol, 57%); MW ($C_{52}H_{60}N_{10}Cl_2Ni_2O_8$) = 1141.40 g.mol⁻¹.

Characterization:

Elemental analysis: Calculated: C = 54.72 % H = 5.30 % N = 12.27 %

Found: C = 55.02 % H = 5.32 % N = 12.13 %

IR (KBr Pellet):

$\tilde{\nu} = 2963, 2895, 2813, 1806, 1601, 1513, 1474, 1444, 1361, 1285, 1250, 1226, 1161, 1092, 1013, 945, 871, 817, 794, 758$ and 623 cm^{-1} .

ESI-MS (Acetonitrile solution):

$m/z =$ Calculated for $[\{\text{Ni}(\text{L-N}_4\text{Me}_2)\}_2(\mu\text{-RC}_4\text{R})(\text{ClO}_4)]^+$: 1041.3; Found: 1041.1.

Calculated for $[\text{Ni}(\text{L-N}_4\text{Me}_2)(\text{RC}_4\text{R})]^+$: 614.3; Found: 614.2.

Calculated for $[\{\text{Ni}(\text{L-N}_4\text{Me}_2)\}_2(\mu\text{-RC}_4\text{R})]^{2+}$: 470.2; Found: 470.1.

Calculated for $[\text{Ni}(\text{L-N}_4\text{Me}_2)]^+$: 326.1; Found: 325.9.

UV-Vis-NIR (Acetonitrile solution, Room temperature):

$\lambda_{\text{max}} (\epsilon_{\text{M}}) = 237$ (sh, 42416), 254 (sh, 37569), 324 (38288), 402 (35180), 575 (sh, 823), 771 (sh, 117) and 1255 (81) nm ($\text{M}^{-1} \text{ cm}^{-1}$).

$[\{\text{Ni}(\text{L-N}_4\text{Me}_2)\}_2(\mu\text{-RC}_4\text{R})(\text{ClO}_4)_2$ [$\text{R} = \text{}^n\text{C}_3\text{H}_7$] (2f):

From 1-pentyne (50 μL , 0.5 mmol) a total yield of 80 mg (0.081 mmol, 65 %) of crystalline dark brown product was obtained.

Yield: 80 mg (0.081 mmol, 65 %); MW ($\text{C}_{48}\text{H}_{50}\text{N}_8\text{Cl}_2\text{Ni}_2\text{O}_8$) = 987.22 $\text{g}\cdot\text{mol}^{-1}$.

Characterization

Elemental analysis: Calculated: C = 51.10 % H = 5.51 % N = 11.35 %

Found: C = 50.97 % H = 5.73 % N = 11.36 %

IR (KBr Pellet):

$\tilde{\nu} = 2965, 2921, 2872, 2817, 1855, 1605, 1582, 1473, 1447, 1378, 1162, 1120, 1099, 1014, 870, 821, 792, 757$ and 623 cm^{-1} .

ESI-MS (Acetonitrile solution):

$m/z =$ Calculated for $[\text{Ni}(\text{L-N}_4\text{Me}_2)(\text{RC}_4\text{R})]^+$: 460.1; Found: 460.0.

Calculated for $[\text{Ni}(\text{L-N}_4\text{Me}_2)]^+$: 326.1; Found: 325.9.

UV-Vis-NIR (Acetonitrile solution, Room temperature):

$\lambda_{\text{max}} (\epsilon_{\text{M}}) = 251 (24818), 316 (\text{sh}, 7411), 386 (7200), 558 (\text{sh}, 506), 794 (\text{sh}, 98) \text{ and } 1281 (73) \text{ nm } (\text{M}^{-1} \text{ cm}^{-1})$.

$[\{\text{Ni}(\text{L-N}_4\text{Me}_2)\}_2(\mu\text{-RC}_4\text{R})](\text{ClO}_4)_2 [\text{R} = \text{Fc}] \cdot \text{EtOH} (2\text{g})$:

From ferrocenylacetylene (72.6 mg, 0.5 mmol) a total yield of 102 mg (0.077 mmol, 61 %) of crystalline brown product was obtained.

Yield: 102 mg (0.077 mmol, 61 %); MW ($\text{C}_{58}\text{H}_{64}\text{N}_8\text{Cl}_2\text{Ni}_2\text{Fe}_2\text{O}_9$) = 1317.19 $\text{g}\cdot\text{mol}^{-1}$.

Characterization

Elemental analysis: Calculated: C = 52.89 % H = 4.90 % N = 8.51 %

Found: C = 52.84 % H = 4.98 % N = 8.45 %

IR (KBr Pellet):

$\tilde{\nu} = 3088, 2916, 2814, 1820, 1604, 1579, 1472, 1444, 1375, 1303, 1213, 1162, 1096, 1012, 870, 828, 792 \text{ and } 623 \text{ cm}^{-1}$

ESI-MS (Acetonitrile solution):

$m/z =$ Calculated for $[\{\text{Ni}(\text{L-N}_4\text{Me}_2)\}_2(\mu\text{-RC}_4\text{R})(\text{ClO}_4)]^+$: 1171.1; Found: 1171.0.

Calculated for $[\text{Ni}(\text{L-N}_4\text{Me}_2)(\text{RC}_4\text{R})]^+$: 744.1; Found: 743.9.

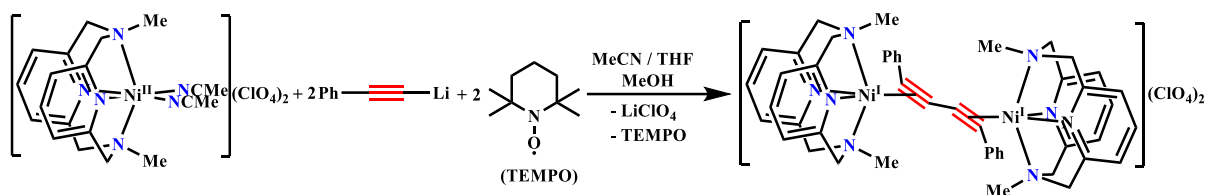
Calculated for $[\{\text{Ni}(\text{L-N}_4\text{Me}_2)\}_2(\mu\text{-RC}_4\text{R})]^{2+}$: 535.1; Found: 534.9.

Calculated for $[\text{Ni}(\text{L-N}_4\text{Me}_2)]^+$: 326.1; Found: 325.9.

UV-Vis-NIR (Acetonitrile solution, Room temperature):

$\lambda_{\text{max}} (\epsilon_{\text{M}}) = 254 (32799), 282 (21742), 374 (18507), 610 (\text{sh}, 532), 770 (\text{sh}, 107) \text{ and } 1255 (75) \text{ nm } (\text{M}^{-1} \text{ cm}^{-1})$.

4.3.3 Stoichiometric Reaction in Presence of Radical Inhibitor TEMPO



Under pure nitrogen atmosphere, a solution of phenylacetylene (55 μL , 0.5 mmol) in absolute THF (10 mL) was cooled to $-78\text{ }^{\circ}\text{C}$. A solution of ${}^n\text{BuLi}$ (200 μL , 2.5 M) in hexane was carefully added dropwise to the cooled solution of phenylacetylene. The resulting mixture was stirred for 0.5 h and then allowed to warm to room temperature. The mixture was stirred for an additional 1 h to give a pale-yellow solution. The *in situ* generated lithium phenylacetylide was then transferred to another flask containing $[\text{Ni}(\text{L}-\text{N}_4\text{Me}_2)(\text{MeCN})_2](\text{ClO}_4)_2$ (152.0 mg, 0.25 mmol) and TEMPO ((2,2,6,6-tetramethylpiperidin-1-yl)oxidanyl) (78.1 mg, 0.5 mmol) dissolved in dry acetonitrile (30 mL) via cannula. The color of the mixture changed from orange to dark brown. The solution was stirred for 2 h. After removing the volatiles, a dark residue obtained was dissolved in a minimum volume of methanol. The solution was refluxed shortly, cooled to room temperature, and allowed to stand for 2-3 days to give dark brown crystals. The second crop could be obtained by reducing the volume of the mother liquor and leaving the solution for another few days at room temperature. A total amount of 88 mg (0.083 mmol, 67%) of dark brown crystalline product $[\{\text{Ni}(\text{L}-\text{N}_4\text{Me}_2)\}_2(\mu\text{-RC}_4\text{R})](\text{ClO}_4)_2$ [R = Ph] (**2a**) was obtained.

Yield: 88 mg (0.083 mmol, 67%); MW ($\text{C}_{48}\text{H}_{50}\text{N}_8\text{Cl}_2\text{Ni}_2\text{O}_8$) = $1055.25\text{ g}\cdot\text{mol}^{-1}$

Characterization

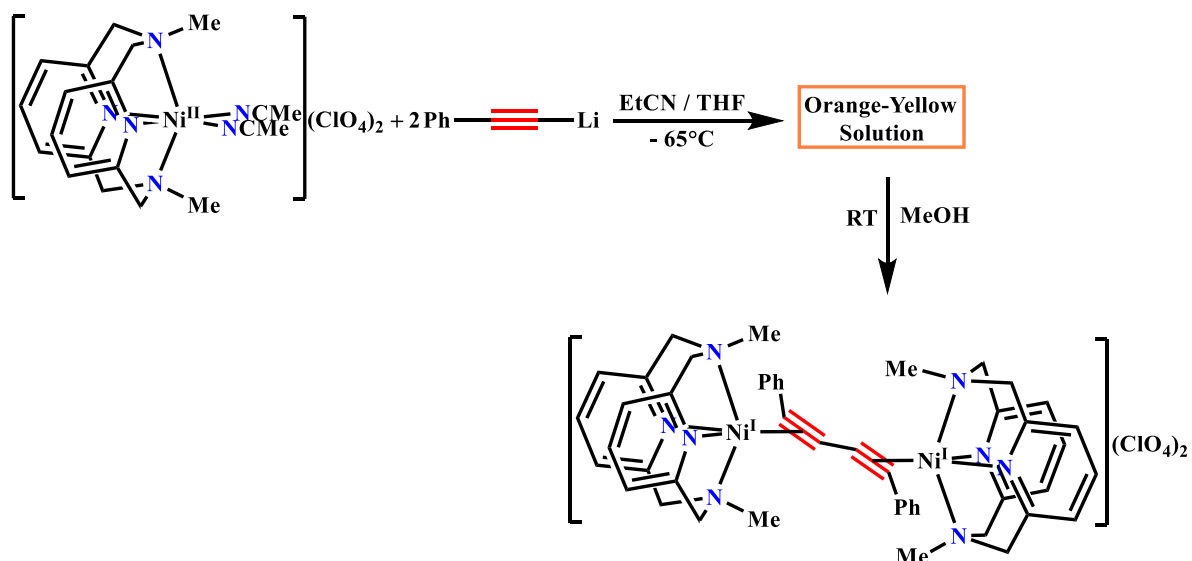
Elemental analysis: Calculated: C = 54.63 % H = 4.78 % N = 10.62 %

Found: C = 54.42 % H = 4.61 % N = 10.55 %

IR (KBr Pellet):

$\tilde{\nu} = 2970, 2904, 2814, 1810, 1605, 1579, 1478, 1445, 1376, 1163, 1134, 1091, 1012, 870, 794, 760, 694, 634$ and 622 cm^{-1} .

4.3.4 Stoichiometric Reaction at Low Temperature to Room Temperature



Under pure nitrogen atmosphere, a solution of phenylacetylene (55 μL , 0.5 mmol) in absolute THF (10 mL) was cooled to -78°C . A solution of $^n\text{BuLi}$ (200 μL , 2.5 M) in hexane was carefully added dropwise to the cooled solution of phenylacetylene. The resulting mixture was stirred for 0.5 h and then allowed to warm to room temperature. The mixture was stirred for an additional 1 h to give a pale yellow solution and was cooled again to -65°C . The *in situ* generated lithium phenylacetylide was then transferred to another flask containing a cooled (-65°C) solution of $[\text{Ni}(\text{L-N}_4\text{Me}_2)(\text{MeCN})_2](\text{ClO}_4)_2$ (1) (151.5 mg, 0.25 mmol) in dry propionitrile (30 mL) via cannula. The color of the mixture changed from violet to orange yellow. After stirring for 8 h, the reaction mixture was allowed to warm to room temperature and stirred further for 2 h. In the course of stirring at room temperature the color of the solution changed from orange-yellow to dark brown. After removing the volatiles, a dark residue obtained was dissolved in a minimum volume of methanol (20 mL). The solution was refluxed shortly, cooled to room temperature, and allowed to stand for 2-3 days to give dark brown crystals. The second crop could be obtained by reducing the volume of the mother liquor and leaving the solution for another few days at room temperature. A total amount of 90 mg of dark brown crystalline product $[\{\text{Ni}(\text{L-N}_4\text{Me}_2)\}_2(\mu\text{-RC}_4\text{R})](\text{ClO}_4)_2$ [R = Ph] (2a) was obtained.

Yield: 90 mg (0.085 mmol, 68%); MW ($\text{C}_{48}\text{H}_{50}\text{N}_8\text{Cl}_2\text{Ni}_2\text{O}_8$) = $1055.25 \text{ g}\cdot\text{mol}^{-1}$

Characterization

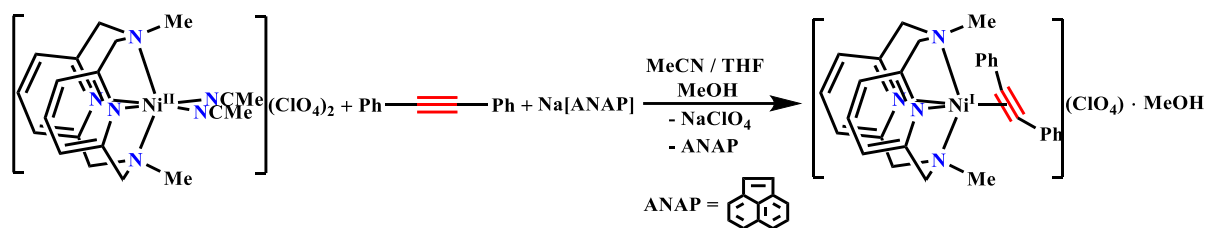
Elemental analysis: Calculated: C = 54.63 % H = 4.78 % N = 10.62 %

Found: C = 54.60 % H = 4.86 % N = 10.70 %

IR (KBr Pellet):

$\tilde{\nu}$ = 2970, 2904, 2814, 1810, 1605, 1579, 1478, 1445, 1376, 1163, 1134, 1091, 1012, 870, 794, 760, 694, 634 and 623 cm^{-1} .

4.3.5 Synthesis of $[\text{Ni}(\text{L-N}_4\text{Me}_2)(\text{PhC}_2\text{Ph})](\text{ClO}_4) \cdot \text{MeOH}$ (**3**)



Under pure nitrogen atmosphere, sodium (14 mg, 0.6 mmol) was added carefully to a yellow solution of acenaphthylene (91.3 mg, 0.6 mmol) in dry THF (10 mL). The mixture was stirred for 2 h at room temperature giving a dark brown solution. The resulting reaction mixture was then transferred to another flask containing $[\text{Ni}(\text{L-N}_4\text{Me}_2)(\text{MeCN})_2](\text{ClO}_4)_2$ (**1**) (304 mg, 0.5 mmol) and diphenylacetylene (107 mg, 0.6 mmol) dissolved in dry acetonitrile (20 mL) via cannula. The color of the mixture changed from violet to dark brown. The solution was stirred for 4 h at room temperature. After removal of solvent, dry THF (20 mL) was added and resulting mixture was filtered. The solid residue was dissolved in MeCN (10 mL) followed by removal of volatiles giving a brown solid. The solid was dissolved in a minimum volume of methanol (10 mL). The solution was refluxed shortly, cooled to room temperature, and kept at $-30\text{ }^\circ\text{C}$ for 2-3 days to afford analytically pure, crystalline products. The yield can be enhanced by a further reduction of the volume of the mother liquid and additional storage of it. A total yield of 146 mg of crystalline brown product $[\text{Ni}(\text{L-N}_4\text{Me}_2)(\text{PhC}_2\text{Ph})](\text{ClO}_4) \cdot \text{MeOH}$ (**3**) was obtained.

Yield: 146 mg (0.229 mmol, 46%); MW ($\text{C}_{31}\text{H}_{34}\text{N}_4\text{ClNiO}_5$) = $636.78\text{ g}\cdot\text{mol}^{-1}$.

Characterization

Elemental analysis: Calculated: C = 58.47 % H = 5.38 % N = 8.80 %

Found: C = 58.64 % H = 5.23 % N = 8.89 %

IR (KBr Pellet):

$\tilde{\nu} = 2965, 2915, 2814, 1885, 1606, 1592, 1579, 1486, 1474, 1442, 1376, 1246, 1162, 1120, 1095, 1013, 869, 791, 758, 693$ and 623 cm^{-1}

ESI-MS (Acetonitrile solution):

$m/z =$ Calculated for $[\text{Ni}(\text{L-N}_4\text{Me}_2)(\text{PhC}_2\text{Ph})]^+$: 425.0; Found: 504.0.

UV-Vis-NIR (Acetonitrile solution, Room temperature):

$\lambda_{\max} (\epsilon_M) = 249 (26720), 324 (\text{sh}, 9120), 364 (11338), 514 (\text{sh}, 208), 675 (34) \text{ and } 1220 (44)$
nm ($M^{-1} \text{ cm}^{-1}$)

Magnetic moment

$\mu = 1.84 \mu_B$

4.3.6 Reactivity of $[\{\text{Ni}(\text{L-N}_4\text{Me}_2)\}_2(\mu\text{-RC}_4\text{R})](\text{ClO}_4)_2$ [R= Ph] (**2a**) with Molecular Oxygen

The complex $[\{\text{Ni}(\text{L-N}_4\text{Me}_2)\}_2(\mu\text{-RC}_4\text{R})](\text{ClO}_4)_2$ [R= Ph] (**2a**) was dissolved in absolute acetonitrile under a pure nitrogen atmosphere at room temperature. Nitrogen was flushed out followed by oxygen in-flow into the solution and then stirring at room temperature. UV-Vis-NIR studies were performed with a solution of **2a** (2.5 mL, 5.9 mM and 0.0236 mM for lower and higher energy region respectively) in acetonitrile using 1 cm cuvette. ESI-MS experiments were performed with a solution of **2a** (5 mL, 1 mM); aliquots were taken at 15, 30, 75, 105 and 210 min and injected to mass spectrometer for analysis. For NMR experiments, a solution of **2a** (16 mg, 0.015 mmol) in CD_3CN (~0.6 mL) was taken and stirred for 24 h. The resulting solution was directly analyzed by ^1H and ^{13}C NMR spectroscopy. To performed EPR measurements, a solution of **2a** (7 mL, 4 mM,) in acetonitrile containing 0.2 M TBAP was used. Aliquots were taken at 0 (immediately), 15, 30, 60, 90, 120, 150 and 180 min and frozen in EPR tubes.

4.3.7 Reactivity of $[\{\text{Ni}(\text{L-N}_4\text{Me}_2)\}_2(\mu\text{-RC}_4\text{R})](\text{ClO}_4)_2$ [R= Ph] (**2a**) with Molecular Oxygen in Presence of Lithium Perchlorate

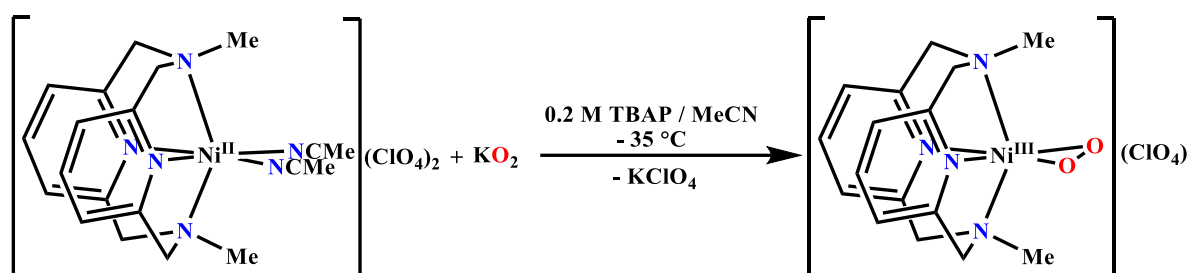
The complex $[\{\text{Ni}(\text{L-N}_4\text{Me}_2)\}_2(\mu\text{-RC}_4\text{R})](\text{ClO}_4)_2$ [R= Ph] (**2a**) (85 mg, 0.08 mmol) and lithium perchlorate (26.5 mg, 0.25 mmol) was dissolved in dry acetonitrile (5 mL) under a pure nitrogen atmosphere at room temperature. Nitrogen was flushed out followed by oxygen in-flow into the solution and then the reaction mixture was stirred for 24 h. The reaction mixture afforded a white precipitate. After decanting the solvent, the solid was washed with acetonitrile (30 mL) and diethyl ether (30 mL) respectively and dried under vacuo. For qualitative characterization of the solid by UV-Vis Spectroscopy, it was dissolved in 0.5 M H_2SO_4 (~1 mL). Then the *in situ* generated H_2O_2 solution (0.1 mL) was added to an aqueous solution of KMnO_4 (2.5 mL, 4 mM, 1 cm cuvette) and resulting changes in absorbance was recorded.

4.3.8 Reactivity of [Ni(L-N₄Me₂)(PhC₂Ph)](ClO₄)·MeOH (3**) with Molecular Oxygen**

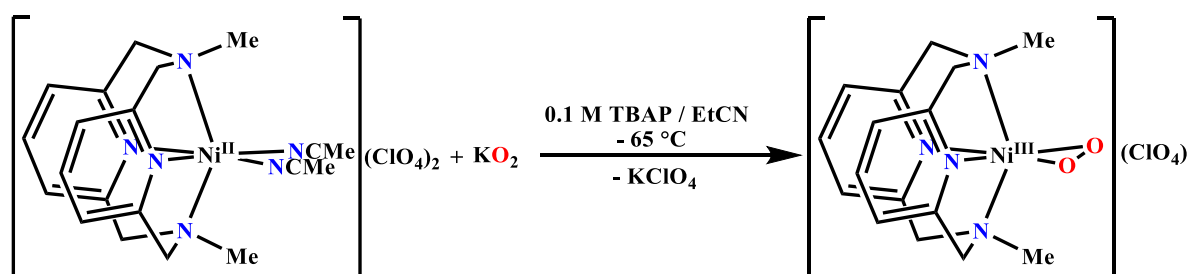
The complex [Ni(L-N₄Me₂)(PhC₂Ph)](ClO₄)·MeOH (**3**) was dissolved in absolute acetonitrile under a pure nitrogen atmosphere at room temperature. Nitrogen was flushed out followed by oxygen in-flow into the solution and then stirring at room temperature. UV-Vis-NIR studies were performed with a solution of **3** (2.5 mL, 9.07 mM and 0.726 mM for lower and higher energy region respectively) in acetonitrile using 1 cm cuvette. ESI-MS experiments were performed with a solution of **3** (5 mL, 1 mM); aliquots were taken at 15, 60, 120, 180, 240, 300 and 420 min and injected to mass spectrometer for analysis. To performed EPR measurements, a solution of **3** (7 mL, 4 mM,) in acetonitrile containing 0.2 M TBAP was used. Aliquots were taken at 0 (immediately), 15, 45, 90, 150, 210, 330 and 390 min and frozen in EPR tubes.

4.3.9 Generation of $[\text{Ni}(\text{L-N}_4\text{Me}_2)(\text{O}_2)]^+$

Generation of $[\text{Ni}(\text{L-N}_4\text{Me}_2)(\text{O}_2)]^+$ (**4**) using KO_2

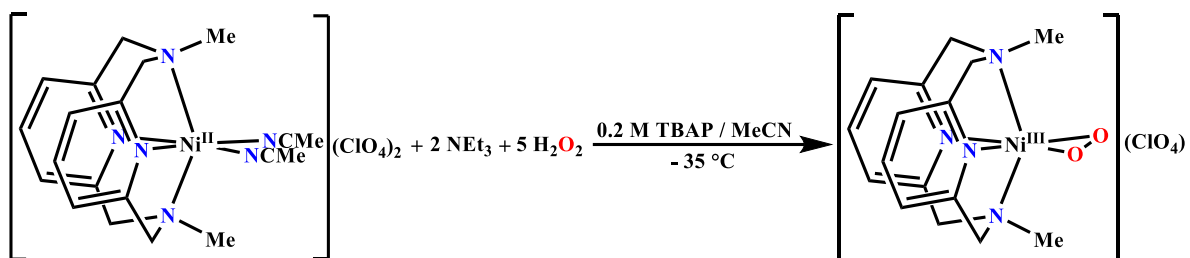


Under an atmosphere of pure nitrogen, solid potassium superoxide (21.5 mg, 0.275 mmol) was added to a cooled ($-35\text{ }^\circ\text{C}$) solution of $[\text{Ni}(\text{L-N}_4\text{Me}_2)(\text{MeCN})_2](\text{ClO}_4)_2$ (**1**) (152.0 mg, 0.25 mmol) in acetonitrile (25 mL) containing 0.2 M TBAP and the reaction mixture was stirred. Aliquots from the reaction mixture were taken at different time intervals in a cooled EPR tubes and frozen in liquid nitrogen.



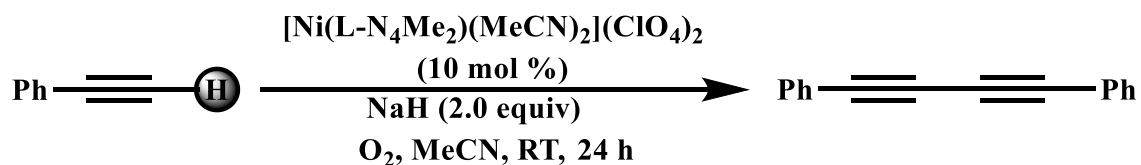
Under an atmosphere of pure nitrogen, solid potassium superoxide (21.5 mg, 0.275 mmol) was added to a cooled ($-65\text{ }^\circ\text{C}$) solution of $[\text{Ni}(\text{L-N}_4\text{Me}_2)(\text{MeCN})_2](\text{ClO}_4)_2$ (**1**) (152.0 mg, 0.25 mmol) in propionitrile (50 mL) containing 0.1 M TBAP and the reaction mixture was stirred. Aliquots from the reaction mixture were taken at different time intervals in a cooled EPR tubes and frozen in liquid nitrogen.

Generation of $[\text{Ni}(\text{L}-\text{N}_4\text{Me}_2)(\text{O}_2)]^+$ (**4**) using H_2O_2 and triethylamine



Under an atmosphere of pure nitrogen, aqueous 30% H_2O_2 (112 μL , 1.0 mmol) was added to a cooled ($-35\text{ }^\circ\text{C}$) solution of $[\text{Ni}(\text{L}-\text{N}_4\text{Me}_2)(\text{MeCN})_2](\text{ClO}_4)_2$ (**1**) (136.1 mg, 0.20 mmol) in 0.2 M TBAP-MeCN (25 mL) containing triethylamine (64 μL , 0.4 mmol) and the reaction mixture was stirred. Aliquots from the reaction mixture were taken after 3 h in a cooled EPR tube and frozen in liquid nitrogen.

4.3.10 Nickel-Mediated Catalytic Reaction



A 10 mL schlenk tube was charged with $[\text{Ni(L-N}_4\text{Me}_2)(\text{MeCN})_2](\text{ClO}_4)_2$ (**1**) (30.4 mg, 0.05 mmol, 10 mol %), NaH (24 mg, 1 mmol), and phenylacetylene (55 μL , 0.5 mmol) under oxygen atmosphere, and dissolved in dry acetonitrile (5 mL). The resulting reaction mixture was stirred for 24 h. After the stipulated time period, all volatile materials were removed under vacuo. The residue was dissolved in diethyl ether and filtered through a short plug of silica. The filtrate was evaporated under vacuo to obtain solid crude product. The yield of the product was determined by $^1\text{H-NMR}$ analysis of the crude product in CDCl_3 using CH_2Br_2 (10 μL , 0.1425 mmol) as an internal reference.

Yield: 78 % with respect to Phenylacetylene.

$^1\text{H-NMR}$ (600 MHz, CDCl_3):

$\delta(\text{ppm}) = 7.53\text{-}7.55$ (m, 4 H), $7.34\text{-}7.39$ (m, 6 H) and 4.93 (s, 2 H, CH_2Br_2).

$^{13}\text{C-NMR}$ (150.9 MHz, CDCl_3):

$\delta(\text{ppm}) = 132.71, 129.42, 128.65, 121.99, 81.76, 74.11$ and 19.13 (CH_2Br_2).

5 Literature

- [1] W. Shi, A. Lei, *Tetrahedron Lett.* **2014**, *55*, 2763.
- [2] P. Siemsen, R. C. Livingston, F. Diederich, *Angew. Chem. Int. Ed. Engl.* **2000**, *39*, 2632.
- [3] G. Zeni, R. B. Panatieri, E. Lissner, P. H. Menezes, A. L. Braga, H. A. Stefani, *Org. Lett.* **2001**, *3*, 819.
- [4] S. F. Mayer, A. Steinreiber, R. V. Orru, K. Faber, *J. Org. Chem.* **2002**, *67*, 9115.
- [5] A. S. Ratnayake, T. Hemscheidt, *Org. Lett.* **2002**, *4*, 4667.
- [6] M. L. Lerch, M. K. Harper, D. J. Faulkner, *J. Nat. Prod.* **2003**, *66*, 667.
- [7] D. Lechner, M. Stavri, M. Oluwatuyi, R. Pereda-Miranda, S. Gibbons, *Phytochemistry* **2004**, *65*, 331.
- [8] A. L. Shi Shun, R. R. Tykwinski, in *Angew. Chem. Int. Ed. Engl.*, Vol. 45, **2006**, pp. 1034.
- [9] N. Panthama, S. Kanokmedhakul, K. Kanokmedhakul, *J. Nat. Prod.* **2010**, *73*, 1366.
- [10] B. Zhang, Y. Wang, S. P. Yang, Y. Zhou, W. B. Wu, W. Tang, J. P. Zuo, Y. Li, J. M. Yue, *J. Am. Chem. Soc.* **2012**, *134*, 20605.
- [11] A. Takahashi, T. Endo, S. Nozoe, *Chem. Pharm. Bull.* **1992**, *40*, 3181.
- [12] T. Kusumi, I. Otani, K. Nishiyama, H. Kakisawa, *Tetrahedron Lett.* **1987**, *28*, 3981.
- [13] M. Yamaguchi, H. J. Park, M. Hirama, K. Torisu, S. Nakamura, T. Minami, H. Nishihara, T. Hiroka, *Bull. Chem. Soc. Jpn.* **1994**, *67*, 1717.
- [14] I. W. Farrell, V. Thaller, J. L. Turner, *J. Chem. Soc., Perkin Trans. 1* **1977**, 1886.
- [15] J. K. M. Sanders, *Angew. Chem., Int. Ed. Engl.* **1995**, *34*, 2563.
- [16] J. M. Tour, *Chem. Rev. (Washington, D. C.)* **1996**, *96*, 537.

- [17] S. Eisler, A. D. Slepko, E. Elliott, T. Luu, R. McDonald, F. A. Hegmann, R. R. Tykwinski, *J. Am. Chem. Soc.* **2005**, *127*, 2666.
- [18] M. Gholami, R. R. Tykwinski, *Chem. Rev. (Washington, DC, U. S.)* **2006**, *106*, 4997.
- [19] J. D. Crowley, S. M. Goldup, A.-L. Lee, D. A. Leigh, R. T. McBurney, *Chem. Soc. Rev.* **2009**, *38*, 1530.
- [20] F. Diederich, *Chem. Commun. (Cambridge)* **2001**, 219.
- [21] R. M. Moriarty, D. Pavlovic, *J. Org. Chem.* **2004**, *69*, 5501.
- [22] J. M. Spruell, W. F. Paxton, J.-C. Olsen, D. Benitez, E. Tkatchouk, C. L. Stern, A. Trabolsi, D. C. Friedman, W. A. Goddard, J. F. Stoddart, *J. Am. Chem. Soc.* **2009**, *131*, 11571.
- [23] C. Glaser, *Ber. Dtsch. Chem. Ges.* **1869**, *2*, 422.
- [24] G. Eglinton, A. R. Galbraith, *Chem. Ind. (London, U. K.)* **1956**, 737.
- [25] A. S. Hay, *J. Org. Chem.* **1960**, *25*, 1275.
- [26] A. S. Hay, *J. Org. Chem.* **1962**, *27*, 3320.
- [27] M. H. Vilhelmsen, J. Jensen, C. G. Tortzen, M. B. Nielsen, *Eur. J. Org. Chem.* **2013**, *2013*, 701.
- [28] H. Y. Gao, H. Wagner, D. Zhong, J. H. Franke, A. Studer, H. Fuchs, in *Angew. Chem. Int. Ed. Engl., Vol. 52*, **2013**, pp. 4024.
- [29] S. Adimurthy, C. C. Malakar, U. Beifuss, *J. Org. Chem.* **2009**, *74*, 5648.
- [30] K. Kamata, S. Yamaguchi, M. Kotani, K. Yamaguchi, N. Mizuno, in *Angew. Chem. Int. Ed. Engl., Vol. 47*, **2008**, pp. 2407.
- [31] H.-F. Jiang, J.-Y. Tang, A. Z. Wang, G.-H. Deng, S.-R. Yang, *Synthesis* **2006**, 1155.
- [32] J. S. Yadav, B. V. S. Reddy, K. B. Reddy, K. U. Gayathri, A. R. Prasad, *Tetrahedron Lett.* **2003**, *44*, 6493.

- [33] Y. Nishihara, K. Ikegashira, K. Hirabayashi, J.-i. Ando, A. Mori, T. Hiyama, *J. Org. Chem.* **2000**, *65*, 1780.
- [34] H. S. F. Bohlmann, E. Inhoffen, G. Grau, *Chem. Ber.* **1964**, *97*, 794.
- [35] G. Zhang, H. Yi, G. Zhang, Y. Deng, R. Bai, H. Zhang, J. T. Miller, A. J. Kropf, E. E. Bunel, A. Lei, *J. Am. Chem. Soc.* **2014**, *136*, 924.
- [36] K. Sonogashira, Y. Tohda, N. Hagihara, *Tetrahedron Lett.* **1975**, 4467.
- [37] R. Rossi, A. Carpita, C. Bigelli, *Tetrahedron Lett.* **1985**, *26*, 523.
- [38] J.-H. Li, Y. Liang, Y.-X. Xie, *J. Org. Chem.* **2005**, *70*, 4393.
- [39] A. Lei, M. Srivastava, X. Zhang, *J. Org. Chem.* **2002**, *67*, 1969.
- [40] H. Sajiki, T. Kurita, M. Abe, T. Maegawa, Y. Monguchi, *Synlett* **2007**, *2007*, 2521.
- [41] S. Atobe, M. Sonoda, Y. Suzuki, T. Yamamoto, H. Masuno, H. Shinohara, A. Ogawa, *Res. Chem. Intermed.* **2012**, *39*, 359.
- [42] S.-N. Chen, W.-Y. Wu, F.-Y. Tsai, *Green Chem.* **2009**, *11*, 269.
- [43] I. J. S. Fairlamb, P. S. Bäuerlein, L. R. Marrison, J. M. Dickinson, *Chem. Commun.* **2003**, 632.
- [44] D. A. Alonso, C. Nájera, M. C. Pacheco, *Adv. Synth. Catal.* **2003**, *345*, 1146.
- [45] M. R. Jlsong Rhee, Shigeru Tsutsumi, *Tetrahedron Lett.* **1969**, *10*, 4593.
- [46] H.-F. Klein, H. Beck-Hemetsberger, L. Reitzel, B. Rodenhäuser, G. Cordier, *Chem. Ber.* **1989**, *122*, 43.
- [47] E. H. Smith, J. Whittall, *Organometallics* **1994**, *13*, 5169.
- [48] J. D. Crowley, S. M. Goldup, N. D. Gowans, D. A. Leigh, V. E. Ronaldson, A. M. Z. Slawin, *J. Am. Chem. Soc.* **2010**, *132*, 6243.
- [49] W. Yin, C. He, M. Chen, H. Zhang, A. Lei, *Org. Lett.* **2009**, *11*, 709.
- [50] Q. Chen, X.-H. Fan, L.-P. Zhang, L.-M. Yang, *Synth. Commun.* **2015**, *45*, 824.

- [51] U. K. Das, R. K. Jena, M. Bhattacharjee, *RSC Adv.* **2014**, *4*, 21964.
- [52] A. Domenech, A. Leyva-Perez, S. I. Al-Resayes, A. Corma, *Electrochem. Commun.* **2012**, *19*, 145.
- [53] X. Meng, C. Li, B. Han, T. Wang, B. Chen, *Tetrahedron* **2010**, *66*, 4029.
- [54] M. E. Krafft, C. Hirose, N. Dalal, C. Ramsey, A. Stiegman, *Tetrahedron Lett.* **2001**, *42*, 7733.
- [55] P. Bharathi, M. Periasamy, *Organometallics* **2000**, *19*, 5511.
- [56] L. Vaska, *Science* **1963**, *140*, 809.
- [57] L. Vaska, *Accounts Chem. Res.* **1968**, *1*, 335.
- [58] L. Vaska, L. S. Chen, C. V. Senoff, *Science* **1971**, *174*, 587.
- [59] L. Vaska, *Acc. Chem. Res.* **1976**, *9*, 175.
- [60] C. R. Landis, C. M. Morales, S. S. Stahl, *J. Am. Chem. Soc.* **2004**, *126*, 16302.
- [61] M. Chen, X. Zheng, W. Li, J. He, A. Lei, *J. Am. Chem. Soc.* **2010**, *132*, 4101.
- [62] M. Zhou, R. H. Crabtree, *Chem. Soc. Rev.* **2011**, *40*, 1875.
- [63] L. Q. Jin, A. W. Lei, *Sci. China: Chem.* **2012**, *55*, 2027.
- [64] M. Costas, M. P. Mehn, M. P. Jensen, L. Que, Jr., *Chem. Rev.* **2004**, *104*, 939.
- [65] T. Punniyamurthy, S. Velusamy, J. Iqbal, *Chem. Rev.* **2005**, *105*, 2329.
- [66] C. J. Cramer, W. B. Tolman, *Acc. Chem. Res.* **2007**, *40*, 601.
- [67] X. Zhao, A. Kong, C. Shan, P. Wang, X. Zhang, Y. Shan, *Catal. Lett.* **2009**, *131*, 526.
- [68] A. N. Campbell, S. S. Stahl, *Acc. Chem. Res.* **2012**, *45*, 851.
- [69] M. T. Kieber-Emmons, M. F. Qayyum, Y. Li, Z. Halime, K. O. Hodgson, B. Hedman, K. D. Karlin, E. I. Solomon, *Angew. Chem., Int. Ed.* **2012**, *51*, 168.
- [70] S. Fukuzumi, K. D. Karlin, *Coord. Chem. Rev.* **2013**, *257*, 187.

- [71] S. Kakuda, R. L. Peterson, K. Ohkubo, K. D. Karlin, S. Fukuzumi, *J. Am. Chem. Soc.* **2013**, *135*, 6513.
- [72] S. Itoh, *Acc. Chem. Res.* **2015**, *48*, 2066.
- [73] E. M. Shepard, D. M. Dooley, *Acc. Chem. Res.* **2015**, *48*, 1218.
- [74] J. B. Gary, C. Citek, T. A. Brown, R. N. Zare, E. C. Wasinger, T. D. P. Stack, *J. Am. Chem. Soc.* **2016**, *138*, 9986.
- [75] S. Gentil, D. Serre, C. Philouze, M. Holzinger, F. Thomas, A. Le Goff, *Angew. Chem., Int. Ed.* **2016**, *55*, 2517.
- [76] X. Wang, G. Wu, X. Liu, C. Zhang, Q. Lin, *Catal. Lett.* **2016**, *146*, 620.
- [77] H. S. G. Wilke, P. Heimbach, *Angew. Chem.* **1967**, *79*, 62.
- [78] S. Otsuka, A. Nakamura, Y. Tatsuno, *J. Amer. Chem. Soc.* **1969**, *91*, 6994.
- [79] B. S. Mandimutsira, J. L. Yamarik, T. C. Brunold, W. Gu, S. P. Cramer, C. G. Riordan, *J. Am. Chem. Soc.* **2001**, *123*, 9194.
- [80] R. Schenker, B. S. Mandimutsira, C. G. Riordan, T. C. Brunold, *J. Am. Chem. Soc.* **2002**, *124*, 13842.
- [81] K. Fujita, R. Schenker, W. Gu, T. C. Brunold, S. P. Cramer, C. G. Riordan, *Inorg. Chem.* **2004**, *43*, 3324.
- [82] M. T. Kieber-Emmons, R. Schenker, G. P. Yap, T. C. Brunold, C. G. Riordan, *Angew. Chem. Int. Ed. Engl.* **2004**, *43*, 6716.
- [83] M. T. Kieber-Emmons, J. Annaraj, M. S. Seo, K. M. Van Heuvelen, T. Tosha, T. Kitagawa, T. C. Brunold, W. Nam, C. G. Riordan, *J. Am. Chem. Soc.* **2006**, *128*, 14230.
- [84] S. Yao, E. Bill, C. Milsmann, K. Wieghardt, M. Driess, *Angew. Chem. Int. Ed. Engl.* **2008**, *47*, 7110.
- [85] D. Nakane, S.-i. Kuwasako, M. Tsuge, M. Kubo, Y. Funahashi, T. Ozawa, T. Ogura, H. Masuda, *Chem. Commun. (Cambridge, U. K.)* **2010**, *46*, 2142.

- [86] C. A. Rettenmeier, H. Wadepohl, L. H. Gade, *Angew. Chem. Int. Ed. Engl.* **2015**, *54*, 4880.
- [87] J. Cho, R. Sarangi, J. Annaraj, S. Y. Kim, M. Kubo, T. Ogura, E. I. Solomon, W. Nam, *Nat. Chem.* **2009**, *1*, 568.
- [88] J. Cho, H. Y. Kang, L. V. Liu, R. Sarangi, E. I. Solomon, W. Nam, *Chem. Sci.* **2013**, *4*, 1502.
- [89] J. Kim, B. Shin, H. Kim, J. Lee, J. Kang, S. Yanagisawa, T. Ogura, H. Masuda, T. Ozawa, J. Cho, *Inorg. Chem.* **2015**, *54*, 6176.
- [90] S. Ferlay, T. Mallah, R. Ouahes, P. Veillet, M. Verdaguer, *Nature* **1995**, *378*, 701.
- [91] O. Sato, T. Iyoda, A. Fujishima, K. Hashimoto, *Science* **1996**, *272*, 704.
- [92] O. Sato, T. Iyoda, A. Fujishima, K. Hashimoto, *Science* **1996**, *271*, 49.
- [93] S.-i. Ohkoshi, H. Tokoro, T. Matsuda, H. Takahashi, H. Irie, K. Hashimoto, *Angew. Chem. Int. Ed.* **2007**, *46*, 3238.
- [94] H. Oshio, H. Onodera, T. Ito, *Chemistry – A European Journal* **2003**, *9*, 3946.
- [95] J. Kim, S. Han, I.-K. Cho, K. Y. Choi, M. Heu, S. Yoon, B. J. Suh, *Polyhedron* **2004**, *23*, 1333.
- [96] M. Nihei, M. Ui, M. Yokota, L. Han, A. Maeda, H. Kishida, H. Okamoto, H. Oshio, *Angew. Chem. Int. Ed.* **2005**, *44*, 6484.
- [97] D. Li, S. Parkin, G. Wang, G. T. Yee, S. M. Holmes, *Inorg. Chem.* **2006**, *45*, 1951.
- [98] N. Masayuki, S. Yoshihiro, S. Naoki, O. Hiroki, *Chem. Lett.* **2010**, *39*, 978.
- [99] Y. Zhang, D. Li, R. Clérac, M. Kalisz, C. Mathonière, S. M. Holmes, *Angew. Chem. Int. Ed.* **2010**, *49*, 3752.
- [100] D. Li, S. Parkin, G. Wang, G. T. Yee, R. Clérac, W. Wernsdorfer, S. M. Holmes, *J. Am. Chem. Soc.* **2006**, *128*, 4214.

- [101] D. Li, R. Clérac, O. Roubeau, E. Harté, C. Mathonière, R. Le Bris, S. M. Holmes, *J. Am. Chem. Soc.* **2008**, *130*, 252.
- [102] M. Nihei, M. Ui, N. Hoshino, H. Oshio, *Inorg. Chem.* **2008**, *47*, 6106.
- [103] C. P. Berlinguette, D. Vaughn, C. Cañada-Vilalta, J. R. Galán-Mascarós, K. R. Dunbar, *Angew. Chem. Int. Ed.* **2003**, *42*, 1523.
- [104] C. P. Berlinguette, A. Dragulescu-Andrasi, A. Sieber, H.-U. Güdel, C. Achim, K. R. Dunbar, *J. Am. Chem. Soc.* **2005**, *127*, 6766.
- [105] M. G. Hilfiger, M. Chen, T. V. Brinzari, T. M. Nocera, M. Shatruk, D. T. Petasis, J. L. Musfeldt, C. Achim, K. R. Dunbar, *Angew. Chem. Int. Ed.* **2010**, *49*, 1410.
- [106] H.-J. Krüger, *unpublished results*.
- [107] H.-J. Krüger, *Coord. Chem. Rev.* **2009**, *253*, 2450.
- [108] H.-J. Krüger, *Chem. Ber.* **1995**, *128*, 531.
- [109] D. Walther, A. Schmidt, T. Klettke, W. Imhof, H. Görls, *Angew. Chem.* **1994**, *106*, 1421.
- [110] B. L. Edelbach, R. J. Lachicotte, W. D. Jones, *Organometallics* **1999**, *18*, 4040.
- [111] C. Müller, R. J. Lachicotte, W. D. Jones, *Organometallics* **2002**, *21*, 1975.
- [112] R. Barrios-Francisco, J. J. García, *Applied Catalysis A: General* **2010**, *385*, 108.
- [113] R. Barrios-Francisco, T. Benítez-Páez, M. Flores-Alamo, A. Arévalo, J. J. García, *Chemistry – An Asian Journal* **2011**, *6*, 842.
- [114] I. Morales-Becerril, M. Flores-Álamo, A. Tlahuext-Aca, A. Arévalo, J. J. García, *Organometallics* **2014**, *33*, 6796.
- [115] M. J. Sgro, D. W. Stephan, *Dalton Transactions* **2010**, *39*, 5786.
- [116] E. Nojman, A. Berlicka, L. Szterenberga, L. Latos-Grażyński, *Inorg. Chem.* **2012**, *51*, 3247.

- [117] S. Sabater, M. J. Page, M. F. Mahon, M. K. Whittlesey, *Organometallics* **2017**, *36*, 1776.
- [118] W. Bonrath, K. R. Pörschke, G. Wilke, K. Angermund, C. Krüger, *Angew. Chem. Int. Ed.* **1988**, *27*, 833.
- [119] U. Rosenthal, S. Pulst, P. Arndt, W. Baumann, A. Tillack, R. Kempe, *znb* **1995**, *50*, 368.
- [120] R. M. Ward, A. S. Batsanov, J. A. K. Howard, T. B. Marder, *Inorg. Chim. Acta* **2006**, *359*, 3671.
- [121] A. W. Addison, T. N. Rao, J. Reedijk, J. Van Rijn, G. C. Verschoor, *J. Chem. Soc., Dalton Trans.* **1984**, 1349.
- [122] R. Thomas, S. S. Mallajyosula, S. Lakshmi, S. K. Pati, G. U. Kulkarni, *J. Mol. Struct.* **2009**, *922*, 46.
- [123] M. J. S. Dewar, *Bull. Soc. Chim. Fr.* **1951**, *18*, C71.
- [124] J. Chatt, L. A. Duncanson, *Journal of the Chemical Society (Resumed)* **1953**, 2939.
- [125] K. Tatsumi, R. Hoffmann, J. L. Templeton, *Inorg. Chem.* **1982**, *21*, 466.
- [126] B. Fang, W. Ren, G. Hou, G. Zi, D.-C. Fang, L. Maron, M. D. Walter, *J. Am. Chem. Soc.* **2014**, *136*, 17249.
- [127] L. Zhang, G. Hou, G. Zi, W. Ding, M. D. Walter, *J. Am. Chem. Soc.* **2016**, *138*, 5130.
- [128] P. F. Eiland, R. Pepinsky, *J. Am. Chem. Soc.* **1952**, *74*, 4971.
- [129] J. D. Dunitz, L. E. Orgel, A. Rich, *Acta Crystallographica* **1956**, *9*, 373.
- [130] T. F. Tekut, C. J. O'Connor, R. A. Holwerda, *Inorg. Chim. Acta* **1993**, *214*, 145.
- [131] A. Kumar Singh, J. I. van der Vlugt, S. Demeshko, S. Dechert, F. Meyer, *Eur. J. Inorg. Chem.* **2009**, *2009*, 3431.
- [132] D. Venegas-Yazigi, D. Aravena, E. Spodine, E. Ruiz, S. Alvarez, *Coord. Chem. Rev.* **2010**, *254*, 2086.

- [133] M. G. Sommer, Y. Rechkemmer, L. Suntrup, S. Hohloch, M. van der Meer, J. van Slageren, B. Sarkar, *Dalton Transactions* **2016**, 45, 17770.
- [134] P.-H. Li, J.-C. Yan, M. Wang, L. Wang, *Chin. J. Chem.* **2004**, 22, 219.
- [135] L. Wang, J. Yan, P. Li, M. Wang, C. Su, *J. Chem. Res.* **2005**, 112.
- [136] J. G. Rodriguez, J. L. Tejedor, A. Rumbero, L. Canoira, *Tetrahedron* **2006**, 62, 3075.
- [137] A. Kusuda, X.-H. Xu, X. Wang, E. Tokunaga, N. Shibata, *Green Chem.* **2011**, 13, 843.
- [138] F. S. Menges, S. M. Craig, N. Toetsch, A. Bloomfield, S. Ghosh, H.-J. Krüger, M. A. Johnson, *Angew. Chem., Int. Ed.* **2016**, 55, 1282.
- [139] G. N. Gorshkova, M. A. Chubarova, A. M. Sladkov, L. Y. Ukhin, V. I. Kasatochkin, *Zh. Fiz. Khim.* **1964**, 38, 2516.
- [140] T. Hoshi, J. Okubo, M. Kobayashi, Y. Tanizaki, *J. Am. Chem. Soc.* **1986**, 108, 3867.
- [141] G. Vives, A. Carella, S. Sistach, J.-P. Launay, G. Rapenne, *New J. Chem.* **2006**, 30, 1429.
- [142] D. C. Powers, T. Ritter, *Topics in organometallic chemistry* **2011**, 503, 129.
- [143] S. Barata-Vallejo, A. Postigo, *Coord. Chem. Rev.* **2013**, 257, 3051.
- [144] W. T. Wei, M. B. Zhou, J. H. Fan, W. Liu, R. J. Song, Y. Liu, M. Hu, P. Xie, J. H. Li, *Angew. Chem. Int. Ed. Engl.* **2013**, 52, 3638.
- [145] J. Xie, J. Li, V. Weingand, M. Rudolph, A. S. Hashmi, *Chemistry* **2016**, 22, 12646.
- [146] A. Mavridis, I. Moustakali-Mavridis, *Acta Crystallogr., Sect. B* **1977**, B33, 3612.
- [147] D. Vojta, G. Baranovic, *Vib. Spectrosc.* **2010**, 52, 178.
- [148] F. Tang, N. P. Rath, L. M. Mirica, *Chem. Commun. (Cambridge, U. K.)* **2015**, 51, 3113.

- [149] J. W. Schultz, K. Fuchigami, B. Zheng, N. P. Rath, L. M. Mirica, *J. Am. Chem. Soc.* **2016**, *138*, 12928.
- [150] Z. Peng, S. A. Freunberger, Y. Chen, P. G. Bruce, *Science* **2012**, *337*, 563.
- [151] J. Yang, D. Zhai, H.-H. Wang, K. C. Lau, J. A. Schlueter, P. Du, D. J. Myers, Y.-K. Sun, L. A. Curtiss, K. Amine, *PCCP* **2013**, *15*, 3764.
- [152] D. Zhai, H.-H. Wang, J. Yang, K. C. Lau, K. Li, K. Amine, L. A. Curtiss, *J. Am. Chem. Soc.* **2013**, *135*, 15364.
- [153] R. S. Sanchez-Carrera, B. Kozinsky, *PCCP* **2014**, *16*, 24549.
- [154] M. Dunuwille, M. Kim, C.-S. Yoo, *The Journal of Chemical Physics* **2016**, *145*, 084701.
- [155] M. S. Seo, J. Y. Kim, J. Annaraj, Y. Kim, Y.-M. Lee, S.-J. Kim, J. Kim, W. Nam, *Angew. Chem., Int. Ed.* **2007**, *46*, 377.
- [156] J. Annaraj, J. Cho, Y.-M. Lee, S. Y. Kim, R. Latifi, S. P. de Visser, W. Nam, *Angew. Chem., Int. Ed.* **2009**, *48*, 4150.
- [157] J.-H. Cho, R. Sarangi, H.-Y. Kang, J.-Y. Lee, M. Kubo, T. Ogura, E. I. Solomon, W.-W. Nam, *J. Am. Chem. Soc.* **2010**, *132*, 16977.
- [158] J. Cho, R. Sarangi, W. Nam, *Acc. Chem. Res.* **2012**, *45*, 1321.
- [159] H. E. Gottlieb, V. Kotlyar, A. Nudelman, *J. Org. Chem.* **1997**, *62*, 7512.
- [160] S. Stoll, A. Schweiger, *Journal of Magnetic Resonance* **2006**, *178*, 42.
- [161] A. Altomare, M. C. Burla, M. Camalli, G. L. Cascarano, C. Giacovazzo, A. Guagliardi, A. G. G. Moliterni, G. Polidori, R. Spagna, *J. Appl. Crystallogr.* **1999**, *32*, 115.
- [162] G. M. Sheldrick, *Acta Crystallogr., Sect. A: Found. Crystallogr.* **2008**, *64*, 112.
- [163] O. Kahn, *Molecular Magnetism*, VCH, **1993**.

- [164] H.-J. Krüger, *2,11-Diaza[3.3](2,6)pyridinophane – A unique Class of Ligands, Habilitation, Universität Hamburg 1997.*
- [165] P. Neelakantan, *Proceedings of the Indian Academy of Sciences - Section A* **1964**, *60*, 422.
- [166] M. H. Brooker, J. B. Bates, *The Journal of Chemical Physics* **1971**, *54*, 4788.
- [167] M. H. Brooker, J. Wang, *Spectrochimica Acta Part A: Molecular Spectroscopy* **1992**, *48*, 999.
- [168] S. L. Georgopoulos, R. Diniz, M. I. Yoshida, N. L. Speziali, H. F. D. Santos, G. M. A. Junqueira, L. F. C. de Oliveira, *J. Mol. Struct.* **2006**, *794*, 63.
- [169] G. E. Walrafen, R. T. W. Douglas, *The Journal of Chemical Physics* **2006**, *124*, 114504.

6 Acknowledgement

First and foremost, I would like to express my sincere gratitude to Prof. Dr. H.-J. Krüger for giving me the opportunity to carry out my Ph.D. work under his supervision. Appreciation goes to him for all his contribution of time, ideas, and funding to make my Ph.D. experience productive and stimulating.

I would like to thank Prof. Dr. Sitzmann and Prof. Dr. Stefan Kubik for being in the examination committee of my dissertation.

I would like to thank Dr. H. Kelm for X-Ray crystallographic measurements and scientific advices.

I would also like to thank Prof. Dr. F. Mayer and his co-worker Dr. S. Demeshko from Georg-August-Universität, Göttingen for SQUID measurements.

I want to thank Mrs. Müller from NMR facility, Mrs. Dusch and Mrs. Ellmer for elemental analysis from the analytical department and Mr. Napast, Mr. Rahm, and Mr. Schröer from the chemical storage facility.

I want to thank Dr. F. Menges and Dr. J. Lang from the group of Prof. Dr. G. N. Schatteburg for ESI-MS measurements. I would also like to thank Prof. Dr. C. van Wüllen for the DFT calculation of the nickel-diyne complex.

I would like to thank Dr. M. Schmitz for Raman measurement.

I would like to acknowledge to Mrs. C. Hofmann and Mrs. H. Dieterich for their kind help during my work in TU Kaiserslautern. I am grateful to ISGS, TU Kaiserslautern for all the support during my stay in Kaiserslautern.

I want to thank my colleagues for their constant help and support. I would also like to acknowledge to my friends for their endless support.

I would like to thank to my parents and family members, especially my wife. They stood by my side in every aspect of my life. Without their support and encouragement, I would have not earned this degree.

7 Appendix

7.1 $[\text{Ni}(\text{L-N}_4\text{Me}_2)(\text{MeCN})_2](\text{ClO}_4)_2$ (1)

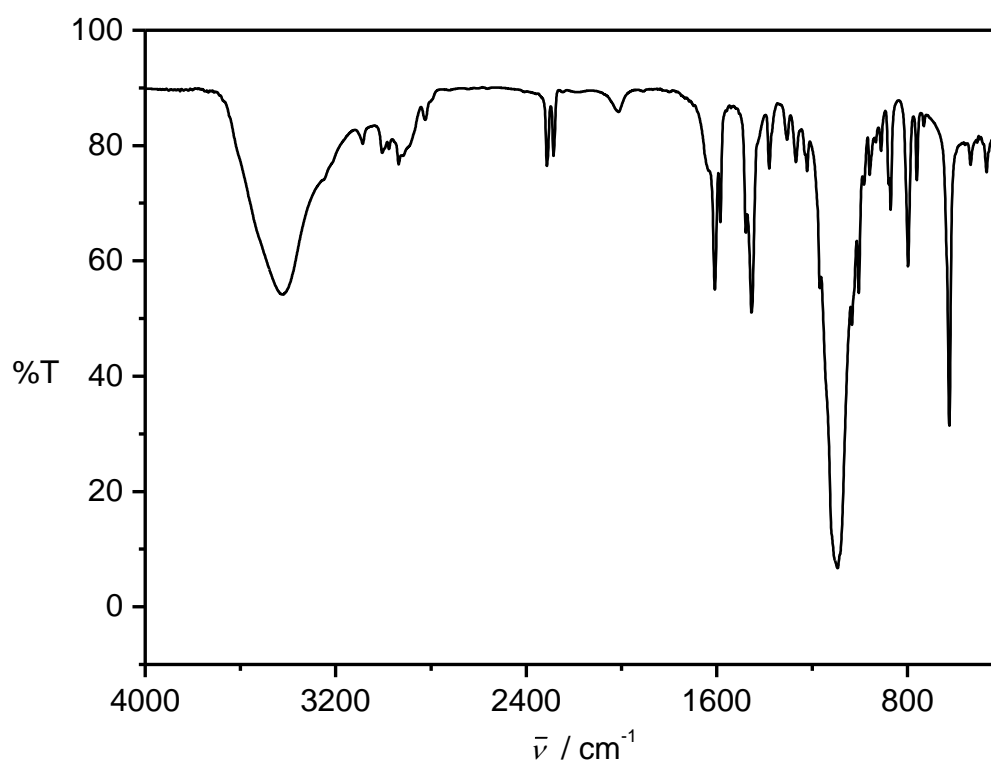


Figure 7.1: IR spectrum of 1 as KBr pellet.

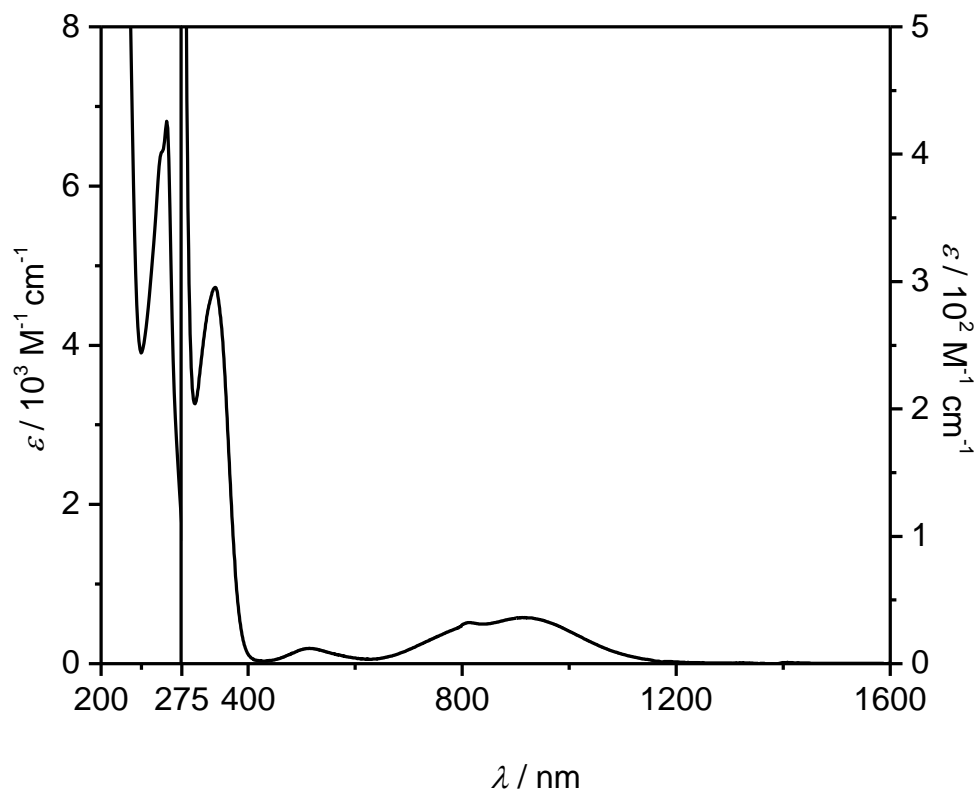


Figure 7.2: UV-Vis-NIR Spectrum of 1 in MeCN.

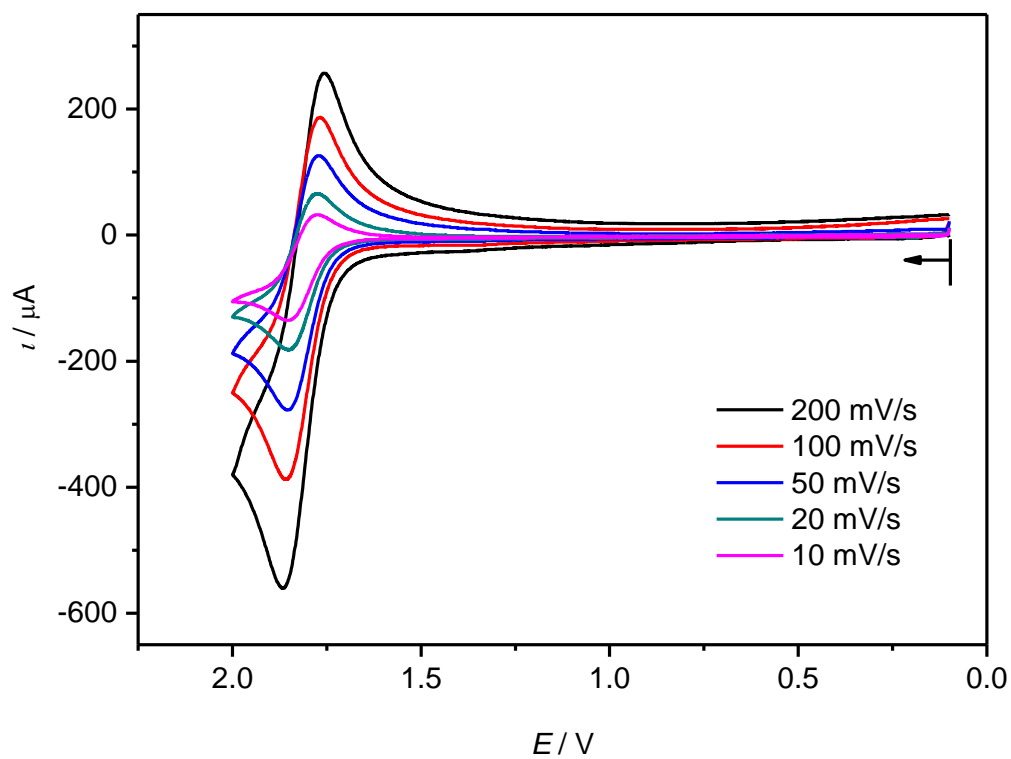


Figure 7.3: Cyclic voltammograms for the oxidation of 1 in 0.2 M TBAP/MeCN sweeping with different scan rates. All potentials are given vs. SCE.

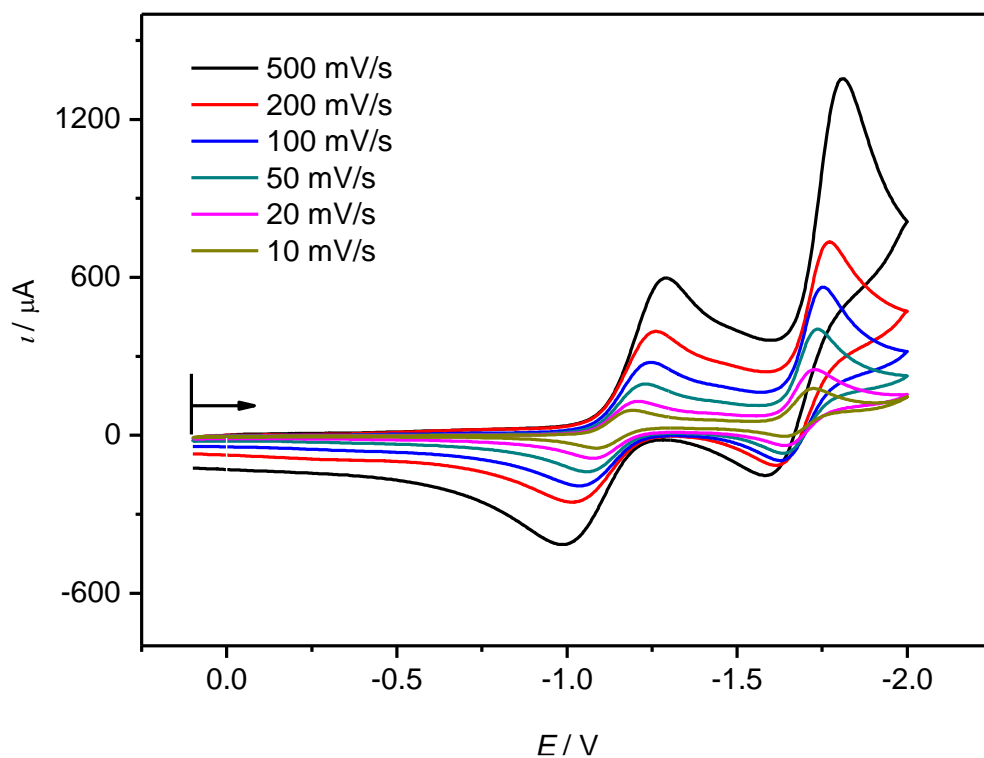


Figure 7.4: Cyclic voltammograms for the reduction of 1 in 0.2 M TBAP/MeCN sweeping with different scan rates. All potentials are given vs. SCE.

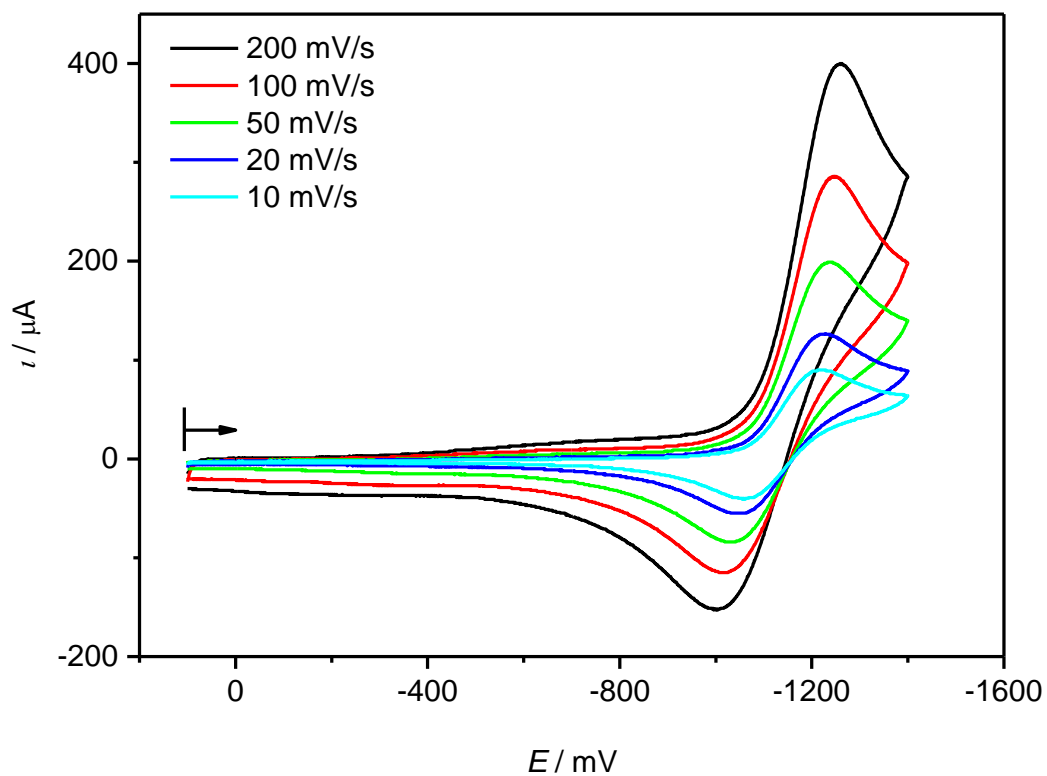


Figure 7.5: Cyclic voltammograms for the first reduction of 1 in 0.2 M TBAP/MeCN sweeping with different scan rates. All potentials are given vs. SCE.

7.2 $[\{\text{Ni}(\text{L-N}_4\text{Me}_2)\}_2(\mu\text{-RC}_4\text{R})](\text{ClO}_4)_2$ (2a-2g)7.2.1 $[\{\text{Ni}(\text{L-N}_4\text{Me}_2)\}_2(\mu\text{-RC}_4\text{R})](\text{ClO}_4)_2$ [R = Ph] (2a)

Table 7.1: Crystal data and structure refinement for 2a [R = Ph] at 150 K

Identification code	16073ocu	
Empirical formula	$\text{C}_{24}\text{H}_{25}\text{ClN}_4\text{NiO}_4$	
Formula weight	527.64	
Temperature	150(2) K	
Wavelength	1.54184 Å	
Crystal system	Triclinic	
Space group	$\text{P}\bar{1}$	
Unit cell dimensions	$a = 8.9628(3)$ Å	$\alpha = 98.221(3)^\circ$
	$b = 11.4221(5)$ Å	$\beta = 108.088(3)^\circ$
	$c = 13.1365(4)$ Å	$\gamma = 104.987(4)^\circ$
Volume	1197.83(8) Å ³	
Z	1	
Density (calculated)	1.463 Mg/m ³	
Absorption coefficient	0.960 mm ⁻¹	
F(000)	548	
Crystal size	0.51 x 0.50 x 0.38 mm ³	
Theta range for data collection	2.86 to 30.00°.	
Index ranges	-12 ≤ h ≤ 12, -13 ≤ k ≤ 16, -18 ≤ l ≤ 10	
Reflections collected	12893	
Independent reflections	6979 [R(int) = 0.0250]	
Completeness to theta = 30.00°	99.7 %	
Absorption correction	Semi-empirical from equivalents	
Max. and min. transmission	0.7118 and 0.6403	
Refinement method	Full-matrix least-squares on F ²	
Data / restraints / parameters	6979 / 0 / 309	
Goodness-of-fit on F ²	1.011	
Final R indices [I > 2σ(I)]	R1 = 0.0406, wR2 = 0.1028	
R indices (all data)	R1 = 0.0544, wR2 = 0.1060	
Largest diff. peak and hole	0.543 and -0.448 e.Å ⁻³	

Table 7.2: Crystal data and structure refinement for 2a [R = Ph] at 190 K

Identification code	11009
Empirical formula	C ₂₄ H ₂₅ ClN ₄ NiO ₄
Formula weight	527.64
Temperature	193(2) K
Wavelength	0.71073 Å
Crystal system	Triclinic
Space group	P $\bar{1}$
Unit cell dimensions	a = 8.9016(10) Å α = 97.887(13)° b = 11.2772(12) Å β = 108.017(13)° c = 13.0297(14) Å γ = 105.406(13)°
Volume	1164.3(2) Å ³
Z	2
Density (calculated)	1.505 Mg/m ³
Absorption coefficient	0.987 mm ⁻¹
F(000)	548
Crystal size	0.53 x 0.47 x 0.36 mm ³
Theta range for data collection	2.55 to 28.00°.
Index ranges	-11 ≤ h ≤ 11, -14 ≤ k ≤ 14, -17 ≤ l ≤ 17
Reflections collected	14244
Independent reflections	5187 [R(int) = 0.0431]
Completeness to theta = 30.00°	92.1 %
Absorption correction	None
Max. and min. transmission	0.7176 and 0.6227
Refinement method	Full-matrix least-squares on F ²
Data / restraints / parameters	5187 / 0 / 309
Goodness-of-fit on F ²	1.058
Final R indices [I > 2σ(I)]	R1 = 0.0333, wR2 = 0.0899
R indices (all data)	R1 = 0.0363, wR2 = 0.0912
Largest diff. peak and hole	0.583 and -0.554 e.Å ⁻³

Table 7.3: Crystal data and structure refinement for 2a [R = Ph] at 293 K

Identification code	11213o	
Empirical formula	C ₄₈ H ₅₀ Cl ₂ N ₈ Ni ₂ O ₈	
Formula weight	1055.28	
Temperature	293(2) K	
Wavelength	0.71073 Å	
Crystal system	Triclinic	
Space group	P $\bar{1}$	
Unit cell dimensions	a = 8.9628(3) Å	α = 98.221(3)°
	b = 11.4221(5) Å	β = 108.088(3)°
	c = 13.1365(4) Å	γ = 104.987(4)°
Volume	1197.83(8) Å ³	
Z	1	
Density (calculated)	1.463 Mg/m ³	
Absorption coefficient	0.960 mm ⁻¹	
F(000)	548	
Crystal size	0.51 x 0.50 x 0.38 mm ³	
Theta range for data collection	2.86 to 30.00°.	
Index ranges	-12 ≤ h ≤ 12, -13 ≤ k ≤ 16, -18 ≤ l ≤ 10	
Reflections collected	12893	
Independent reflections	6979 [R(int) = 0.0250]	
Completeness to theta = 30.00°	99.7 %	
Absorption correction	Semi-empirical from equivalents	
Max. and min. transmission	0.7118 and 0.6403	
Refinement method	Full-matrix least-squares on F ²	
Data / restraints / parameters	6979 / 0 / 309	
Goodness-of-fit on F ²	1.011	
Final R indices [I > 2σ(I)]	R1 = 0.0406, wR2 = 0.1028	
R indices (all data)	R1 = 0.0544, wR2 = 0.1060	
Largest diff. peak and hole	0.543 and -0.448 e.Å ⁻³	

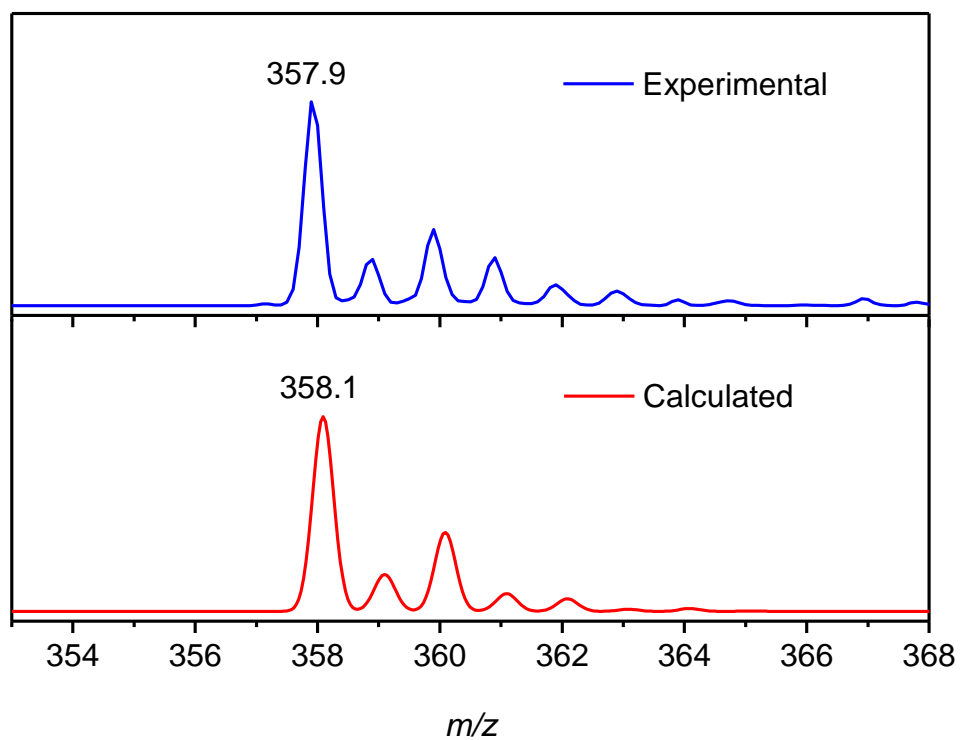


Figure 7.6: The experimental and calculated isotope distribution for $[\text{Ni}(\text{L-N}_4\text{Me}_2)(\text{O}_2)]^+$.

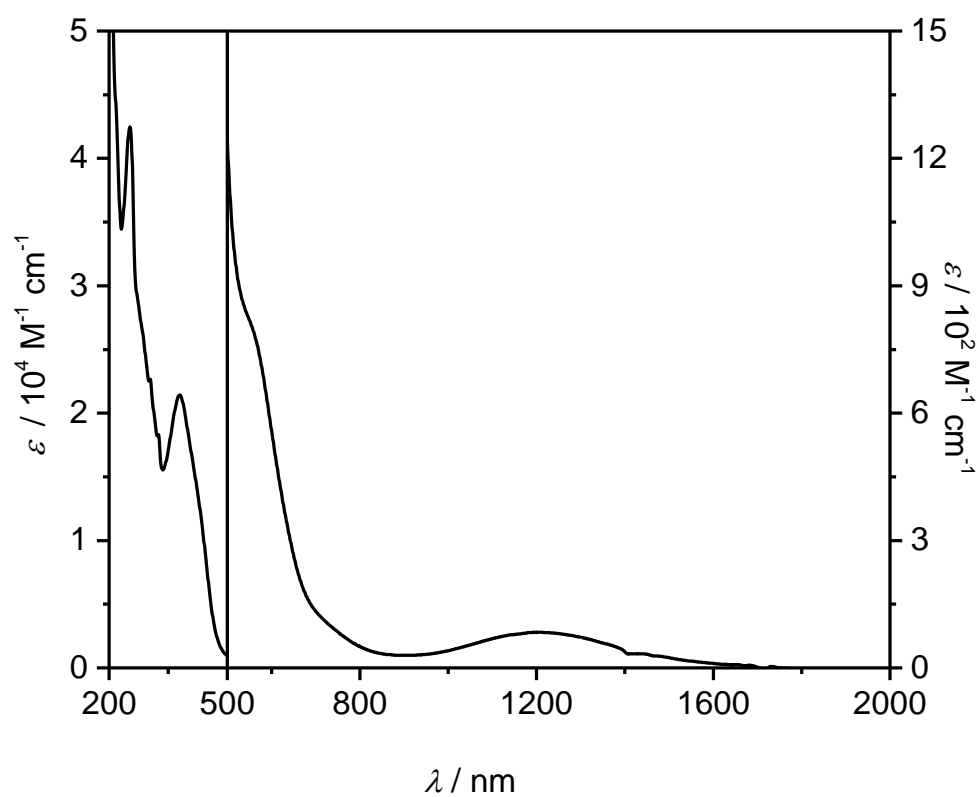


Figure 7.7: UV-Vis-NIR spectrum of 2a in MeCN.

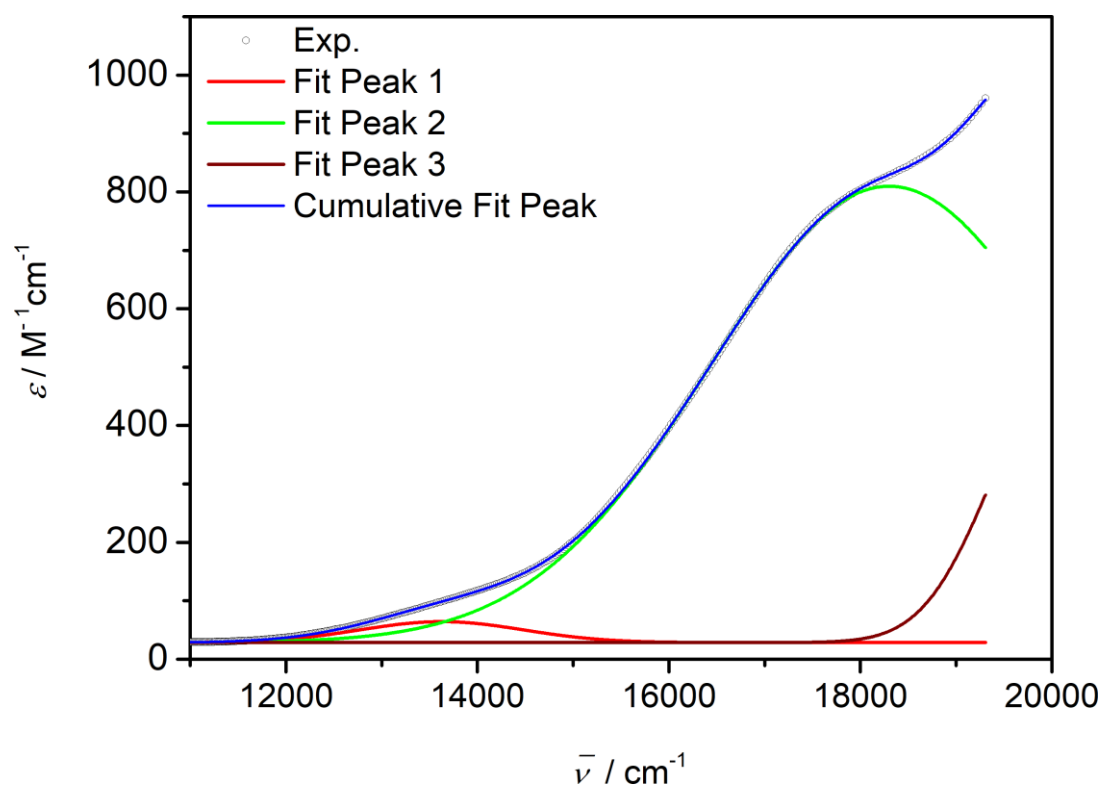


Figure 7.8: Deconvoluted UV-Vis-NIR spectrum of 2a; convolution is performed in 11001 – 19305 cm^{-1} range using Gaussian function.

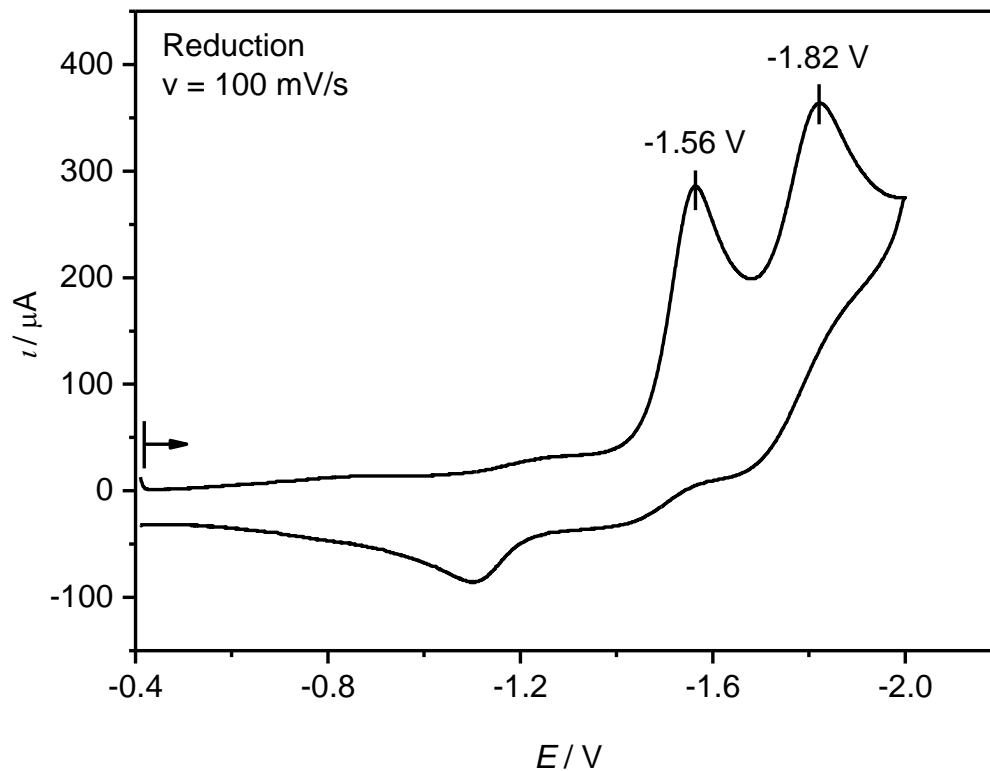


Figure 7.9: Cyclic voltammogram for the reduction of 2a in 0.2 M TBAP/MeCN sweeping with a scan rate of 100 mV s^{-1} . All potentials are given vs. SCE.

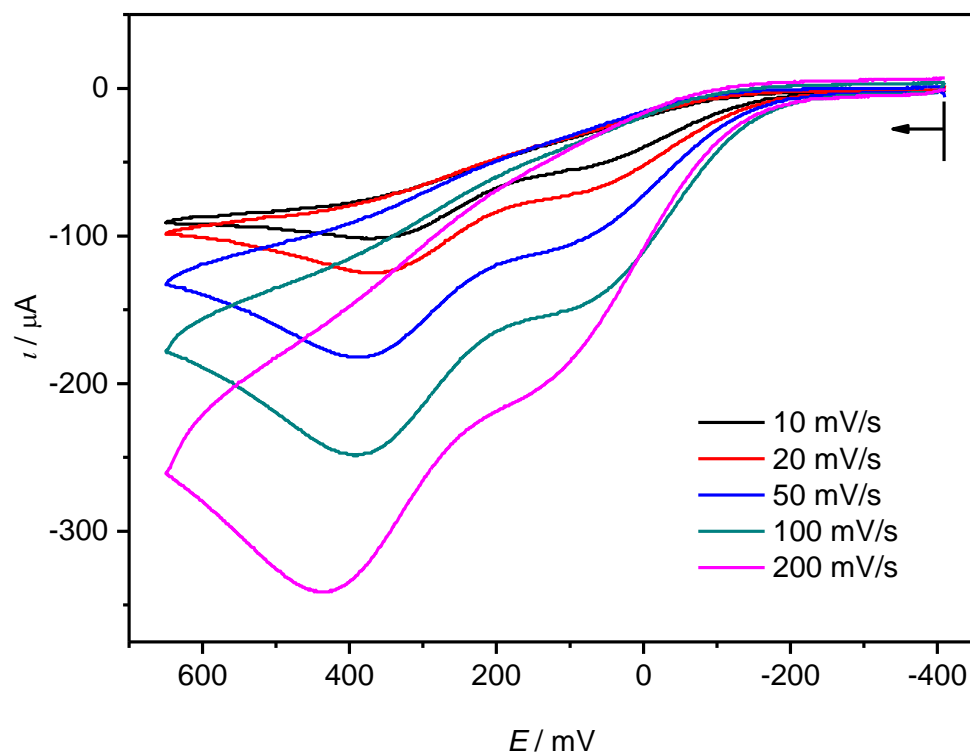


Figure 7.10: Cyclic voltammograms for the oxidation of 2a in 0.2 M TBAP/MeCN sweeping with different scan rates. All potentials are given vs. SCE.

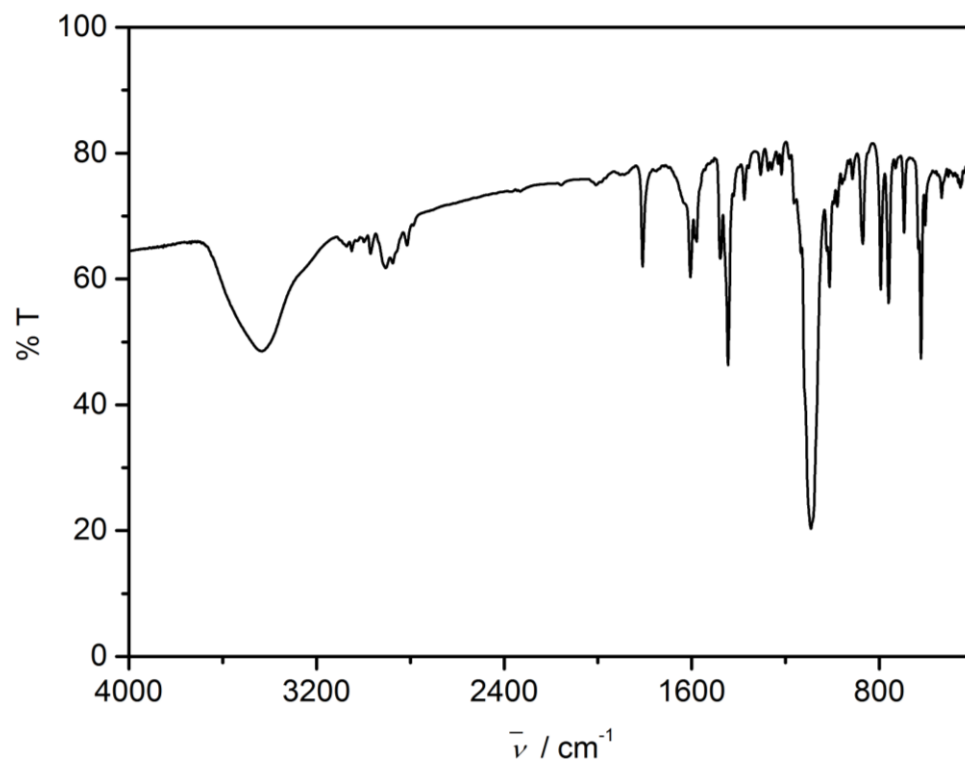


Figure 7.11: IR spectrum of 2a as KBr pellet, prepared by stoichiometric reaction in presence of TEMPO.

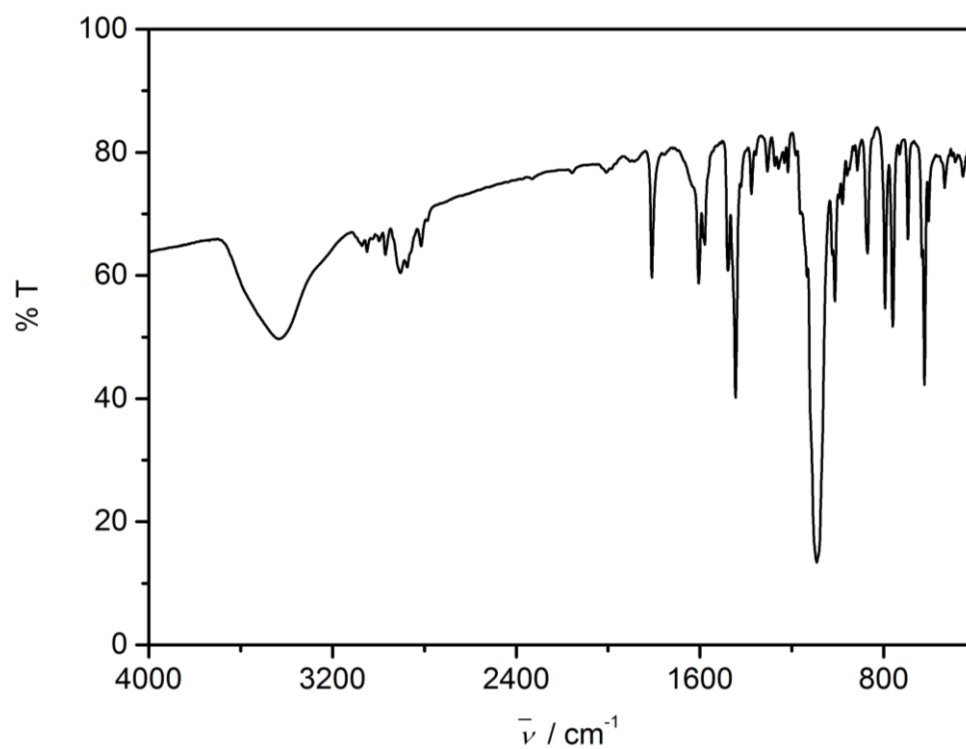


Figure 7.12: IR spectrum of 2a as KBr pellet, prepared by stoichiometric reaction at low temperature to room temperature.

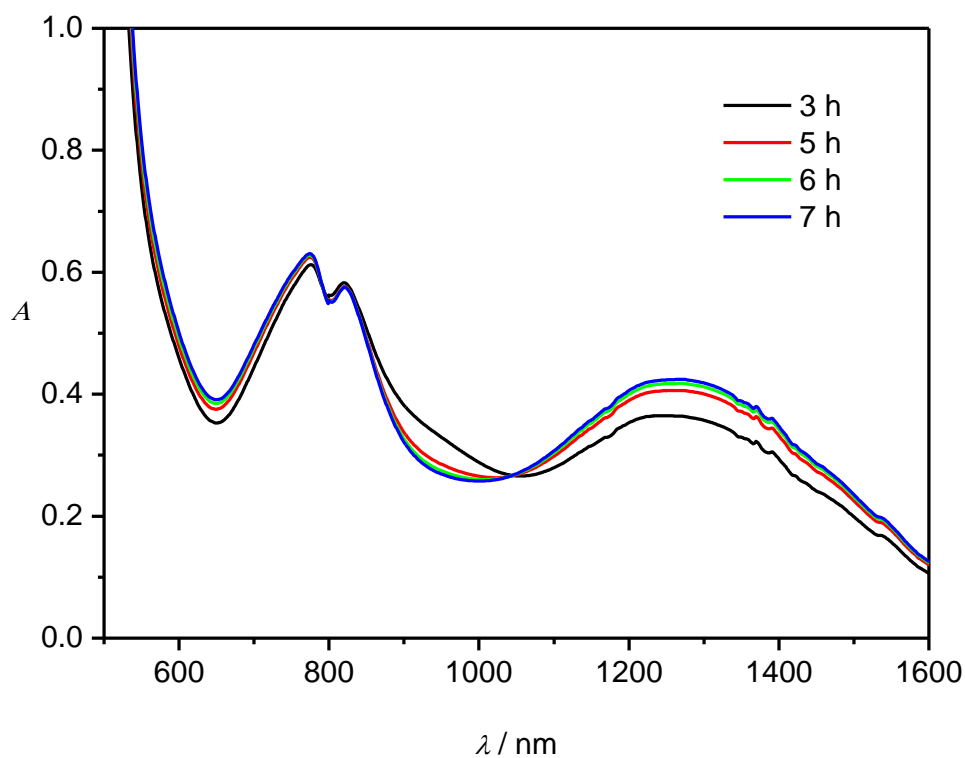


Figure 7.13: UV-Vis-NIR spectral change during the reaction of 1 with PhCClLi at -60°C in EtCN.

7.2.2 $\{[Ni(L-N_4Me_2)]_2(\mu-R_4R)](ClO_4)_2 [R = C_6H_4Me-4] (2b)$ Table 7.4: Crystal data and structure refinement for 2b [R = C₆H₄Me-4] at 293 K

Identification code	11214oa	
Empirical formula	C ₅₀ H ₅₄ Cl ₂ N ₈ Ni ₂ O ₈	
Formula weight	1083.33	
Temperature	293(2) K	
Wavelength	0.71073 Å	
Crystal system	Triclinic	
Space group	P $\bar{1}$	
Unit cell dimensions	a = 9.0140(4) Å	$\alpha = 100.958(3)^\circ$
	b = 11.9024(5) Å	$\beta = 107.618(4)^\circ$
	c = 13.3942(5) Å	$\gamma = 107.150(4)^\circ$
Volume	1245.65(9) Å ³	
Z	1	
Density (calculated)	1.444 Mg/m ³	
Absorption coefficient	0.925 mm ⁻¹	
F(000)	564	
Crystal size	0.41 x 0.39 x 0.18 mm ³	
Theta range for data collection	2.82 to 30.00°.	
Index ranges	-12 ≤ h ≤ 10, -16 ≤ k ≤ 16, -18 ≤ l ≤ 18	
Reflections collected	13503	
Independent reflections	7242 [R(int) = 0.0310]	
Completeness to theta = 30.00°	99.8 %	
Absorption correction	Semi-empirical from equivalents	
Max. and min. transmission	0.8512 and 0.7029	
Refinement method	Full-matrix least-squares on F ²	
Data / restraints / parameters	7242 / 0 / 319	
Goodness-of-fit on F ²	0.910	
Final R indices [I > 2σ(I)]	R1 = 0.0344, wR2 = 0.0783	
R indices (all data)	R1 = 0.0483, wR2 = 0.0810	
Largest diff. peak and hole	0.245 and -0.337 e.Å ⁻³	

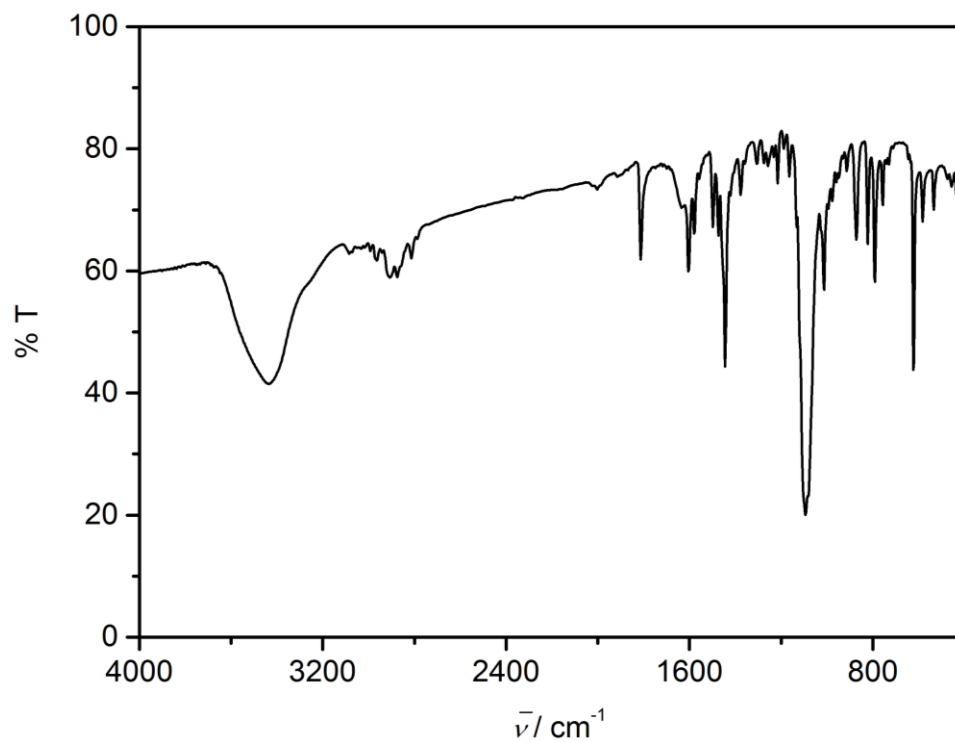


Figure 7.14: IR spectrum of 2b as KBr pellet.

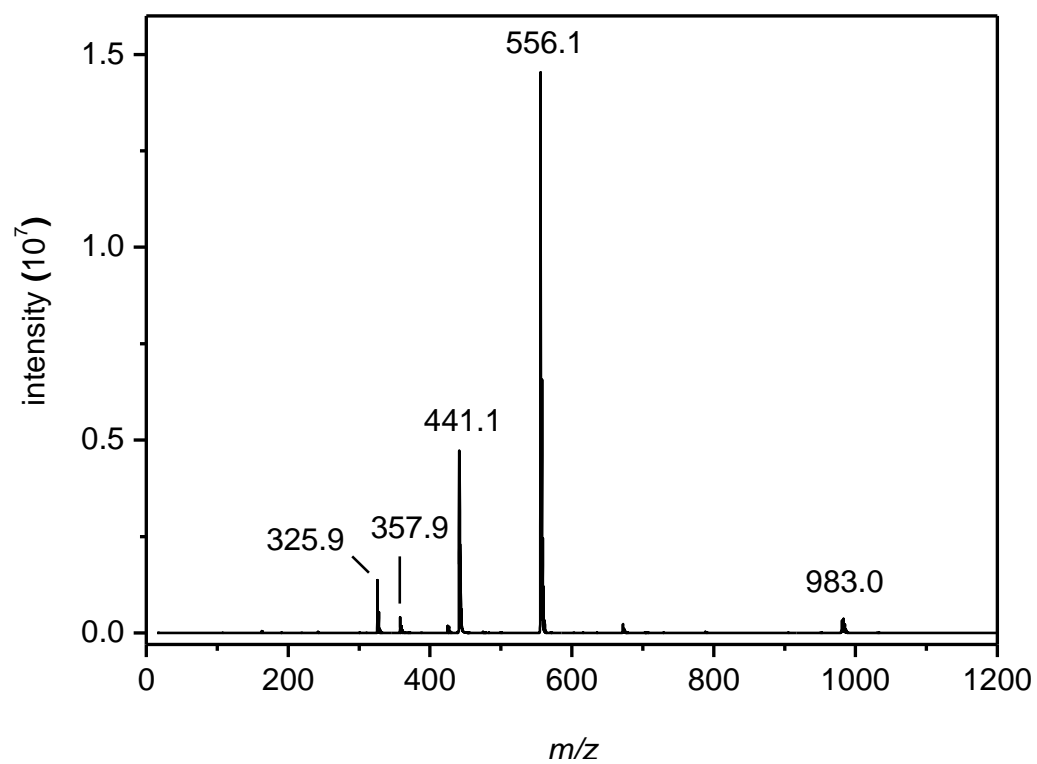


Figure 7.15: ESI-MS spectrum of 2b in MeCN.

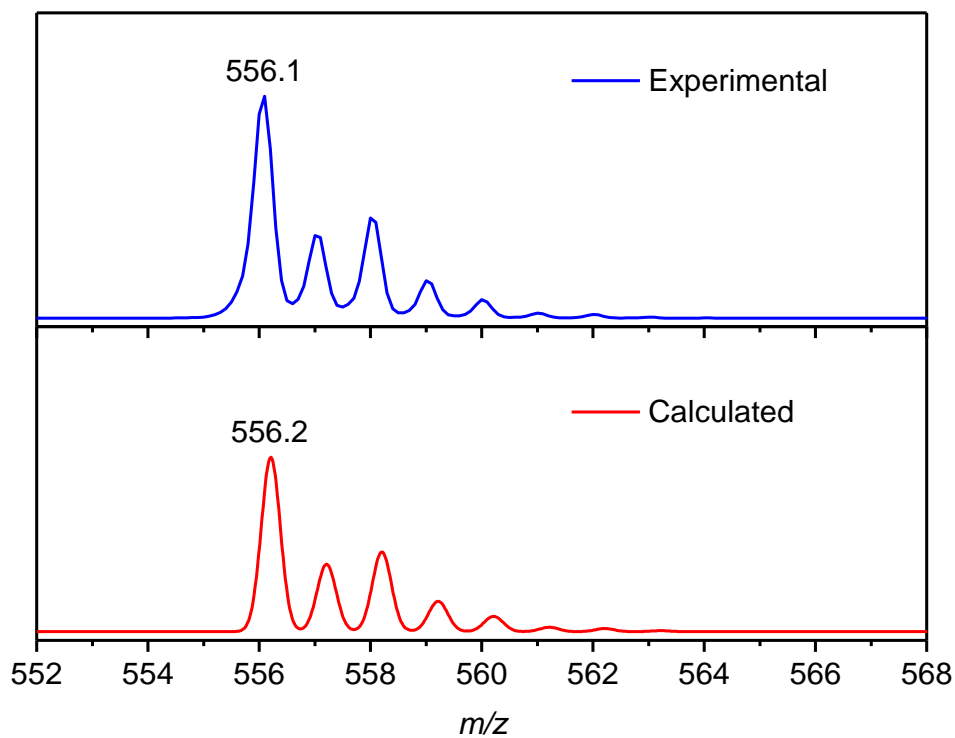


Figure 7.16: The experimental and calculated isotope distribution for $[\text{Ni}(\text{L}-\text{N}_4\text{Me}_2)(\text{RC}_4\text{R})]^+$ [$\text{R} = \text{C}_6\text{H}_4\text{Me}-4$].

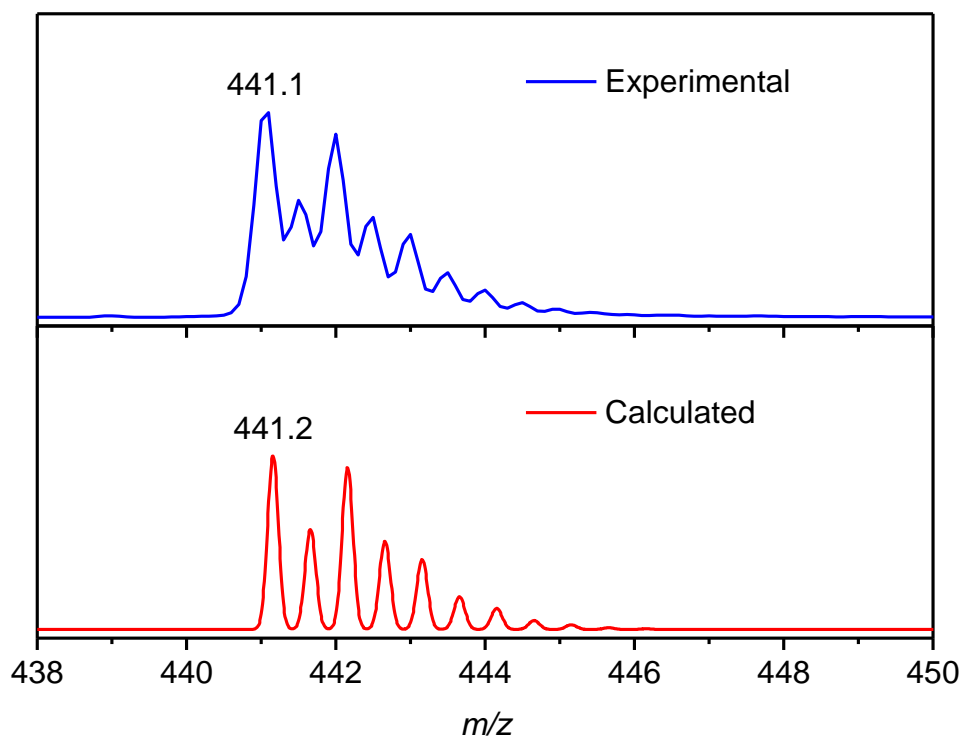


Figure 7.17: The experimental and calculated isotope distribution for $[\{\text{Ni}(\text{L}-\text{N}_4\text{Me}_2)\}_2(\mu\text{-RC}_4\text{R})]^{2+}$ [$\text{R} = \text{C}_6\text{H}_4\text{Me}-4$].

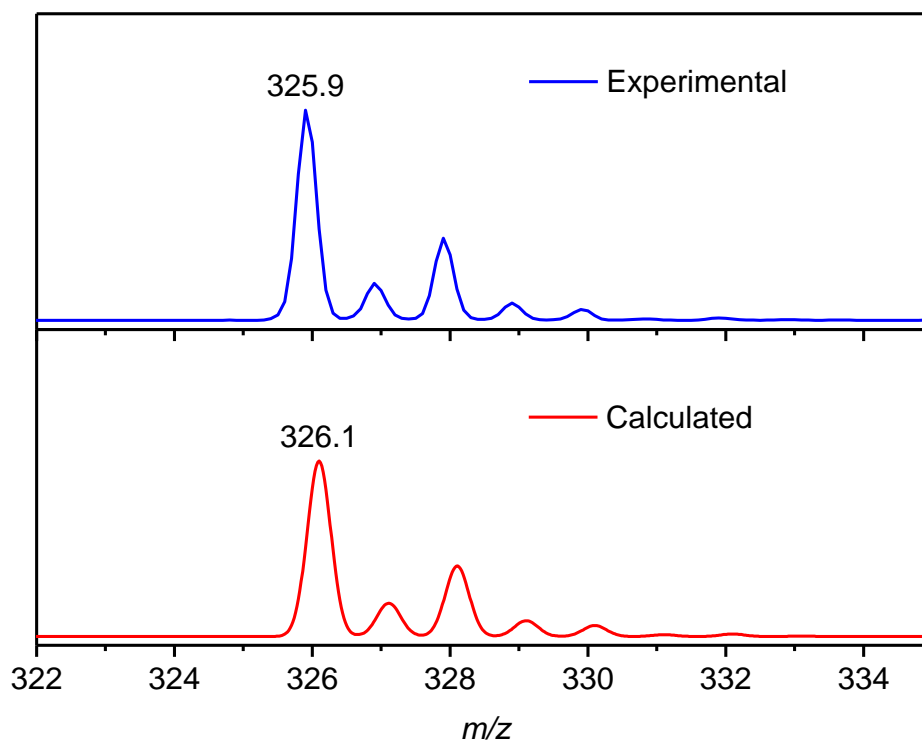


Figure 7.18: The experimental and calculated isotope distribution for $[\text{Ni}(\text{L-N}_4\text{Me}_2)]^+$.

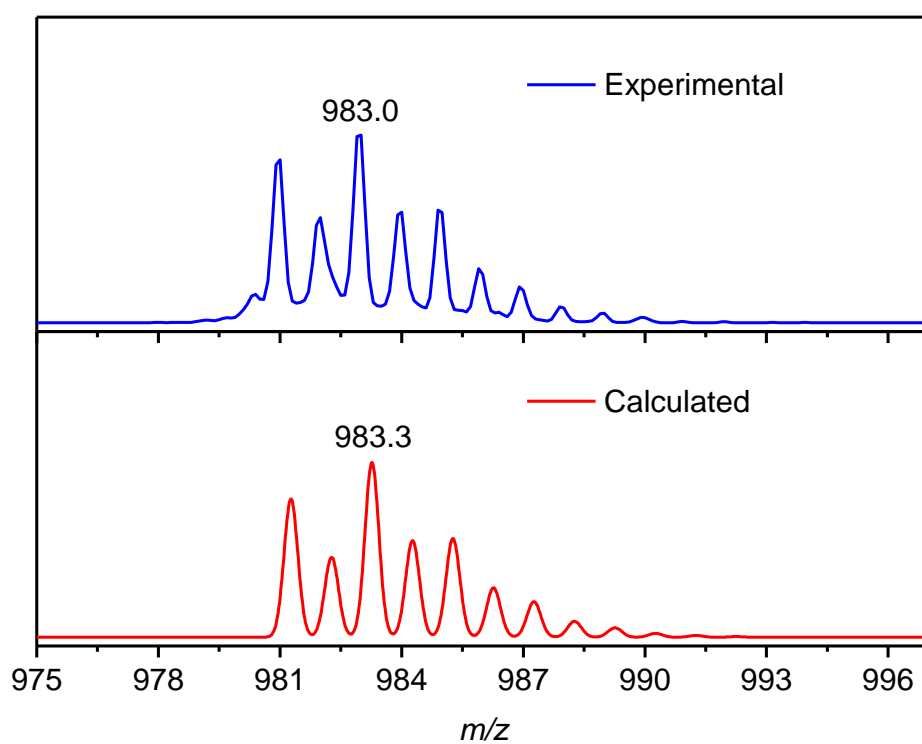


Figure 7.19: The experimental and calculated isotope distribution for $[\{\text{Ni}(\text{L-N}_4\text{Me}_2)\}_2(\mu\text{-RC}_4\text{R})(\text{ClO}_4)]^+$ [$\text{R} = \text{C}_6\text{H}_4\text{Me-4}$].

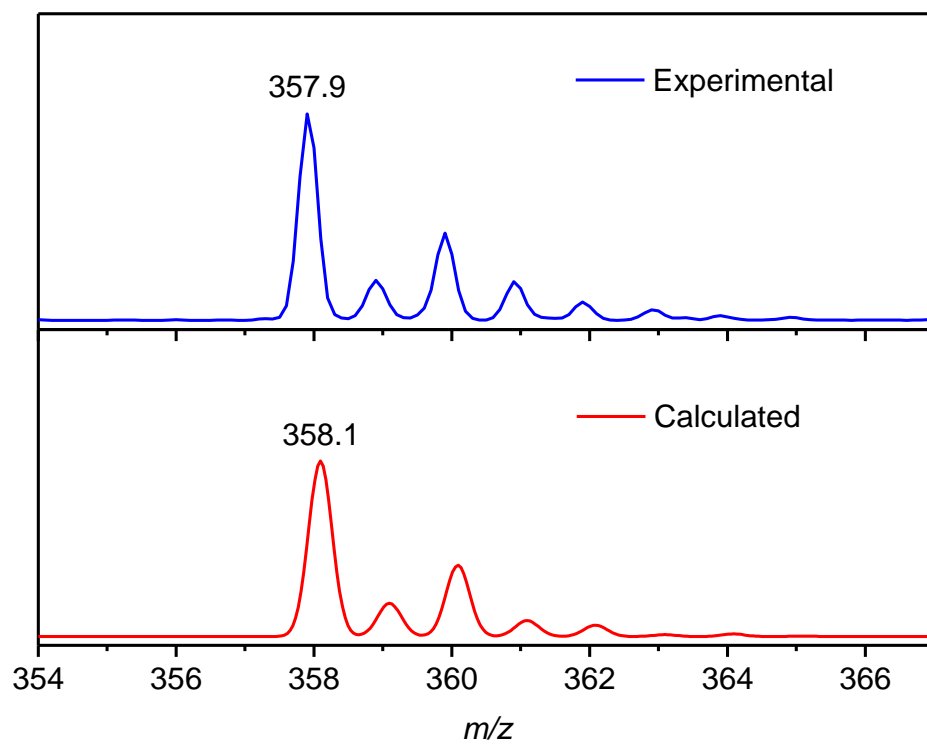


Figure 7.20: The experimental and calculated isotope distribution for $[\text{Ni}(\text{L}-\text{N}_4\text{Me}_2)(\text{O}_2)]^+$ [$\text{R} = \text{C}_6\text{H}_4\text{Me}-4$].

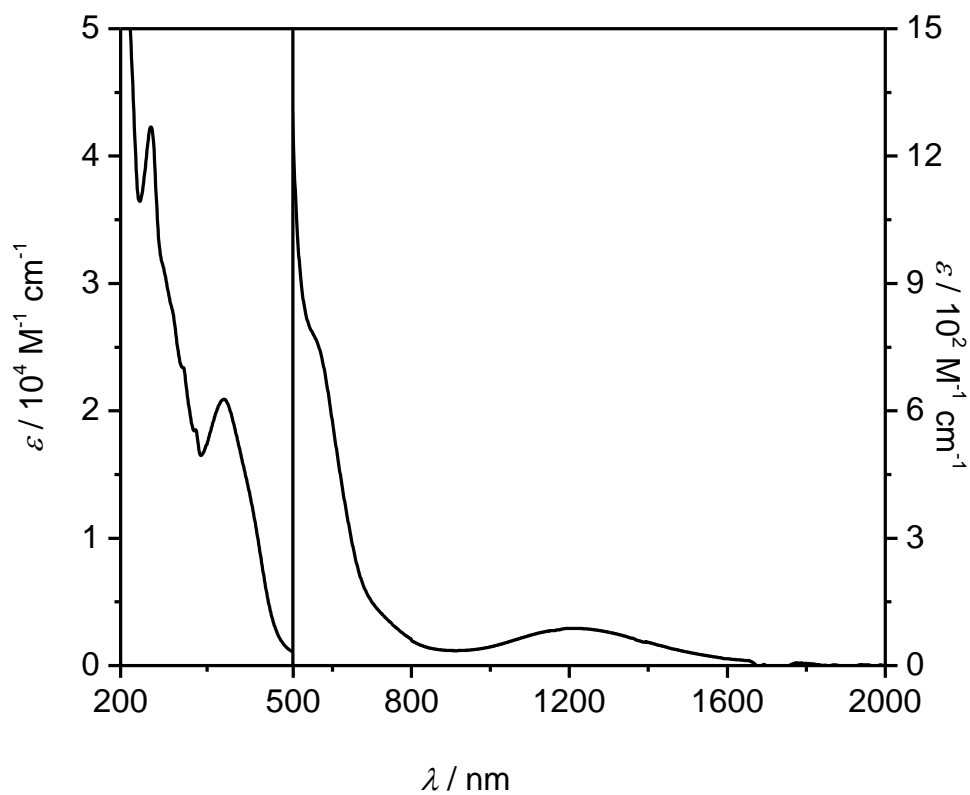


Figure 7.21: UV-Vis-NIR spectrum of 2b in MeCN.

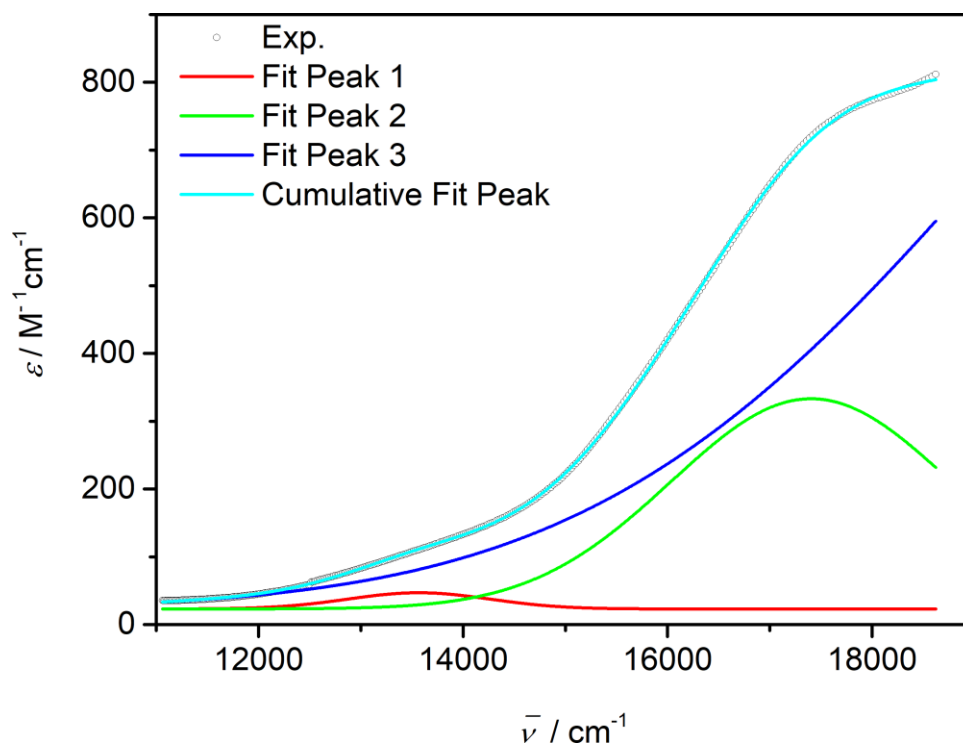


Figure 7.22: Deconvoluted UV-Vis-NIR spectrum of 2b; convolution is performed in 11062 – 18620 cm^{-1} range using Gaussian function.

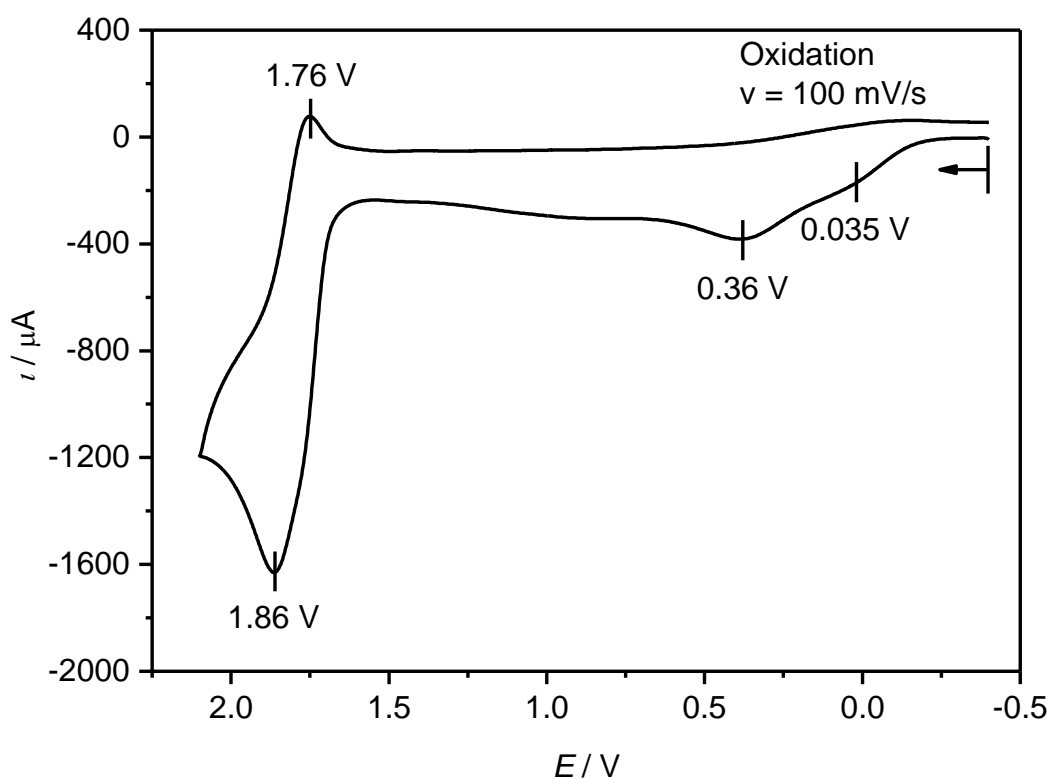


Figure 7.23: Cyclic voltammogram for the oxidation of 2b in 0.2 M TBAP/MeCN sweeping with a scan rate of 100 mV s^{-1} . All potentials are given vs. SCE.

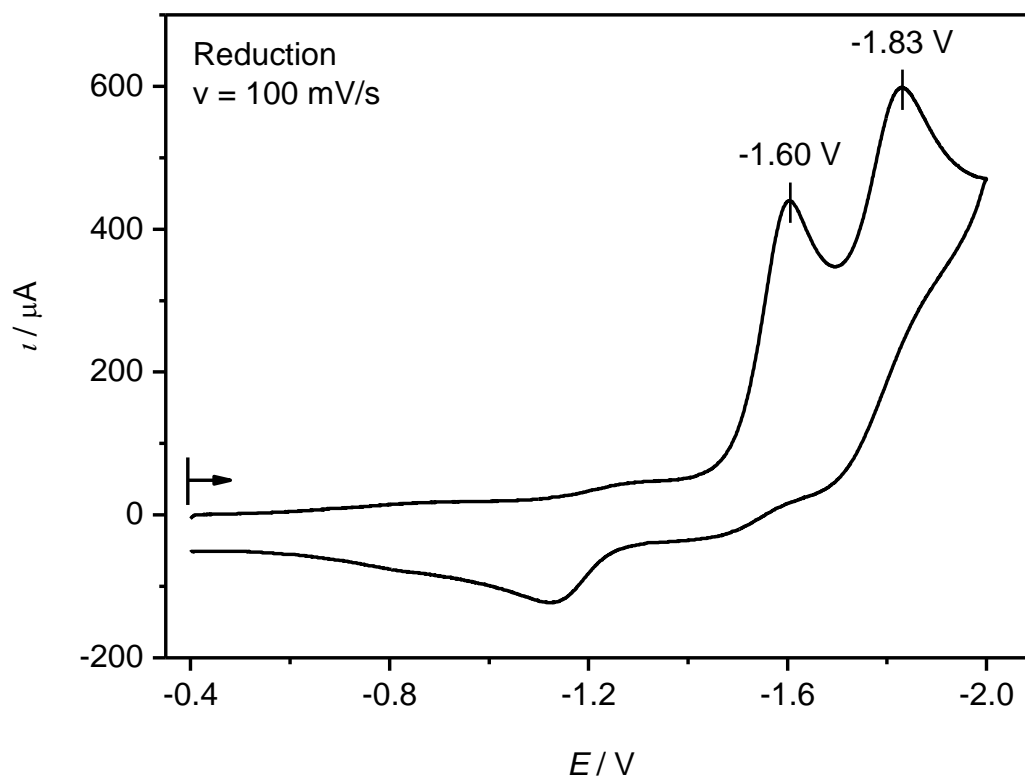


Figure 7.24: Cyclic voltammogram for the reduction of 2b in 0.2 M TBAP/MeCN sweeping with a scan rate of 100 mV s^{-1} . All potentials are given vs. SCE.

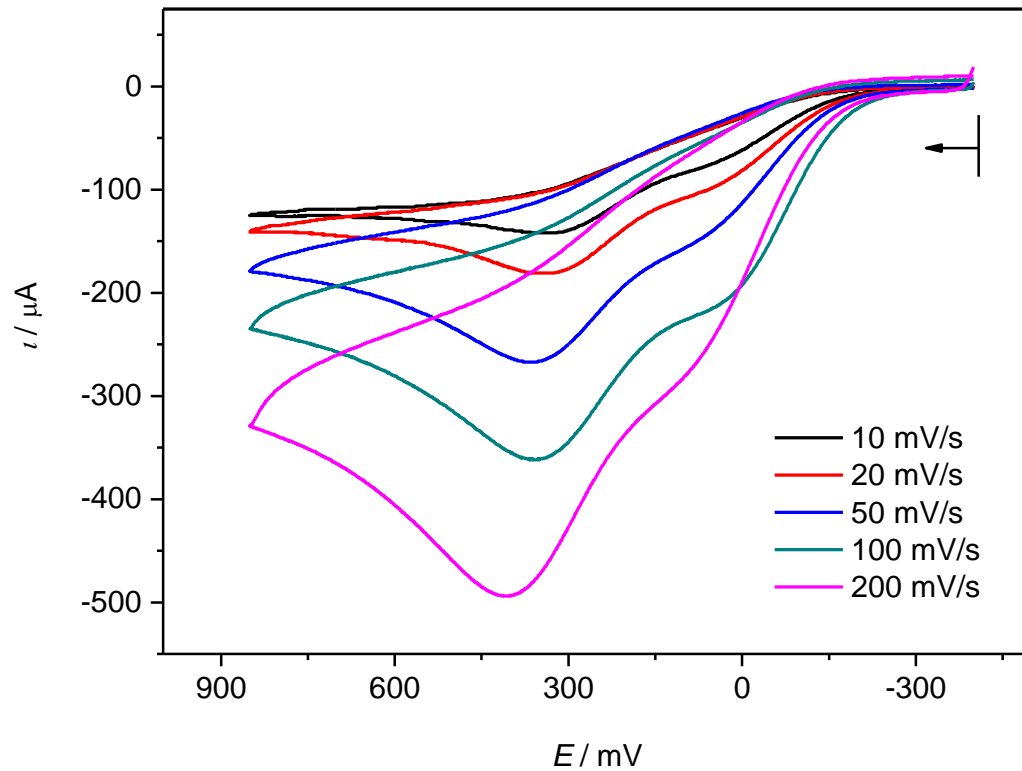


Figure 7.25: Cyclic voltammograms for the oxidation of 2b in 0.2 M TBAP/MeCN sweeping with different scan rates. All potentials are given vs. SCE.

7.2.3 $\{[Ni(L-N_4Me_2)]_2(\mu-R_4R)](ClO_4)_2 [R = C_6H_4F-4] (2c)$ Table 7.5: Crystal data and structure refinement for 2c [R = C₆H₄F-4] at 150 K

Identification code	17030occ
Empirical formula	C ₄₈ H ₄₈ Cl ₂ F ₂ N ₈ Ni ₂ O ₈
Formula weight	1091.26
Temperature	150(2) K
Wavelength	1.54184 Å
Crystal system	Triclinic
Space group	P $\bar{1}$
Unit cell dimensions	a = 8.9133(6) Å α = 98.609(6)° b = 11.0724(8) Å β = 108.412(6)° c = 13.4334(10) Å γ = 104.660(6)°
Volume	1178.25(16) Å ³
Z	1
Density (calculated)	1.538 Mg/m ³
Absorption coefficient	2.644 mm ⁻¹
F(000)	564
Crystal size	0.200 x 0.170 x 0.070 mm ³
Theta range for data collection	3.582 to 62.589°.
Index ranges	-10 ≤ h ≤ 10, -12 ≤ k ≤ 10, -15 ≤ l ≤ 15
Reflections collected	7338
Independent reflections	3727 [R(int) = 0.0233]
Completeness to theta = 30.00°	98.9 %
Absorption correction	Analytical
Max. and min. transmission	0.852 and 0.637
Refinement method	Full-matrix least-squares on F ²
Data / restraints / parameters	3727 / 0 / 318
Goodness-of-fit on F ²	1.067
Final R indices [I > 2σ(I)]	R1 = 0.0398, wR2 = 0.0971
R indices (all data)	R1 = 0.0491, wR2 = 0.1039
Extinction coefficient	n/a
Largest diff. peak and hole	0.324 and -0.571 e.Å ⁻³

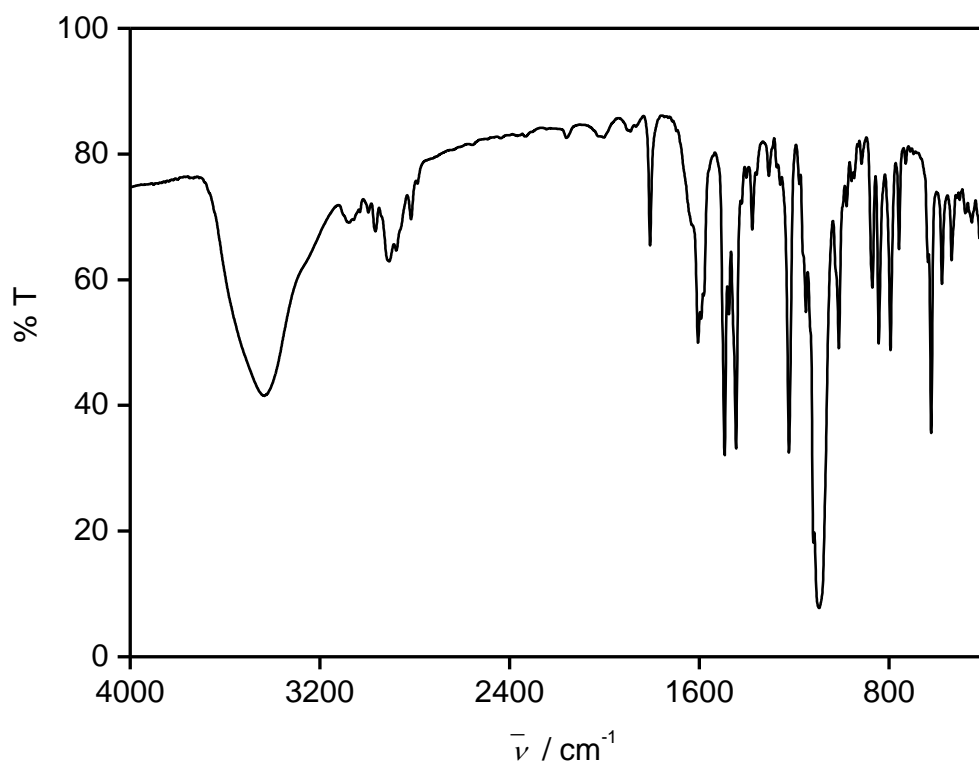


Figure 7.26: IR spectrum of 2c as KBr pellet.

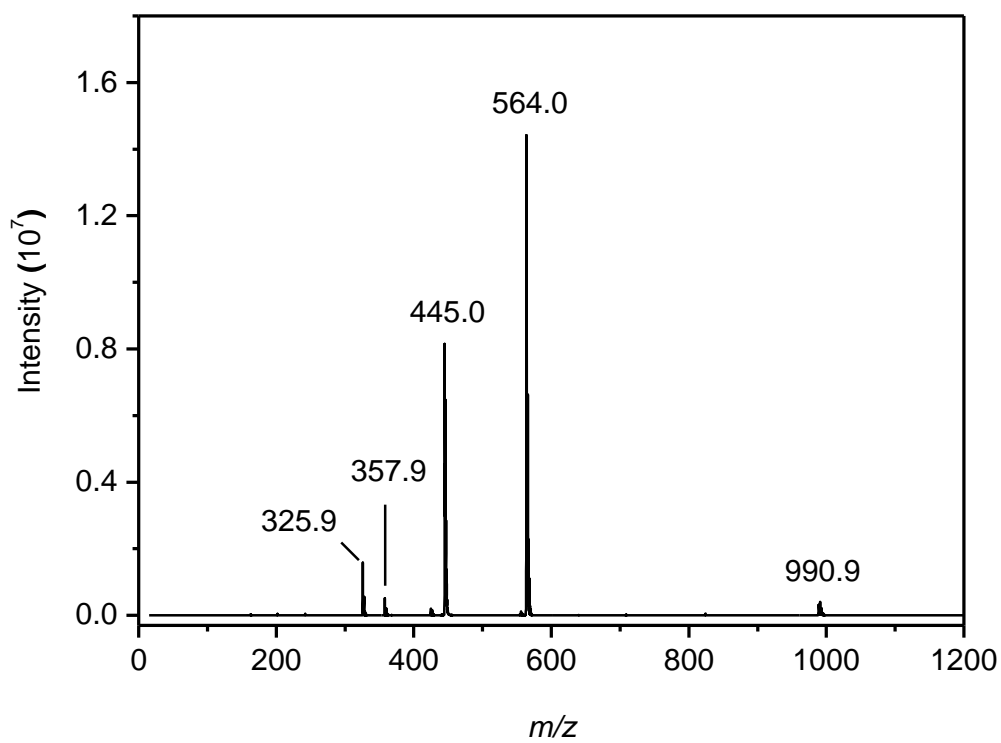


Figure 7.27: ESI-MS spectrum of 2c in MeCN.

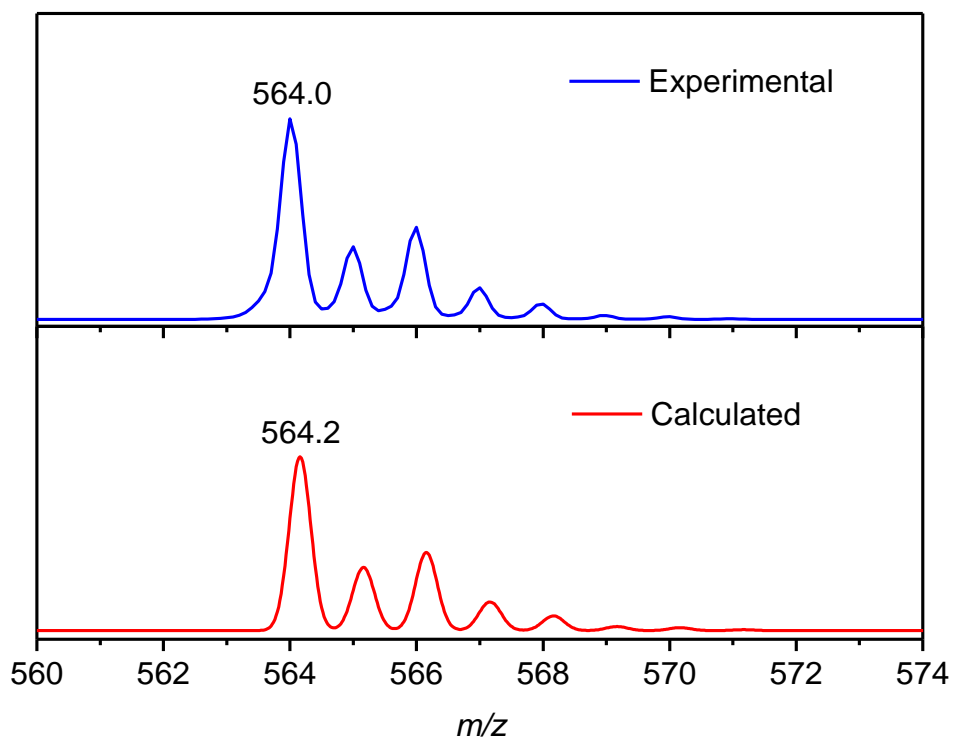


Figure 7.28: The experimental and calculated isotope distribution for $[\text{Ni}(\text{L-N}_4\text{Me}_2)(\text{RC}_4\text{R})]^+$ [$\text{R} = \text{C}_6\text{H}_4\text{F-4}$].

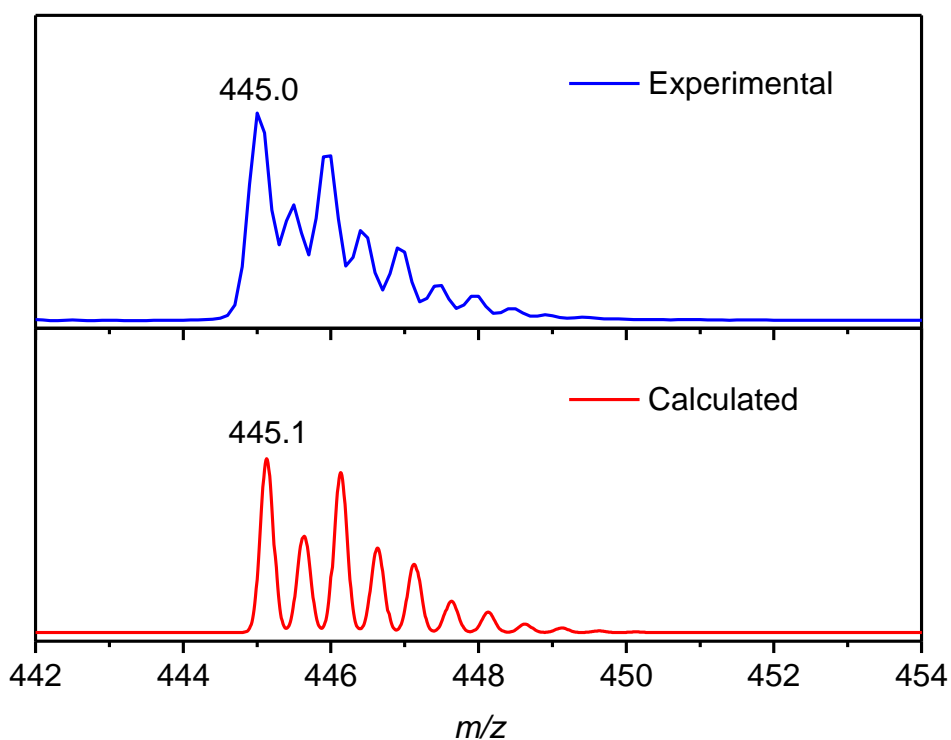


Figure 7.29: The experimental and calculated isotope distribution for $[\{\text{Ni}(\text{L-N}_4\text{Me}_2)\}_2(\mu\text{-RC}_4\text{R})]^{2+}$ [$\text{R} = \text{C}_6\text{H}_4\text{F-4}$].

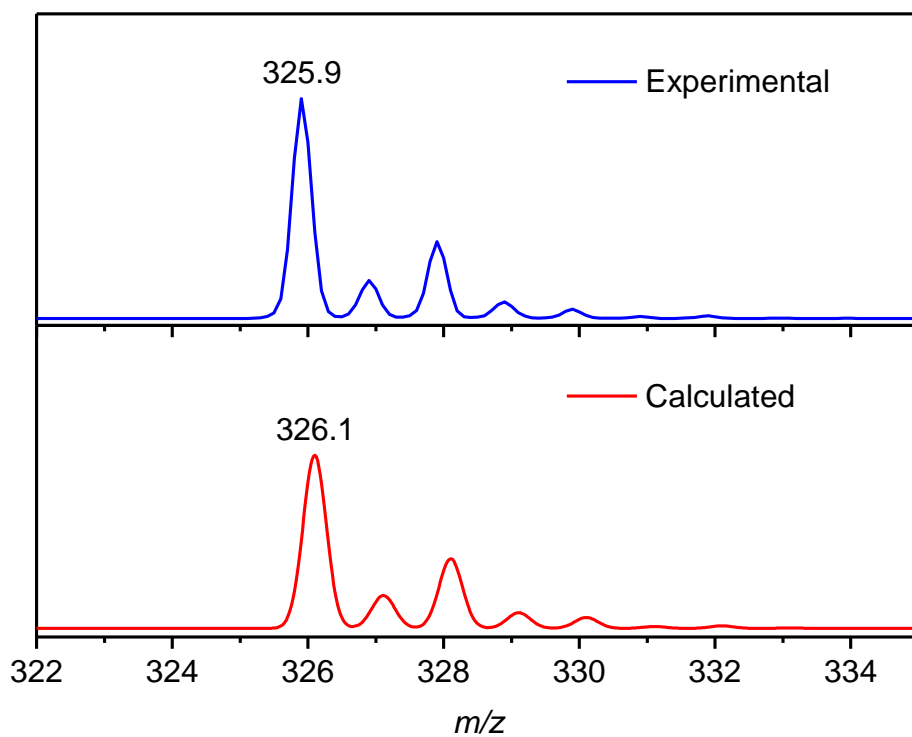


Figure 7.30: The experimental and calculated isotope distribution for $[\text{Ni}(\text{L-N}_4\text{Me}_2)]^+$.

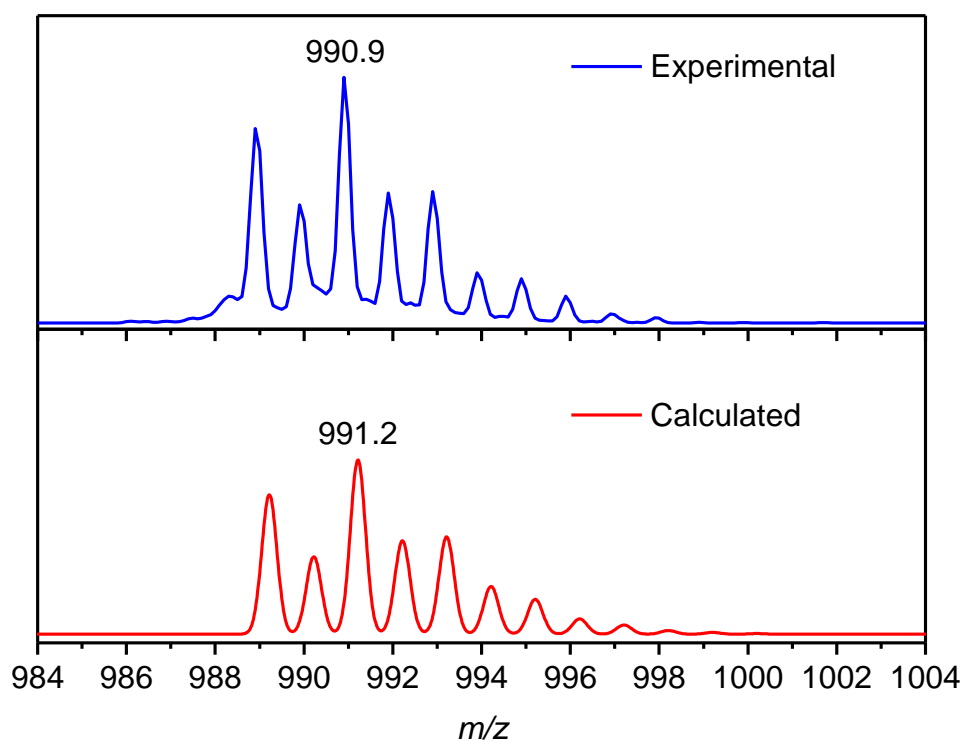


Figure 7.31: The experimental and calculated isotope distribution for $[\{\text{Ni}(\text{L-N}_4\text{Me}_2)\}_2(\mu\text{-RC}_4\text{R})(\text{ClO}_4)]^+$ [$\text{R} = \text{C}_6\text{H}_4\text{F-4}$].

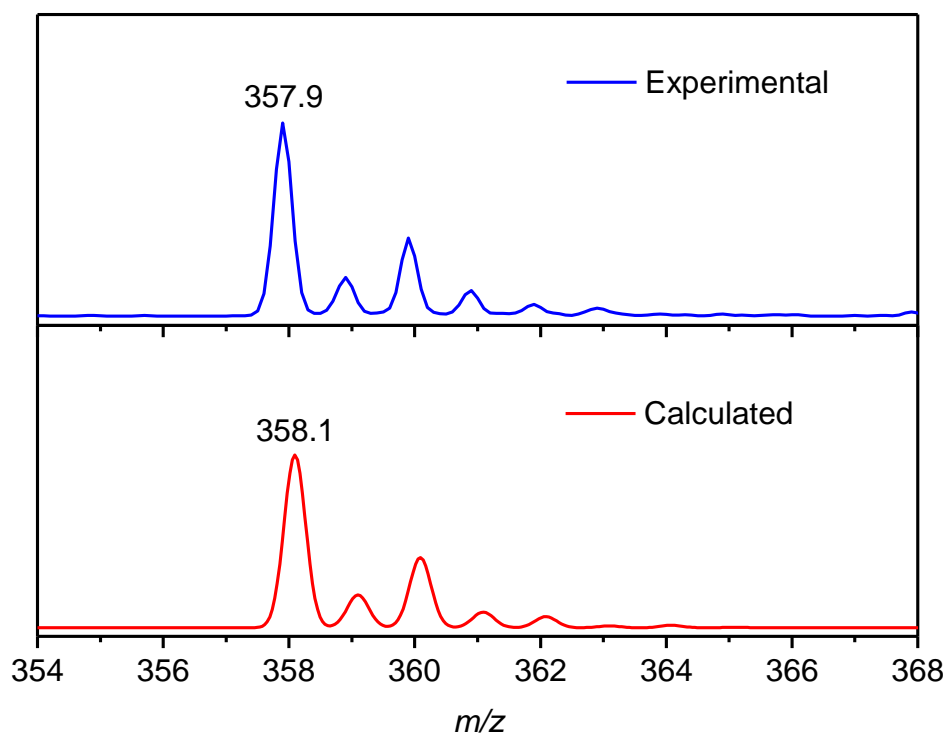


Figure 7.32: The experimental and calculated isotope distribution for $[\text{Ni}(\text{L-N}_4\text{Me}_2)(\text{O}_2)]^+$.

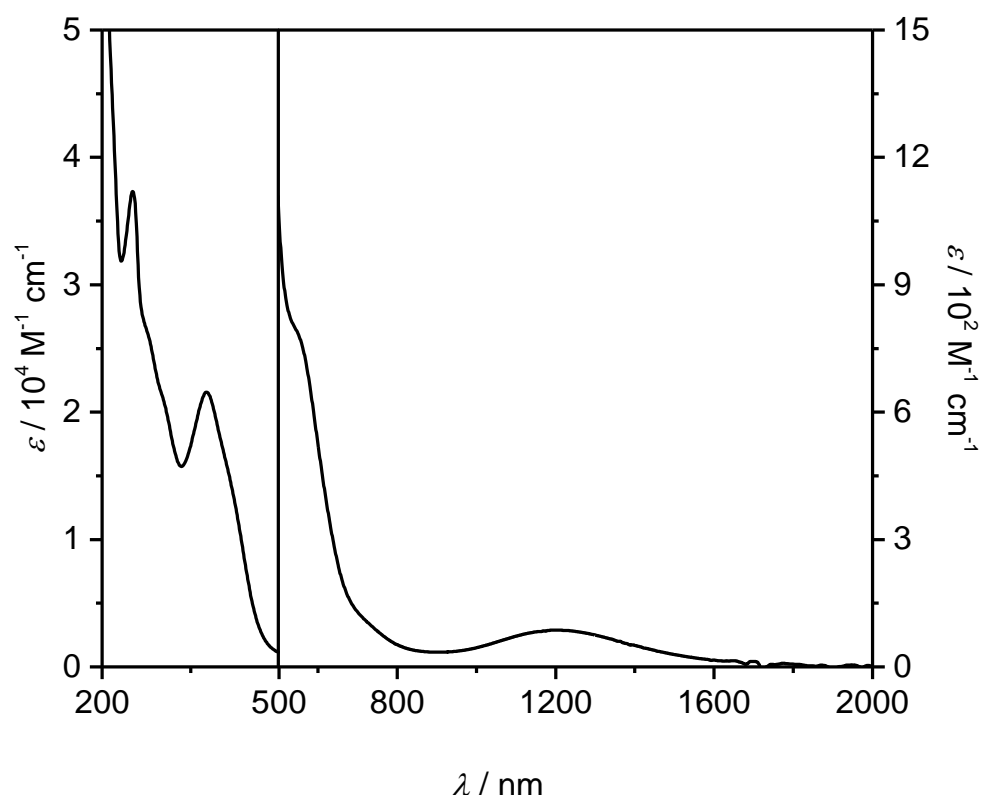


Figure 7.33: UV-Vis-NIR spectrum of 2c in MeCN.

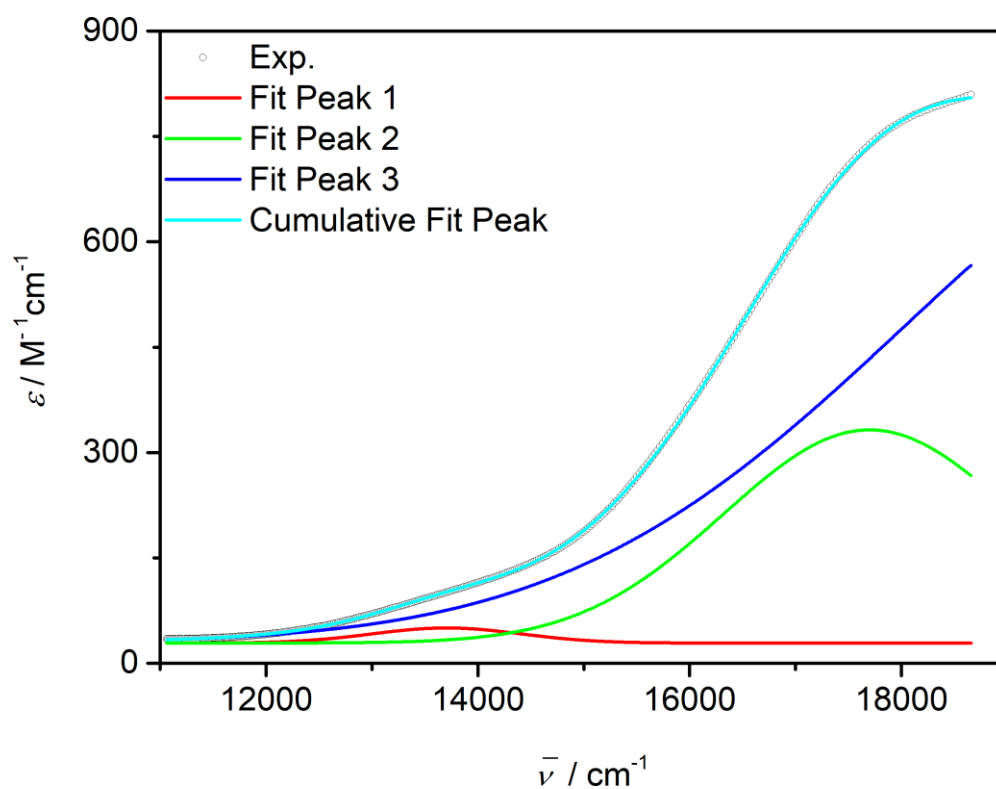


Figure 7.34: Deconvoluted UV-Vis-NIR spectrum of 2c; convolution is performed in 11062 – 18656 cm^{-1} range using Gaussian function.

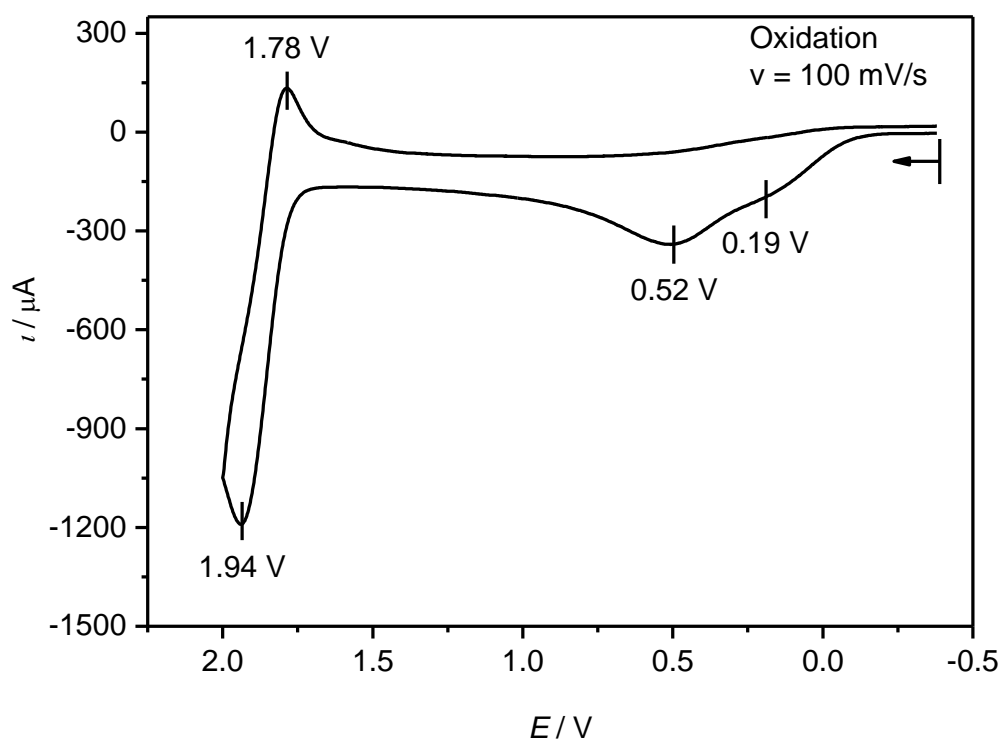


Figure 7.35: Cyclic voltammogram for the oxidation of 2c in 0.2 M TBAP/MeCN sweeping with a scan rate of 100 mV s^{-1} . All potentials are given vs. SCE.

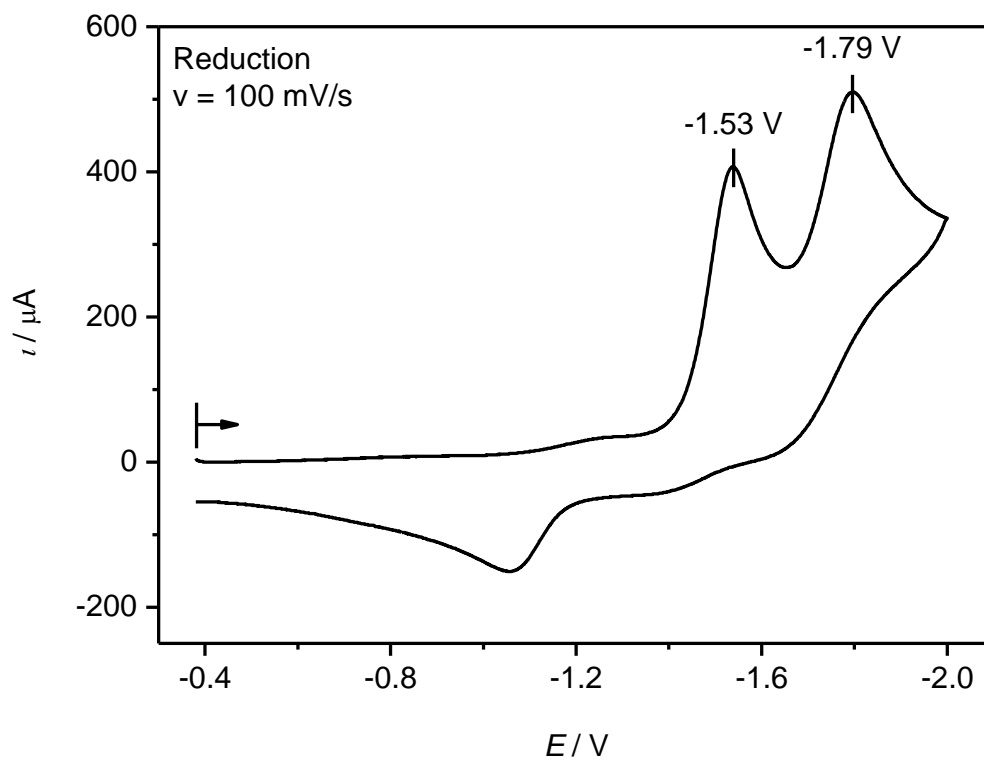


Figure 7.36: Cyclic voltammogram for the reduction of 2c in 0.2 M TBAP/MeCN sweeping with a scan rate of 100 mV s^{-1} . All potentials are given vs. SCE.

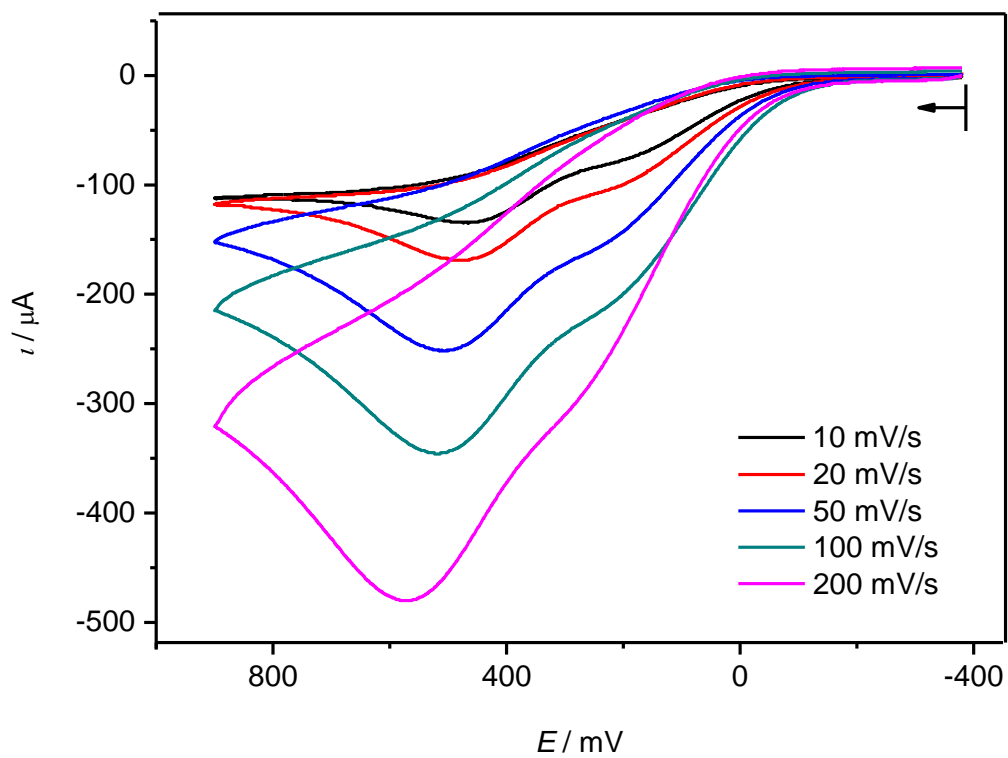


Figure 7.37: Cyclic voltammograms for the oxidation of 2c in 0.2 M TBAP/MeCN sweeping with different scan rates. All potentials are given vs. SCE.

7.2.4 $[\{Ni(L-N_4Me_2)\}_2(\mu-R_4R)](ClO_4)_2 [R = C_6H_4OMe-4] (2d)$ Table 7.6: Crystal data and structure refinement for 2d [R = C₆H₄OMe-4] at 150 K

Identification code	13042o	
Empirical formula	C ₅₀ H ₅₄ Cl ₂ N ₈ Ni ₂ O ₁₀	
Formula weight	1115.33	
Temperature	150(2) K	
Wavelength	0.71073 Å	
Crystal system	Triclinic	
Space group	P $\bar{1}$	
Unit cell dimensions	a = 8.9455(5) Å	$\alpha = 97.826(4)^\circ$
	b = 11.3861(5) Å	$\beta = 108.007(5)^\circ$
	c = 13.5739(7) Å	$\gamma = 106.135(4)^\circ$
Volume	1225.16(11) Å ³	
Z	1	
Density (calculated)	1.512 Mg/m ³	
Absorption coefficient	0.946 mm ⁻¹	
F(000)	580	
Crystal size	0.36 x 0.36 x 0.27 mm ³	
Theta range for data collection	2.80 to 30.00°.	
Index ranges	-8 ≤ h ≤ 12, -16 ≤ k ≤ 14, -19 ≤ l ≤ 17	
Reflections collected	12286	
Independent reflections	7124 [R(int) = 0.0182]	
Completeness to theta = 30.00°	99.7 %	
Absorption correction	Semi-empirical from equivalents	
Max. and min. transmission	0.7843 and 0.7271	
Refinement method	Full-matrix least-squares on F ²	
Data / restraints / parameters	7124 / 0 / 328	
Goodness-of-fit on F ²	1.050	
Final R indices [I > 2σ(I)]	R1 = 0.0296, wR2 = 0.0678	
R indices (all data)	R1 = 0.0344, wR2 = 0.0701	
Largest diff. peak and hole	0.415 and -0.347 e.Å ⁻³	

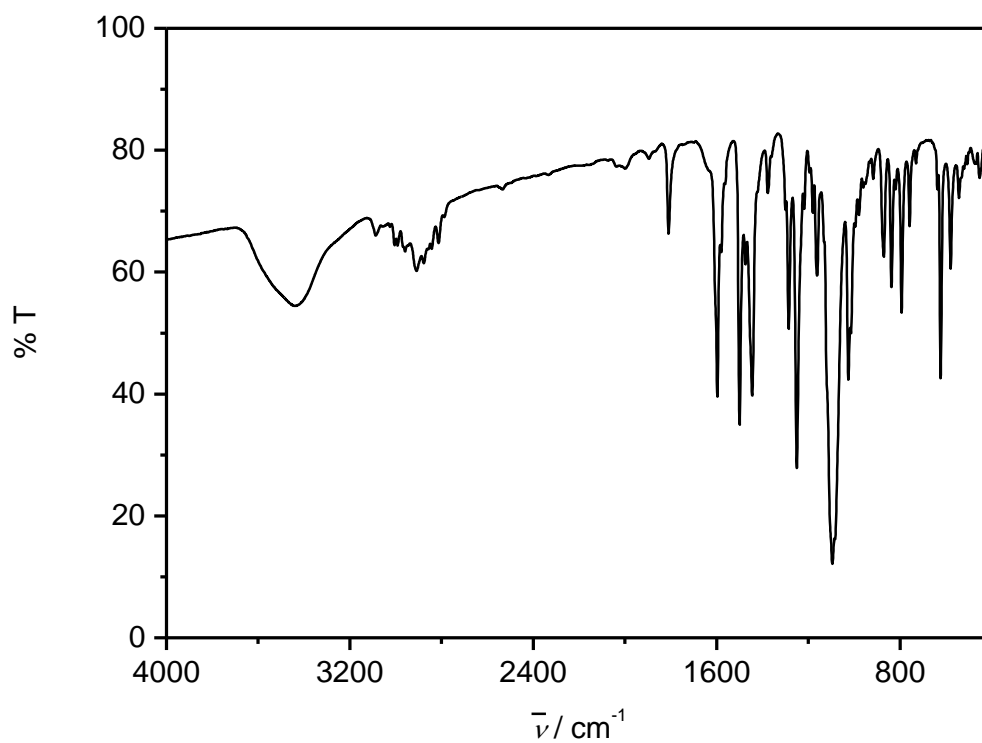


Figure 7.38: IR spectrum of 2d as KBr pellet.

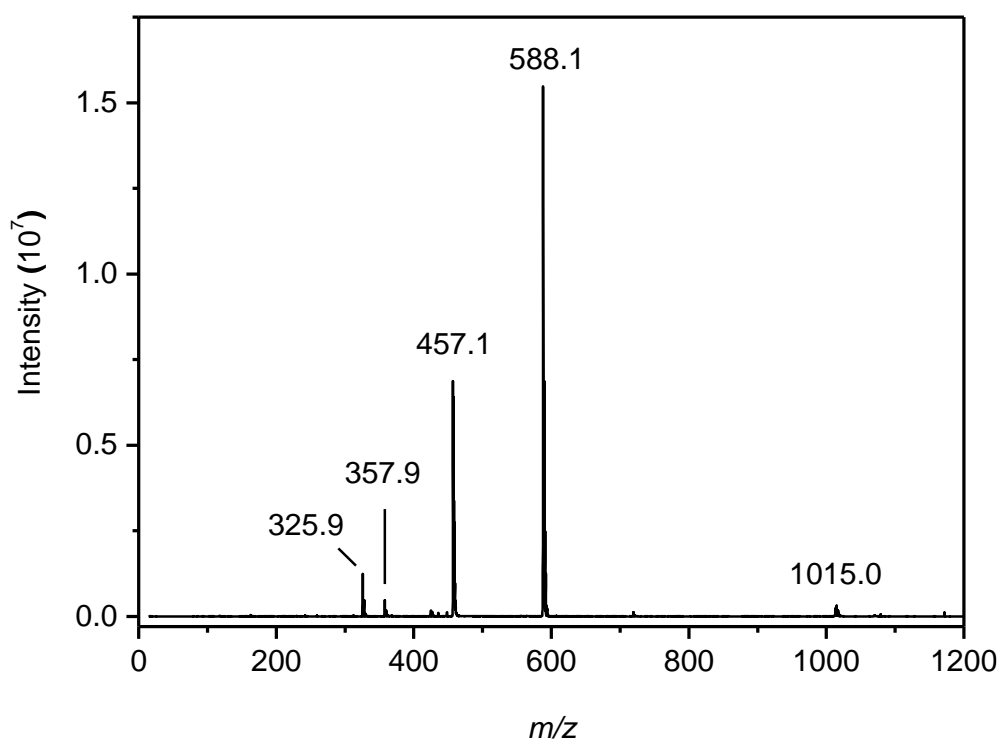


Figure 7.39: ESI-MS spectrum of 2d in MeCN.

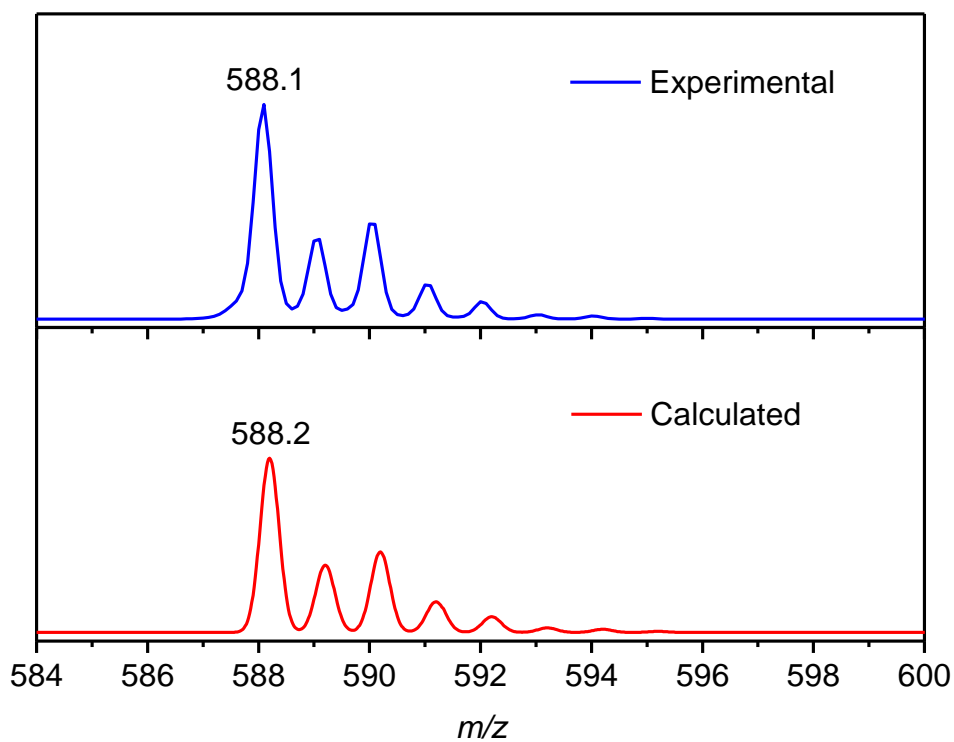


Figure 7.40: The experimental and calculated isotope distribution for $[\text{Ni}(\text{L}-\text{N}_4\text{Me}_2)(\text{RC}_4\text{R})]^+$ [$\text{R} = \text{C}_6\text{H}_4\text{OMe-4}$].

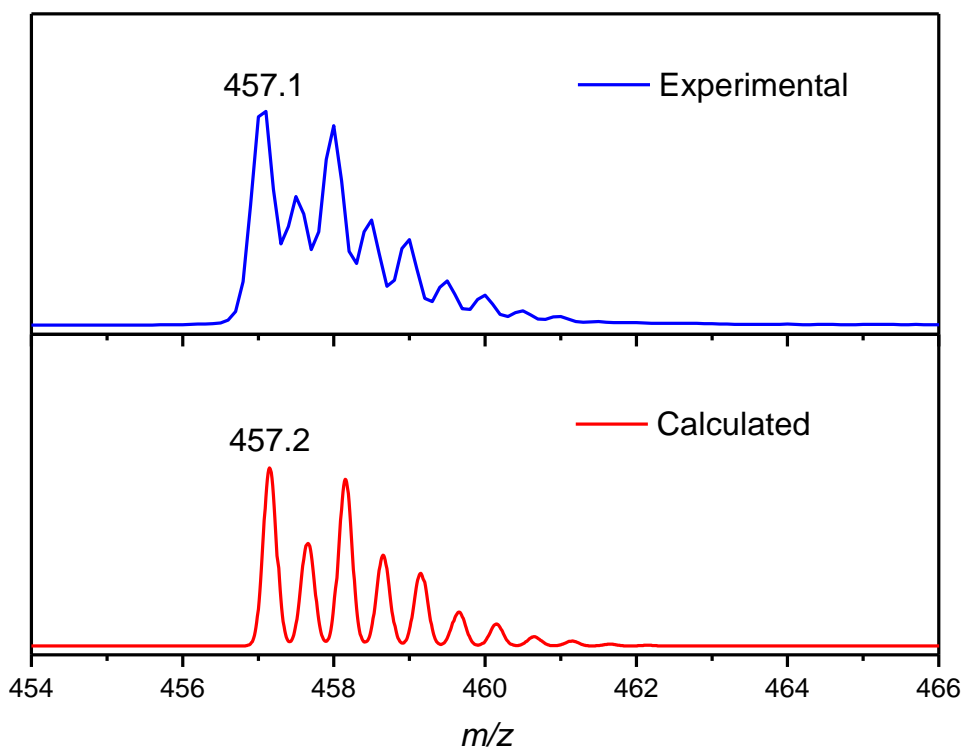


Figure 7.41: The experimental and calculated isotope distribution for $[\{\text{Ni}(\text{L}-\text{N}_4\text{Me}_2)\}_2(\mu\text{-RC}_4\text{R})]^{2+}$ [$\text{R} = \text{C}_6\text{H}_4\text{OMe-4}$].

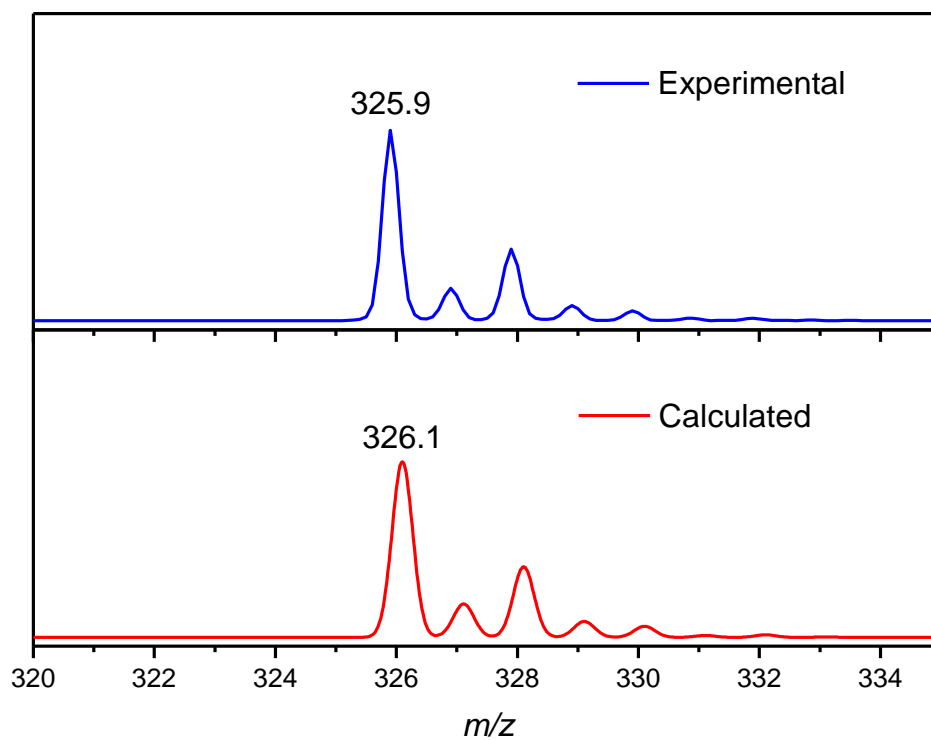


Figure 7.42: The experimental and calculated isotope distribution for $[\text{Ni}(\text{L-N}_4\text{Me}_2)]^+$.

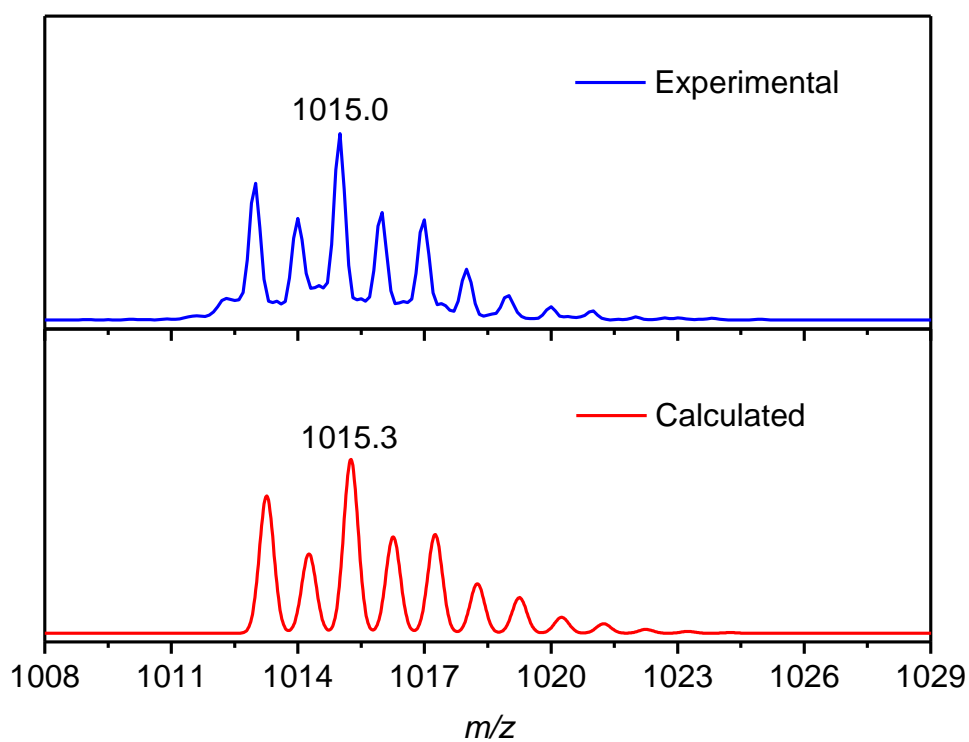


Figure 7.43: The experimental and calculated isotope distribution for $[\{\text{Ni}(\text{L-N}_4\text{Me}_2)_2(\mu\text{-RC}_4\text{R})(\text{ClO}_4)\}]^+$ [$\text{R} = \text{C}_6\text{H}_4\text{OMe-4}$].

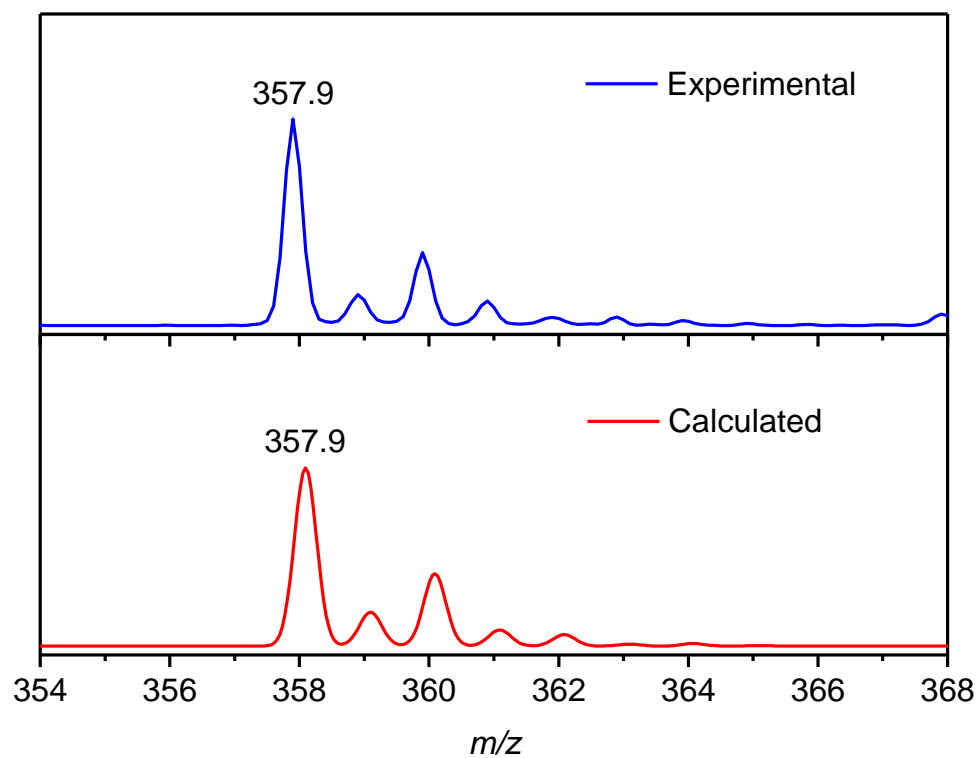


Figure 7.44: The experimental and calculated isotope distribution for $[\text{Ni}(\text{L-N}_4\text{Me}_2)(\text{O}_2)]^+$.

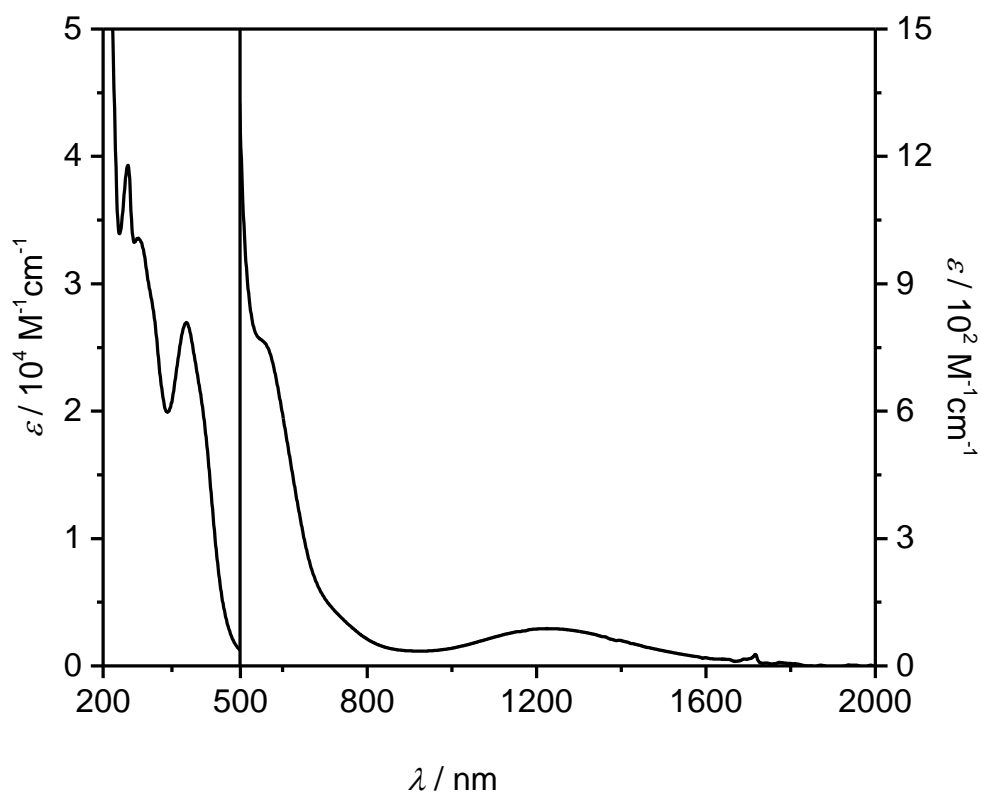


Figure 7.45: UV-Vis-NIR spectrum of 2d in MeCN.

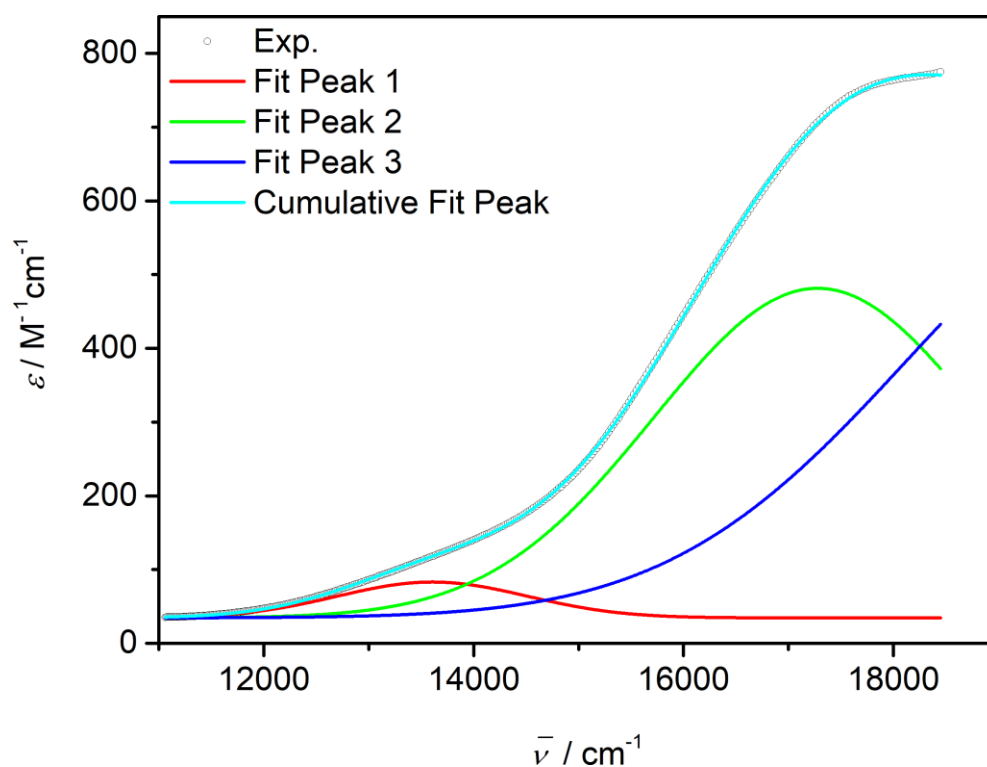


Figure 7.46: Deconvoluted UV-Vis-NIR spectrum of 2d; convolution is performed in 11000 – 18450 cm^{-1} range using Gaussian function.

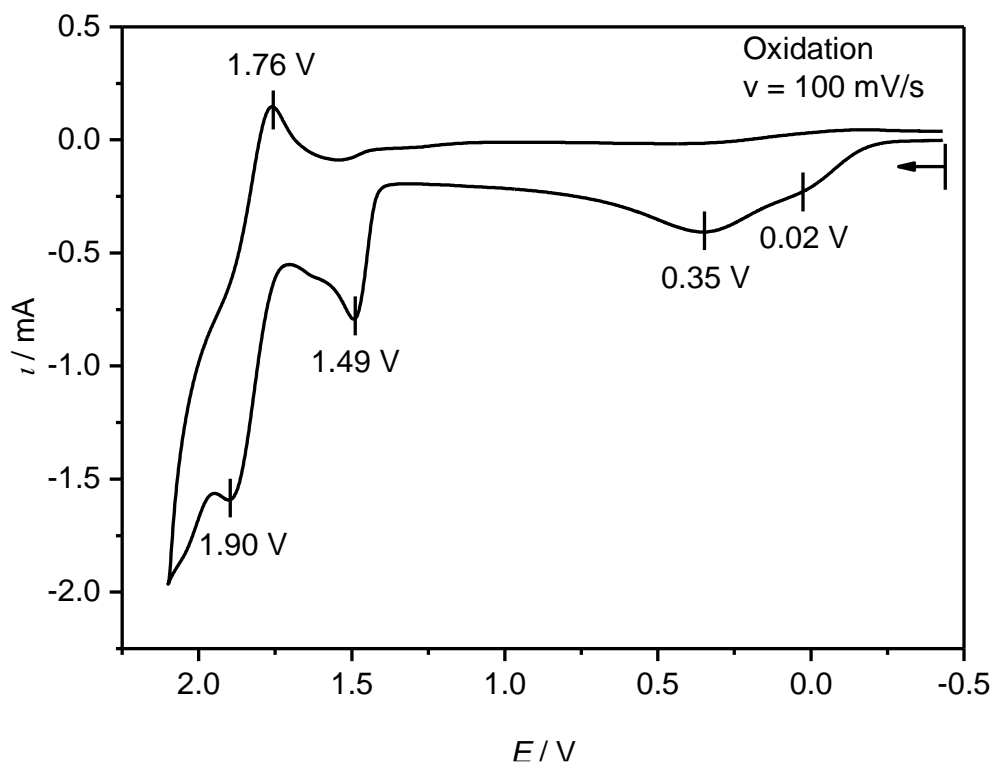


Figure 7.47: Cyclic voltammogram for the oxidation of 2d in 0.2 M TBAP/MeCN sweeping with a scan rate of 100 mV s^{-1} . All potentials are given vs. SCE.

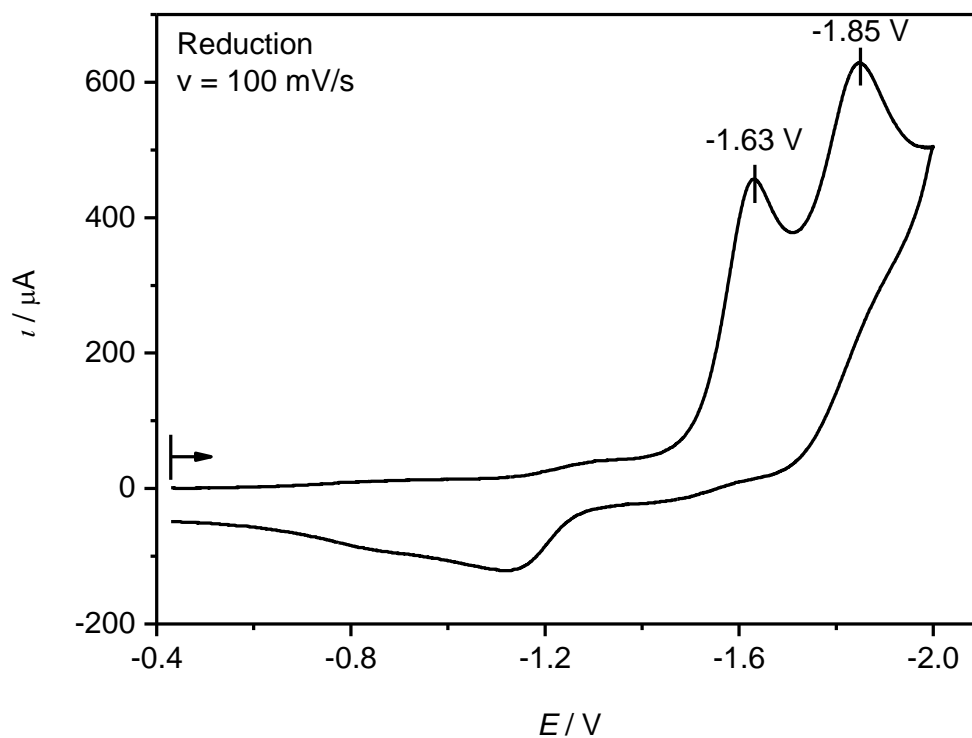


Figure 7.48: Cyclic voltammogram for the reduction of 2d in 0.2 M TBAP/MeCN sweeping with a scan rate of 100 mV s^{-1} . All potentials are given vs. SCE.

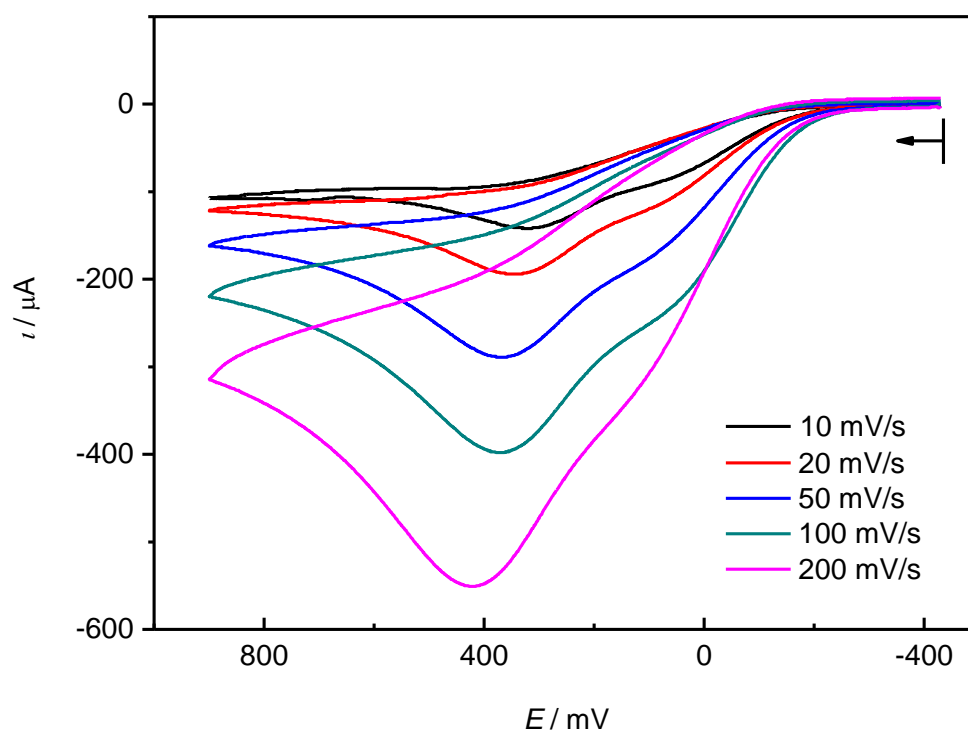


Figure 7.49: Cyclic voltammograms for the oxidation of 2d in 0.2 M TBAP/MeCN sweeping with different scan rates. All potentials are given vs. SCE.

7.2.5 $\{[Ni(L-N_4Me_2)]_2(\mu-R_4R)\}(ClO_4)_2$ [$R = C_6H_4NMe_2-4$] (2e)Table 7.7: Crystal data and structure refinement for 2e [$R = C_6H_4NMe_2-4$] at 150 K

Identification code	13206od
Empirical formula	$C_{52}H_{60}Cl_2N_{10}Ni_2O_8$
Formula weight	1141.42
Temperature	150(2) K
Wavelength	0.71073 Å
Crystal system	Triclinic
Space group	$P\bar{1}$
Unit cell dimensions	$a = 12.0739(5)$ Å $\alpha = 110.472(4)^\circ$. $b = 14.4830(6)$ Å $\beta = 94.892(3)^\circ$. $c = 16.7908(7)$ Å $\gamma = 105.787(4)^\circ$.
Volume	2593.4(2) Å ³
Z	2
Density (calculated)	1.462 Mg/m ³
Absorption coefficient	0.894 mm ⁻¹
F(000)	1192
Crystal size	0.520 x 0.220 x 0.090 mm ³
Theta range for data collection	2.749 to 30.000°.
Index ranges	-16 ≤ h ≤ 16, -20 ≤ k ≤ 20, -23 ≤ l ≤ 23
Reflections collected	33410
Independent reflections	15107 [R(int) = 0.0321]
Completeness to theta = 30.00°	99.7 %
Absorption correction	Semi-empirical from equivalents
Max. and min. transmission	1.00000 and 0.79657
Refinement method	Full-matrix least-squares on F ²
Data / restraints / parameters	15107 / 0 / 675
Goodness-of-fit on F ²	1.048
Final R indices [I > 2σ(I)]	R1 = 0.0398, wR2 = 0.0851
R indices (all data)	R1 = 0.0529, wR2 = 0.0906
Extinction coefficient	n/a
Largest diff. peak and hole	0.613 and -0.569 e.Å ⁻³

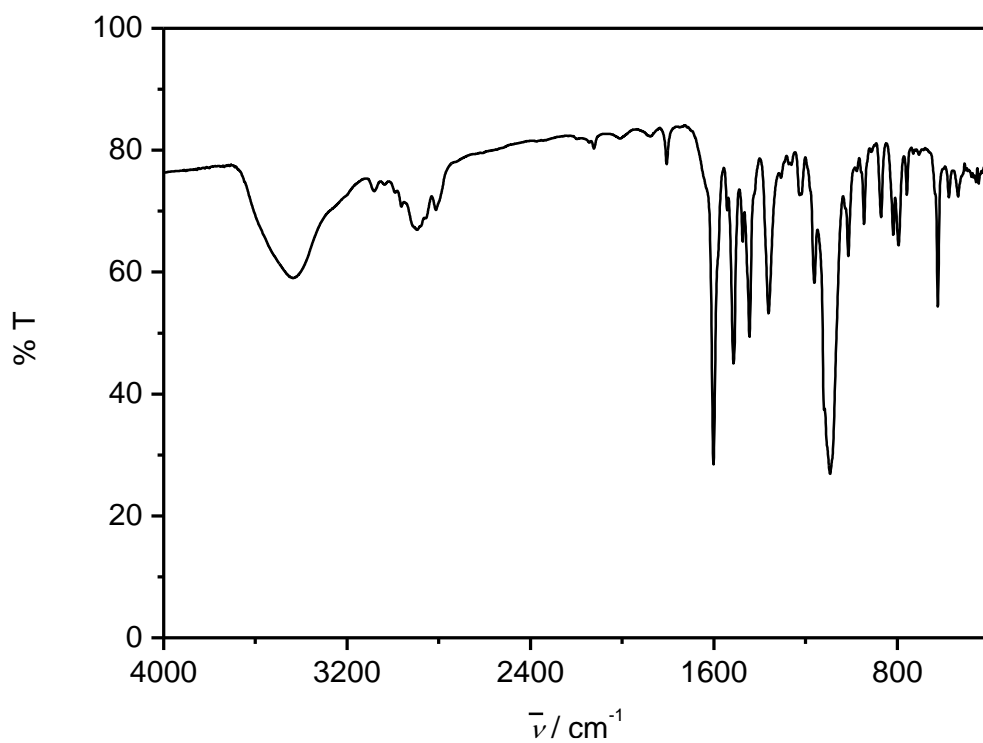


Figure 7.50: IR spectrum of 2e as KBr pellet.

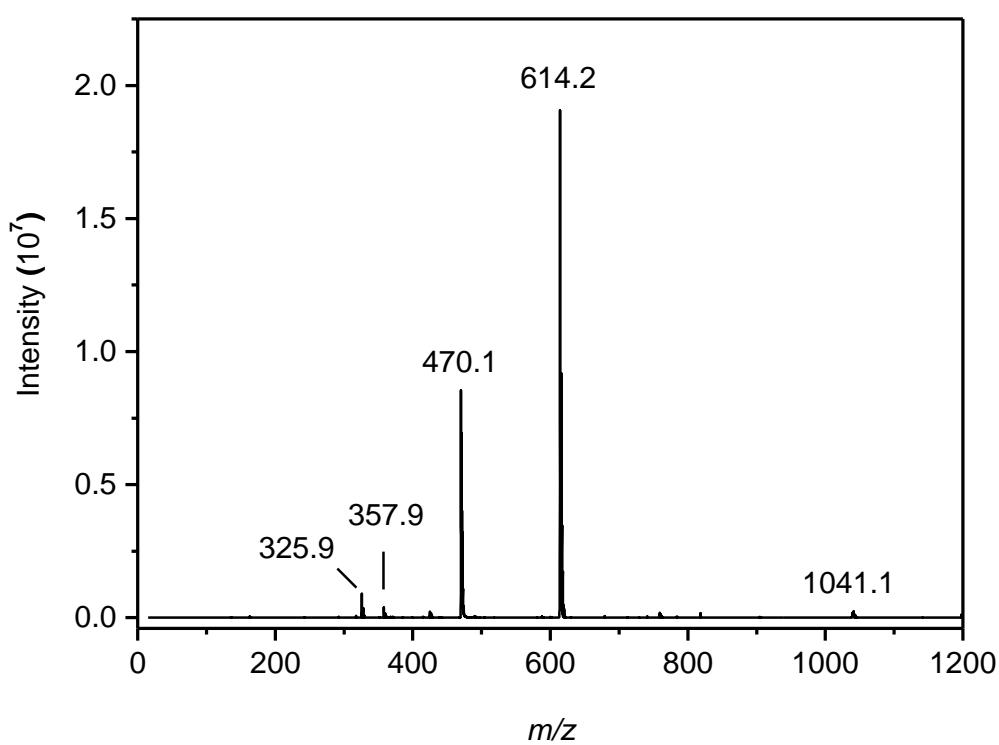


Figure 7.51: ESI-MS spectrum of 2e in MeCN.

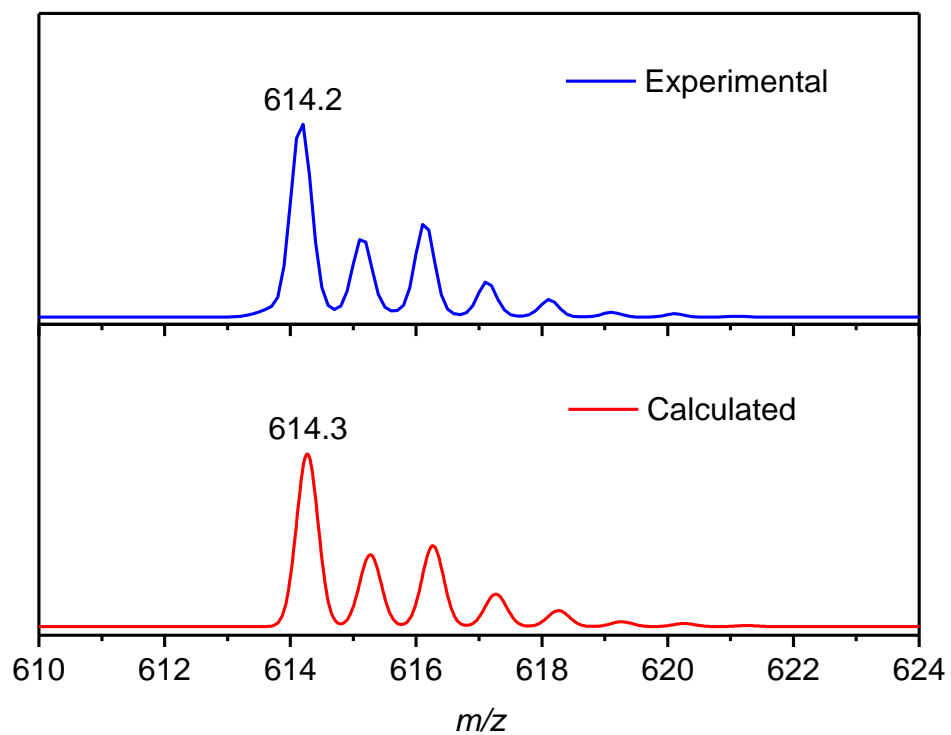


Figure 7.52: The experimental and calculated isotope distribution for $[\text{Ni}(\text{L-N}_4\text{Me}_2)(\text{RC}_4\text{R})]^+$ [$\text{R} = \text{C}_6\text{H}_4\text{NMe}_2-4$].

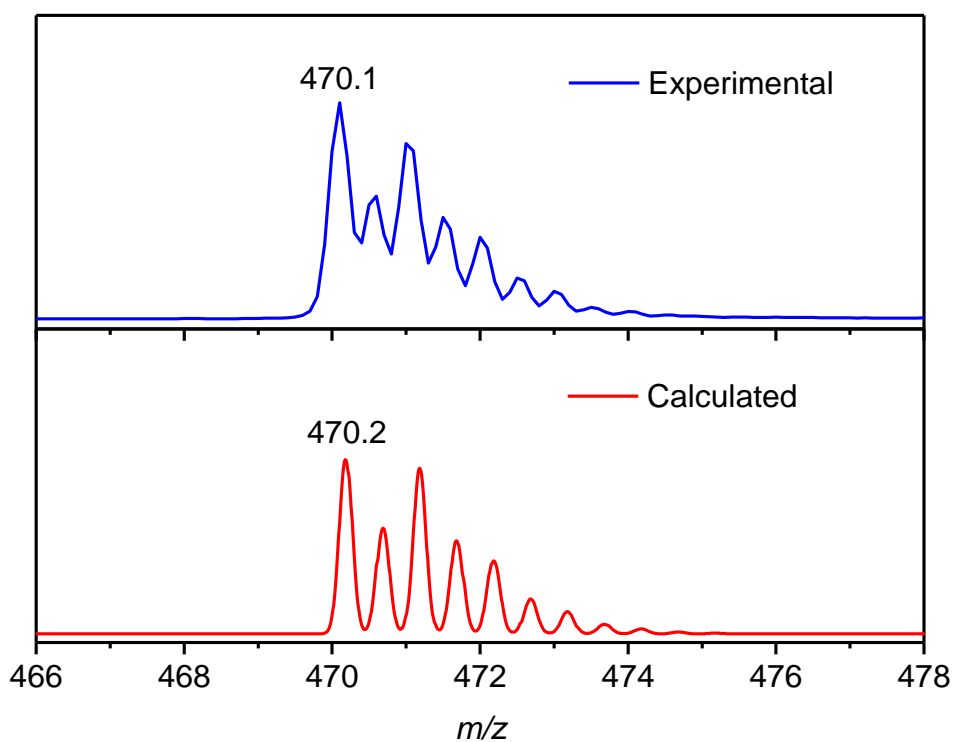


Figure 7.53: The experimental and calculated isotope distribution for $[\{\text{Ni}(\text{L-N}_4\text{Me}_2)\}_2(\mu\text{-RC}_4\text{R})]^{2+}$ [$\text{R} = \text{C}_6\text{H}_4\text{NMe}_2-4$].

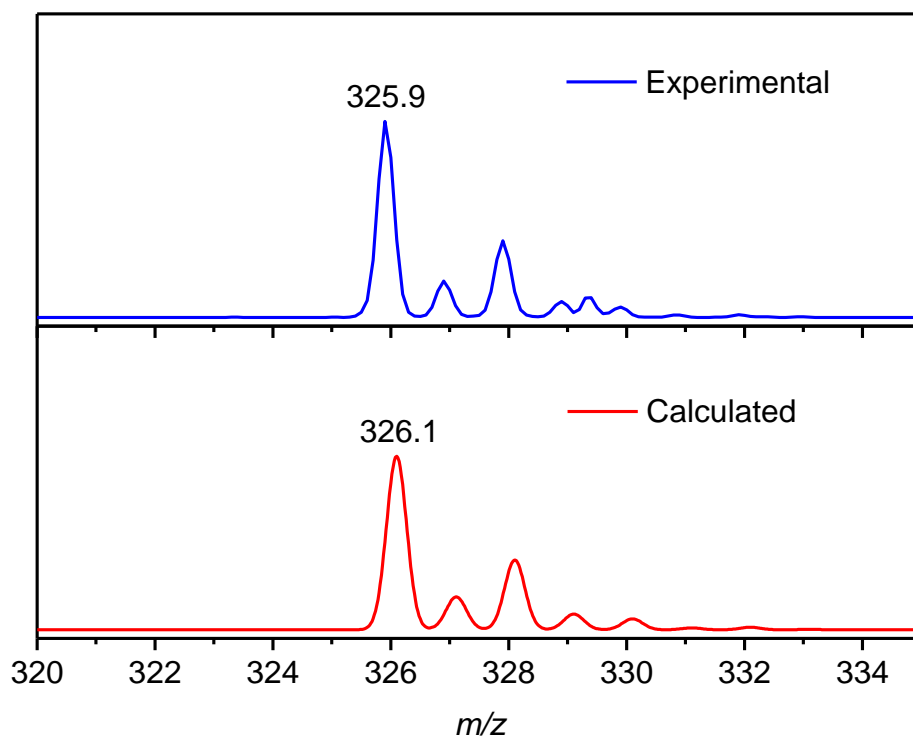


Figure 7.54: The experimental and calculated isotope distribution for $[\text{Ni}(\text{L-N}_4\text{Me}_2)]^+$.

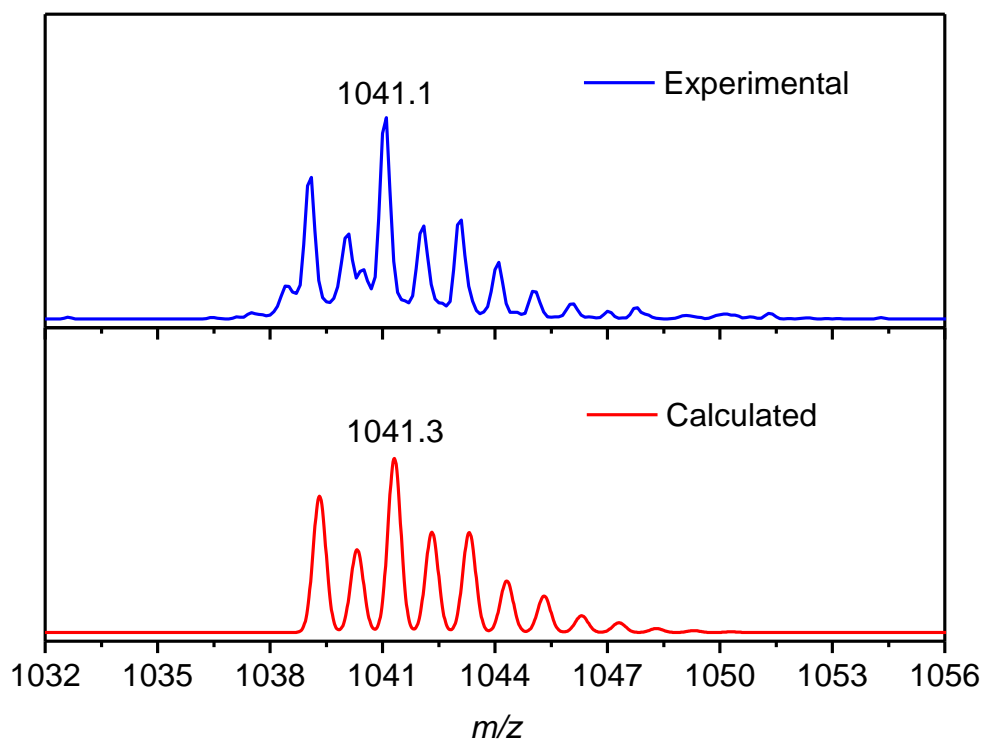


Figure 7.55: The experimental and calculated isotope distribution for $[\{\text{Ni}(\text{L-N}_4\text{Me}_2)_2(\mu\text{-RC}_4\text{R})(\text{ClO}_4)\}]^+$ [$\text{R} = \text{C}_6\text{H}_4\text{NMe}_2\text{-4}$].

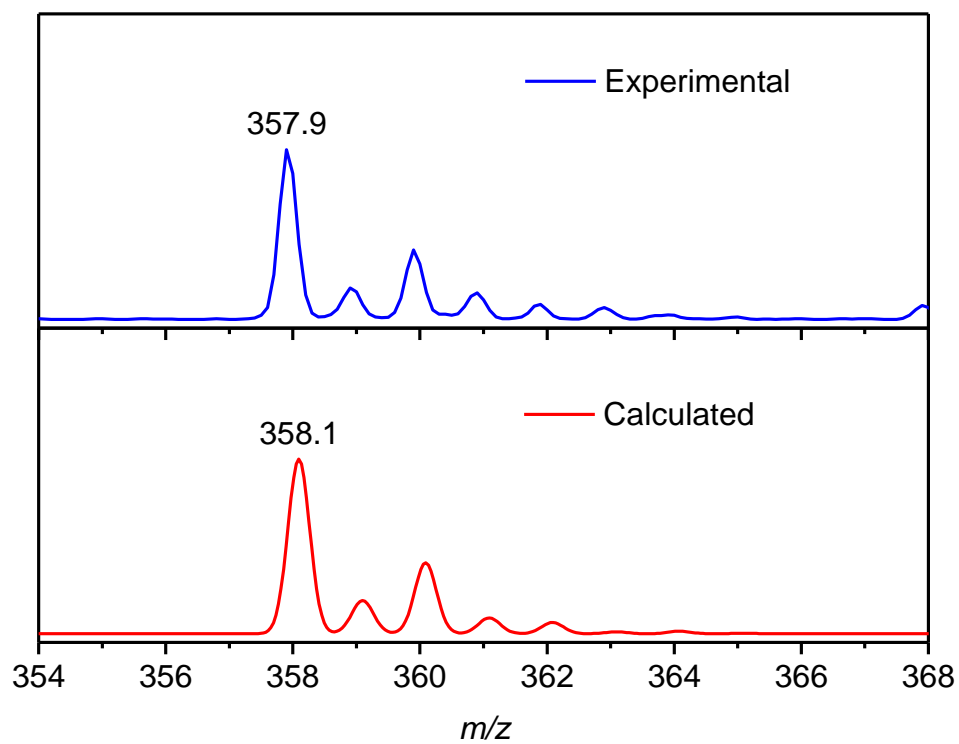


Figure 7.56: The experimental and calculated isotope distribution for $[\text{Ni}(\text{L-N}_4\text{Me}_2)(\text{O}_2)]^+$.

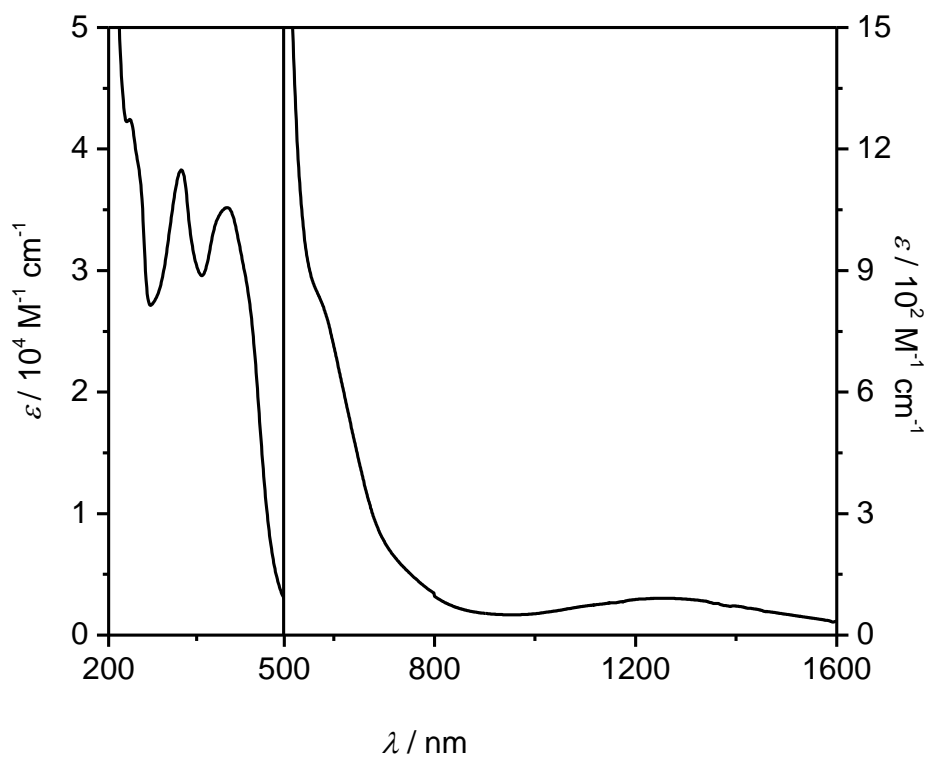


Figure 7.57: UV-Vis-NIR spectrum of 2e in MeCN.

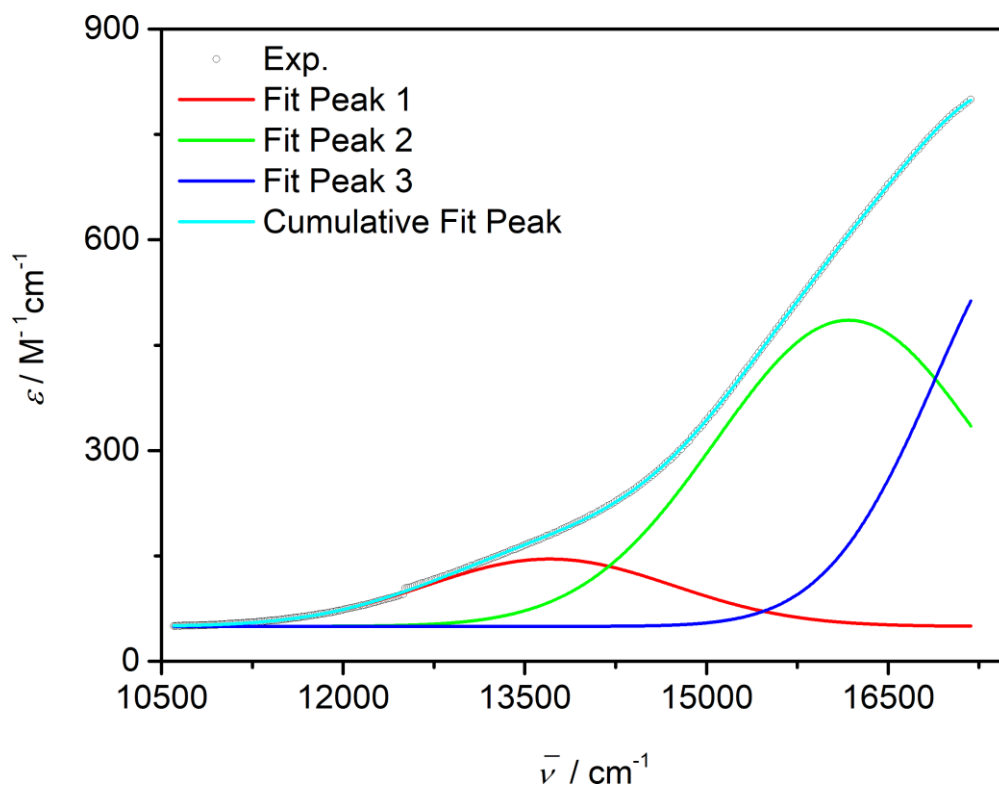


Figure 7.58: Deconvoluted UV-Vis-NIR spectrum of 2e; convolution is performed in 10604 – 17180 cm^{-1} range using Gaussian function.

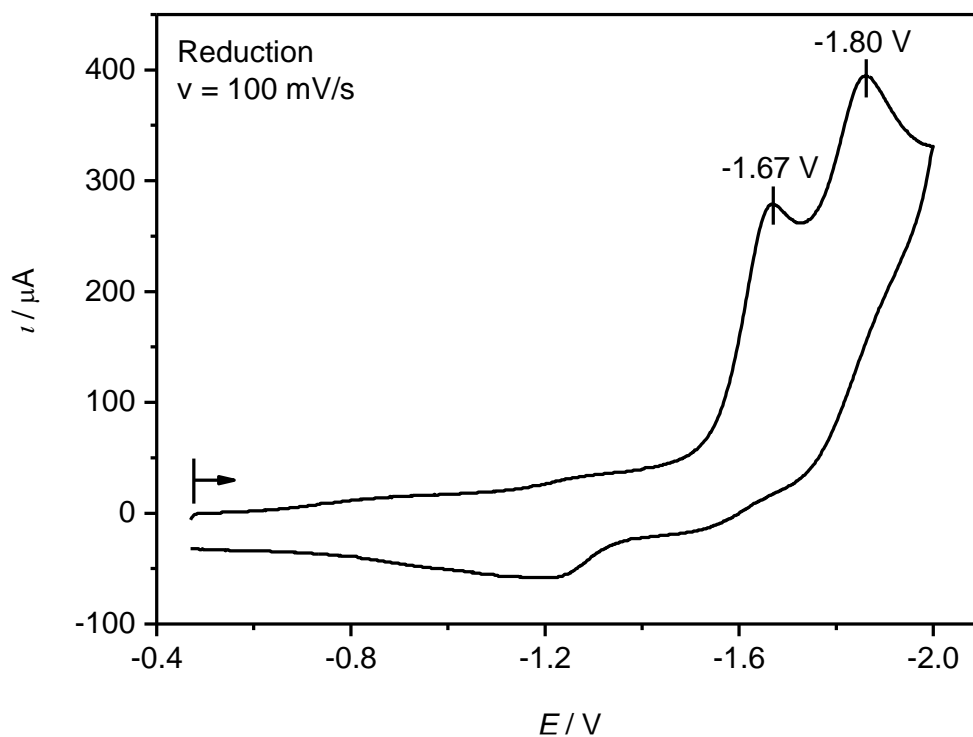


Figure 7.59: Cyclic voltammogram for the reduction of 2e in 0.2 M TBAP/MeCN sweeping with a scan rate of 100 mV s^{-1} . All potentials are given vs. SCE.

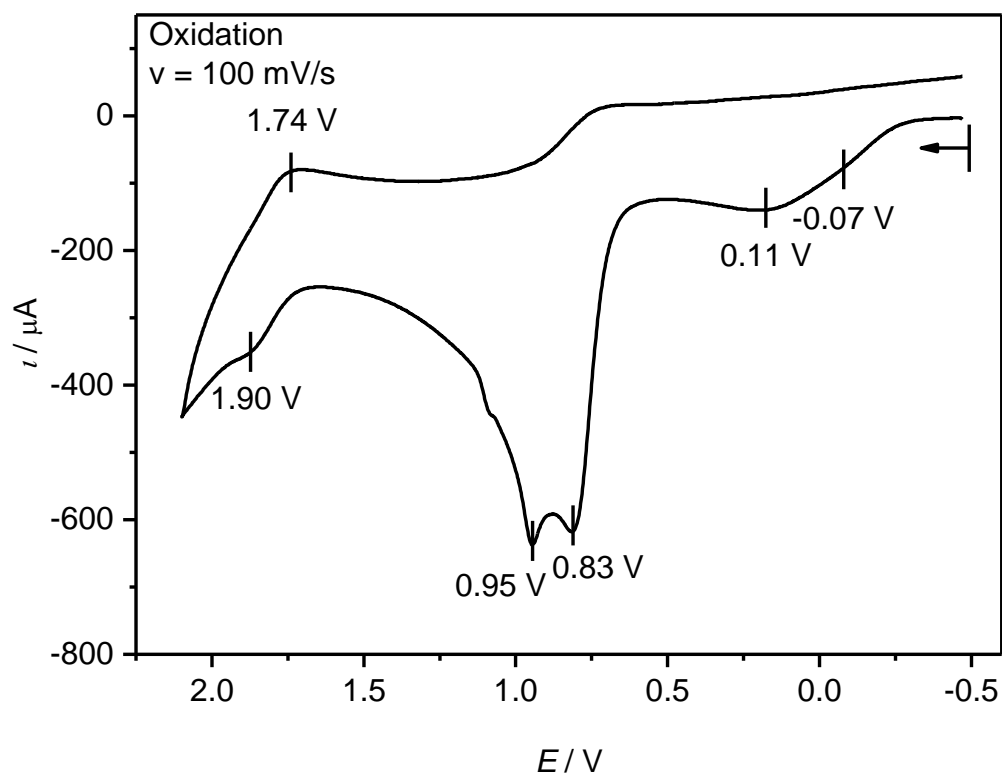


Figure 7.60: Cyclic voltammogram for the oxidation of $2e$ in 0.2 M TBAP/MeCN sweeping with a scan rate of 100 mV s^{-1} . All potentials are given vs. SCE.

7.2.6 $\{[Ni(L-N_4Me_2)]_2(\mu-R_4R)\}(ClO_4)_2 [R = {}^n C_3H_7] (2f)$ Table 7.8: Crystal data and structure refinement for 2f [R = ${}^n C_3H_7$] at 150 K

Identification code	14041o	
Empirical formula	$C_{42}H_{54}Cl_2N_8Ni_2O_8$	
Formula weight	987.25	
Temperature	150(2) K	
Wavelength	0.71073 Å	
Crystal system	Monoclinic	
Space group	P 21/n	
Unit cell dimensions	a = 11.6006(3) Å	$\alpha = 90^\circ$
	b = 13.7058(3) Å	$\beta = 99.558(2)^\circ$
	c = 14.2543(3) Å	$\gamma = 90^\circ$
Volume	2234.91(9) Å ³	
Z	2	
Density (calculated)	1.467 Mg/m ³	
Absorption coefficient	1.023 mm ⁻¹	
F(000)	1032	
Crystal size	0.360 x 0.180 x 0.130 mm ³	
Theta range for data collection	2.887 to 29.991°	
Index ranges	-16 ≤ h ≤ 13, -8 ≤ k ≤ 19, -20 ≤ l ≤ 14	
Reflections collected	12268	
Independent reflections	6495 [R(int) = 0.0257]	
Completeness to theta = 30.00°	99.6 %	
Absorption correction	Semi-empirical from equivalents	
Max. and min. transmission	1.00000 and 0.83775	
Refinement method	Full-matrix least-squares on F ²	
Data / restraints / parameters	6495 / 0 / 283	
Goodness-of-fit on F ²	1.048	
Final R indices [I > 2σ(I)]	R1 = 0.0359, wR2 = 0.0816	
R indices (all data)	R1 = 0.0499, wR2 = 0.0882	
Extinction coefficient	n/a	
Largest diff. peak and hole	0.584 and -0.444 e.Å ⁻³	

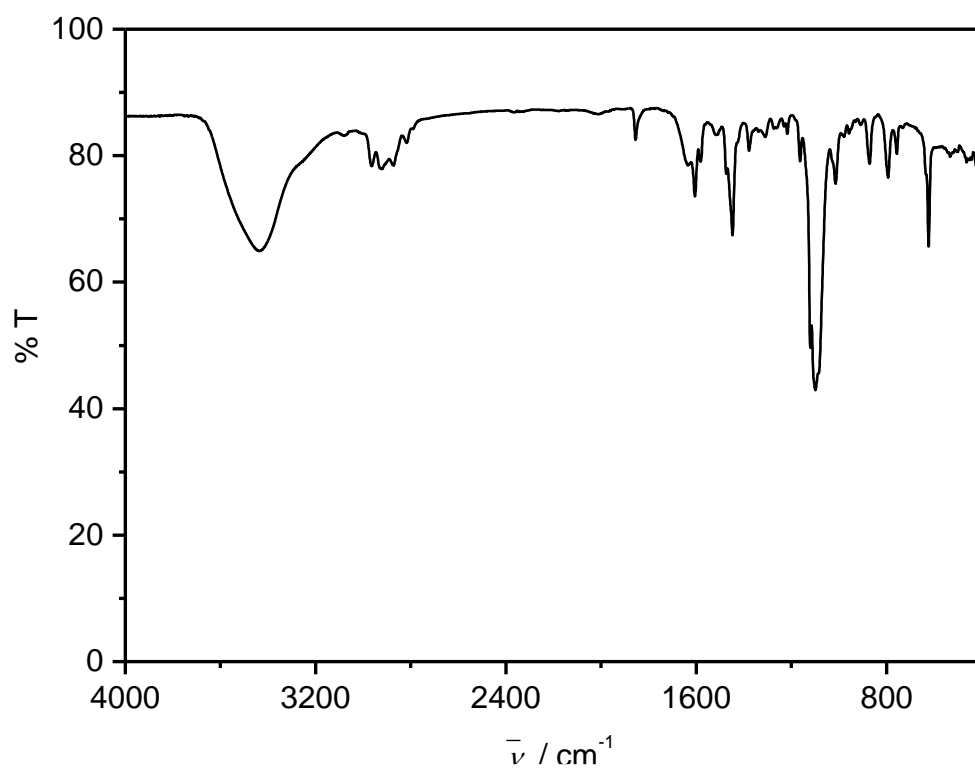


Figure 7.61: IR spectrum of 2f as KBr pellet.

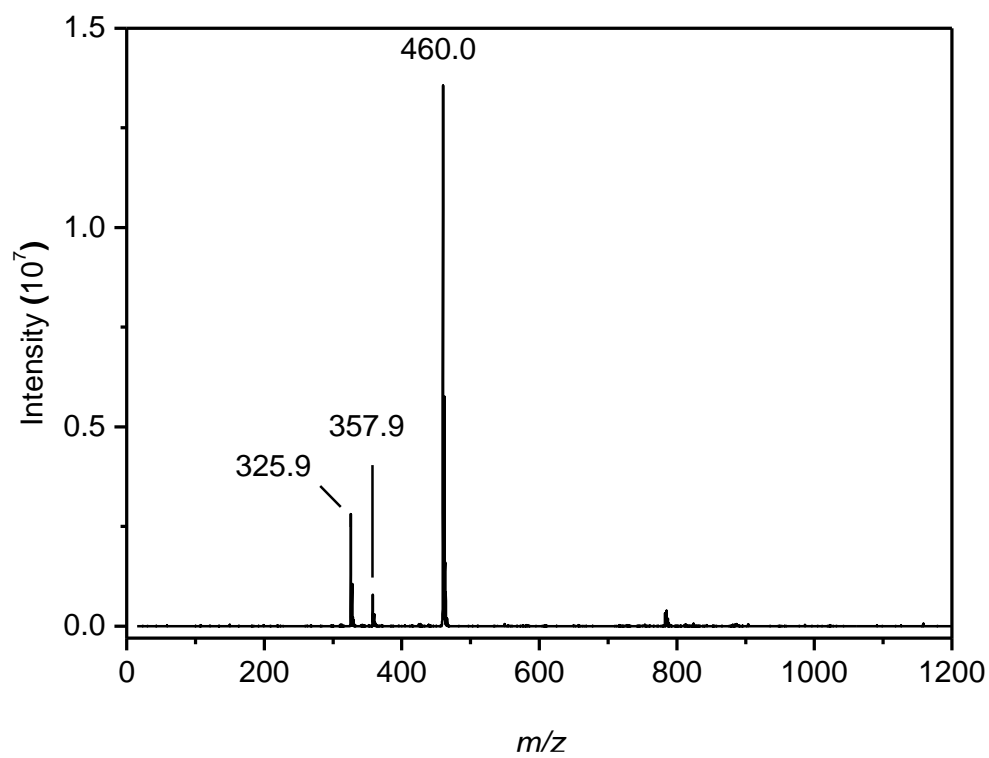


Figure 7.62: ESI-MS spectrum of 2f in MeCN.

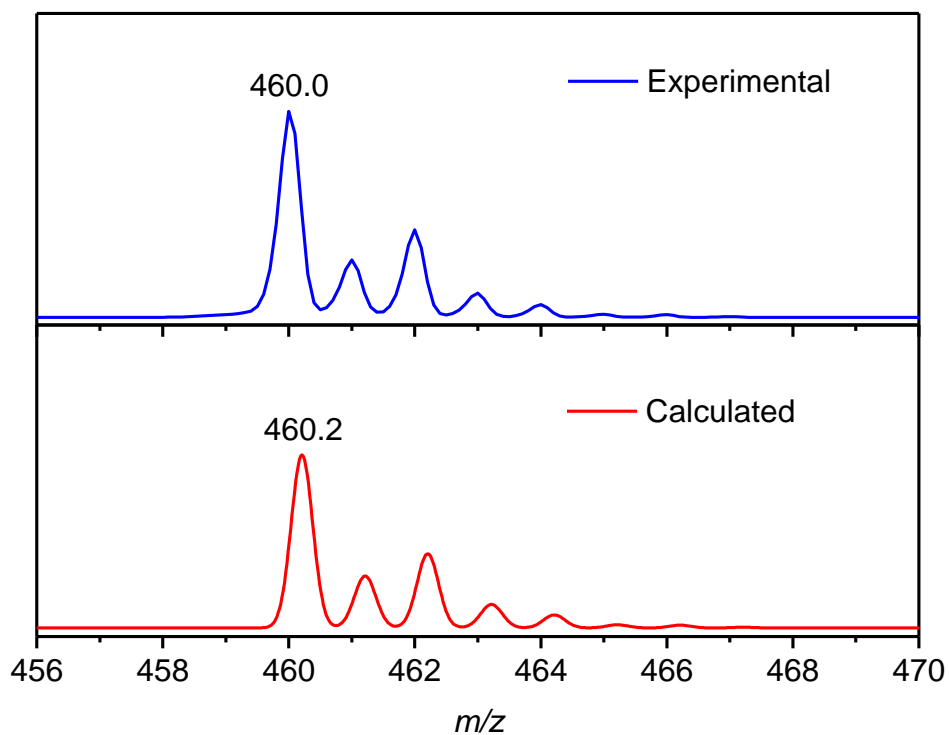


Figure 7.63: The experimental and calculated isotope distribution for $[\text{Ni}(\text{L}-\text{N}_4\text{Me}_2)(\text{RC}_4\text{R})]^+$ [$\text{R} = {}^{13}\text{C}_3\text{H}_7$].

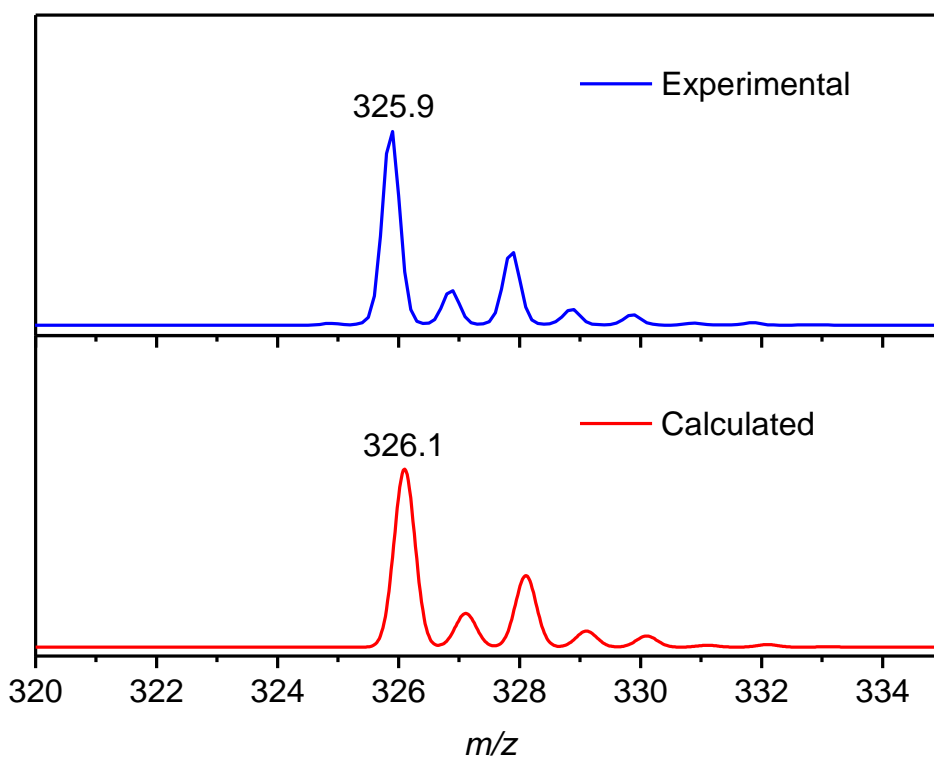


Figure 7.64: The experimental and calculated isotope distribution for $[\text{Ni}(\text{L}-\text{N}_4\text{Me}_2)]^+$.

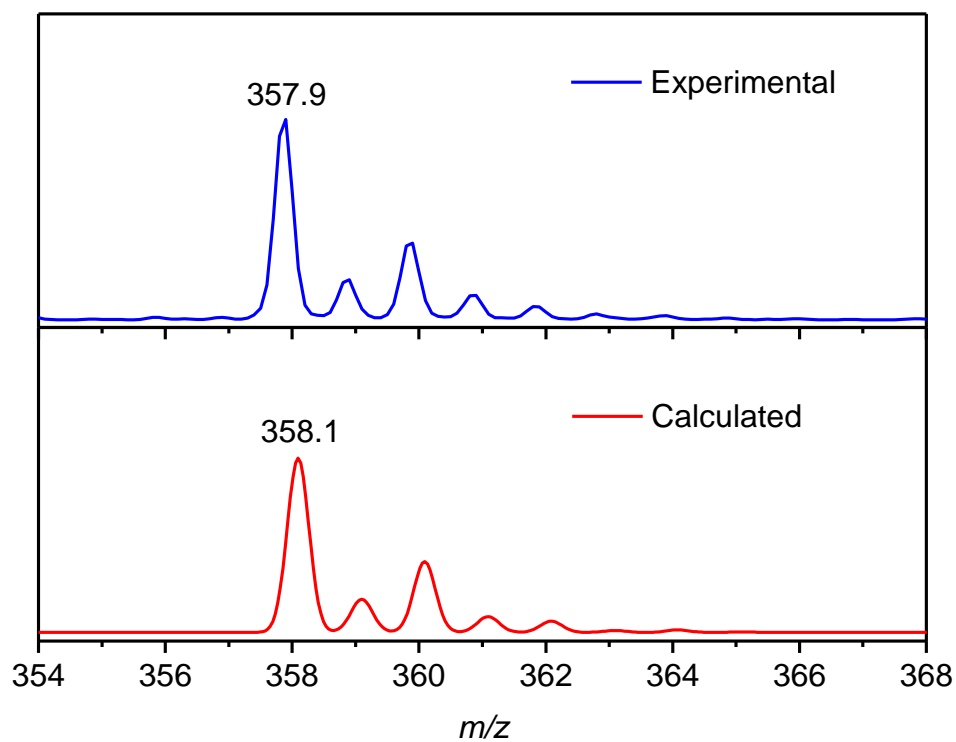


Figure 7.65: The experimental and calculated isotope distribution for $[\text{Ni}(\text{L}-\text{N}_4\text{Me}_2)(\text{O}_2)]^+$.

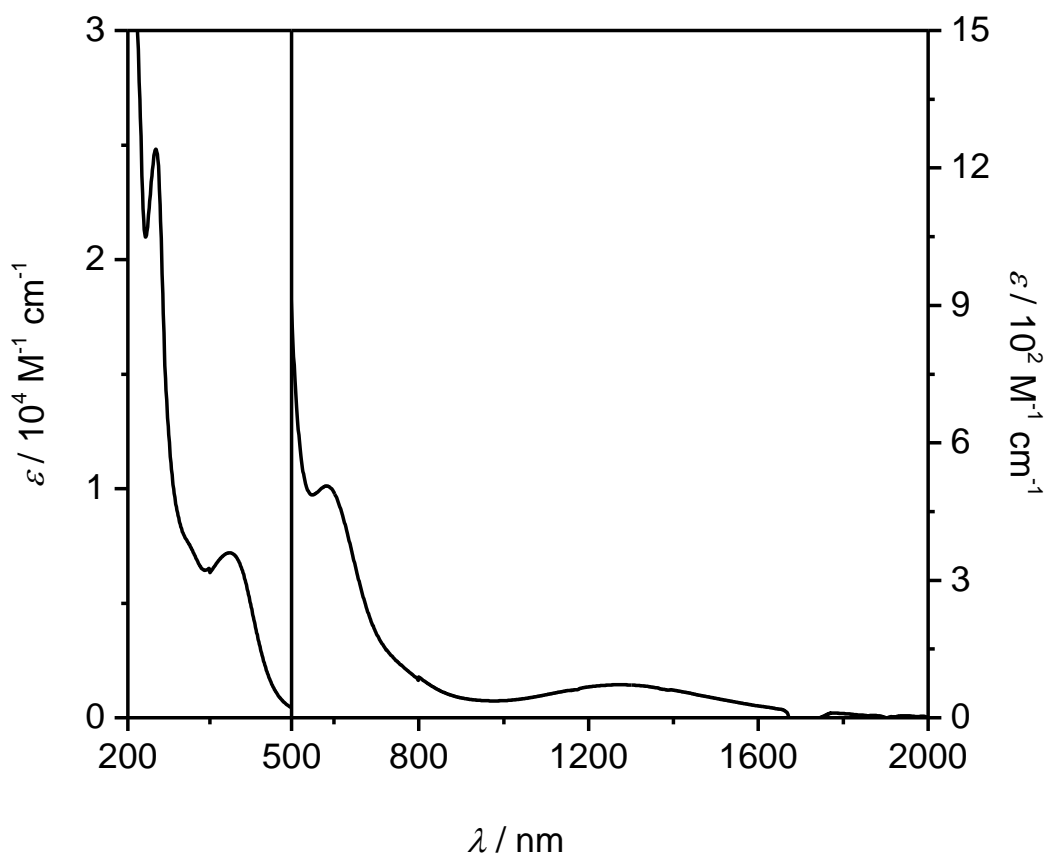


Figure 7.66: UV-Vis-NIR spectrum of 2f in MeCN.

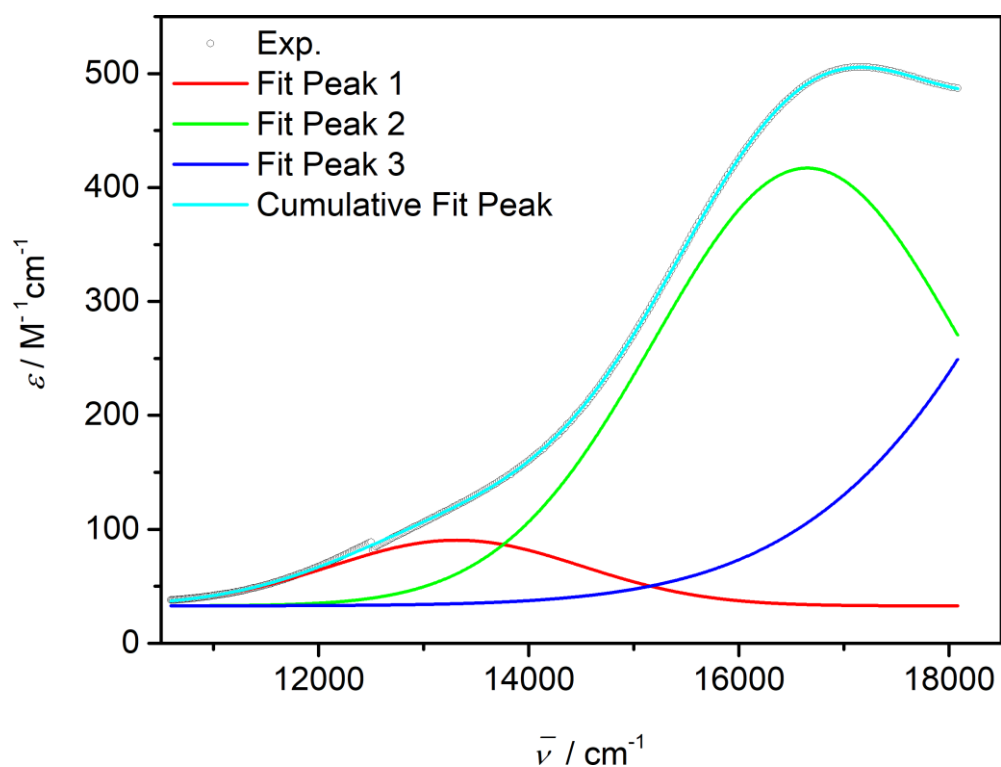


Figure 7.67: Deconvoluted UV-Vis-NIR spectrum of 2f; convolution is performed in 10593 – 18083 cm^{-1} range using Gaussian function.

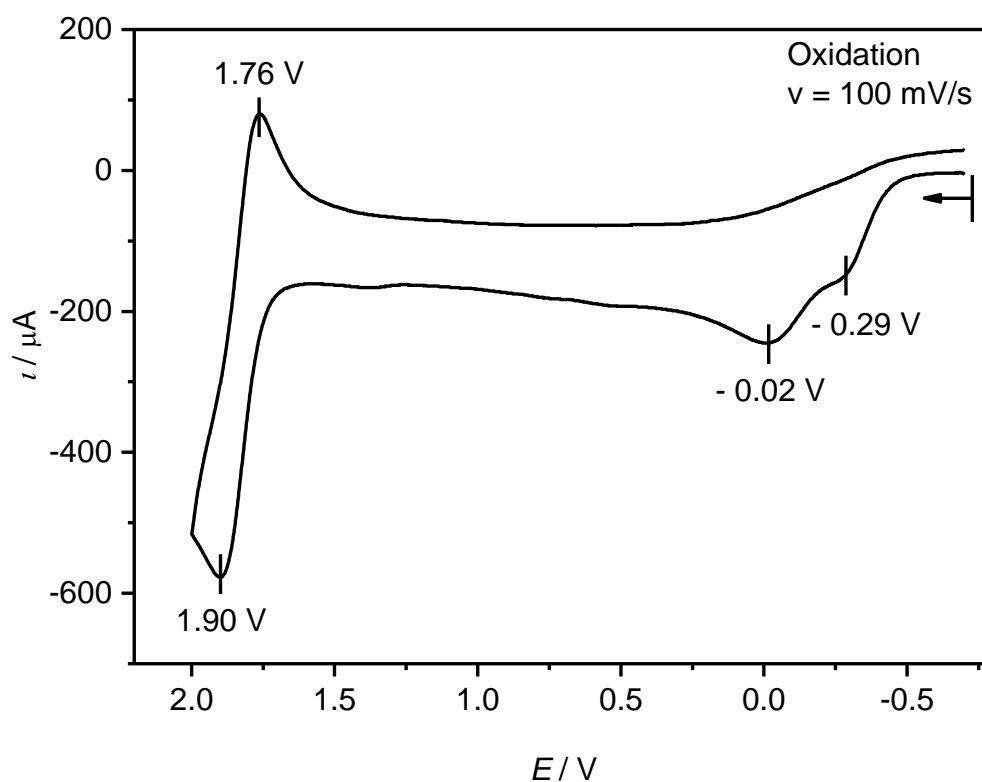


Figure 7.68: Cyclic voltammogram for the oxidation of 2f in 0.2 M TBAP/MeCN sweeping with a scan rate of 100 mV s^{-1} . All potentials are given vs. SCE.

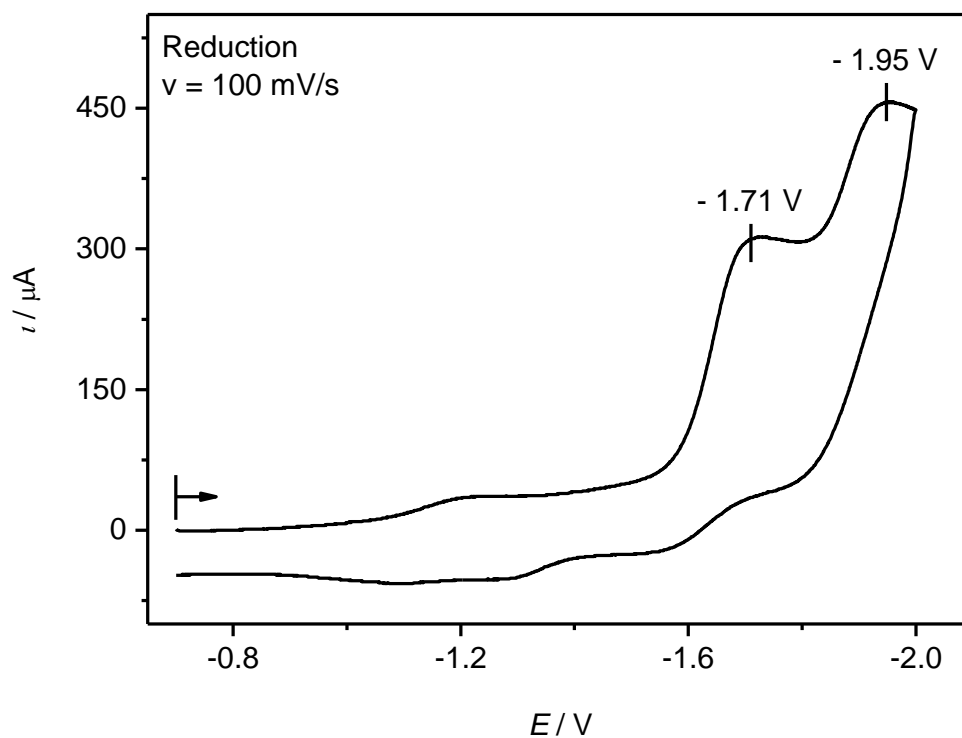


Figure 7.69: Cyclic voltammogram for the reduction of 2f in 0.2 M TBAP/MeCN sweeping with a scan rate of 100 mV s^{-1} . All potentials are given vs. SCE.

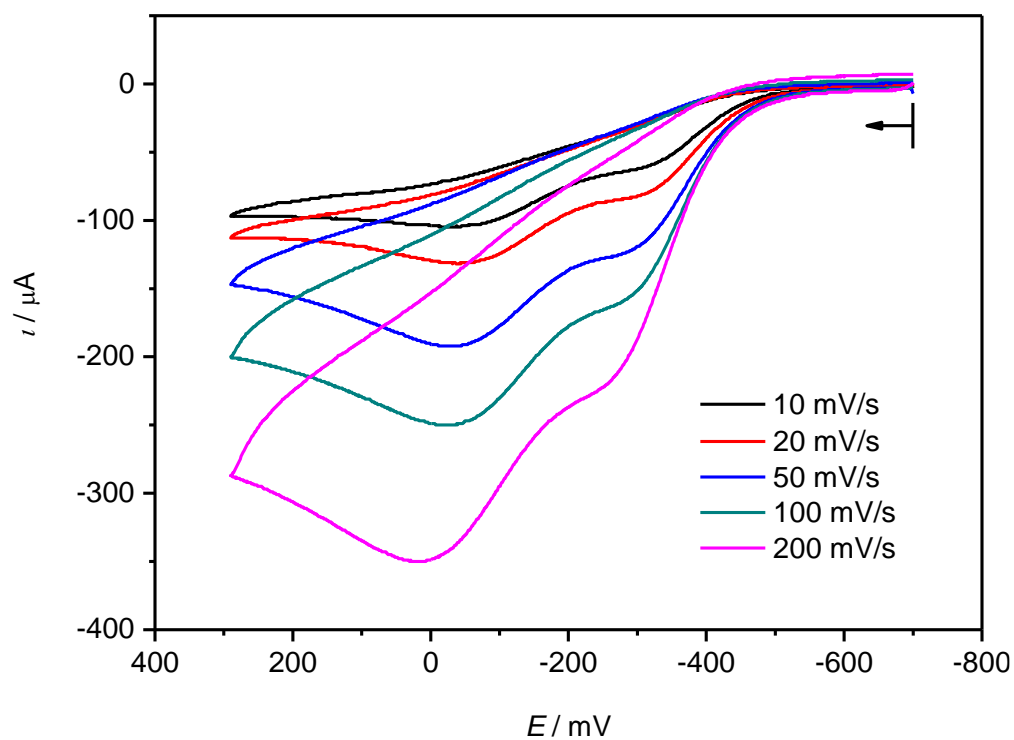


Figure 7.70: Cyclic voltammograms for the oxidation of 2f in 0.2 M TBAP/MeCN sweeping with different scan rates. All potentials are given vs. SCE.

7.2.7 $\{[Ni(L-N_4Me_2)]_2(\mu-R_4R)\}(ClO_4)_2 \cdot EtOH [R = Fc] (2g)$

Table 7.9: Crystal data and structure refinement for 2g [R = Fc] at 150 K

Identification code	13219o
Empirical formula	C ₅₈ H ₆₄ Cl ₂ N ₈ Ni ₂ Fe ₂ O ₉
Formula weight	1317.19
Temperature	150(2) K
Wavelength	0.71073 Å
Crystal system	Monoclinic
Space group	C 2/c
Unit cell dimensions	a = 20.2681(6) Å α = 90° b = 15.1999(10) Å β = 96.392(3)°. c = 36.2651(13) Å γ = 90°.
Volume	11102.8(9) Å ³
Z	8
Density (calculated)	1.576 Mg/m ³
Absorption coefficient	1.343 mm ⁻¹
F(000)	5456
Crystal size	0.400 x 0.260 x 0.210 mm ³
Theta range for data collection	2.861 to 30.000°.
Index ranges	-28 ≤ h ≤ 28, -21 ≤ k ≤ 15, -51 ≤ l ≤ 18
Reflections collected	30297
Independent reflections	16191 [R(int) = 0.0239]
Completeness to theta = 30.00°	99.8 %
Absorption correction	Analytical
Max. and min. transmission	0.758 and 0.602
Refinement method	Full-matrix least-squares on F ²
Data / restraints / parameters	16191 / 47 / 812
Goodness-of-fit on F ²	1.071
Final R indices [I > 2σ(I)]	R1 = 0.0371, wR2 = 0.0758
R indices (all data)	R1 = 0.0486, wR2 = 0.0797
Extinction coefficient	n/a
Largest diff. peak and hole	0.444 and -0.535 e.Å ⁻³

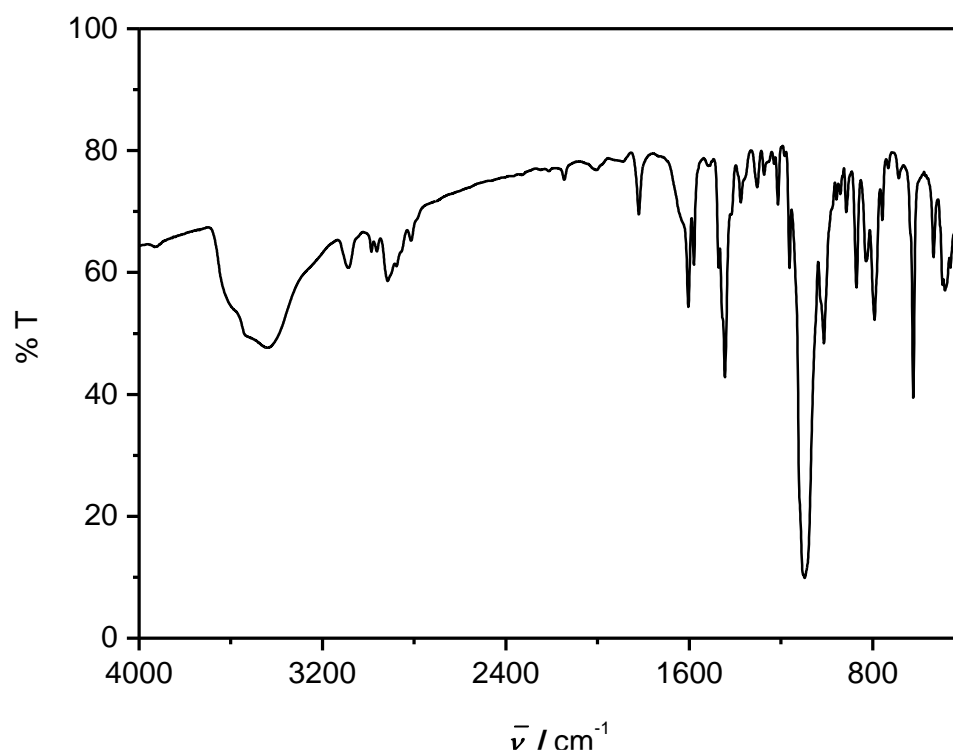


Figure 7.71: IR spectrum of 2g as KBr pellet.

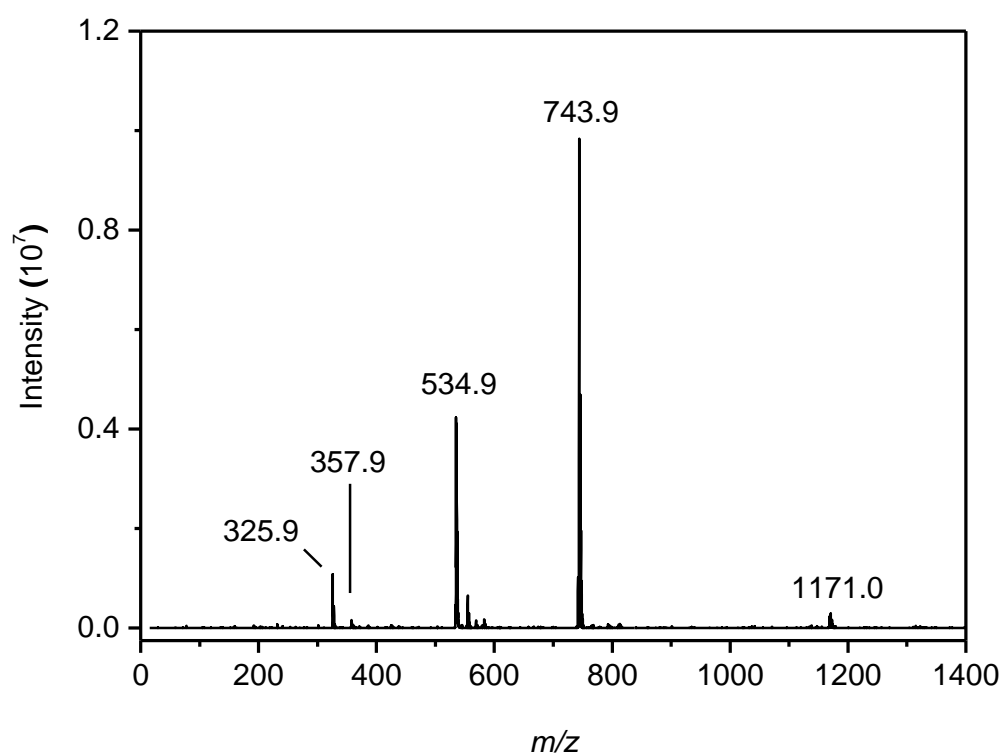


Figure 7.72: ESI-MS spectrum of 2g in MeCN.

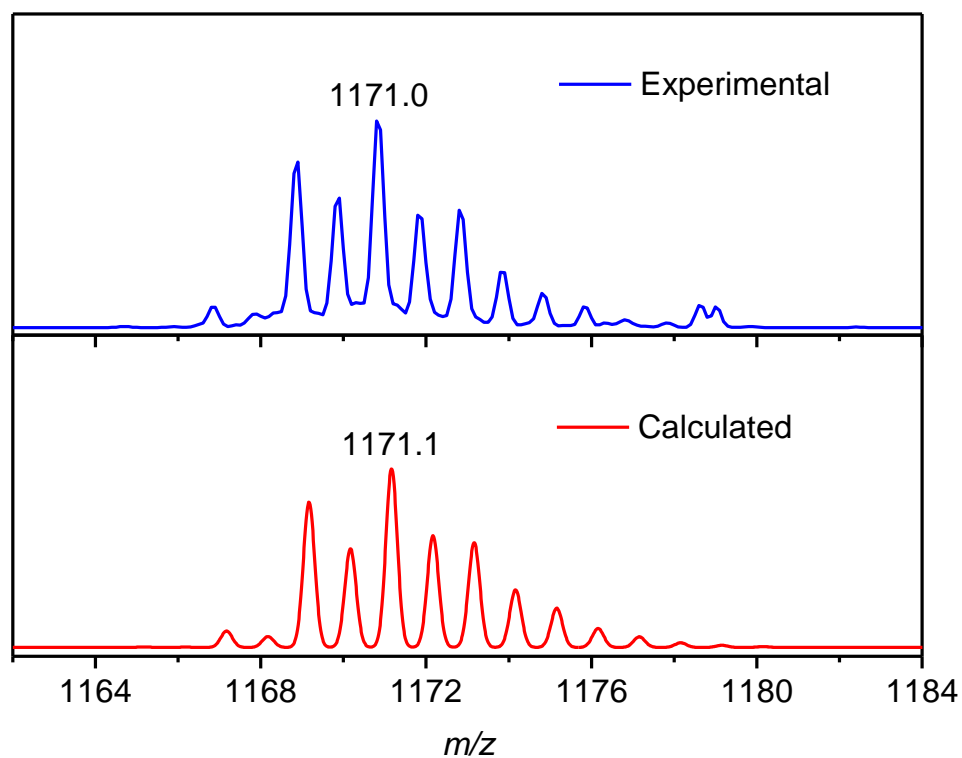


Figure 7.73: The experimental and calculated isotope distribution for $[\{\text{Ni}(\text{L}-\text{N}_4\text{Me}_2)\}_2(\mu\text{-RC}_4\text{R})(\text{ClO}_4)]^+$ [$\text{R} = \text{Fc}$].

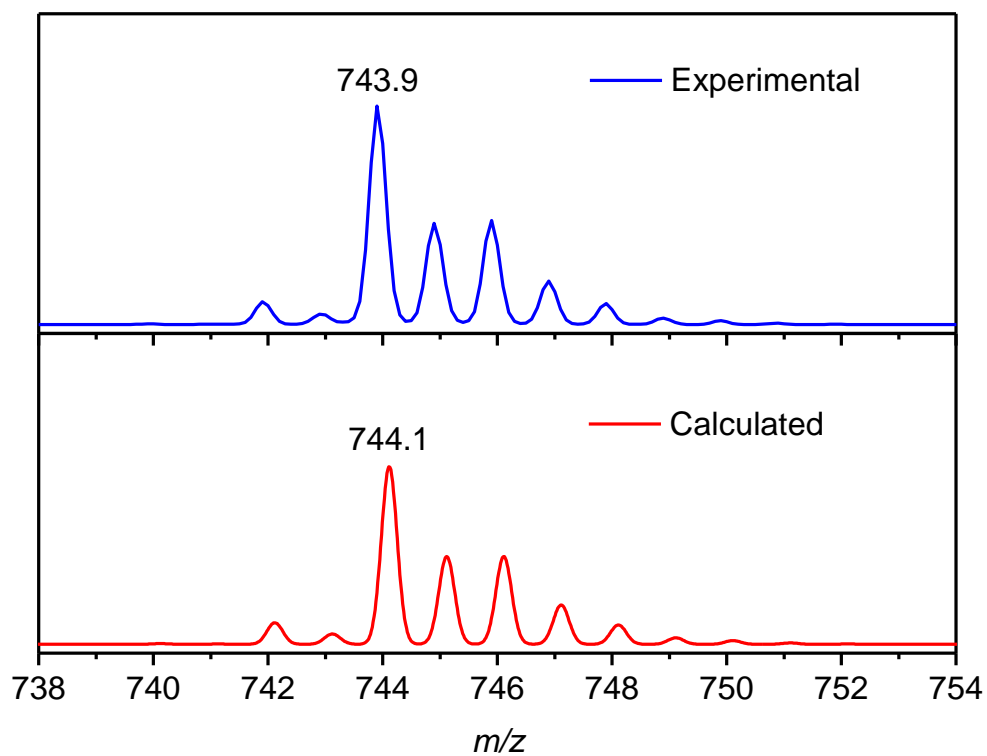


Figure 7.74: The experimental and calculated isotope distribution for $[\text{Ni}(\text{L}-\text{N}_4\text{Me}_2)(\mu\text{-RC}_4\text{R})(\text{ClO}_4)]^+$ [$\text{R} = \text{Fc}$].

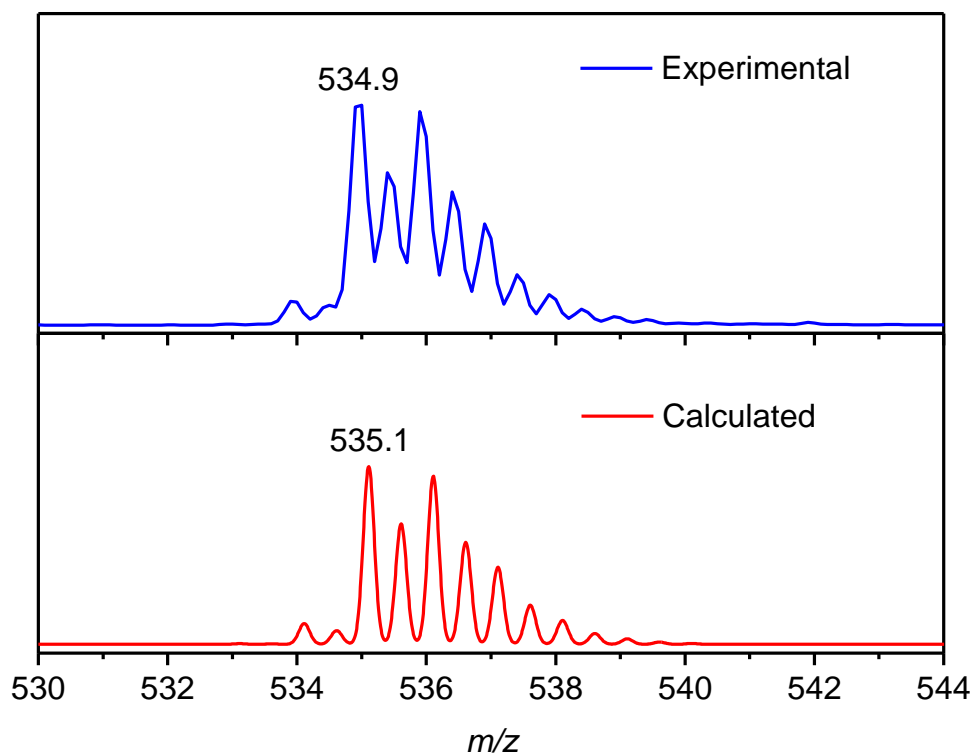


Figure 7.75: The experimental and calculated isotope distribution for $[\{\text{Ni}(\text{L}-\text{N}_4\text{Me}_2)\}_2(\mu\text{-RC}_4\text{R})]^{2+}$ [$\text{R} = \text{Fc}$].

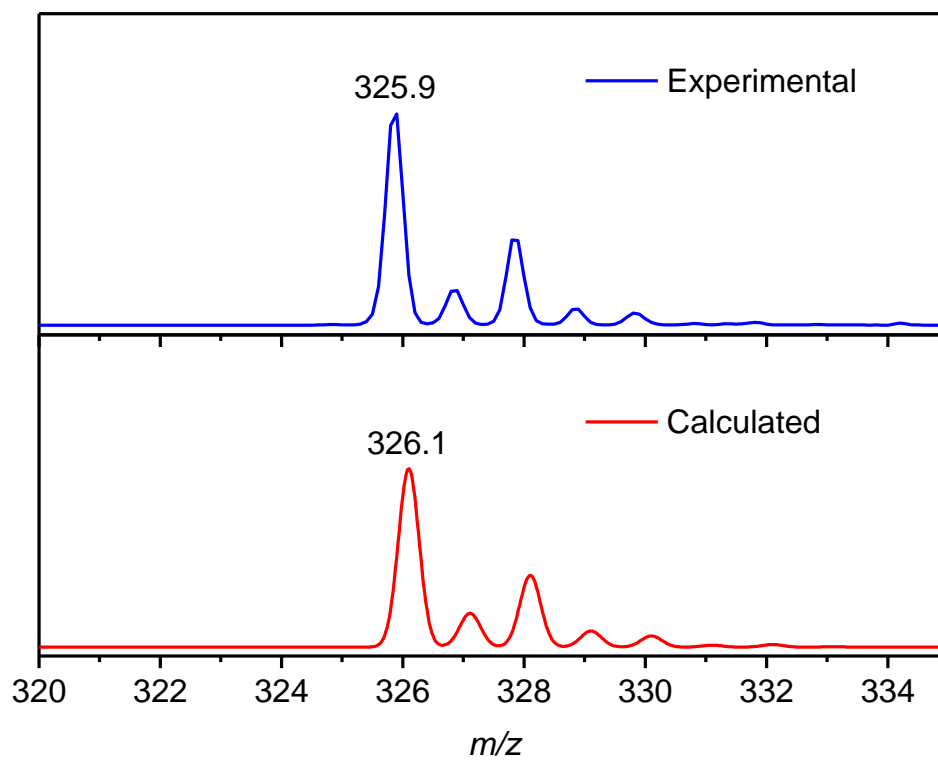


Figure 7.76: The experimental and calculated isotope distribution for $[\text{Ni}(\text{L}-\text{N}_4\text{Me}_2)]^+$.

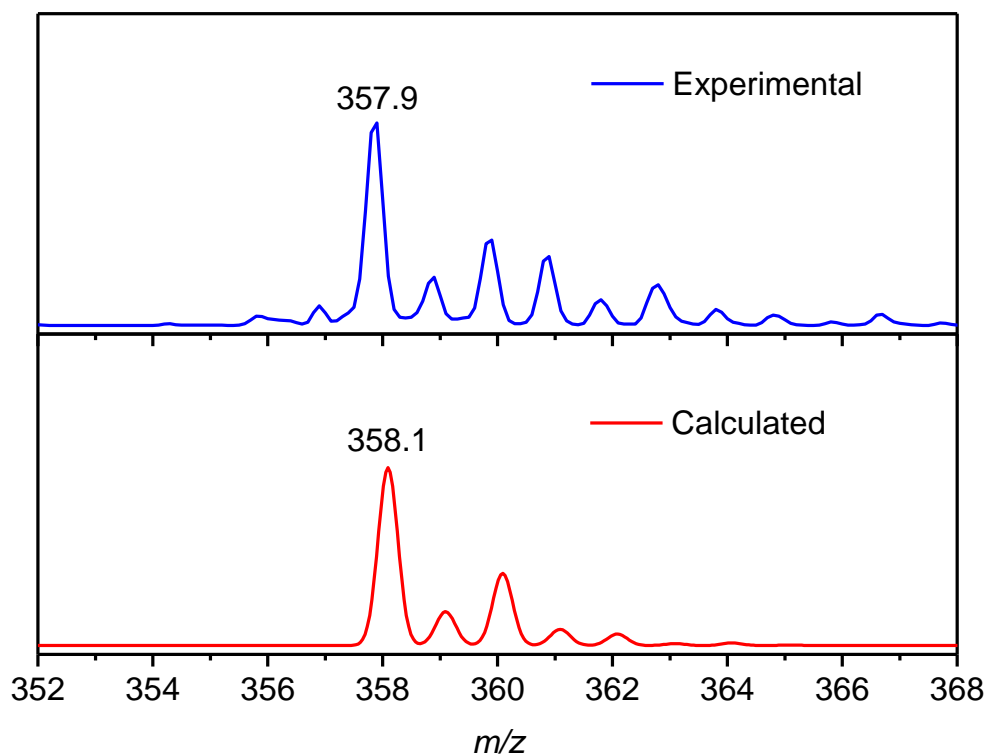


Figure 7.77: The experimental and calculated isotope distribution for $[\text{Ni}(\text{L}-\text{N}_4\text{Me}_2)(\text{O}_2)]^+$.

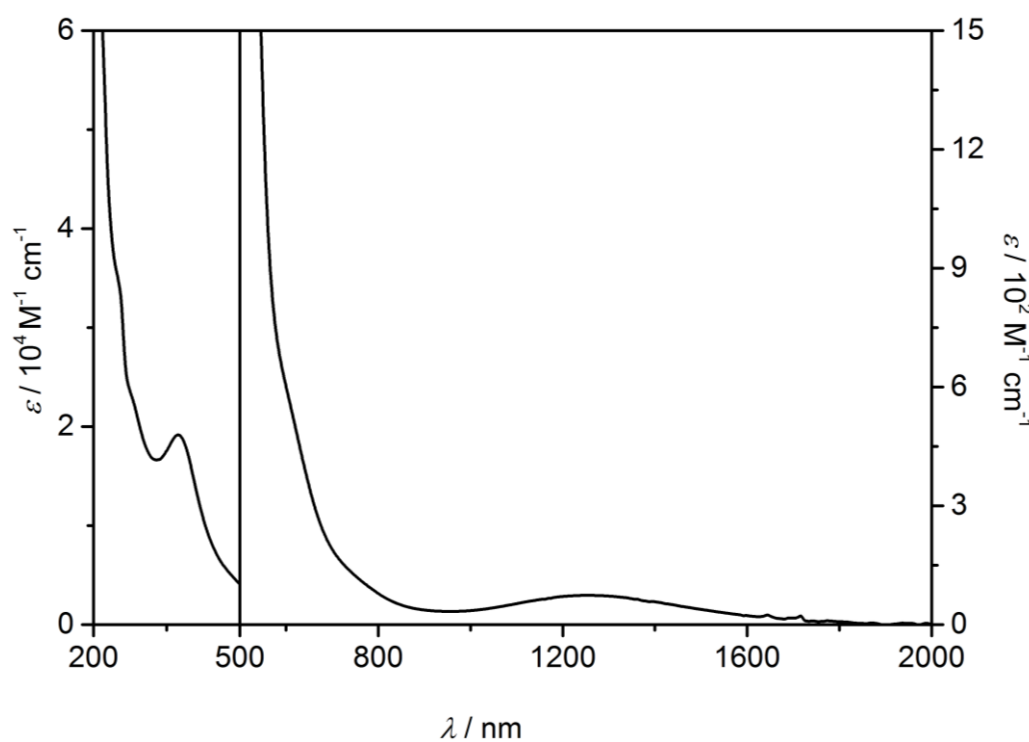


Figure 7.78: UV-Vis-NIR spectrum of 2g in MeCN.

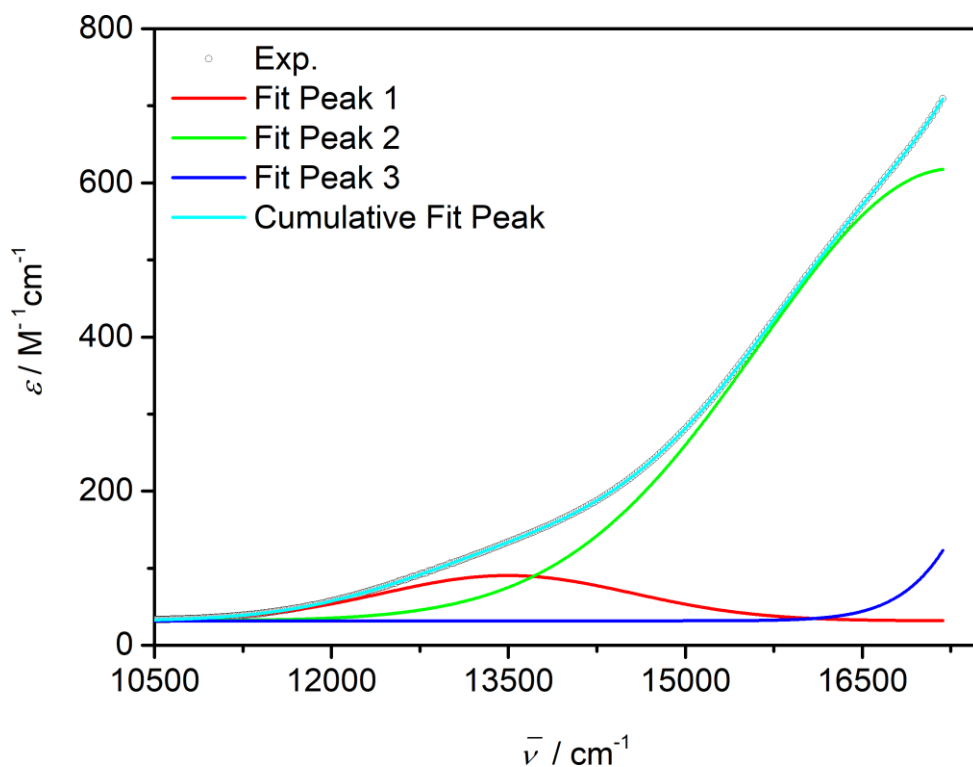


Figure 7.79: Deconvoluted UV-Vis-NIR spectrum of 2g; convolution is performed in 10593 – 18083 cm^{-1} range using Gaussian function.

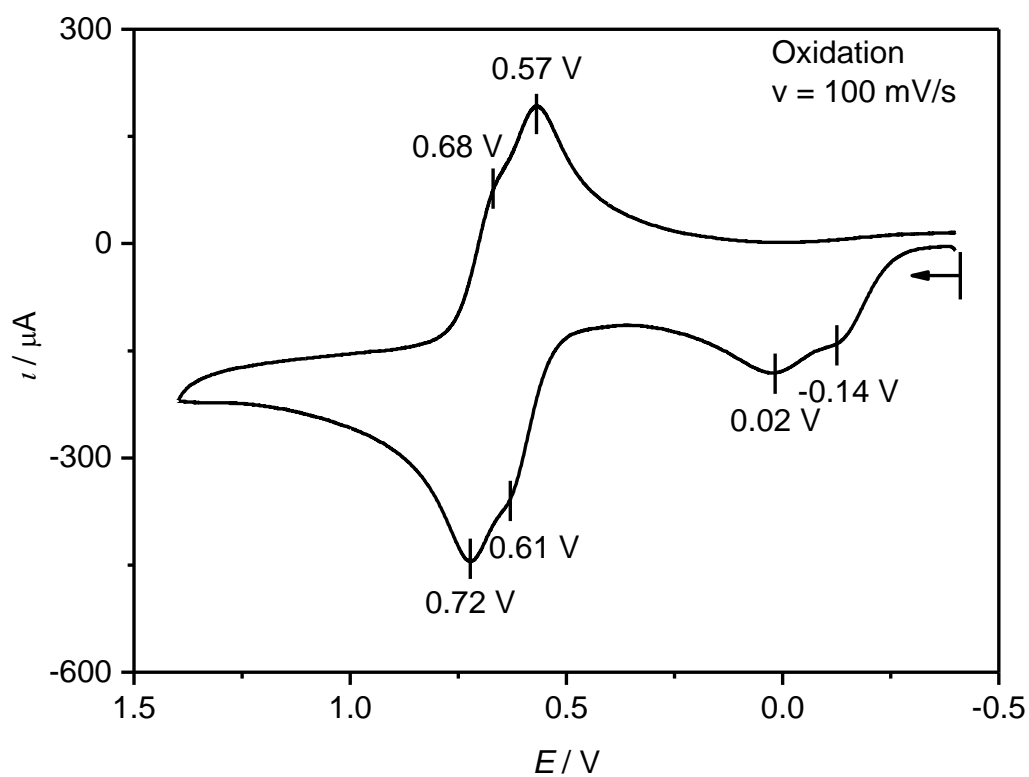


Figure 7.80: Cyclic voltammogram for the oxidation of 2g in 0.2 M TBAP/MeCN sweeping with a scan rate of 100 mV s^{-1} . All potentials are given vs. SCE.

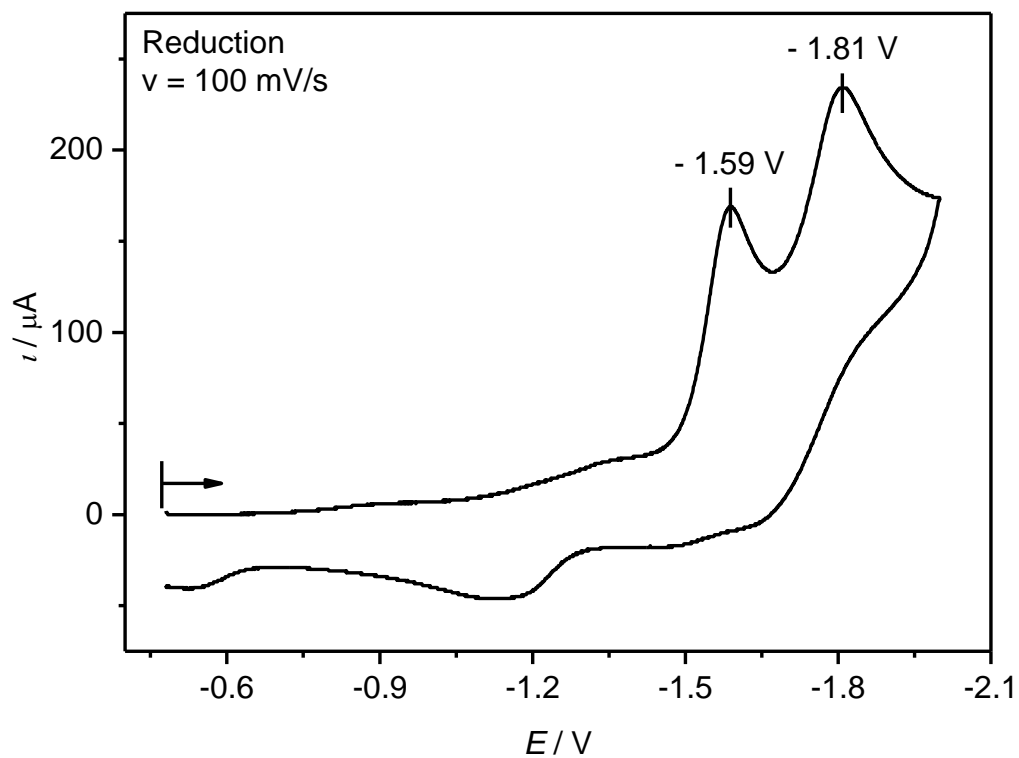
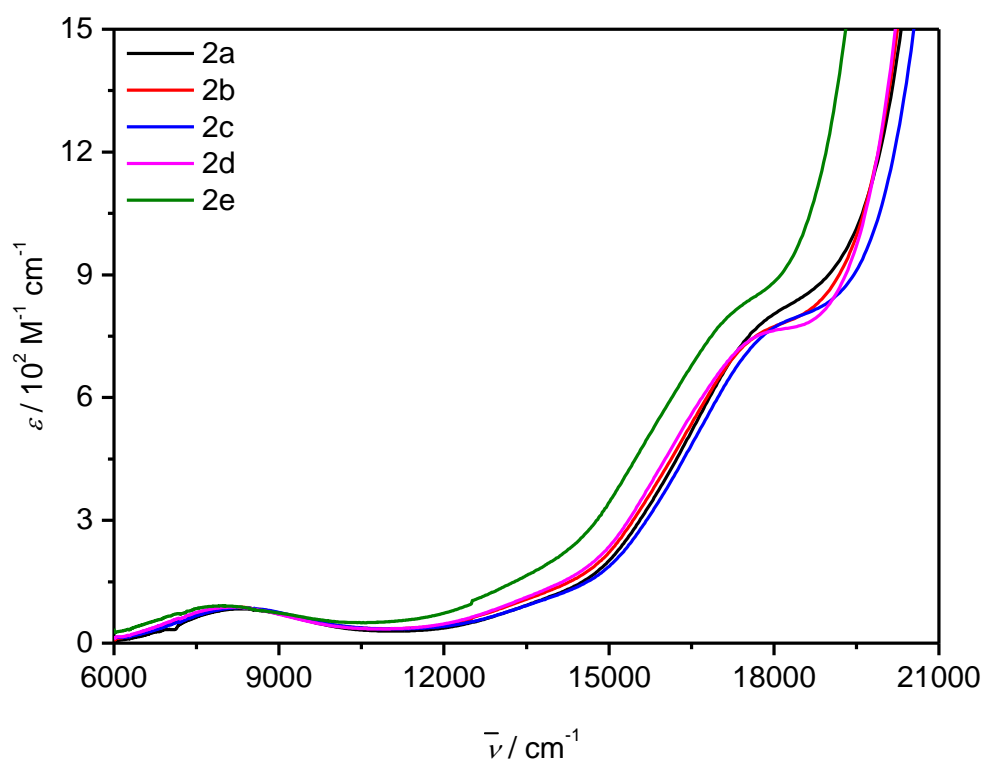


Figure 7.81: Cyclic voltammogram for the reduction of 2g in 0.2 M TBAP/MeCN sweeping with a scan rate of 100 mV s^{-1} . All potentials are given vs. SCE.

Table 7.10: Parameters obtained from simulation of the SQUID data

Complex	Spin	g	J [cm^{-1}]	PI [%]	TIP [$10^{-4} \text{ cm}^3 \text{ mol}^{-1}$]
2a [R = Ph]	$S_1 = \frac{1}{2}, S_2 = \frac{1}{2}$	2.252, 2.252	- 44.27	1.2	1.00
2b [R = C ₆ H ₄ Me-4]	$S_1 = \frac{1}{2}, S_2 = \frac{1}{2}$	2.254, 2.254	- 39.27	1.1	1.60
2c [R = C ₆ H ₄ F-4]	$S_1 = \frac{1}{2}, S_2 = \frac{1}{2}$	2.341, 2.341	- 46.23	4.1	2.50
2d [R = C ₆ H ₄ OMe-4]	$S_1 = \frac{1}{2}, S_2 = \frac{1}{2}$	2.252, 2.252	- 42.56	0.1	1.57
2e [R = C ₆ H ₄ NMe ₂ -4]	$S_1 = \frac{1}{2}, S_2 = \frac{1}{2}$	2.285, 2.285	- 41.53	2.0	1.09
2f [R = ⁿ Pr]	$S_1 = \frac{1}{2}, S_2 = \frac{1}{2}$	2.272, 2.272	- 33.83	2.0	1.72
2g [R = Fc]	$S_1 = \frac{1}{2}, S_2 = \frac{1}{2}$	2.296, 2.296	- 37.55	11.7	4.32

Figure 7.82: UV-Vis-NIR spectra of 2a-2e (region 6000 – 21000 cm^{-1}) in MeCN.

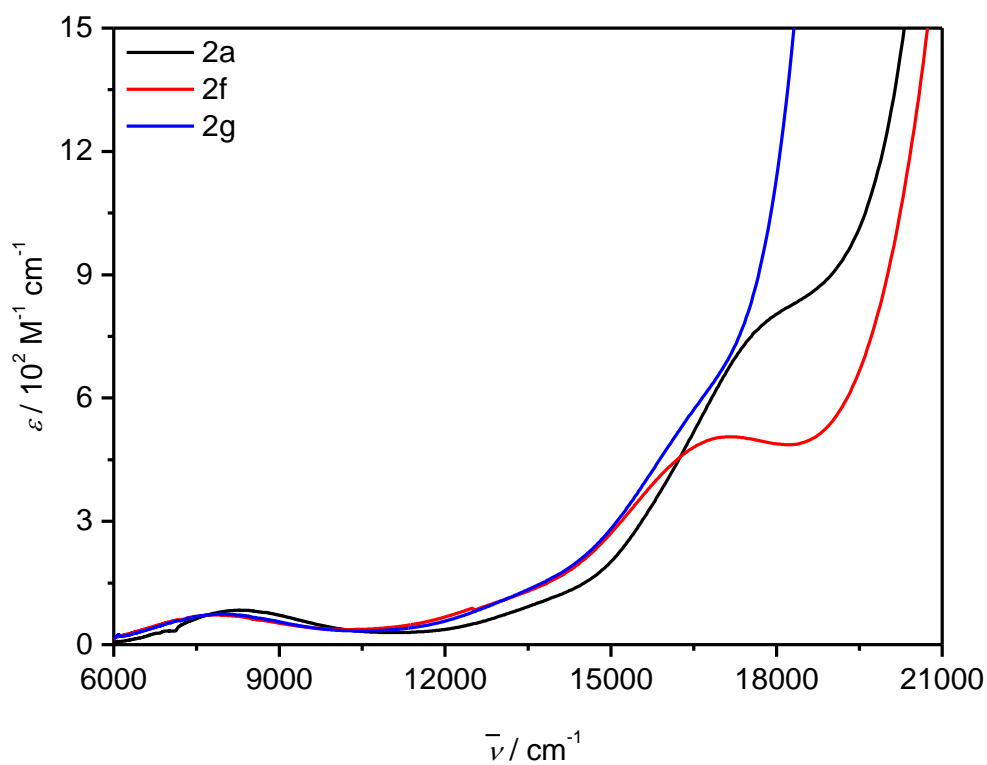


Figure 7.83: UV-Vis-NIR spectra of 2a, 2f and 2g (region 6000 – 21000 cm^{-1}) in MeCN.

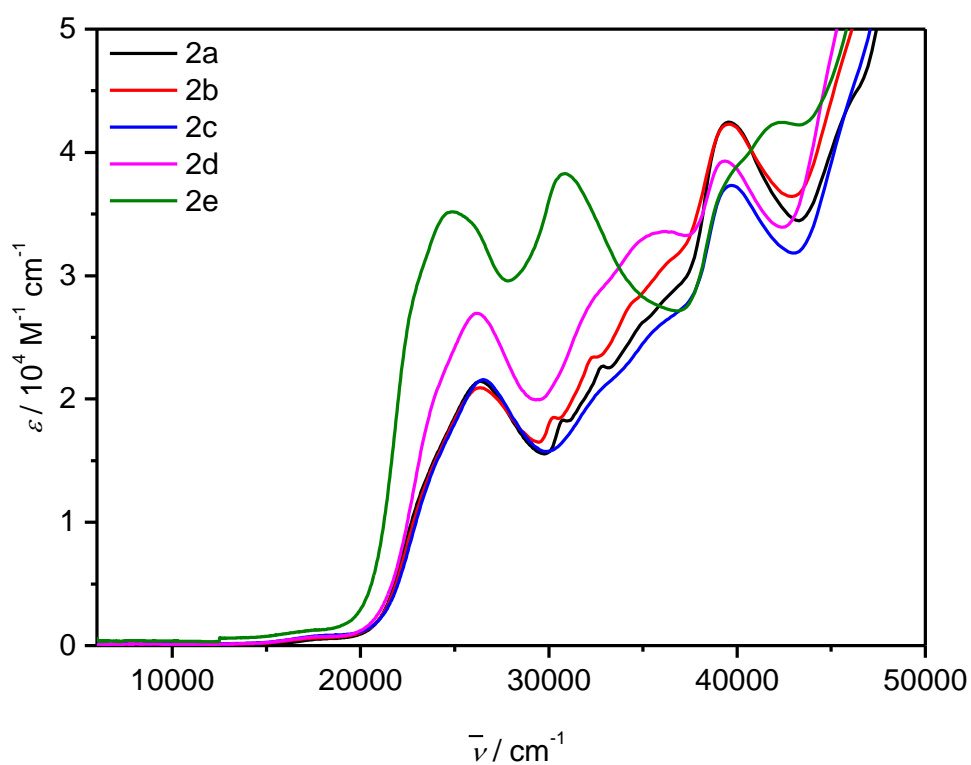


Figure 7.84: UV-Vis spectra of 2a-2e (region 6000 – 50000 cm^{-1}) in MeCN.

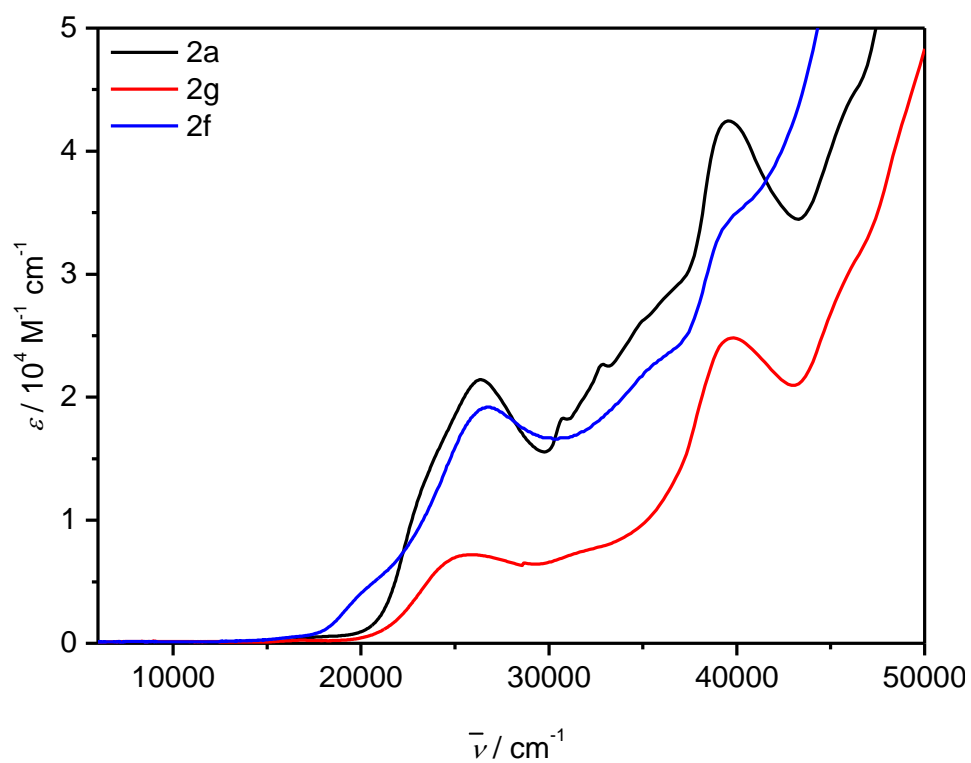


Figure 7.85: UV-Vis spectra of 2a, 2f and 2g (region 6000 – 50000 cm^{-1}) in MeCN.

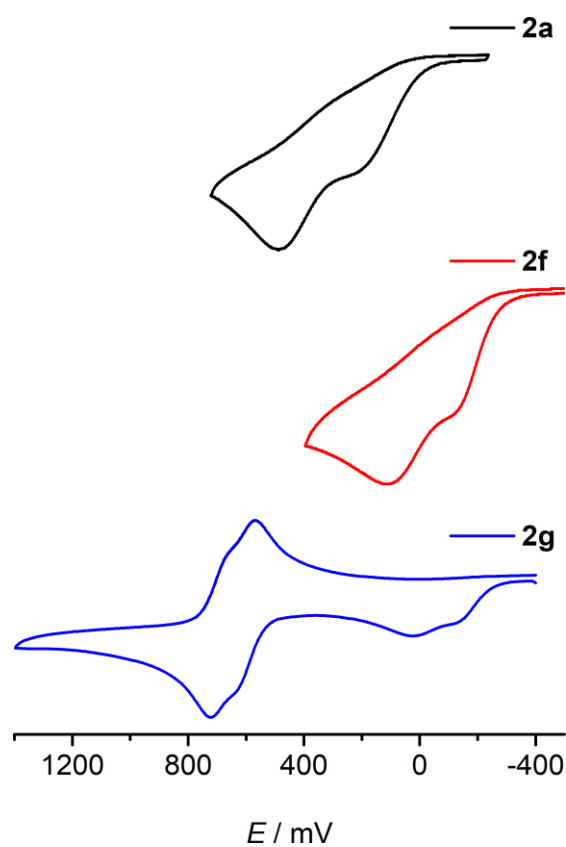


Figure 7.86: Cyclic voltammograms for the oxidation of 2a, 2g and 2g in 0.2 M TBAP/MeCN sweeping with different scan rates. All potentials are given vs. SCE.

7.3 [Ni(L-N₄Me₂)(PhC₂Ph)](ClO₄) · MeOH (3)

Table 7.11: Crystal data and structure refinement for 6 at 150 K

Identification code	14300o	
Empirical formula	C ₃₁ H ₃₄ ClN ₄ NiO ₅	
Formula weight	636.78	
Temperature	150(2) K	
Wavelength	0.71073 Å	
Crystal system	Triclinic	
Space group	P $\bar{1}$	
Unit cell dimensions	a = 10.3408(6) Å	$\alpha = 72.486(5)^\circ$
	b = 12.4332(6) Å	$\beta = 67.131(5)^\circ$
	c = 13.2816(7) Å	$\gamma = 88.881(4)^\circ$
Volume	1491.19(15) Å ³	
Z	2	
Density (calculated)	1.418 Mg/m ³	
Absorption coefficient	0.787 mm ⁻¹	
F(000)	666	
Crystal size	0.510 x 0.480 x 0.200 mm ³	
Theta range for data collection	2.829 to 28.999°	
Index ranges	-14 ≤ h ≤ 14, -16 ≤ k ≤ 16, -14 ≤ l ≤ 18	
Reflections collected	15250	
Independent reflections	7889 [R(int) = 0.0235]	
Completeness to theta = 30.00°	99.8 %	
Absorption correction	Semi-empirical from equivalents	
Max. and min. transmission	1.00000 and 0.96476	
Refinement method	Full-matrix least-squares on F ²	
Data / restraints / parameters	7889 / 22 / 449	
Goodness-of-fit on F ²	1.033	
Final R indices [I > 2σ(I)]	R1 = 0.0351, wR2 = 0.0857	
R indices (all data)	R1 = 0.0435, wR2 = 0.0911	
Extinction coefficient	n/a	
Largest diff. peak and hole	0.415 and -0.420 e.Å ⁻³	

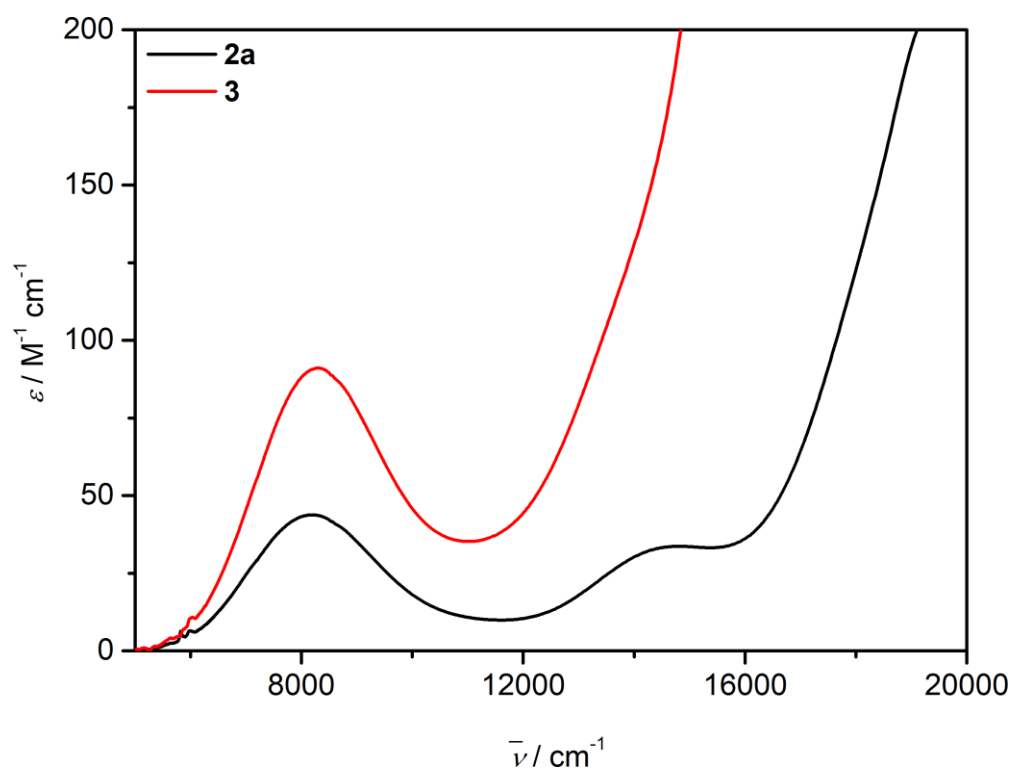


Figure 7.87: UV-Vis-NIR spectra of 2a and 3 in MeCN.

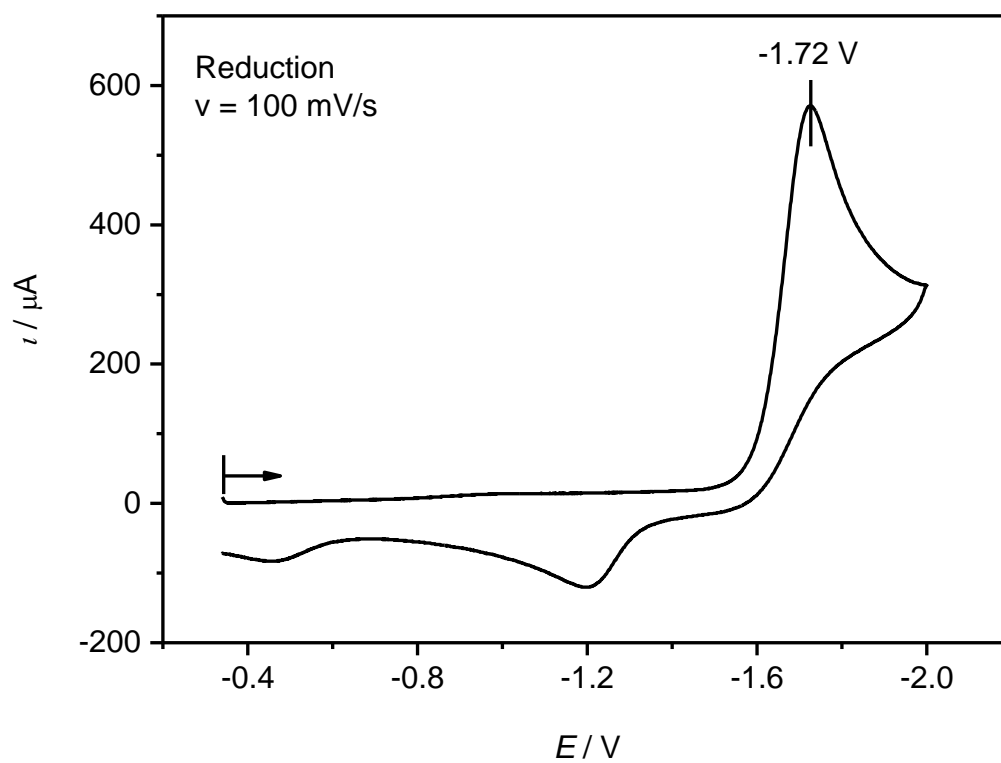


Figure 7.88: Cyclic voltammogram for the reduction of 3 in 0.2 M TBAP/MeCN sweeping with a scan rate of 100 mV s^{-1} . All potentials are given vs. SCE.

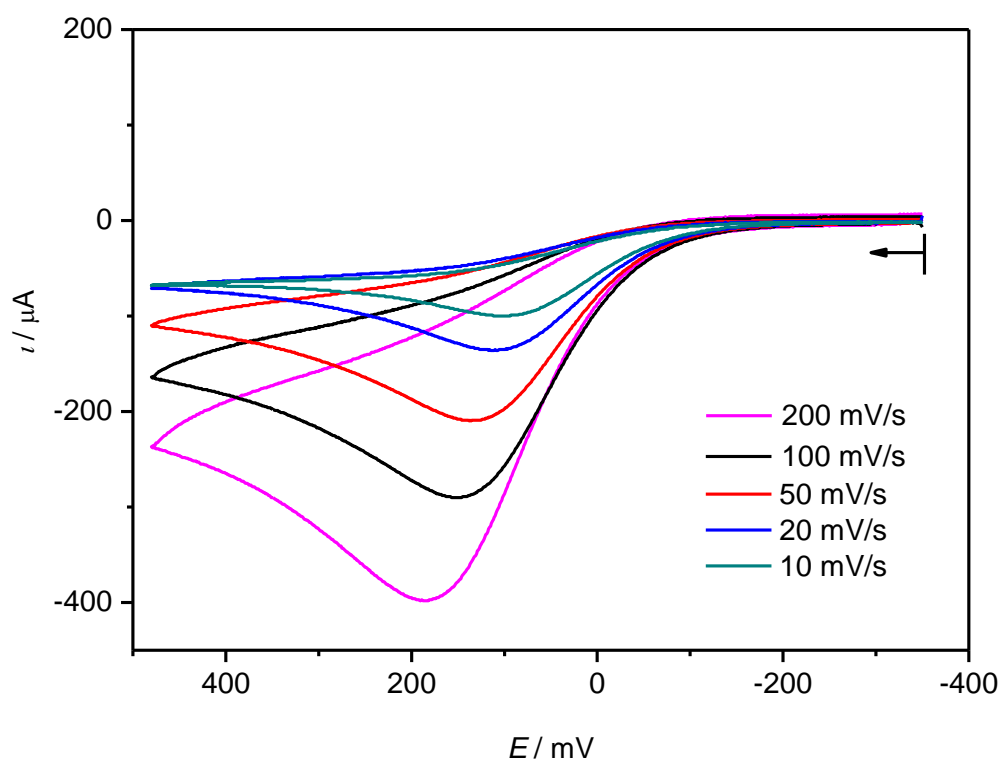


Figure 7.89: Cyclic voltammograms for the first oxidation of 3 in 0.2 M TBAP/MeCN sweeping with different scan rates. All potentials are given vs. SCE.

7.4 Reactivity of $[\{\text{Ni}(\text{L-N}_4\text{Me}_2)\}_2(\mu\text{-RC}_4\text{R})](\text{ClO}_4)_2$ [$\text{R} = \text{Ph}$] (2a) with Oxygen

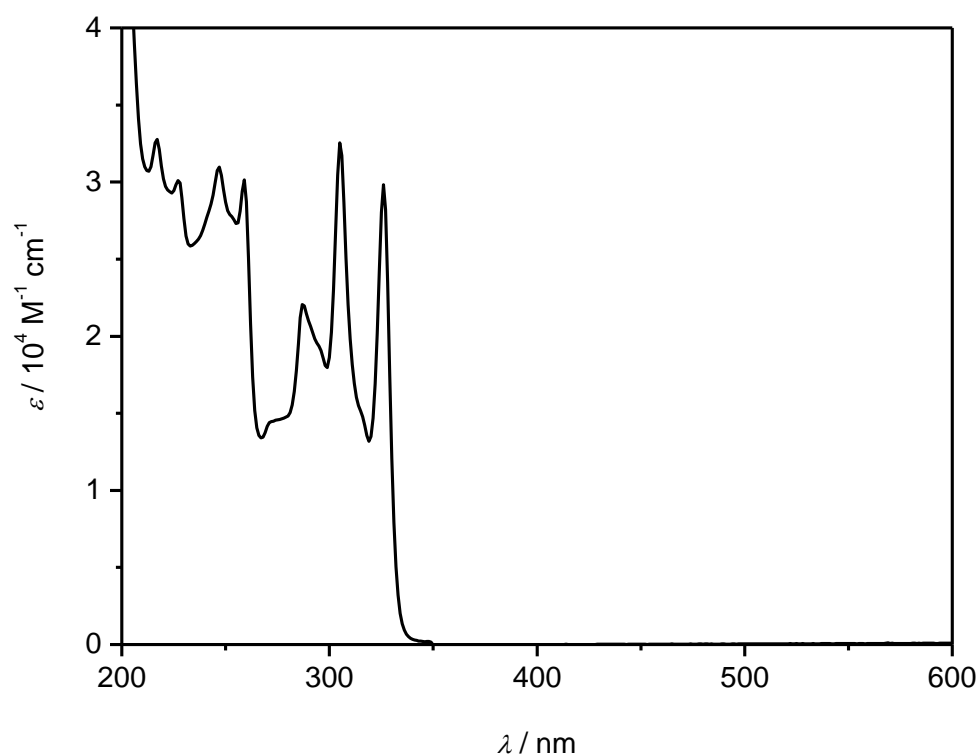


Figure 7.90: UV-Vis spectrum of diphenyldiacetylene (PhC₄Ph) in MeCN.

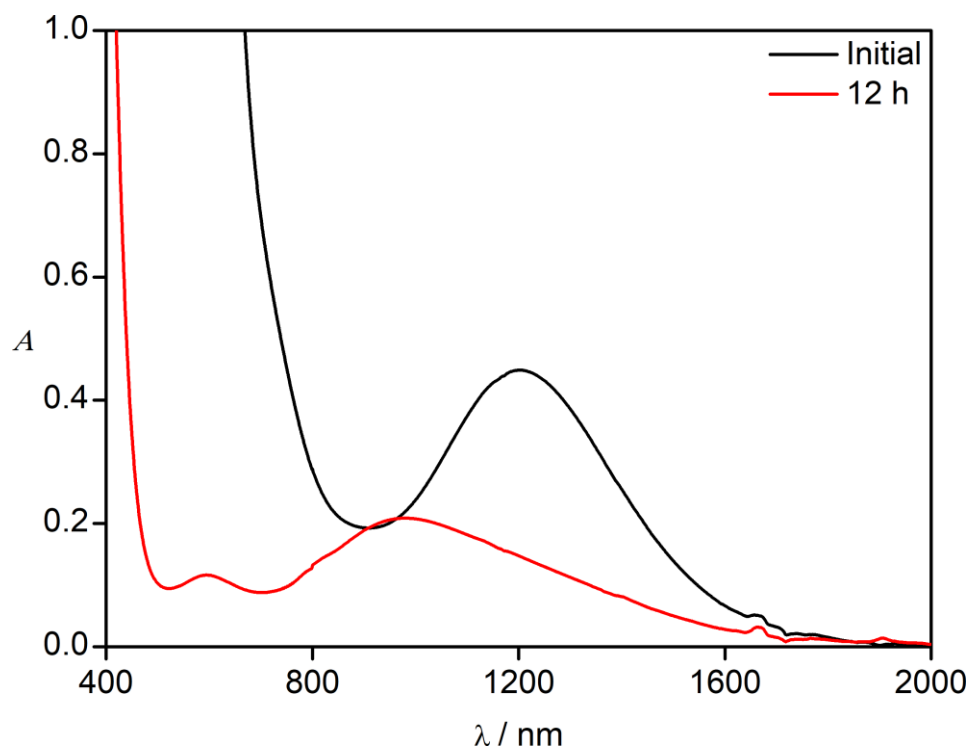


Figure 7.91: UV-Vis-NIR spectral change during the reaction of 2a (5.33 mM) and O₂ in MeCN at room temperature; initial (0 min) and 12 h.

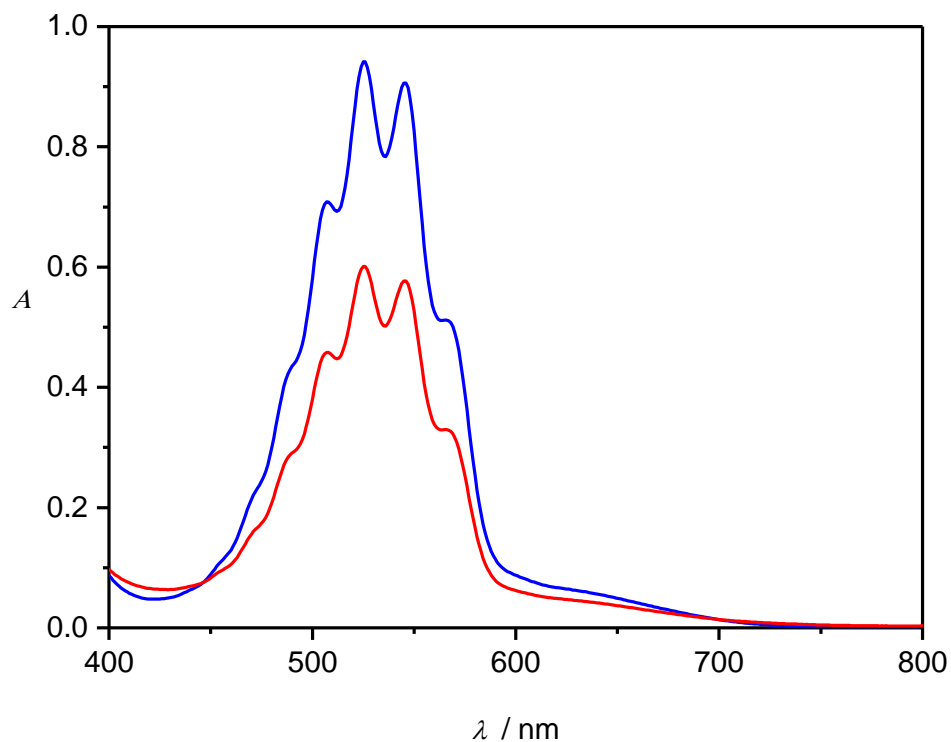


Figure 7.92: UV-Vis spectrum showing the change in absorption of KMnO_4 (2.5 mL of a 4 mM aqueous solution; blue line) which occurs upon the addition of H_2O_2 (0.1 mL of H_2SO_4 solution, red line) which is produced in the reaction between H_2SO_4 (~ 1 mL, 0.5 M) and white solid (Li_2O_2).

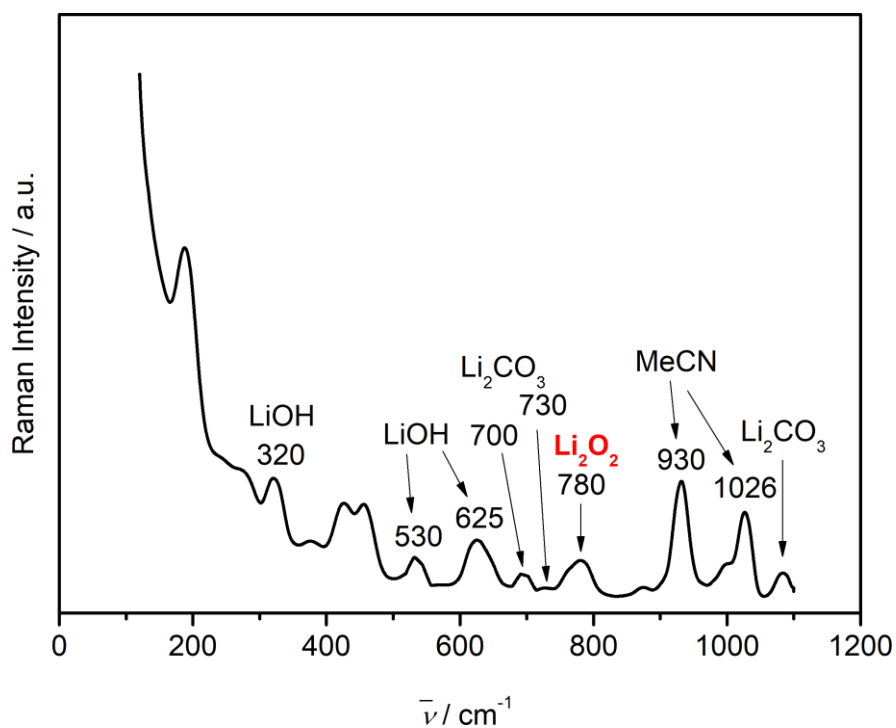


Figure 7.93: Raman spectrum of the solid isolated from the reaction of 2a and O_2 in presence of LiClO_4 . Li_2CO_3 and LiOH could be formed by the reaction of Li_2O_2 and air. MeCN: reaction solvent.^[150-154, 165-169]

7.5 Reactivity of $[\text{Ni}(\text{L-N}_4\text{Me}_2)(\text{PhC}_2\text{Ph})](\text{ClO}_4)\cdot\text{MeOH}$ (3) with Oxygen

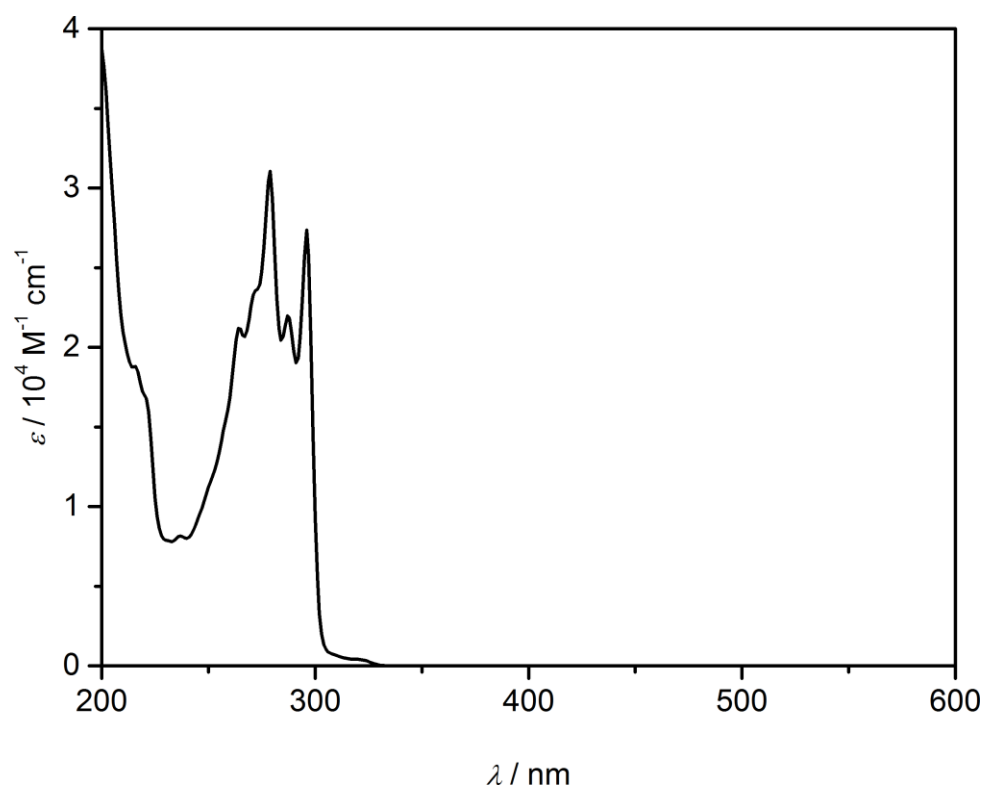


Figure 7.94: UV-Vis spectrum of diphenylacetylene (PhC₂Ph) in MeCN.

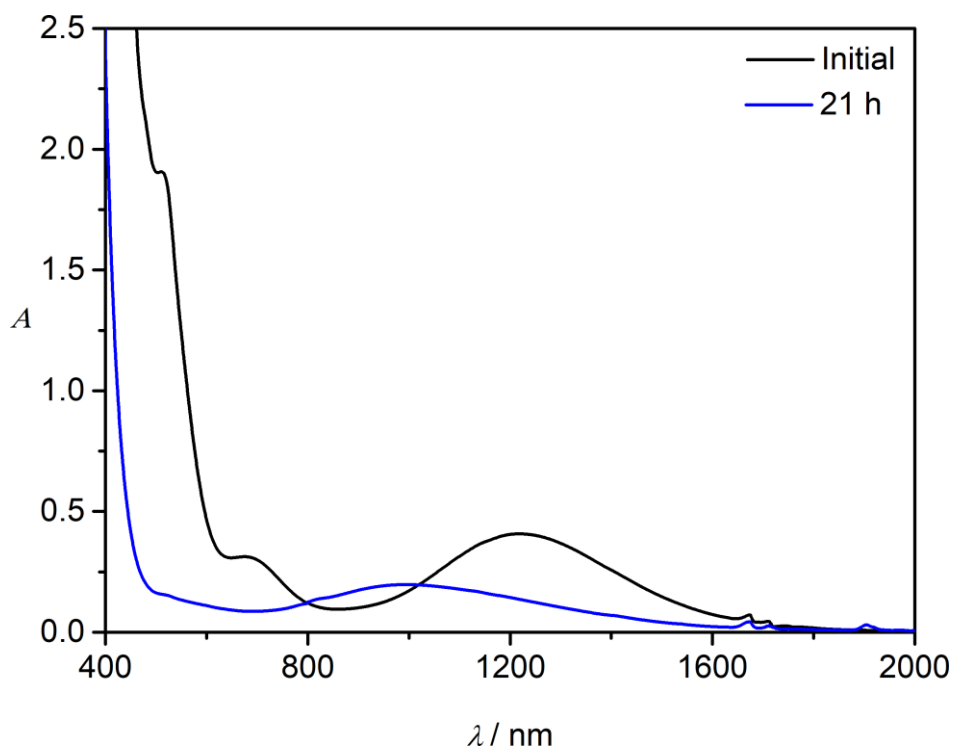


Figure 7.95: UV-Vis-NIR spectral change during the reaction of 6 (9.07 mM) and O₂ in MeCN at room temperature; initial (0 min) and 21 h.

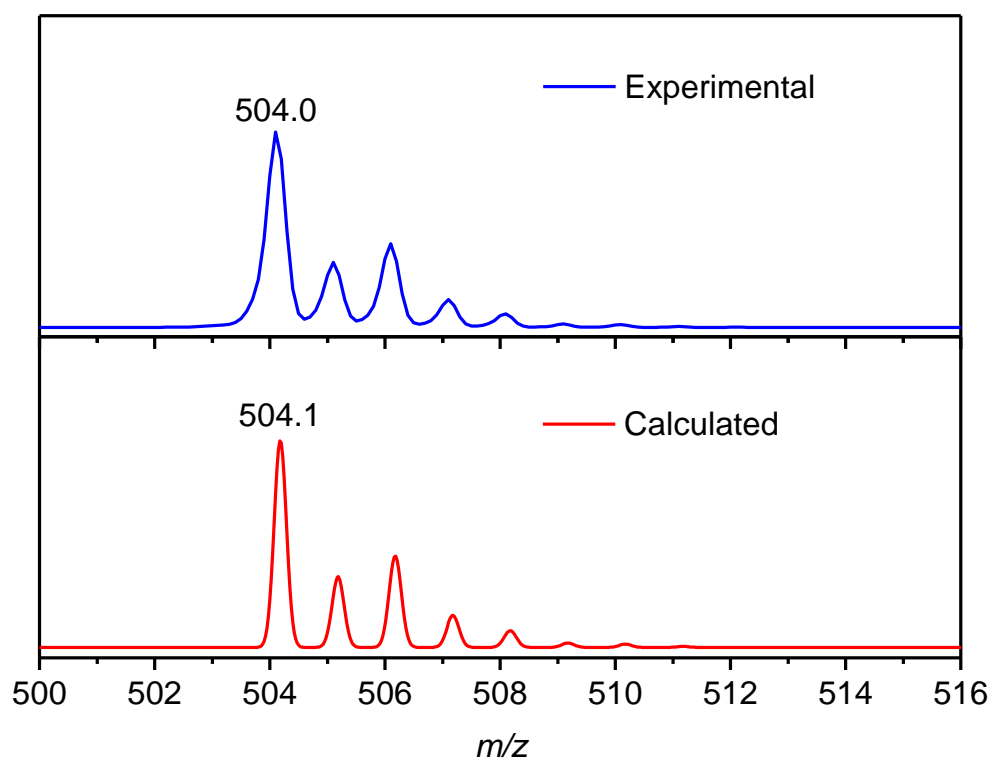


Figure 7.96: The experimental and calculated isotope distribution for $[\text{Ni}(\text{L}-\text{N}_4\text{Me}_2)(\text{PhC}_2\text{Ph})]^+$.

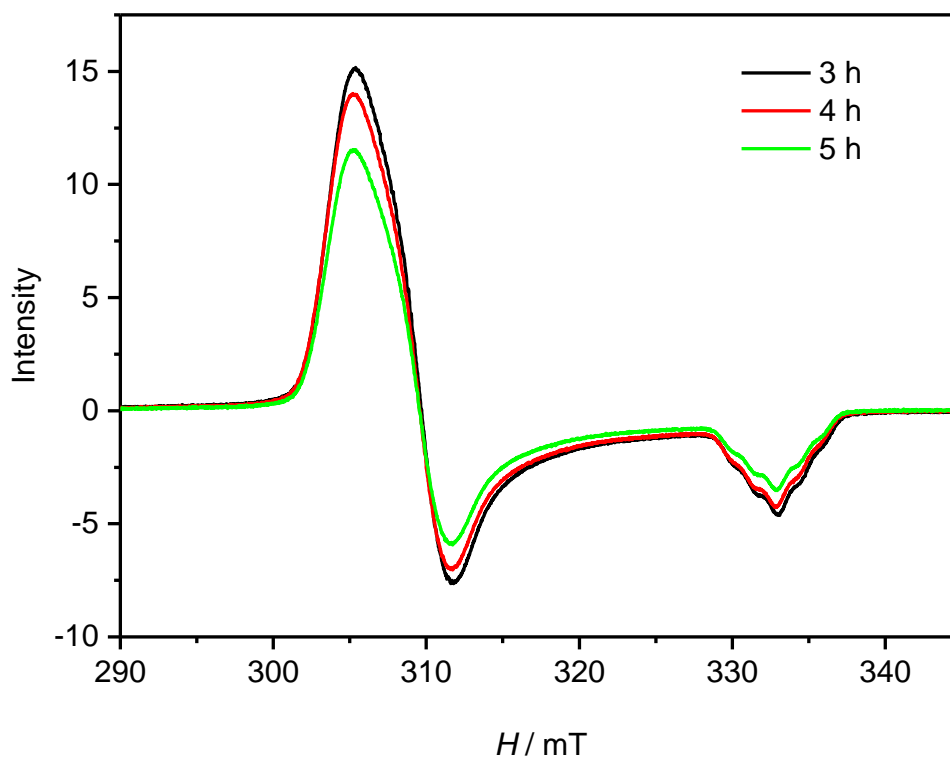
7.6 $[\text{Ni}(\text{L-N}_4\text{Me}_2)(\text{O}_2)]^+$ (5)

Figure 7.97: X-Band EPR spectra of the solutions from the reaction of 1 with KO_2 in 0.2 M TBAP-MeCN at -35°C at different time interval (3-5 h). All spectra are recorded at 77 K.

7.7 Nickel-Mediated Catalytic Reaction

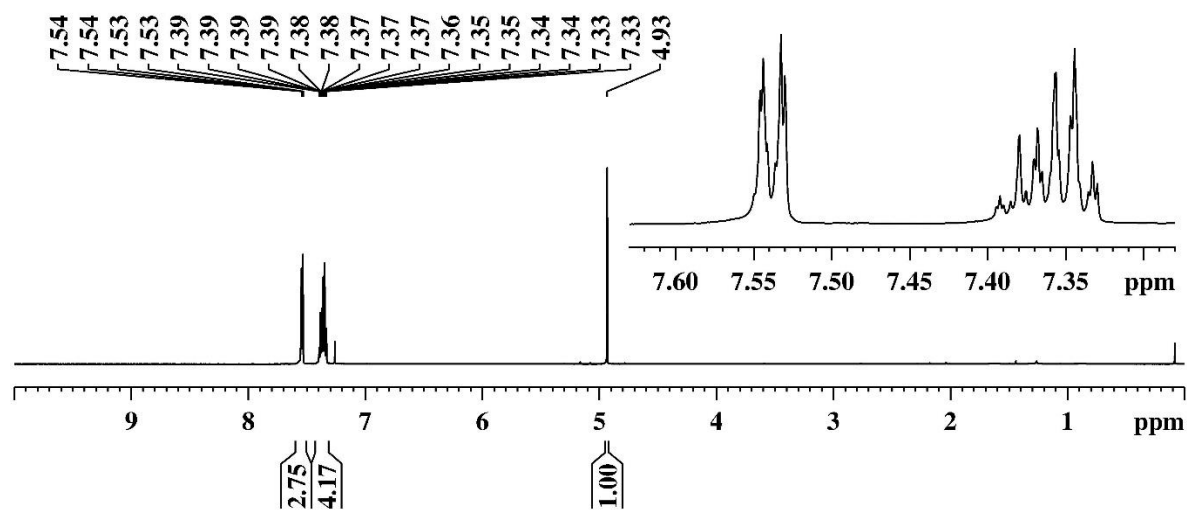


Figure 7.98: $^1\text{H-NMR}$ (600 MHz) spectrum of crude product of catalytic reaction in CDCl_3 using CH_2Br_2 as an internal reference. Inset shows the magnified region.

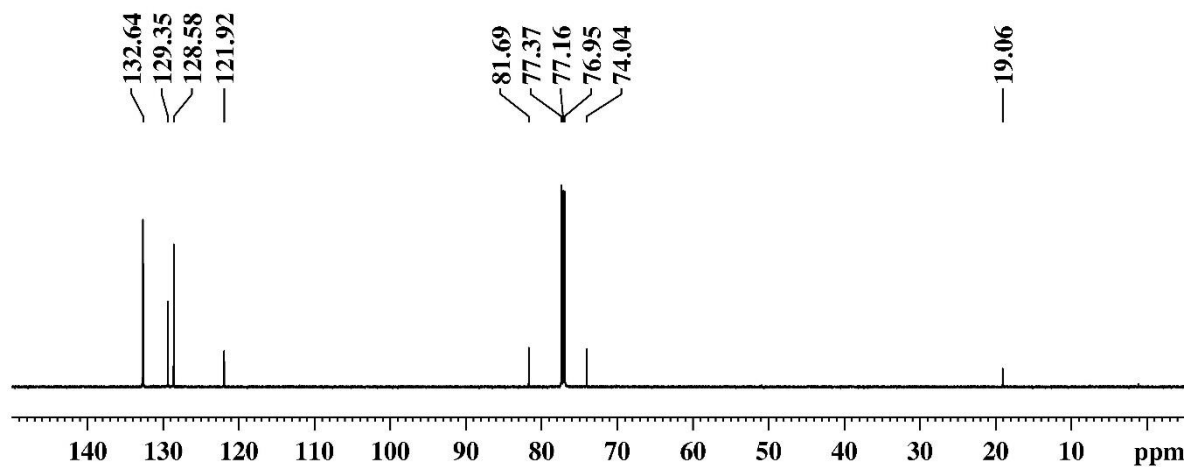


Figure 7.99: $^{13}\text{C-NMR}$ (150.9 MHz) spectrum of crude product of catalytic reaction in CDCl_3 using CH_2Br_2 as an internal reference.

7.8 Spectroscopy Studies on Catalytic Reaction

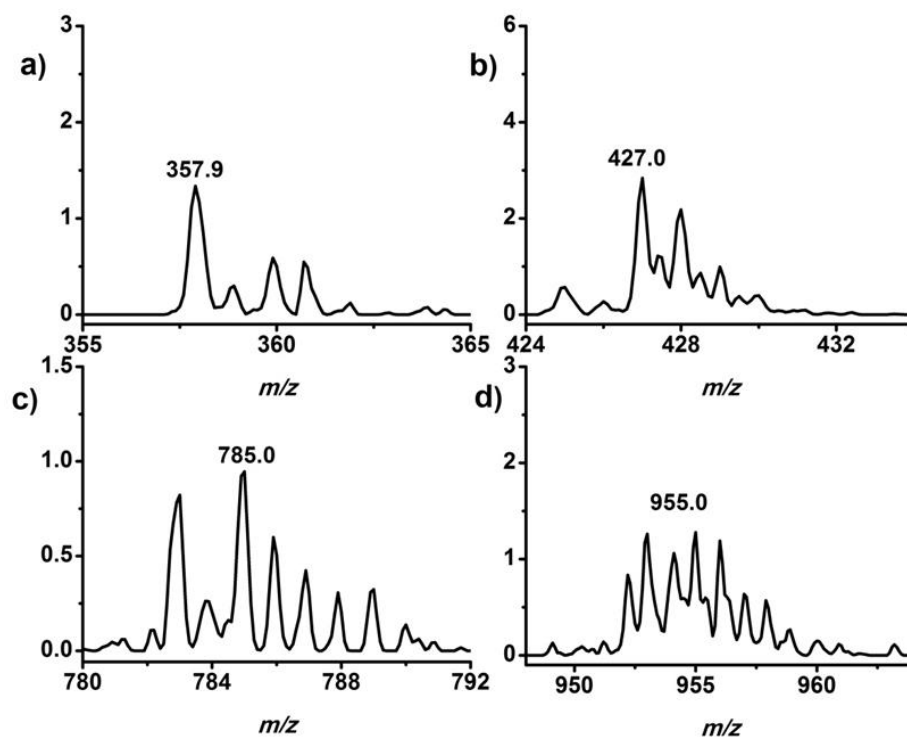


Figure 7.100: The expanded regions of ESI-MS spectrum of the catalytic reaction mixture in MeCN. a) $m/z = 355 - 365$; b) $m/z = 424 - 434$; c) $m/z = 780 - 792$ and d) $m/z = 948 - 964$. Y components: Intensity (10^4).

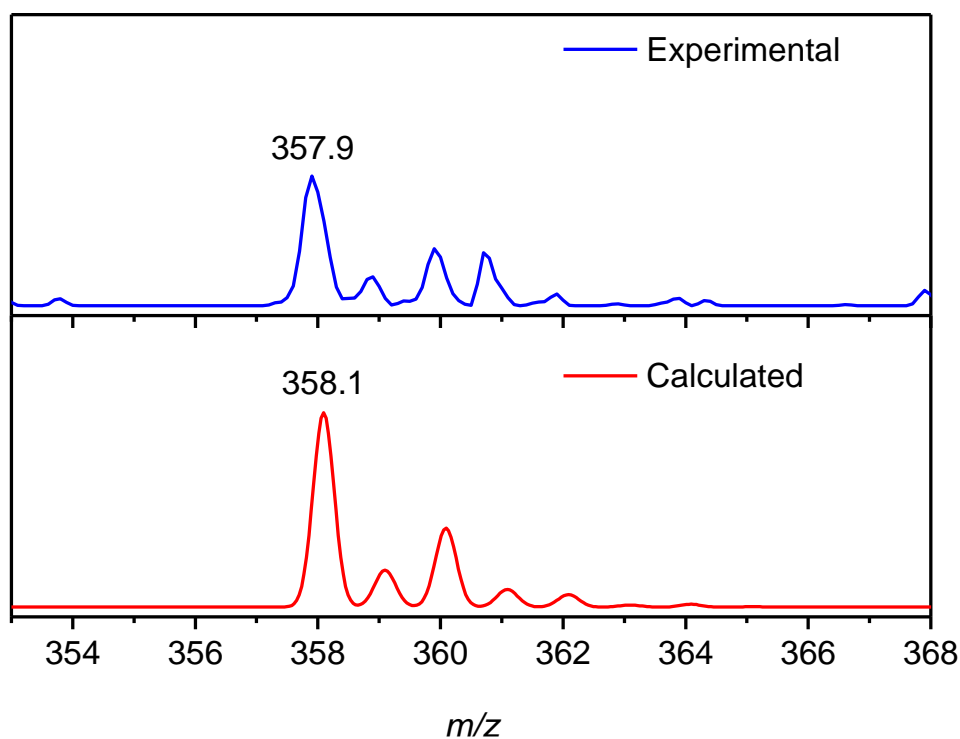


Figure 7.101: The experimental and calculated isotope distribution for $[\text{Ni}(\text{L-N}_4\text{Me}_2)(\text{O}_2)]^+$.

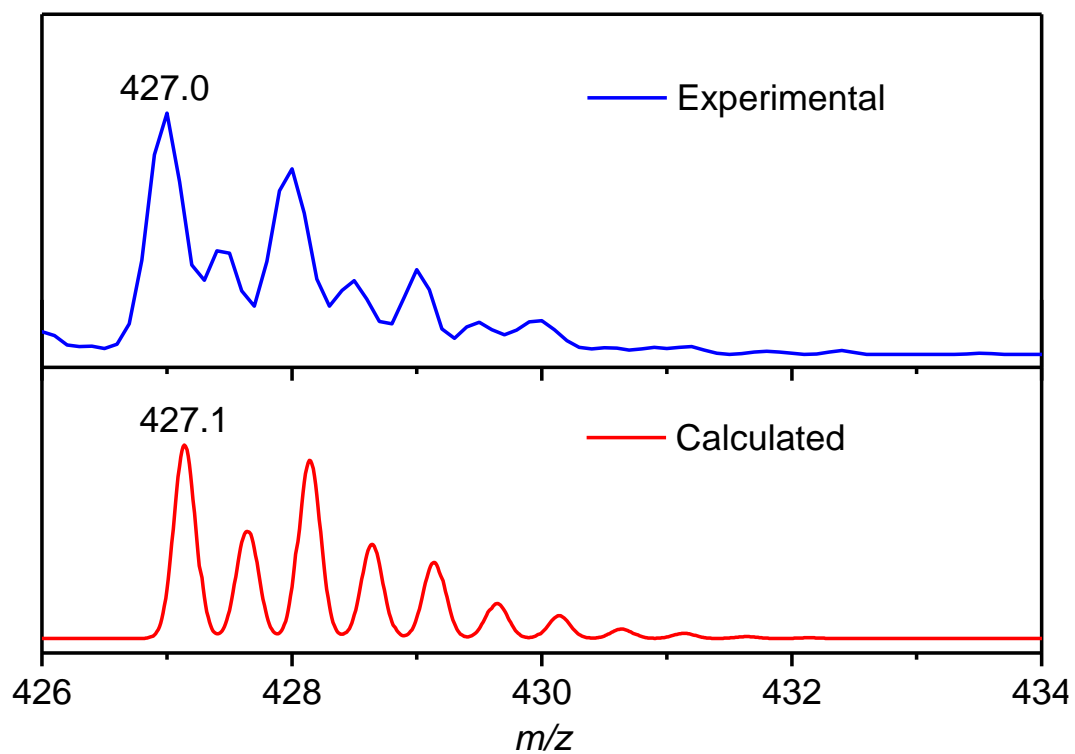


Figure 7.102: The experimental and calculated isotope distribution for $[\text{Ni}(\text{L-N}_4\text{Me}_2)_2(\mu\text{-PhC}_4\text{Ph})]^{2+}$.

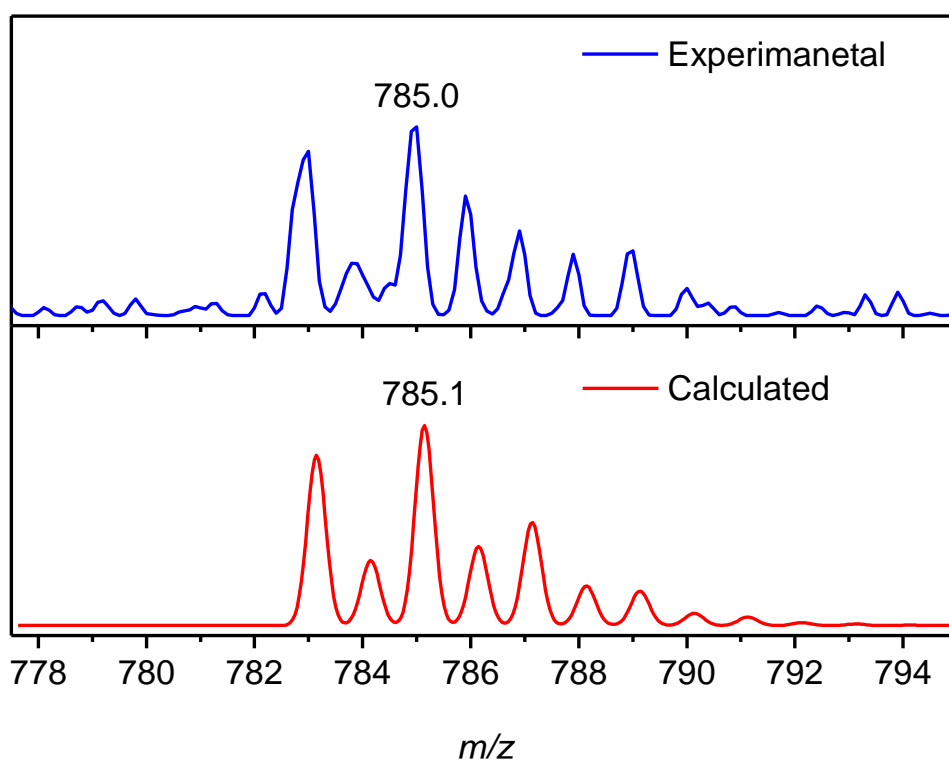


Figure 7.103: The experimental and calculated isotope distribution for $[\text{Ni}(\text{L-N}_4\text{Me}_2)_2(\text{O}_2)(\text{ClO}_4)]^+$.

8 Curriculum Vitae

SUBRATA GHOSH

EDUCATION

Technische Universität Kaiserslautern, Germany 2010-Present

Ph.D., Inorganic Chemistry

Thesis title: "A Mechanistic Insight into the Nickel-Catalyzed Homocoupling Reaction of Terminal Alkynes"

Supervisor: Prof. Hans –Jörg Krüger, Ph.D.

Indian Institute of Technology, Kanpur, India 2008 - 2010

M.Sc., Chemistry

Thesis title: "Investigation of C-H...Cl Hydrogen Bonding Using Inorganic Supramolecular Synthons; Synthesis and Characterization of Fe(III) Complex with a Tetradentate 4N Ligand"

Supervisor: Prof. Rabindranath Mukherjee

C.P.I. = 8.5/10

University of Calcutta, India 2005 - 2008

B.Sc., Chemistry (Honours)

Marks: 72.5 %, Class: 1st Class

PUBLICATION

- [1] "Capture of CO₂ by a cationic Ni^I complex in the gas phase and characterization of the bound activated CO₂ molecule through cryogenic ion vibrational predissociation spectroscopy"

F. S. Menges, S. M. Craig, N. Tötsch, A. Bloomfield, S. Ghosh, H.-J. Krüger, M. A. Johnson, *Angew. Chem. Int. Ed.* **2016**, *55*, 1282 –1285 (**Hot Paper**) (**Frontispiece**).

CONFERENCES

- [1] Oral presentation at **13. Koordinationschemie-Treffen**, Potsdam, Germany, **2017**.
- [2] Oral presentation at **15th Ferrocene Colloquium**, Mainz, Germany, **2017**.
- [3] Participant at "Methods in Molecular Energy Research: Theory and Spectroscopy Summer School", Essen, Germany, **2013**.
- [4] Oral presentation at **8. Koordinationschemie-Treffen**, Dortmund, Germany, **2012**.